Development of Gold Nanoparticles for Targeting PD-L1-Presenting Breast Cancers

by

Derek James Blevins

B.Sc., University of Calgary, 2017

A Dissertation Submitted in Partial Fulfillment of the Requirements for the Degree of

DOCTOR OF PHILOSOPHY

in the Department of Chemistry

We acknowledge and respect the lək̓ʷəŋən peoples on whose traditional territory the university stands and the Songhees, Esquimalt and W̱SÁNEĆ peoples whose historical relationships with the land continue to this day.

Supervisory Committee

Development of Gold Nanoparticles for
Targeting PD-L1-Presenting Breast Cancers

by

Derek James Blevins

B.Sc., University of Calgary, 2017

Supervisory Committee

Professor Jeremy Earle Wulff, Supervisor
Department of Chemistry (University of Victoria)

Professor Matthew Moffitt, Departmental Member
Department of Chemistry (University of Victoria)

Associate Professor Lisa Reynolds, Outside Member
Department of Biochemistry and Microbiology (University of Victoria)

Abstract

Our goal was to selectively target the immunosuppressive programmed cell death protein ligand 1 (PD-L1) presenting cancer cells with gold nanoparticles (AuNP). Initially, small molecules, described as antagonists for the PD-1/PD-L1 interaction, were considered as promising targeting agents for the gold platform. The competitive binding profiles of these molecules were evaluated using surface plasmon resonance (SPR). However, we found that none of the small molecule candidates were capable of disrupting the interaction, despite their apparent cell-based efficacy in other literature. Our findings indicate that the molecules were being mischaracterized as immunomodulators directly blockading the PD-1/PD-L1 interaction. In addition, we found no evidence of direct binding with the small molecules to either PD-1 or PD-L1, indicating they would not be suitable candidates as targeting agents. Instead, a commercially available monoclonal antibody (mAb, αPD-L1; from BioXCell) was found as a suitable alternative for targeting and blockading PD-L1 directly from PD-1.

The antibody was conjugated with α-lipoic acid (αLA) through its NHS-ester such that the thiolated mAb may be grafted to functionalize the gold cores. The degree of functionalization on the gold core was quantified in vitro using SPR, where the relationship between valency and molecular weights of the gold core and unbound mAb binding to PD-L1 was studied.

This SPR method was primarily used further to optimize the AuNP formulations until they were deemed suitable for cellular work. Gold cores with a surface area coated in 25% αLA-mAb and 75% PEG_{2000} had shown a near maximal response of binding relative to the unbound mAb, indicating a high degree of functionalized nanoparticles. This formulation was then moved forward into cellular work with naïve human white blood cells (Jurkat) that were stimulated with PHA (to produce PD-1), and the stimulation suppressed by the presence of PD-L1.

In addition to AuNP formulation, we sought to investigate controlled release mechanisms indicative of the reducing character of the tumour microenvironment. We developed a series of disulfide tethers with a fluorogenic dye that induces turn-on fluorescence upon disulfide exchange, expected to show selectivity for the higher concentration of glutathione. Instead, we found that the common, but necessary, additive, fetal bovine serum (FBS), was triggering the premature release of our tethered fluorophore, disrupting our intended controlled-release studies. Through systematic investigation, we found that unwanted turn-on fluorescence from our dithiodiacid tethers was ultimately occurring due to esterase activity found in the FBS. This activity was shut down when methyl groups were installed at the α-position to the carbonyl carbon. Future work may use these bulkier dithiodiacid tethers for selective release in other AuNP formulations.

Immunotherapeutic efficacy of the functionalized AuNPs was investigated by showing consistent stimulation in the presence of immunosuppressive PD-L1. Naïve Jurkat cells were stimulated with phytohemagglutinin (PHA), where the cell density would significantly increase relative to basal cell growth, and in the presence of solubilized PD-L1, show no change in density attributed to T cell exhaustion. When AuNPs were present, the cell density would reflect that of “uninhibited” stimulation control, regardless of PD-L1 presence, indicating the potential immunotherapeutic benefit of recovery from immune exhaustion.

Table of Contents

Summary of Contents

Table of Figures

Table of Tables

Table of Schemes

List of Abbreviations

4-MU	4-methylumbelliferone
ADCs	antibody-drug conjugates
APC	antigen-presenting cell
ATR-IR spectroscopy	attenuated total reflectance infrared spectroscopy
AuNPs	gold nanoparticles
B7 superfamily	immunoglobulin homologs that contain Ig-V and Ig-C domains
BBB	blood-brain barrier
BC-loop	domain of PD-L1
BCA	bicinchoninic acid
BMS	Bristol-Myers Squibb
CA-170	small molecule from Aurigene Pharmaceuticals and Curis Inc.
CAP chip	capture chip
CM chip	carboxymethyl dextran
CTLA-4	cytotoxic T-lymphocyte associated protein 4
Cys	cysteine
DCM	dichloromethane
DDC	dicyclohexyl carbodiimide
DIC	*N,N'*-diisopropyl carbodiimide
DIPEA	diisopropyl ethylamine
DLS	dynamic light scattering
DMAP	*N,N'*-dimethylamino pyridine
DMEM	Dulbecco's Modified Eagle Medium
DNA	deoxyribonucleic acid
EC_{50}	effective concentration 50%
ECM	extracellular matrix
EDC	1-ethyl-3-(3-dimethylaminopropyl) carbodiimide

ELISA	enzyme-linked immunosorbent assay
EPR effect	enhanced permeation and retention effect
EtOAc	ethyl acetate
FBS	fetal bovine serum
FDA	(U.S.) Food and Drug Administration
GFP	green fluorescent protein
GRAS	general regarded as safe
GSH	glutathione (reduced formed)
GSSG	glutathione (oxidized formed)
H_2O_2	hydrogen peroxide
HATU	1-[bis(dimethylamino)methylene]-1*H*-1,2,3-triazolo[4,5-*b*]pyridinium 3-oxid hexafluorophosphate
HBTU	*N,N,N',N'*-tetramethyl-*O*-(1*H*-benzotriazol-1-yl)uronium hexafluorophosphate
HDR	hydrodynamic radius
HEK293	human embryonic kidney 293 (no PD-L1 expression)
HER2	human epithelial growth hormone receptor 2
Hex	hexanes
HNDF	human normal dermal fibroblasts
HSQC	heteronuclear single quantum coherence NMR spectroscopy
IC_{50}	inhibitor concentration 50% - concentration that results in 50% activity
ICI	immune checkpoint inhibition
ICIs	immune checkpoint inhibitors
IgG	immunoglobulin gamma (aka mAb)
IL-2	interleukin-2
IL-6	interleukin-6
K_D	dissociation constant (ratio of on- and off-rates at equilibrium)
k_{off}	rate of dissociation
k_{on}	rate of association/binding

LD_{50}	lethal dose to 50% a population - whole organisms
mAb	monoclonal antibody
mAbs	monoclonal antibodies
MB-MDA-231	metastatic breast MD Anderson 231 (has PD-L1 expression)
*m*CPBA	*meta*-chloroperoxybenzoic acid
MeCN	acetonitrile
MEM	minimal essential medium
MHC II	major histocompatibility complex II
MWCO	molecular weight cutoff
NHS	*N*-hydroxysuccinimide
nM	nanomolar (concentration; $1 \cdot 10^{-9}$ mol/L)
NMR	nuclear magnetic resonance
PCL	polycaprolactone
PLGA	poly(lactic-co-glycolic) acid
PD-1	programmed cell death protein 1
PDB	protein databank
PD-L1	programmed cell death protein ligand 1
PD-L2	programmed cell death protein ligand 2
PDT	photodynamic therapy
PEG	polyethylene glycol
PHA	phytohemagglutinin
PIC	protease inhibitor cocktail
PKC	protein kinase C
PLA	polylactic acid
pM	picomolar (concentration; $1 \cdot 10^{-12}$ mol/L)
PMA	phorbol 12-myristate 13-acetate
PNP(s)	polymer nanoparticle(s)

PTFE	polytetrafluoroethylene
PTT	photothermal therapy
RES	reticuloendothelial system
RGD peptide	internalization peptide with motif of *arginine-glycine-aspartate*
ROS	reactive oxygen species
RPMI 1640	Roswell Park Memorial Institute 1640 medium
RU	response unit
SA chip	streptavidin chip
SN-38	7-ethyl-10-hydroxycamptothecin
SNT	peptide motif of *serine-asparagine-threonine*
SPR	surface plasmon resonance
TCEP	tris-carboxyethyl phosphine
TEM	transmission electron microscopy
TME	tumour microenvironment
TNBC	triple-negative breast cancer
TNFα	tumour necrosis factor alpha
Tris	*tris*(hydroxymethyl) aminomethane
U-251	malignant glioma cell line
U-87	Uppsala 87 malignant glioma
UV-vis spectroscopy	ultraviolet-visible light spectroscopy
VISTA	variable-domain Immunoglobulin suppressor of T cell activation; V-domain Ig suppressor of T cell activation
αCD28	a mAb that targets CD28
αCD3	a mAb that targets CD3
αLA	alpha-lipoic acid
αPD-L1	a mAb that targets PD-L1
µM	micromolar (concentration; $1 \cdot 10^{-6}$ mol/L)

I want to thank my family and group for their unending support that helped me finally finish this thing. Especially from my grandparents and mom who gave me the opportunity to live and study out here on gorgeous Vancouver Island.

1. Introduction

The Impact of Gold as a Nanomedicine

The purpose of this research is to develop targeted gold nanoparticles (AuNPs) to treat triple-negative breast cancer (TNBC) in a novel bi-functional manner. The first function emulates that of modern immunotherapeutic agents by targeting PD-L1 presenting triple-negative breast cancer; the second function is delivery of the gold core to improve sensitivity of tumour cells to ionizing radiation. In the literature, there are metal nanoparticles capable of targeting and radiosensitizing, and other particles capable of immunotherapeutic response, but not together.[1–5] We want to design a nanoparticle with targeting, selective radiosensitization, and immunotherapeutic functions present but characterized in simple *in vitro* models (i.e., SPR, cellular work). Eventually and ideally these functions will continue to be measurable in more complex model systems (i.e., tissue- and animal-based work), warranting their potential benefit as an immunotherapeutic and radiotherapeutic agent when placed in a patient (Scheme 1.1).

Our intent is to provide evidence of a dual-functional particle series and characterize those intended effects, but achieving these proofs of function is not sufficient in achieving a suitable drug candidate. When designing a new drug, the initial focus of the drug candidate does not prioritize characterizing potential pharmacokinetic and -dynamic properties (e.g., off-targeting effects, toxicity, and evaluating the total selectivity), and instead appears to focus on whether it can perform its intended function. While simple *in vitro* (1-D) models may demonstrate limited efficacy, they fail to characterize effects that could be anticipated in more complex scenarios. These data may only be observable *in vivo* (i.e., biodistribution, off-targeting effects, clearance rate, toxicity), but to obtain them may only be possible if the drug candidate shows promise at performing its intended function, making development feel cyclical.

Metal nanoparticles are innovative to drug delivery systems and show promise in controlled settings, but many will fail to acquire approval for clinical use due to lack in risk assessment (e.g., adverse effects outside the scope of the intended function) where patient safety outweighs the potential efficacy.[6,7] Due to the limited research of pharmacokinetic data for gold particles, there is hesitation for their use in a clinical setting,[8–11] but with more recent advancements in characterization they are becoming more frequently approved for clinical phase I studies.[8] The hesitation derives from the lack of studies describing the long- and short-term health effects of the particles and their relationship with the host, despite many *in vitro* studies demonstrating the gold core as a useful radiosensitizer,[12,13] immune-inducer,[14,15] and imaging agent.[16,17] With such a diverse array of applications, it is unfortunate that they are not being used more broadly. There is too much uncertainty of stability of the cores, their potential toxicity to non-targeted tissues, and how the metabolized drug could become problematic to the patient without resolution.[18] While more *in vitro* investigations modeling pharmacokinetic and pharmacodynamic studies would improve confidence of safety, there is no standardization in particle processing. Therefore, with more comprehensive *in vitro* investigation characterizing ADME properties (adsorption, distribution, metabolism, excretion), in addition to the intended efficacious effects, should reduce the barrier preventing the use of metal nanoparticles. [7]

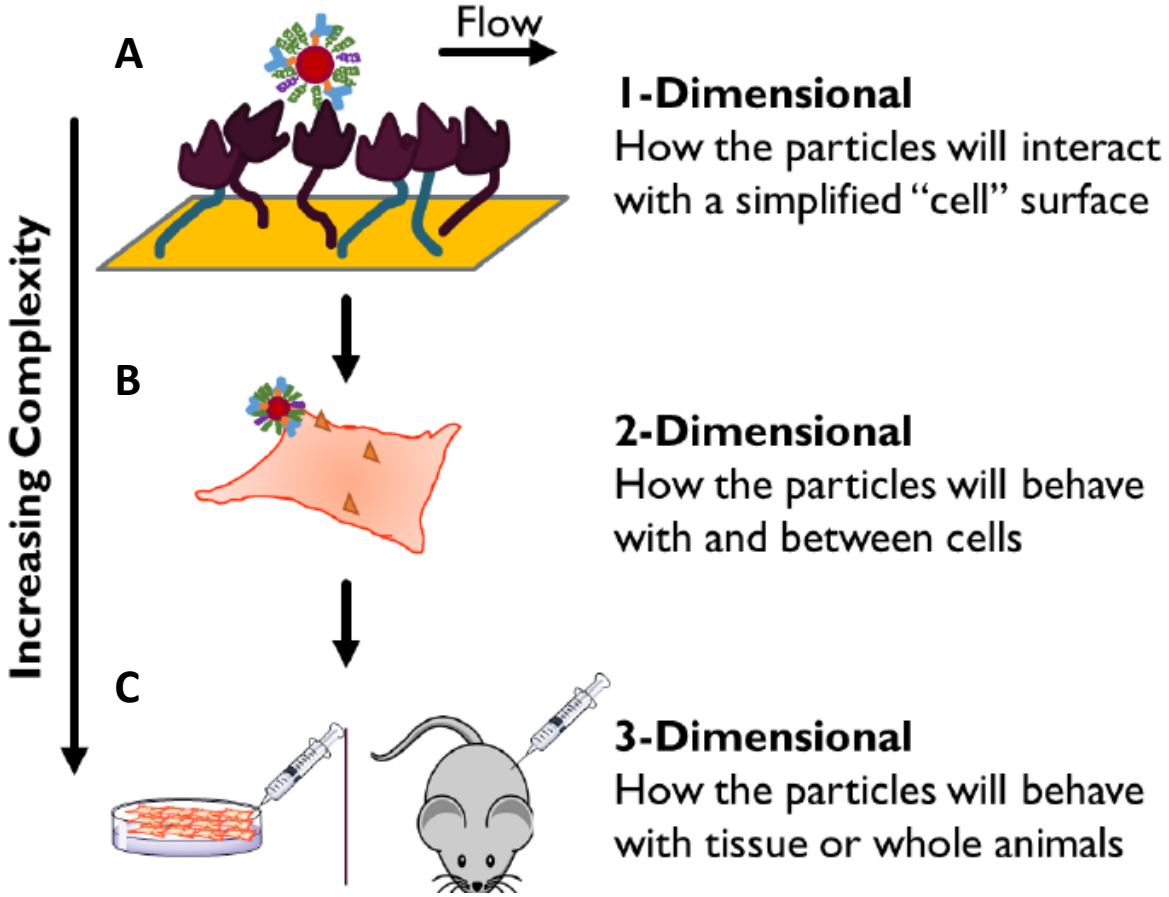

*Scheme 1.1. Proposed "fail-fast" models of characterization. The characterized function should be persistent in more complex systems (i.e., protein specificity (**A**), cell selectivity (**B**), efficacy in organisms (**C**)).*

Although there is evidence indicating selectivity/specificity with initial proof-of-concept studies incorporating directly relevant cells, there is not much investigation beyond the region of interest/disease site.[19–21] More thorough characterization of how particles interact outside of the disease site will benefit both development of new systems, as well as take into consideration the impact those nanoparticles may have on the patient, which is ultimately the reason why many nanoparticle systems are not being used.[22] By providing information that helps describe or predict data typically acquired only through animal studies (e.g., biodistribution, pharmacokinetic data, toxicity and specificity studies), we acquire more information that is useful in describing how the particles might behave outside the tumour site. Although this information appears as supplementary to the intended effects as a drug, providing it should warrant more confidence in nanoparticle use and their safety for clinical trials.

Fully comprehensive characterization of any novel drug candidate will improve its likelihood for clinical approval. For example, by characterizing the toxicological profile of AuNPs on potential off-targeting tissues (e.g., non-cancerous cells both presenting PD-L1 and not), there is now provided evidence at which the vehicles themselves could present a problem. Additionally, these effects would be useful in determining an appropriate dosing – but this model is limited as it does not take into consideration the removal of particles as they are excreted. Moreover, by determining toxicity/off-targeting effects in low-

risk scenarios, we expect to mitigate them in more complex environments. This is one aspect that provides a small scope into determining the safety of AuNPs before looking at the truly complex system of a whole animal, where troubleshooting may be more burdensome. Off-targeting effects and other uncertain consequences in hosts are a large and compelling argument to not put something foreign into a patient.

Zhang *et al*. performed a comprehensive study in 2010 detailing the various methods of gold particle administration, and found that oral administration had led to *some* intestinal damage, which could attributed to metal toxicity due to aggregation and poor uptake.[23] Their comprehensive experimental analysis intended to highlight the toxicological limits of gold nanoparticle when administered in mice. Unfortunately, since most of the gold particles arrived at the liver (likely due to opsonization),[24] subsequent doses would also be expected to deposit there, eventually leading to gold aggregation and potential toxicity. This possibility of subsequent dose-dependent metal toxicity is another factor that prevents more AuNP clinical use.[22,25]

Gold particle synthesis and functionalization is easy and well-characterized; nanoparticle size, shape, and function can manipulated with minimal protocol adjustments.[3,16,22,26–30] Metal nanoparticles have two components, the metal core and the corona surrounding it. Nanoparticle cores can vary in shape and size, typically between 5 – 100 nm, and their synthesis is aptly described in the literature.[31–33]

The corona surrounding the core stabilizes the particles, preventing aggregation and deposition.[34–36] In many cases these stabilizing agents are biocompatible polymers (e.g., polyethylene glycol (PEG),[12,37,38] polycaprolactone (PCL),[39,40] poly(lactic-co-glycolic) acid (PLGA)[41–43]). The polymers like PEG and PLGA are also used to help protect the particle from the reticuloendothelial system (RES), by evading opsonin protein adsorption through hydration, which would otherwise would lead to excretion and/or degradation via the liver and kidneys, and improving circulation times in the bloodstream.[24,44,45] Polymers like PCL with more hydrophobic character have shown better particle uptake into cells.[39,46,47] Although improving half-life circulation and reducing clearance rates may help deliver the particles passively, specifically through the enhanced permeability and retention (EPR) of tumours, there is no selectivity to differentiate between the healthy and diseased sites, and thus further modifications are required to improve delivery.[28,48] The EPR effect physically limits the particles and their targetability, as the porous nature attributed to blood vessel formation (angiogenesis) for resource collection and restricts the particle size to less than 200 nm.[5,31,49] However, the particles may not have sufficient penetration to overcome the complexity of the tumour environment.

Ideally, the nanoparticles would enter the tumour dependent on the presence of porous vasculature, but this is not always the case. The simplification and assumptions about “typical” tumours include physical and environmental characteristics attributed to the tumour microenvironment (TME). For example, the TME is hypoxic, acidic, and has a more reducing environment relative to other somatic tissues (Figure 1.1).[13,49,50] While there is evidence to suggest these distinct characteristics are present in cultured conditions and animal models, these may not be present in every tumour. Due to the unfortunate heterogeneity of cancer, we cannot rely on the EPR and passive targeting alone, which implies that other targeting methods should be considered.

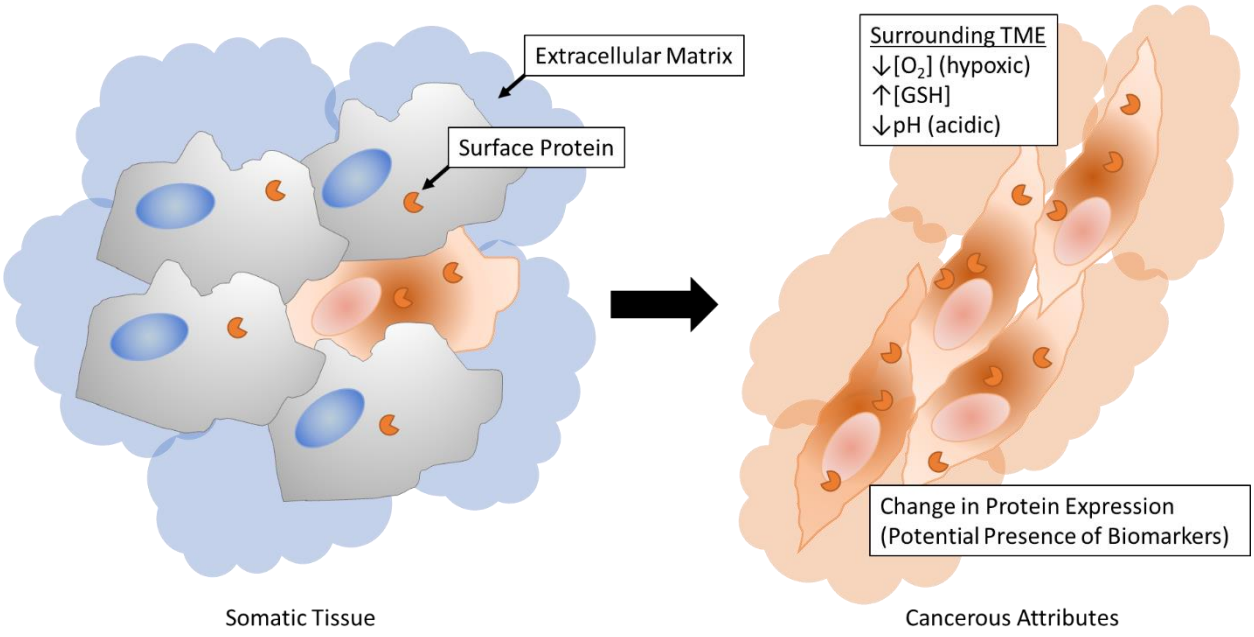

Figure 1.1. The expected physiological differences in the extracellular matrices between normal somatic cells (blue) relative to cancerous tissue (orange). The matrix surrounding tumour cells is described as hypoxic, acidic, and more reducing relative to their "healthy" counterparts. These environmental differences arise from changes in genetic expression. Furthermore, the physicochemical characteristics of the TME are used in nanotechnologies as triggers for controlled release to help distinguish between the tissue types. Another physical difference is found in the genetic expression levels, where there may be higher populations of certain proteins on the tumour surface relative to the derived tissue.

Functionalizing the AuNPs with a targeting agent (i.e., modifying the corona) improves selective delivery and uptake, and overall reduces off-targeting adverse effects.[10,51,52] By transitioning from passive to active targeting there is often an increased efficacy in drug delivery because the targeting agent promotes direct interaction between the drug and diseased tissue.[51–55] In many cases the "targets" of the targeting agents are highly expressed surface proteins, also known as biomarkers.[56–58] Unfortunately, *which* biomarkers are presented will vary on a tumour-to-tumour basis due to the intrinsic heterogeneity of cancer cells. In part, this heterogeneity results from poor regulation of checkpoints in cellar reproduction (Figure 1.2), which leads to both abnormal growth and differential protein production, relative to healthy cells.[59–62]

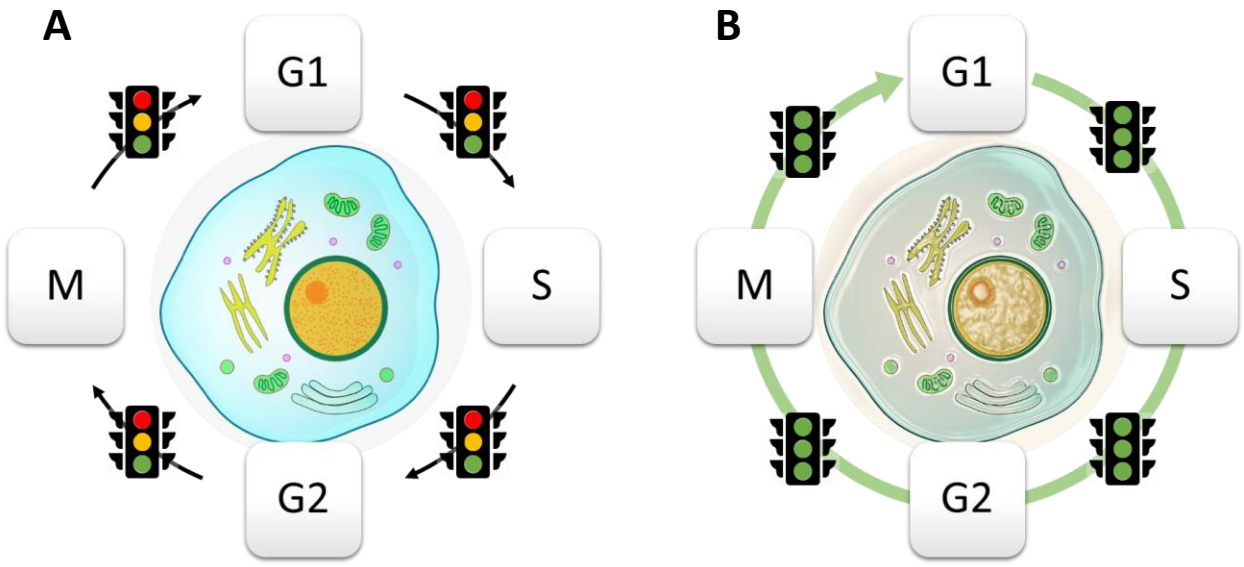

Figure 1.2. Differences in the cell cycle between a healthy cell (**A**) and representative unregulated cancer cells (**B**). The four stages of a normal cell are defined as **G1** (growth phase I), **S** (synthesis, DNA replication), **G2** (growth phase II), and **M** (mitosis, cell division). In healthy cells, each stage is tightly regulated (stoplights) to make sure there are sufficient resources to allocate *before* undergoing the following step. Whereas cancer cells ignore these tightly regulated cell functions, only the fit cells will continue to grow, eventually resulting in a tumour. Note: in reality, the stages of the cycle are not evenly split into quadrants.

A prevalent form of targeting agents are antibodies, proteins of high specificity created innately by the immune system.[63–65] By employing antibodies on the corona, the gold particles will have greater selectivity for the antigen, and therefore have a greater likelihood arriving at those sites. Despite their promise as a "magic bullet", antibodies are not sustainable on an industrial scale and often have poor uptake and physical limitations due to their large size, and thus other alternative targeting agents should be investigated.[66,67]

As stated earlier, this research is primarily focused on developing PD-L1-targeting gold nanoparticles with two proposed functions. The first series of experiments will demonstrate the selectivity of the particles as an effective targeting agent for PD-L1-presenting cells, and hopefully the binding and blockade of the PD-1/PD-L1 interaction may result in recovery of T cell exhaustion.[68,69] The other intended function of the gold core is to selectively sensitize the tumour such that less radiation may be administered, thereby reducing the likelihood of a secondary tumour.[70,71] Both functions would be expected to greatly improve patient survivability, in parallel to current combination treatments, but ideally on one drug-particle species.

Currently, AuNPs are a promising drug delivery platform, theragnostic agent, and antibacterial agent, but they struggle to complete clinical trials.[5,72,73] There is a lack of standardization relating to investigations of adverse effects, which would be useful in predicting how the drug may interact outside *the tumour site* and determining the prospective safety of that drug.[7,11] With a greater understanding of the toxicological profile of AuNPs there would be less hesitation about their use. The lack of data attributed to long- and

short-term health effects contribute to the risk aversion preventing AuNPs from being more widely used, despite being well-studied and FDA-approved.[8,73–76] Additionally, more sophisticated delivery systems will further increase the risk of propagated variation within batches (i.e., core sizes, bare AuNP vs single coating vs two coating agents, etc.). This could be remedied with more stringent processing and characterization. Unfortunately, current AuNP synthesis struggles at scaling up production, which limits the approach characterizing all apparent variables in a relatively "risk-free" setting. But there are a handful of groups that are trying to achieve this monumental task.[5,11,22,23,77]

Ideally the proposed functions would be characterized *in vivo*, but these studies are expensive and complex relative to *in vitro* research. To resolve this, the research I am proposing revolves around using a systematic approach to validate the functions from lower to higher orders of complexity (Scheme 1.1). "If it worked with cells, it would work with animals," is a fallacious argument because during the transition from a 2-D to a 3-D model there are exponentially more variables in higher order, complex systems that may not be accounted for. By directly observing the intended effects in a simple system, we expect that the mechanism will persist in more biologically relevant systems.

The Double-Edged Blade of Oversimplification; The Failure to Address the Complexity of Treating Cancers

Cancers are too simply described for how complex the disease operates. There are environmental and physiological factors that are used to describe and target cancerous states, such as the physiological differences that are expected to surround the tumour (Figure 1.1). Some of the physical factors used to describe a cancer are the location of where the cancer occurs, and the loss in regulated genetic function in specialized cells, which results in a change in the physical genetic expression. When cells lose their regulated genetic function, it leads to genetic irregularity derived from those specialized cells that *could* show changes in the expression of proteins relative to otherwise normal tissues (Figure 1.2). While both figures describe the attributes of cancers, they are reductive. These descriptors appear as mutually exclusive; however, they are occurring simultaneously and thus fail to accurately describe the heterogeneity of cancers to the public. Furthermore, the amount of information required treat the disease in an appropriate manner and unfortunately not all cancers are equally treatable.

There are five main regimens that are used to broadly treat cancers – chemotherapy, radiotherapy, immunotherapy, genetic therapy, and surgery.[66,78–80] However, due to heterogeneity of cancers, not all of them are suitable for each patient. Nanomedicines are advantageous as they improve selectivity and allow for combinations of these regimens to be more accessible, resulting in greater patient survival.[78,79,81]

Unfortunately, there is no guarantee on predicting when or where these irregular genetic functions occur. In many cases, these genetic irregularities are caught and self-regulated to shut down oncogenic behaviour through controlled cell death, or apoptosis. However, if the irregular cell behaviour is not rectified, those cells will continue to proliferate into a tumour. External factors like smoking or drinking alcohol are voluntary and increase the risk of inducing these effects,[60] some external factors are involuntary like exposure to damaging radiation,[70] or unfortunately, in some cases, are hereditary and occur spontaneously.[82] Regardless, if the cells manage to survive their damaged state, there is a chance they can develop into a tumour.

However, the irregular cell growth in cancer cells can result in characteristic protein expression (i.e., biomarkers), and these are often the first step in recognizing a cancer.[56,57,83] Although biomarkers show promise for more personalized regimens, not all cancers are expected to express them. In the best-case scenario, biomarkers are surface receptor proteins often associated with cell proliferation and may be treated with target-specific substrate mimics. Unfortunately, the expected higher expression may not be attributed to every tumour, and other broadly targeting regimens would be more suitable, but pose a risk with the lack of specificity. In other words, there is a poor correlation between biomarker-dependence and cancers in target-specific therapy.

To obtain any of that prior information, a biopsy is required. Despite the immense information that can learned from a biopsy, they are an invasive method to obtain the genetic information. Nonetheless, they offer a first-line resource in determining which regimen will be most appropriate to treat – whether determining a broad treatment or biomarker-specific chemotherapy.

In broad-scope chemotherapy, potent cytotoxic molecules are used to effectively halt cell cycle function. Unfortunately, these potent molecules are non-selective and have no ability to differentiate between diseased and healthy tissues, which leads to adverse cell death elsewhere in a patient. Adding a biomarker-targeting group onto the cytotoxic agent is an excellent first step in developing a targeted treatment to help improve the selectivity. For example, antibody-drug conjugates (ADCs) use biomarker-specific antibodies to improve drug efficacy, by improving the selectivity and reducing adverse effects.[84,85]

Many of the proteins identified as biomarkers are overexpressed growth signal receptors and checkpoint proteins, which results in the irregular growth cycle described earlier.[86] Generally speaking, it is easier to target a surface-expressed signal receptor than it is to target an internalized checkpoint protein (e.g., BRCA1).[87,88]

There are other physical factors of cancers that are used to mitigate potential off-targeting beyond surface protein expression, such as the characteristics of the tumour microenvironment (TME; Figure 1.1).[89] The TME is described as a highly reducing, slightly acidic extracellular matrix relative to otherwise healthy tissues. There is empirical evidence to suggest that passive uptake of chemotherapeutic reagents to the tumour site are attributed to angiogenesis, which allow for better pooling of those reagents at the disease site.[90–93] Despite these characteristics being present *in vitro*, there has been difficulty proving their existence *in vivo*. However, the physiochemical TME characteristics incentivized the design for triggerable controlled release that improves selectivity of non-selective chemotherapeutics,[94–97] by retaining the reagent within the vehicle until some tumour-specific external stimulus (e.g., change in pH or redox) triggers the release of the drug payload.

The characteristics of the TME are not the only physical properties used to deliver chemotherapeutics to the tumour space for the passive uptake.[52] Passive targeting therapies rely on the transient pooling at the tumour sites through the enhanced permeation and retention (EPR) effect, where the molecules enter the tumour site by the negative interstitial pressure contributing to blood vessel formation. However, relying on these attributes can lead to other barriers that limit successful delivery of nanomedicines, specifically relating to size exclusion and clearance, where non-selectively delivered drugs could cause detrimental off-targeting effects or be removed entirely. Modifying nanomedicines to accommodate

some of these barriers may reduce efficacy of delivery due to overengineering (e.g., adding a stealth polymer to improve circulation time to reduce clearance of the drug by opsonization, may also reduce likelihood of uptake at tumour site for being too large). Furthermore, with each new component for successful delivery there is increased risk of heterogeneity in the drug system, and more stringent characterization is required.

Despite incorporating a targeting agent to improve selectivity, there is a large risk where the drug would be removed from circulation prematurely due to opsonization.[24,98] This occurs due to adsorption of opsonin proteins, which are used to trigger degradation by hepatic tissue macrophages. Opsonin adsorption can be avoided by using a stealth polymer like PEG.[44,99] When a drug is recognized by the immune system, the data of the antigen will be transferred to antigen-presenting cells (APCs) to protect from future interference, which will results in an innate resistance in subsequent use to the circulating drug, and other strategies would be implemented to overcome this problem.[100] Additionally, these drug clearance factors will result in a high likelihood of off-targeted pooling at the kidneys and liver, which could be detrimental if not studied accordingly.[38,101,102] In many cases of early drug delivery and design, using biocompatible polymers and surface proteins helps avoid opsonization – improving the half-life in circulation. However, this does not address specificity for targeting.

Current Treatments and their Caveats (The Intent of Clinical AuNPs)

The suitability, compatibility, and efficacy of cancer treatment is tumour dependent on a genetic level. Cancer treatment therapies can be generalized into two major categories: chemotherapy and radiotherapy.[65,103,104] Other more specific regimens of treatment include but are not limited to: targeted drug therapy, immunotherapy,[68,105,106] gene therapy,[79,107,108] and stem cell therapy.[69,109] These can be used either separately or in tandem to combat cancer.[110–113]Despite being presented as individual methods of treatment, cancer regimens have shown greater efficacy in patient survival when taken in combination, when suitable.[69,71,114,115]

Chemotherapy is a drug regimen that attempts to use controlled doses of toxins to kill fast–growing cells. Chemotherapeutic agents often mimic substrates necessary for cell proliferation and growth processes, with the intent of disrupting the cellular machinery and halting their activity and inducing apoptosis.[59,65]

Radiotherapy is another regimen that relies on tumour location and dimensions for effective treatment.[65,116] Some radiotherapies use ionizing radiation that irreparably damages DNA resulting in cell death. However, this form of treatment requires overestimating the volume such that the surrounding tissue is also critically exposed and damaged. In brief, when a patient is subjected to ionizing radiation that damages DNA, and if the DNA is not appropriately repaired, it will result in local cell death.[59] However, like chemotherapeutics, photons are unable to discriminate between healthy and diseased tissues, and the damage induced can lead to other oncogenic effects.[70,117] The photons interact with atoms through the photoelectric or Compton effect.[5,118–120] In general, both scenarios involve ionizing radiation that causes the expulsion of secondary photoelectrons from the atom. The photoelectrons will cascade causing the formation of reactive oxygen species (ROS), and these species damage the cellular environment that will eventually lead to apoptosis. In the best-case scenario, the collateral tissues are also destroyed. However in some cases, the damage may induce a new, secondary cancer.[59,70] Another form of

radiotherapy uses localized non-ionizing radiation and noble metals to effectively "cook" the affected region with photothermal (PTT)[22,121] and photodynamic therapies (PDT).[11,18]

Both chemo- and radiotherapies are imperfect solutions since both lack specificity and selectivity necessary to treat the cancer alone. Both therapies also risk adverse effects such as collateral damage in off-targeting,[122] and innate resistance from subsequent exposure.[13,123] In the former case, chemotherapeutic reagents will circulate outside the tumour site and could cause detrimental damage to otherwise healthy cells. The latter, while more *focused*, also will damage surrounding healthy tissue, as more drug would be required to become efficacious that may result in more surrounding tissue damage.[124] Similarly for radiation-based therapies, by wholly enveloping the tumour to ionizing radiation the surrounding cells are also exposed in a non-selective manner and consistent dosing may result in more radioresistant. In the worst-case scenario for **both** regimens, these off-targeting effects could induce a secondary cancer.[59,70]

Gold particles are a valuable asset in making radiotherapy safer by mitigating exposure, through targeted delivery to a tumour less radiation to be administered to the patient.[119,125,126] Hainfeld *et al*. had demonstrated this by passively treating tumours in mice, with or without AuNPs, and at high or low amounts of ionizing radiation. They found that tumours treated with AuNPs and a lower dose of radiation had similar efficacy to a "normal" dose without particles.[1,2,125] This beneficial effect is known as radiosensitization, and it greatly reduces the collateral damage in tissues during radiation-based therapies, which also reduces the risk of secondary therapy-induced cancers.[70,127] However, successful delivery of the core to the tumour site is difficult without functionalizing the corona with a targeting agent.

Targeted drug delivery improves selectivity in chemotherapy by targeting biomarkers present on the cell surface to help focus delivery of the drugs.[3,4,41,128–131] As previously mentioned, biomarkers can assist in the prognosis of a cancer. The presence of biomarkers means the tumour would be suitable for targeted drug delivery. However, these biomarkers are not always present in all cancers due to their genetic variation, thus further innovation is required.

For example, breast cancers are commonly tested for the expression levels of "cell growth" signal proteins: estrogen receptor, progesterone receptor, and human epidermal growth factor receptor.[56,129–131] The degree of expression is often much higher than basal levels making them prime for target therapies, but they may not always be present due to the heterogeneity of cancers.[65,132] Unfortunately, there is an aggressive subtype of breast cancer which lacks these receptors, aptly named *triple-negative* breast cancer (TNBC), making initial tumour targeting difficult.[65,82,130] Despite an ineligibility for traditional endocrine-targeted therapy, there are other potential biomarkers associated with TNBC.[82,133–136] One of these biomarkers is the immune checkpoint protein, PD-L1.[130,137,138]

Broadly speaking, immunotherapy intends to utilize the host's immune system to selectively target and mitigate tumour growth.[139,140] Immune checkpoint inhibition (ICI) therapy, is subtype of immunotherapy that targets proteins that may be suppressing immune activity, allowing for the immune system recognize and destroy the tumour (Scheme 1.2).[4,141–144] Programmed cell death protein ligand 1 (PD-L1) is an immune system checkpoint protein that prevents an immune response when it binds its receptor, programmed cell death protein 1 (PD-1). These proteins are checkpoints that turn down T cell activation

upon binding (Scheme 1.2).[55,114,145,146] Other forms of immunotherapy are oncolytic vaccines,[4,69] the selective delivery of gene manipulation to lyze cancer cells, or reprogrammed host T cells to selectively combat tumour cells (CAR-T) therapy.[69,109]

PD-L1 is often constitutively expressed on critical organs derivative to the central nervous system, such that when the immune response is provoked, these organs are not targeted (Scheme 1.3).[81,146,147] Unfortunately, there are higher expression levels of PD-L1 in many aggressive cancers, such as TNBC, which results in the tumour evading the immune response (Scheme 1.2). However as described earlier, this higher expression level also establishes PD-L1 as a biomarker, making it as a prime candidate for ICI.[141,142,148–150]

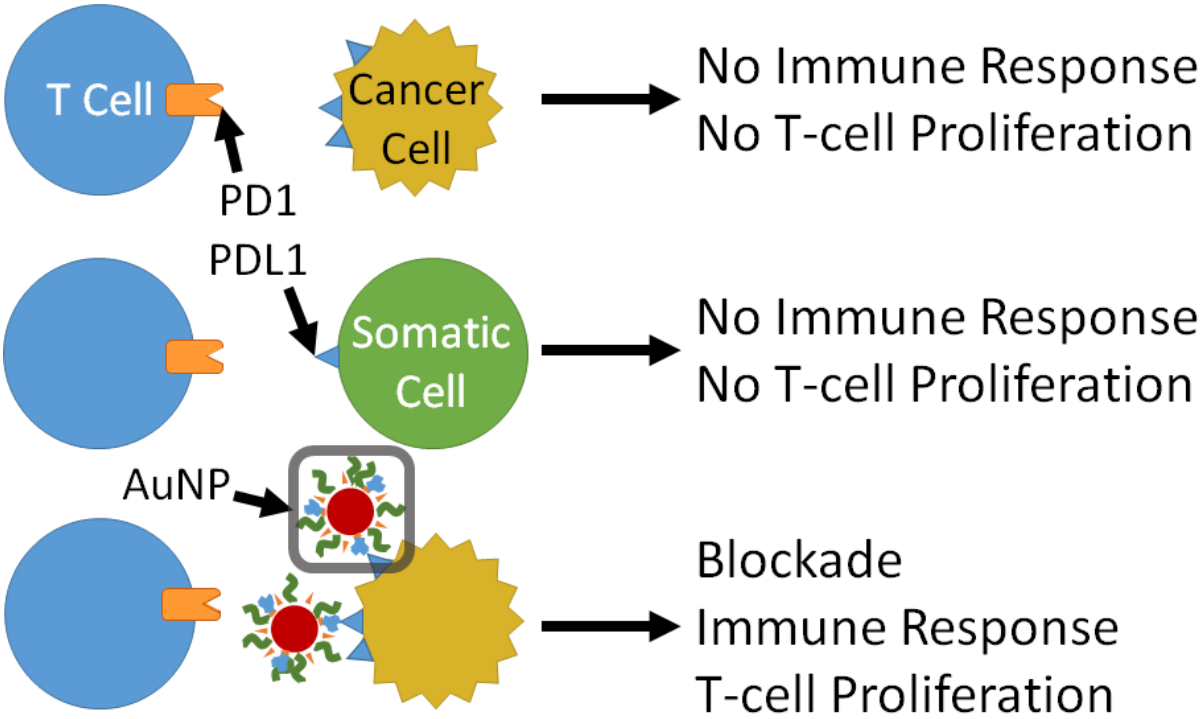

Scheme 1.2. PD-L1 overexpression can result in immune evasion and undetected cell growth, but by targeting and blockading this from recognition with its receptor, PD-1, there is the possibility of recovering immune activity and using the immune system to kill cancer cells.

Current ICI treatments use antibodies that target and block immunomodulating proteins like PD-L1 and its receptor, PD-1 (Scheme 1.2). To date, there are only eight FDA-approved drug antibodies for three immunomodulating targets: PD-L1 (3), PD-1 (3), and cytotoxic T-lymphocyte associated protein 4 (CTLA-4; 2).[151–158] By targeting these proteins, there is an expected blockade between immune cells and cancer cells (Scheme 2), that should release the immunosuppressive signal and recover the T cells from exhaustion which allows for the immune system to resume proinflammatory activity and recognize the cancer. Despite the short-term efficacy in antibody treatment alone, when they are combined with other regimens (i.e., chemotherapeutic agents like doxorubicin and paclitaxel) there is improved survivability.[110,148,159] These effects can be similarly observed in antibody-drug conjugates to reduce off-

targeting effects from non-selective chemotherapeutic reagents, but not all PD-L1-targeting antibodies are capable of disrupting the PD-1/PD-L1 interaction.[158,160–162]

Gold Nanoparticles Almost in the Clinic

One of the first targeted gold nanoparticles (AuNPs) developed for clinical use was CYT-0691 (Aurimmune) which was used in the treatment of solid tumours.[5,9] The formulation was designed with colloidal gold stabilized with polyethylene glycol (PEG) and decorated with tumour necrosis factor alpha (TNFα) as the targeting agent.[9] Aurimmune is briefly described as a "PEGylated, 30 nm AuNP conjugated with TNFα". Although the precise formulation is never explicitly stated, it can be speculated that TNFα was conjugated to polymer-stabilized AuNPs through EDC/NHS coupling to the polymer.[9,163] Despite its promise as a radiosensitizer in principle, there have been no patient studies to prove its efficacy.[164]

There is a lack of standardization in the synthesis and formulation of metal-based nanomedicines.[6,165,166] One of the primary reasons for this are the many variables that affect formation and formulation of the particles, which may lead batch variation between lab groups and even within the same formulation, therefore stringency is crucial. Although peptide coupling to polymer stabilized particles is common practice in functionalization, there is a lack in characterizing the process efficiency.[12,28] Similarly, there is little characterization done to determine to what extent the particles have been functionalized, other than assuming all particles are homogenously and evenly decorated.[3,11,12,41,45,167,168] This type of poor characterization results in uncertainty between batches, which is fundamentally one of the reasons why AuNPs have still not been approved for clinical use.[78] Therefore, reliable synthesis and characterization are crucial for these processes.

Simple *in vitro* models can characterize the proof-of-function, but with a limited scope at the target location. Although the ideal mechanism of action has been characterized, this does not consider the broader scope as the drug circulates throughout the patient. The increase in variables and barriers between the drug and disease site grows exponentially, which will reduce efficacy as we transition away from single protein targeting to cell specificity to including whole avenues where the drug may leave via excretion. More specifically, off-targeting is a risk that is not often characterized but could be characterized *in vitro* to emphasize the efficacy and safe aspects of the drug. Investigating cytotoxicity profiles in cell lines beyond the region of interest as secondary cell data, as a preliminary alternative, which could be useful in downstream animal studies (three-dimensional assays, Scheme 1.1). This may help establish a baseline of fundamental toxicity levels, and they could potentially be proportional to the LD_{50} observed in animals, which could be used in assessing the upper limits of a dosing regimen. Many innovative particles fail approval for clinical trials not because of the lack of efficacy, but due to the lack of confidence about the safety of the particles; there is a fear of toxicity of how the rest of the body may react to them post-administration.[26] Media often highlights what is relevant to the story, but are not critical enough to the broader audience, which overshadows the possible repercussions are shown as off-targeting in Scheme 1.3.

Most nanomedicines are likely administered via direct injection, which overrides some pharmacokinetic barriers between administration and delivery. Unfortunately, a majority of the injected entities will likely be recognized by the reticuloendothelial system (RES) and removed to the liver, rather than migrating to

the disease site.[169] This fast removal from the bloodstream by the RES could result in accumulation of particles in the liver or kidneys, putting them at risk of toxicity.[48] Having both primary and secondary cell data should elicit more confidence about the safety of the particles.

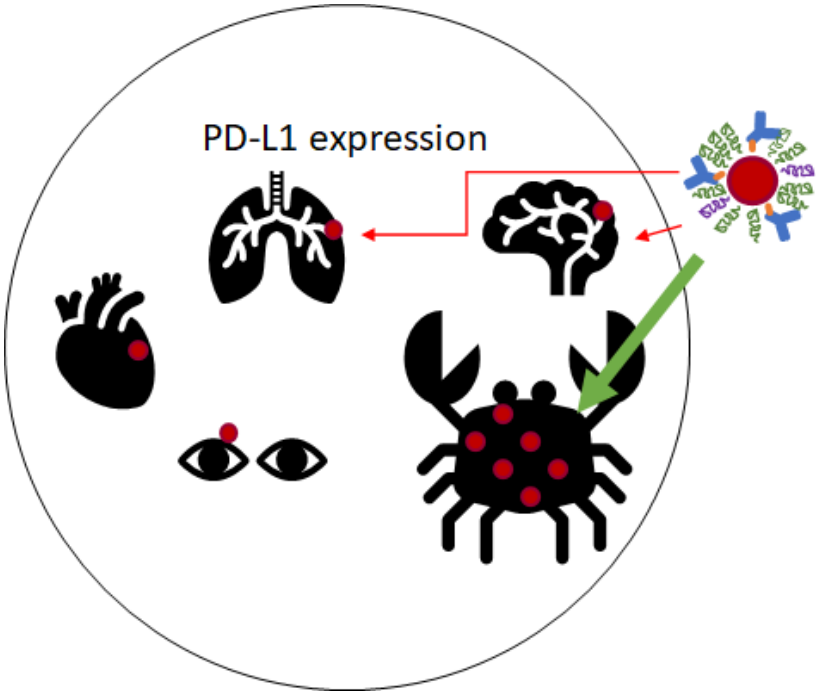

Scheme 1.3. Functionalized AuNPs actively targeting PD-L1 should primarily be found at the cancer (crab). Unfortunately, there are other PD-L1-expressing organs (brain, eyes, heart, lungs) that should also be investigated prior to clinical trials with a view towards potential adverse effects. These are the high-risk tissues where the particles could accumulate.

Functionalizing a targeting agent to the vehicle improves the deliverability and selectivity. Gold nanoparticles, like Aurimmune, were functionalized to target TNFα to make tumours more sensitive to radiotherapy,[9,170] as well as improve delivery of the core to improve sensitivity with localized photothermal therapies.[11,18] Similarly, our particles intend to target PD-L1 on TNBCs should also selectively sensitize the cancer cells. The work of Shao *et al*. aims to further characterize the two proposed functions of Aurimmune *in vitro* in a systematic manner.[17] The purpose for *in vitro*-based studies rather than animal experiments is mainly emphasized in cost, reproducibility, and higher throughput.[26,166,171] Using *in vitro* models to characterize function in an iterative manner helps focus the development of a nanomedicine in a similar systematic way. Unfortunately, Aurimmune has not advanced from Phase I/II clinical trials.[9]

Intent, Rationale of Work, and Hypotheses

This thesis work comprises the synthesis and characterization of functionalized AuNPs with the intent to selectively target and block the PD-1/PD-L1 interaction resulting in an immunotherapeutic benefit similar to other ICIs. Alongside this, we expect selective delivery of the gold core such that we may use these particles as radiosensitizers to reduce collateral damage in radiotherapies. Ideally, we want to characterize these effects through simple and non-expensive models, with the goal of eventually carrying forward into more complex and biologically relevant scenarios (Scheme 1.1).

This work prioritizes 1-D binding studies to determine the activity of functionalized AuNPs for their selectivity and competitivity for blockading the PD-1/PD-L1 interaction using SPR. These competitive effects are expected to persist in more complex settings, such as achieving T cell recovery from immune exhaustion.

Alongside the development and synthesis of the gold cores, we aim to optimize a formulation capable of disrupting the PD-1/PD-L1 interaction. We expect that successful targeting and blockading of the PD-1/PD-L1 interaction by SPR should translate to potential immunotherapeutic recovery when investigated in cell culture, similar to current ICI therapies. We expect that blockading the immunosuppressing proteins should allow for persistent expression of pro-inflammatory cytokines (e.g., IL-2 or IL-6), which will orthogonally validate the immunotherapeutic claim *in vitro* and may be measured using the appropriate enzyme-linked immunosorbent assay (ELISA).

We also investigated other properties that *may* be suitable in other iterations of this proposed drug formulation. The first of these was elucidating the disruption of PD-1/PD-L1 with small molecules using SPR, to *not* rely on monoclonal antibodies as targeting agents (Chapter 2). A second objective was characterizing triggerable release mechanisms which take advantage of the tumour microenvironment to maintain the expected dual effects of the AuNPs (Chapter 3). If successful, this approach would allow us to cleave the targeting agent from the AuNP surface following localization, and could also be used to deliver cytotoxic agents to the tumour site. Although not all optimizable variables were addressed, this work should be applicable to all iterations of other metal-based nanomedicines, not restricted to the targeting agent or target, nor physical properties (e.g., size, shape, etc.).

We aim to design, characterize, and validate targeting gold nanoparticles through *in vitro* assays shown in Scheme 1.1, in an iterative and rational manner for the purpose of eventually treating triple-negative breast cancers that express PD-L1. Although we expect to develop AuNPs that are suitable for both enhancing tumour regressing effects in radio- and immunotherapies, developing a formulation appropriate for *in vivo* testing is difficult. Therefore, this thesis is more focused on the selectivity and targeting aspects of the core using mostly *in vitro* techniques. In addition, by targeting PD-L1, we expect some degree of competitive binding that removes the immunosuppressing effect of the PD-1 signal recognition on activated immune cells. This would result in cytotoxic activity and potential tumour cell death in a comingling assay, which could be characterized by measuring cytokine activity as an orthogonal output of validation.

Although the AuNPs in this thesis are developed to target PD-L1-presenting TNBCs, the synthesis and characterization of the particles are not limited to strictly PD-L1. Instead, I want this work to help motivate and encourage development of other nanomedicines for more personalized medicines in cancer treatment. More personalized medicines can effectively mitigate potential adverse effects on patients and overcome the tumour heterogeneity barrier that currently limits modern treatment methods.

2. Surface Plasmon Resonance is used to Characterize the Binding Affinity of Proposed Antagonists of PD-1/PD-L1

This following chapter was adapted from an earlier publication in ACS Medicinal Chemistry Letters.[172]

Blevins, D. J., Hanley, R., Buldoc, T., Powell, D. A., Gignac, M., Walker, K., Carr, M. D., Hof, F., Wulff, J. E. *ACS Med. Chem. Lett*. **2019**, *10* (8), 1187–1192.

*This chapter focuses on the determining whether small molecules (**3**–**5**) originally described by Aurigene Pharmaceutical Services Inc. (Aurigene) were suitable targeting agents for our prospective AuNPs, using surface plasmon resonance (SPR) as the primary technique to characterize affinity and selectivity of the small molecules. The small molecule synthesis and purification was performed by Dr. Ronan Hanley. The synthesized compounds were then characterized for their biological activity in cells with the help of Dr. David Powell. Michael Gignac performed protein synthesis and purification. Dr. Mark D. Carr and Dr. Kayleigh Walker performed earlier binding measurements by NMR, provided protein constructs.*[173] *Trevor Buldoc performed the primary analysis with PD-1-ligand SPR data with compounds **3**–**6**, whereas Derek Blevins optimized the assay for other proteins such as PD-L1, PD-L2, and VISTA, as well as characterizing the αPD-L1 mAb described in Chapter 4. The relevant supplementary data are found starting on page 155.*

Foreword

To deliver the gold core for uptake and sensitization, we need an appropriate targeting agent to effectively target PD-L1-presenting TNBCs. Without targeting agents the AuNPs are indiscriminate and aimless leading to poor uptake efficiency at the disease site in biodistribution studies, where, instead, a majority of the particles are opsonized to the liver.[10,77,101,125] In these passive targeting investigations the expectation is the EPR effect will be the major discriminatory factor between diseased and health tissues. However, in the cases where a targeting agent was conjugated on the gold surface, there was a substantially higher population found at the disease site than without, indicating the targeting agent improved the selectivity.[10,51] While the presence of target improves deliverability, not all targeting agents are equal.

The majority of first-pass active targeting cases rely on antibodies for their high selectivity, facile validation of targeting, and strong potency of targeting for their antigen.[16,41,110] Despite their promise and reliability of treatment, these biomolecules come with a handful of limitations.

Firstly, “normal” antibodies are large biomolecules (150 000 g/mol, ~15 nm diameter),[174] and this unfortunately comes with poor uptake and internalization.[175–177] Much of their clinical targetability is limited to surface-expressed proteins or peripheral metabolites due to this size limitation.[41,84,105,113,128] While the addition of high specificity greatly improves efficacy of non-selective drugs, antibodies are still limited by shallow penetration.

Secondly, while antibodies are endogenously made biomolecules, the targeting immunomodulating proteins can risk inducing an immunogenic response from off-targeting.[178] In addition to this, antibodies have long circulation times and low clearance, which increases the likelihood of those immunogenic off-targeting events, this makes antibodies difficult to dose in long-term therapies. The low clearance also increases the risk of resistance, where the subsequent doses will be greatly inefficacious.[53,115,141]

Lastly, there are many barriers inhibiting the industrial scaleup of antibodies as drug agents, such as batch-to-batch variability, where protein expression is not uniform, and some antigen-binding sites may not be homogenous. As antibodies are produced endogenously, they are best synthesized from animals, however the expression system may be innately immunogenic (i.e., rodent-expressed), and further processing is needed to humanize the antibodies, reducing the immunogenic risk.[105] These large proteins are expensive to synthesize on an industrial scale and cannot be classified as homogeneous, as there will always be variations between proteins (i.e., residue mutations, misfolding). We assume high fidelity in protein expression systems which result in consistent translation to maintain homogeneity of those expressed and folded proteins, but this is not always the case. Furthermore, their innate complexity and inability for full characterization can hinder their regulatory approval for use in clinics.

Small molecules, by contrast, lack many of the limitations presented by antibodies. They are relatively inexpensive, and fully characterizable, if the target is previously established. However, developing an entirely new small molecule for targeting may take years to establish a lead compound.[179] Although small molecules may lack specificity, they are less likely to induce an immunogenic response and will have a better rate of clearance making them exceptional for dosing. Achieving selective delivery may be a challenge, especially when many small molecule drugs are toxic to cellular machinery (i.e., chemotherapeutics), but nanomedicine can overcome these potential adverse effects by encapsulating them into carriers to mitigate broadly toxic off-targeting effects.[180–182]

Small molecules are not often used as targeting agents, due to the lower potency in antigen recognition. While some substrates may have a high binding specificity, analogous molecules may not fit the same way. Similar to antibodies, the ability to help improve targeting of a drug vehicle is limited to targeting surface biomarkers indicative of the diseased-state.[183,184] In other cases, these molecules are quite hydrophobic and planar making them difficult to deliver, especially as their targets are extracellular domains of proteins.[55,66,175] Other small molecules with high toxicity and no selectivity, can be compartmentalized into nanoparticles to reduce off-targeting leeching (i.e., encapsulation in polymer nanoparticles)[182,185–187], or they can be covalently bound to antibodies to improve the specificity and further improve the potency when delivered as antibody-drug conjugates (ADCs).[84,122,188]

Small molecules are intentionally designed as a potent drug alone, whereby further optimization has the intent of increasing potency or selectivity. It is uncommon that a small molecule is designed and optimized as a targeting agent without the prior scope fleshed out, as most modifications would decrease potency relative to the parent compound. This lower potency may be overcome by having the tether-conjugated ligands having a higher effective concentration. By grafting onto a surface and increasing the effective concentration, the polyvalency of these small molecules can have a synergistic effect resulting in an apparent tighter binding to the target. Although the individual tether molecules may bind weakly, the high concentration of other tethered substrates will also have a greater likelihood of binding. The higher overall valency of targeting increases the effective opportunity for binding and thereby could effectively increase activity relative to the parent drug alone (Scheme 2.1).

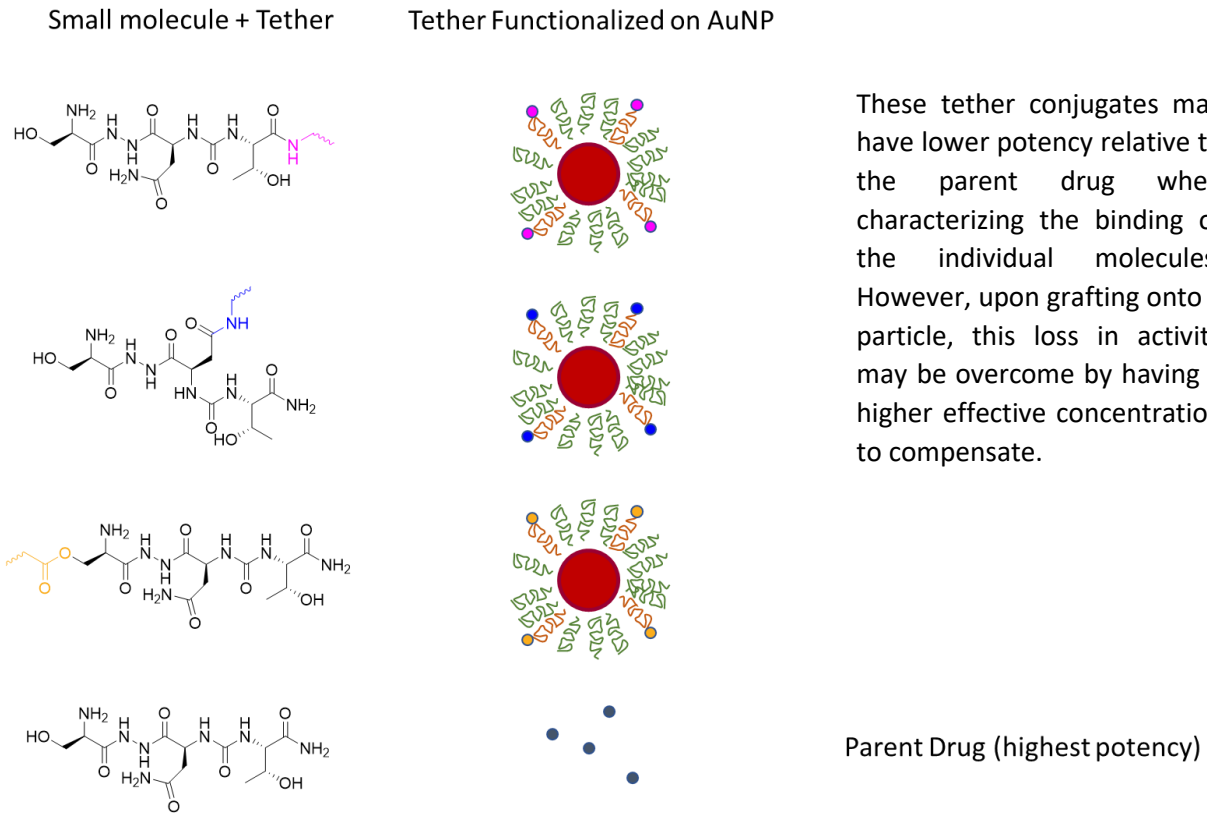

Figure 2.1. Small molecule targeting agents may lose potency relative to their parent compound as individual molecules, but this may be compensated upon functionalization by having an increased apparent concentration.

Regardless, any form of active targeting improves efficacy of delivery. As small molecules can be fully characterized, and are expected to be non-immunogenic, and have usually moderate potency, they are a promising alternative to targeting with antibodies.

While there is promise in the development of small molecules targeting these checkpoint proteins,[55,142,189] all current clinical treatments rely on antibodies (Table 2.1). Immune checkpoint inhibition with mAbs result in short-term efficacy of high tumour reduction, however there is often secondary resistance and subsequent autoimmune attacks,[190,191] and with low clearance. These are a few of the barriers that make treatment with mAbs difficult in long-term therapies. Using small molecules instead of antibodies would overcome these limitations.

Triple-negative breast cancers (TNBCs) have low expression levels of the three most common biomarkers for endocrine-based chemotherapies – estrogen receptor, progesterone receptor, and the human epithelial growth hormone factor receptor.[65] However, in the past decade there has been evidence of other biomarkers associated with TNBCs, including the immune checkpoint protein, programmed cell death protein ligand 1 (PD-L1),[65,130,192] which would allow for other avenues of targeted therapy. To date, treatments that target PD-L1 or its receptor, PD-1, use mAbs (Table 2.1).[83,141,193] Despite this, there are groups investigating the development of small molecules as potential immunotherapeutic agents.

Aurigene Pharmaceuticals Services Limited (Aurigene) is a company actively pursuing the development of small molecules with immunomodulating effects, derived from peptide fragments of PD-1 (Figure 2.3).

Their small molecules were characterized by a cell assay investigating recovery of T cell activity in the presence of inhibiting PD-L1-presenting cancer cells. Through their process, they found a hit in 2011 related to the PD-L1-binding site of PD-1 (**1**) and began varying the physical structure to prevent from endogenous degradation by using unnatural amino acids (**L**-enantiomers) and cyclizing the peptide derivative (**2**) (Figure 2.1).

Herein we intend to provide evidence of the targeting effects of compounds **3**–**5** (Scheme 2.2; Figure 2.2) by using a direct-binding assay to characterize how the molecules bind and, hopefully, disrupt the PD-1/PD-L1 interaction. Our aim is to characterize the selectivity of the compounds and, if they show higher specificity for PD-L1, this could warrant them as potential targeting agents for our gold platform. If there is any indication of competitive binding, these molecules can be claimed a direct disruptors of the PD-1/PD-L1 interaction and help reinforce the apparent immunomodulating effects observed in Aurigene's patents.[194–196]

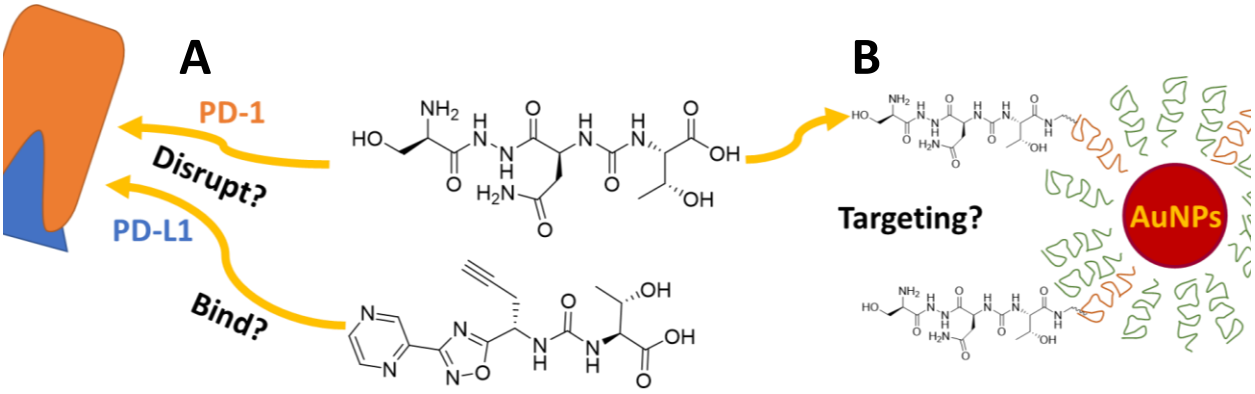

Figure 2.2. **A**. The intent to characterize the mechanism of action of proposed small molecules from Aurigene that target PD-L1 and disrupt the PD-1/PD-L1 binding as potential immunotherapeutic agents. **B**. Expectation to use those small molecules as targeting agents for AuNP delivery, similar to mAbs as ICIs.

Small Molecules or Antibodies – Rationalizing Targeting

Antibodies are highly selective and can be developed with high specificity, making them excellent targeting agents to almost anything.[122,197] However, antibodies rarely target beyond surface markers expressed on tissues. These molecules are large (~150 000 g/mol) and this often results in poor delivery as they may be unable to access the disease site of interest, and therefore not everything may be equally *targetable*.[175–177] In the case of cytosolic or nuclear targets, there are clever ways to internalize mAbs through other biophysical means of delivery (i.e., lysosome and clathrin-mediated endocytosis) but these pathways are not guaranteed and may still result in poor efficacy.[198] As a trade-off to poor penetration, mAbs have a long circulatory half-life and modest clearance rate, these make dosing difficult long-term as the patient may be insensitive, and the long retention time increases the risk for adverse effects from off-targeting resulting in immunogenicity, where subsequent doses are adverse to the patient and ineffective.[189,197] This limits the scope of antibody targeting to mostly surface-expressed proteins and circulatory-based targets, but these three factors often result in poor efficacy in the long-term. Despite the highly selective targeting and promise of disrupting the PD-1/PD-L1 interaction, antibodies are not as successful in follow-up treatments. Although, they are commonly used in immunotherapy and these adverse effect occur, clinical trials have found that combination-based therapies can overcome this subsequent insensitivity.[81,141,150,159,178]

Conversely, small molecules have the potential to overcome each of the barriers expected by antibodies and other large biologics. Small molecules have a higher bioavailability and are likely non-immunogenic, as they are wholly characterizable as homogenous. The clearance of small molecules is expected to be much shorter, and therefore more suitable for long-term doses.[55,197,199] However, due to being smaller molecules, there are other developmental trade-offs, (i.e., improved specificity to a mutation may be more difficult to deliver, but opens the door to having a library of drugs which may be more suited for some patients more than others).

Despite the comprehensive understanding of the PD-1/PD-L1 interaction and how promising these proteins are immunotherapeutic targets, there are only a handful of small molecules capable of potentially disrupting the immunosuppressive signal, but these have not been approved for clinical trials.[67,141,177,200,201] Furthermore, despite the compelling evidence of immunomodulation with compounds **3**–**5** in their respective patents, there have been no published findings of their affinity to either PD-1 or PD-L1. The intent of these SPR experiments was to determine whether any of the small molecules are suitable for targeting PD-L1, and characterizing their ability to disrupt the PD-1/PD-L1 interaction prior to functionalizing them onto a nanoparticle surface.

Materials and Methods

1. Expression, Refolding, and Purification of Extracellular PD-L1

E. coli BL21(DE3) cells were transfected with a pET28a(+) vector containing the sequence for the extracellular region of PD-L1 (A18-T239) with codon usage optimized for expression in *E. coli*. Cells were cultured in LB media treated with 50 µg/mL Kanamycin at 37 °C to an OD_{600} of 0.9. The expression of PD-L1 as insoluble inclusion bodies was induced with the addition of 1 mM IPTG. The cells were cultured for a further 5 hours before being collected by centrifugation. Cell pellets from 1 L culture were resuspended in 35 mL phosphate-based saline (137 mM NaCl, 2.7 mM KCl, 10 mM Na_2HPO_4, 1.8 mM KH_2PO_4, pH 7.4) treated with protease inhibitors (Roche), and lysed by sonication. Inclusion bodies containing PD-L1 were collected from the cell lysate by centrifugation at 15 000 RPM for 20 minutes. Inclusion body pellets were then washed three times by resuspension in wash buffer followed by centrifugation. The first two washes were performed using a buffer containing 50 mM Tris, pH 8.0, 200 mM NaCl, 10 mM EDTA, 0.5% (v/v) Triton-X100, 10 mM DTT. The final wash was done in the same buffer excluding the detergent. Washed inclusion body pellets from 1 L original culture were resolubilized by shaking for 1 hour at 37 °C in 20 mL solubilization buffer (50 mM Tris buffer, pH 8.0, 5 M guanidine, 200 mM NaCl, 20 mM DTT). Resolubilized PD-L1 was refolded by drop-wise dilution 100-fold into refolding buffer (100 mM Tris, pH 8.0, 1 M arginine, 0.5 mM $glutathione_{ox}$, 2 mM $glutathione_{red}$). The refolding mixture was then concentrated by tangential flow filtration before being dialyzed into gel filtration buffer (10 mM Tris, pH 8.0, 20 mM NaCl). Folded PD-L1 was separated from misfolded aggregates and contaminants by size exclusion chromatography using a 16/60 Superdex 75 column (GE Healthcare) equilibrated with 10 mM Tris, pH 8.0, 20 mM NaCl. The purified protein was verified by SDS-PAGE as a band at 25 kDa.

2. Expression, Refolding, and Purification of Extracellular PD-1

E. coli BL21-CodonPlus RIL was transfected with a pET28a(+) vector containing the sequence for the extracellular domain of PD-1 (P34-E150). The strain was grown in LB media treated with 50 µg/mL Kanamycin overnight at 37 °C to an OD_{600} of 0.9. 1 mM. Isopropyl β-D-1-thiogalactopyranoside (IPTG) was added to induce expression of the vector, and the culture was incubated another 4 hours after induction.

The cultures were then spun down at 4 °C. The pellets were resuspended in 35 mL phosphate-based saline (137 mM NaCl, 2.7 mM KCl, 10 mM Na_2HPO_4, 1.8 mM KH_2PO_4, pH 7.4) treated with protease inhibitors (Millipore), and lysed by sonication. The cell lysate was spun down twice at 15 000 RPM for 20 minutes to pellet inclusion bodies of protein. The inclusion bodies were resuspended by a glass homogenizer in 30 mL wash buffer (100 mM Tris, pH 8.0, 200 mM NaCl, 10 mM EDTA, 0.5% (v/v) Triton-X100, 10 mM DTT). This was performed a second time with the absence of Triton-X100. The inclusion bodies were then resolubilized in 20 mL suspension buffer (100 mM Tris buffer, pH 8.0, 5 M guanidine, 200 mM NaCl, 20 mM DTT) and left to shake for 1 hour at 37 °C. This suspension was centrifuged for 20 minutes at 15 000 rpm. The solution was resolubilized and added dropwise dilute 100-fold in stirred refold buffer (100 mM Tris buffer, pH 8.0, 0.4 M arginine, 2 mM EDTA, 0.5 mM $glutathione_{ox}$, 2 mM $glutathione_{red}$) at 4 °C and let stir overnight. The resulting solution containing PD-1 protein was then concentrated to 50 mL and dialyzed into gel filtration buffer (10 mM Tris buffer, pH 8.0, 20 mM NaCl) for purification. Protein was purified by size exclusion chromatography at 78 mL by Superdex S75 exclusion column. The purified protein was verified by SDS-PAGE as a band at 13 kDa. The concentrated protein was then dialyzed in appropriate HBS-EP+ running buffer for SPR analyses.

3. SPR Binding Assays

All SPR related materials and buffer were manufactured by GE Healthcare Lifesciences unless otherwise noted. Assays were performed on a BiaCore X100 with no changes to sample flow and binding parameters.

All chips were immobilized with their respective protein under the default conditions for an aimed response level. The target immobilized response was calculated to give an expected R_{max} of 100 RU based on the equation 1, where the MW is the molecular weight of the ligand (immobilized protein) or the analyte (compounds being flowed). The immobilization was run under default conditions provided by the BiaCore X100 (GE Healthcare Life Sciences).

$$R_{ligand} = \frac{R_{max} * MW_{ligand}}{MW_{analyte}} \quad (1)$$

3a. In vitro binding assay: Adsorbed Human PD-1

Human biotinylated-PD-1 (BPS Bioscience, Catalog 71106) was adsorbed to a gold surface by binding to streptavidin-coated sensor chip (SA chip, GE Healthcare). The ligand response (R_{ligand}) was 2029.9 RU. The analytes were flowed through with HBS-EP^+ (10 mM HEPES buffer, pH 7.4, 150 mM NaCl, 3 mM EDTA, 0.05% (v/v) P20, 0.5% (w/v) DMSO) at a concentration of 100 nM at 10 µL/min. Each of the compounds, **3**–**6**, were titrated by SPR to determine their ability to inhibit the PD-1/PD-L1 interaction. The concentration of PD-L1 was held constant at 500 nM. Compounds **3**–**6** were also titrated in the absence of PD-L1, to determine their ability to bind to the adsorbed PD-1.

3b. In vitro binding assay: Adsorbed Human PD-L1

Human biotinylated-PD-L1 (BPS Bioscience, Catalog 71105) was adsorbed to a gold surface by binding to a separate SA chip (GE Healthcare). PD-L1 was immobilized from 100 nM aliquot with a final ligand response (R_{ligand}) of 2681.8 RU. Compounds **3**–**6** were flowed across the chip of adsorbed PD-L1 in the presence of PD-1 (1 µM) to determine their efficacy as inhibitors in triplicate, unless otherwise stated. Compounds **3**–**6** were also titrated in the absence of PD-1, to determine their ability to bind to the adsorbed PD-L1.

3c. In vitro binding assay: Adsorbed Human PD-L2

Human biotinylated-PD-L2 (BPS Bioscience, Catalog 71108) was adsorbed to a gold surface by binding to another SA chip (GE Healthcare). The final response of the immobilized ligand was 3794.0 RU. Compounds **3**–**6** were titrated by flowing across the chip of adsorbed PD-L2 in the presence of PD-1 (0.75 µM) to determine their efficacy as inhibitors HBS-EP$^+$ buffer in triplicate. Compounds **3**–**6** were also titrated in the absence of PD-1, to determine their ability to bind to the adsorbed PD-L2.

3d. In vitro binding assay: Adsorbed Human VISTA

Human biotinylated-VISTA (BPS Bioscience, Catalog 71327) was adsorbed to an SA chip (GE Healthcare) under continuous flow of HBS-EP$^+$. The final response of the immobilized ligand was 5482.6 RU. Compounds **3**–**6** were flowed across the chip of adsorbed VISTA to detect any potential binding in HBS-EP$^+$ buffer in triplicate.

4. Synthesis of Test Compounds

Compound **3** was synthesized by WuXi Apptec, following the protocol established in the patent from Aurigene, with minor modifications. Santai Labs synthesized compounds **4** and **5**, following the protocol established in the patents from Aurigene. Compound **6** was synthesized in house, following the general protocol established in the patent from Bristol-Myers Squibb, with minor modifications. All final products were characterized by NMR and LCMS prior to use. Test solutions were assayed again by LCMS at the conclusion to the research, to confirm that they had not degraded during the time required to complete the measurements. Total synthesis is found in the supplementary materials on page 155.

Targeting PD-L1 – the Importance of Selectivity

While passive targeting chemotherapeutics are useful in many cases, transient "targeting" of the EPR effect is not sufficient for aggressive cancers. Ultimately, we want to use gold nanoparticles as a platform for radiosensitizing the tumour as it greatly reduces likelihood of radiation-induced secondary tumours;[70,117] however, due to the lack of standardization, there is fear that the metal vehicle is adversely toxic due to the wide range of variables and varying results in the literature.[18]

The main purpose for targeting agents is to help direct the nanomedicines to the disease. In many cases, the target is a biomarker, but as previously alluded, these biomarkers are not consistently present on every tumour, and will be likely expressed elsewhere. Personalizing nanomedicine should help reduce those unintended consequences as the drug is present elsewhere (i.e., circulating throughout the patient).

PD-L1 and its receptor, PD-1, are important immunosuppressing proteins that downregulate the pro-inflammatory response attributed with T cell activation.[146,202–204] PD-1 is expressed constitutively in our immune system, and PD-L1 is expressed on critical somatic tissue and antigen-presenting cells (APCs).[205,206] The immune-privilege of constitutive PD-L1 expression is found on critical tissues involved in our central nervous system and circulatory system (i.e., brain, eyes, heart, and lungs) such that our immune response does not actively target those organs, which would otherwise result in an autoimmune response.[146,147,206] The binding interaction between PD-1 and PD-L1 causes a down-regulation of T cell proliferative gene expression, thus disrupting cytotoxic activity of the immune system. Certain aggressive cancers, such as pancreatic cancer, breast cancers , and non-small lung carcinomas, have evolved to express PD-L1 as a means of immune evasion.[206,207] In these cases, PD-L1 expresses constitutively, allowing the tumour to masquerade as an immune privileged tissue and evade detection.[138,208–210] Overexpression

of PD-L1 is therefore a strong prognostic biomarker in oncology, and a potential target to improve therapeutic efficacy in more selective treatments.[136,138,205–213]

Pharmaceutical companies have sought to develop modulators for the PD-1/PD-L1 complex to recover lymphocyte activity. Current treatment are antibody-based therapies targeting either PD-1 or PD-L1 (Table 2.1). Despite the remarkable success of these antibodies,[148,155,157,159,193,214–219] there are considerable drawbacks such as poor bioavailability, immunogenicity, and the high cost of industrial scale production.[63,105,215] Small molecule inhibitors have the potential to overcome these barriers, and multiple research groups are pursuing these objectives.[67,149,220] However, there are no currently FDA-approved small molecule inhibitors capable of blocking the PD-1/PD-L1 interaction.[177,189]

Table 2.1. List of current FDA-approved immunotherapeutic antibodies that block the PD-1/PD-L1 interaction. There are currently four αPD-1 mAbs and three αPD-L1 mAbs.

Name (Common Name)	Company	Target	FDA-Approved Year
Nivolumab (Opdivo)[216]	Bristol-Myers Squibb	PD-1	2014
Pembrolizumab (Keytruda)[218]	Merck	PD-1	2014
Atezolizumab (Tecentriq)[159]	Genentech/Roche	**PD-L1**	2016
Avelumab (Bavencio)[141,155]	Merck	**PD-L1**	2017
Durvalumab (Imfinzi)[156,159]	AstraZeneca	**PD-L1**	2017
Cemiplimab (Libtayo)[157]	Regeneron/Sanofi	PD-1	2018
Dostarlimab (Jemperli)[159,214]	GlaxoSmithKline	PD-1	2021

Aurigene has an extensive patent portfolio of peptides and peptidomimetic small molecules that mimic various regions of the PD-1 protein sequence. The most promising peptidomimetic compounds are reported to exhibit nanomolar (nM) potency in a phenotypic cell-based splenocyte recovery assay, which Aurigene used to scout their small molecules and classify as PD-1/PD-L1 inhibitors (Scheme 2.1).[194–196,221,222] Aurigene derived these small molecules through iterative cleavage experiments starting with fractions of the PD-L1 binding interface on PD-1 (Figure 2.3, **1**) and incorporating unnatural amino acid residues to improve their half-life and potency (Figure 2.3, **2**).

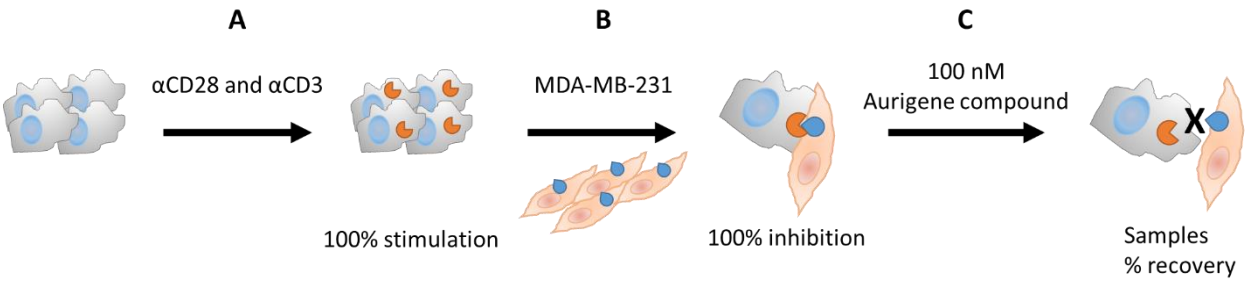

Scheme 2.1. Synopsis of splenocyte recovery assay as reported by Aurigene. **A**. Mouse splenocytes are stimulated with αCD3 and αCD28 to induce PD-1 and cytokine production. **B**. Stimulated splenocytes are inhibited by comingling with PD-L1-presenting MB-MDA-231 cells. **C**. The comingled cells are injected with 100 nM of Aurigene compound to disrupt the PD-1/PD-L1 interaction, as reported by cytokine production normalized to the concentration observation in the control (**A**). Sample recovery measured the number of cytokines detected with respect to uninhibited stimulation after spiking with the molecule, indicative of the small molecules recovering T cell activity.

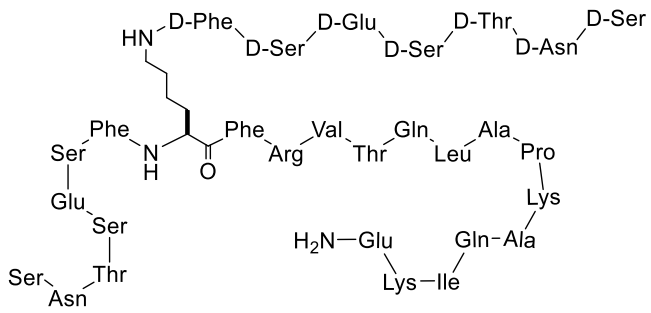

WO 2011/0318373 A1
Compound 1

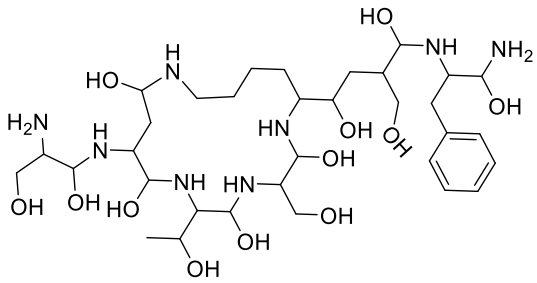

WO 2013/144704 A1
Compound 2 (57% recovery)
Stereochemistry not disclosed.

Figure 2.3 Aurigene's initial most potent PD-L1-binding peptide substrates. Compound **1** was a fraction of the PD-L1 binding site but incorporates some unnatural amino acids (D-enantiomers).[221] Compound **2** is a cyclic peptide, however the stereochemistry of the residues was not disclosed, therefore no stereochemistry is shown.[222] Both compounds were derived from the PD-L1 binding site on PD-1. The shorthand residues are L-enantiomers. Derived fragments shown in Figure 2.5and B, respectively.

However, no direct protein binding experiments have been reported for this family of small molecules. We selected three of the most potent molecules from the peptidomimetic immunomodulator series (Figure 2.4, **3**–**5**), and aimed to characterize them using a surface plasmon resonance (SPR)-based method. Each test compound was chosen with an eye toward maximizing potency and drug-like properties, while optimally representing the compounds claimed within each patent. We were hoping to orthogonally validate Aurigene's cell data, which is highlighted in each of their small molecule patents, while also directly addressing the specificity and affinity of those molecules to PD-L1, such that we may conjugate to the AuNP surface as a means of targeting *and* blockading (Figure 2.2B).

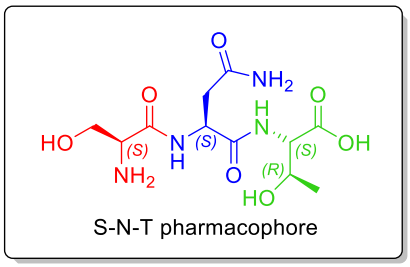

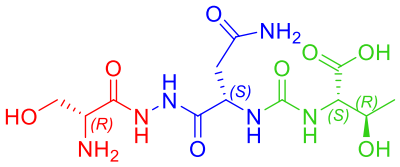

Aurigene 1
WO2013/237580
Compound 3
68% recovery

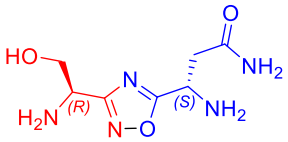

Aurigene 2
WO2015/033299
Compound 4
92% recovery

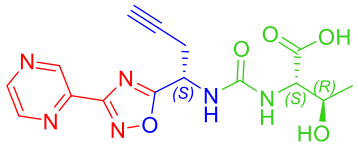

Aurigene 3
WO2016/142886
Compound 5
93% recovery

Figure 2.4. Aurigene's most potent small molecule peptidomimetic compounds capable of recovering T cell activity, inhibited by PD-L1-presenting MB-MDA-231 TNBC cells, from three patents themed around immunomodulating small molecules. They are highlighted by the tripeptide pharmacophore of serine (red), asparagine (blue), and threonine (green). The SNT residues of the pharmacophore is also shown in Figure 2.5C.

A Brief Critical History on the Development of Aurigene's Inhibitors

In 2011, compound **1** was discovered using truncated segments of the PD-L1-binding site on PD-1 in a competitive assay with PD-1 to determine what tertiary structure would be an appropriate hit. Then through an iterative process, Aurigene began investigating which derivative sequences of residues were most potent for recovery of T cell exhaustion. By incorporating unnatural amino acids that resemble the enantiomer of the binding domain regions, they could reduce metabolic degradation from proteases, improving the half-life of activity.

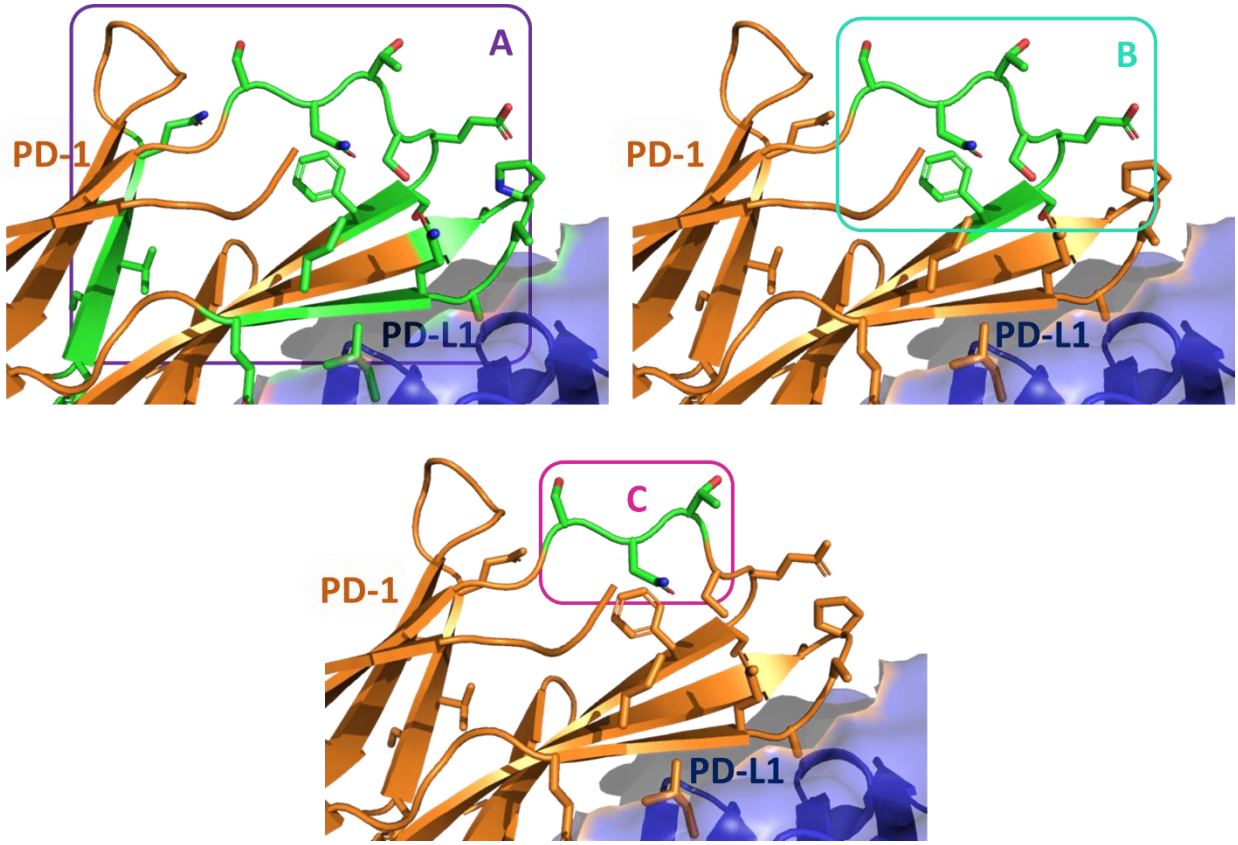

Figure 2.5. Binding interface of PD-1 and PD-L1 (from PDB: 4XQK) highlighting the residues that Aurigene used to establish their library of potential small molecule inhibitors of the PD-1/PD-L1 complex. **A**. Highlights the residues of compound **1** in green. **B**. Highlights the residues of cyclic peptide **2** in green. **C**. Highlights the SNT pharmacophore displayed in peptidomimetic compounds **3–5**.

Compound **1** was discovered through a systematic approach, where unnatural (L) amino acids were incorporated into the peptide to deter protease degradation. Using strictly D-amino acids would result in metabolic recycling and a short half-life. By replacing the residues with their L-enantiomers, the amino acids would not fit into the conventional active sites of proteases, reducing likelihood of metabolic degradation. Compound **2** cyclizes the peptide fragment, which also reduces metabolic degradation by preventing exoprotease activity. However, it is unknown whether the small molecule is entirely composed on one enantiomer or a mixture of natural and unnatural residues.

Compounds **1** and **2**, and their successors, were validated using a splenocyte recovery assay, which is a cell-based assay with a phenotypic output measuring cytokine production from murine white blood cells after co-mingling with PD-L1-presenting TNBC cells (Scheme 2.1). Aurigene's molecules were evaluated for recovery by using a competitive cell-based assay that comingled murine white blood cells with PD-L1-presenting TNBC cells. In brief, they initially incubate the white blood cells with αCD3 and αCD28 antibodies to emulate antigen-presenting cell (APC) signals inducing T cell activation, which will upregulate production of PD-1 and pro-inflammatory cytokines, indicative of proliferative T cell stimulation (Scheme 2.1A). The stimulated, PD-1-presenting white blood cells are then co-incubated with PD-L1-presenting MB-MDA-231 cells to halt said activation, stagnating the concentration of interleukins

present. These two extremes are the controls that are representative of the maximum stimulation (uninhibited ceiling) and maximum upon inhibition, respectively (Scheme 2.1B). Lastly, Aurigene would then inject 100 nM of their peptidomimetic compounds and remeasure the cytokine concentration and normalized to the maximum stimulation control, affording them the claim of high potency of these molecules from such low concentrations (Scheme 2.1C). The cytokine production is measured using a cytokine specific ELISA kit (i.e., IL-2, IL-6).

Aurigene filed another series of patents during 2013, focusing on peptidomimetic compounds with the same rationale – to prevent protease degradation. Interestingly, these patents show an iterative increase in potency (as presented by their percent recovery) and they all derive from the same serine, asparagine, and threonine (SNT) pharmacophore (Figure 2.4, box). Compound **3** is composed of L-serine (R-enantiomer) and L-asparagine, and the unnatural D-threonine with a respectable 68% recovery. Compounds **3**–**5** are "peptide mimicking" as the backbone is structurally similar to naturally occurring amides. However, to prevent metabolic degradation, they incorporate bioisosteres (e.g., diacylhydrazine, urea, 1,2,4-diazaoxazole) that are chemically different from the backbone amides. To be more explicit, the asparagine residue in compound **3** was inverted during installation, resulting in the diacylhydrazide and urea moieties conjugating the serine and threonine, respectively. These unnatural peptide bonds allow for protection from metabolic degradation and thus have longer half-lives. Compounds **5** and **6** incorporate 1,2,4-oxadiazoles to conjugate the serine and asparagine residues, which resulted in a much higher T cell recovery (93% and 92% recovery, respectively) than compound **3** prior.

Although Aurigene's splenocyte recovery assay data is compelling, offering phenotypic evidence that these peptidomimetic compounds were disrupting the PD-1/PD-L1 interaction on the cellular level, there was no evidence of direct disruption between these molecules and the proteins. We wanted to validate their claims by measuring their effectiveness as modulators to disrupt the proteins directly and determine if these molecules have any specificity of PD-1 or PD-L1, to lend them as targeting agents. To do so, we used SPR as a simplified, surrogate PD-L1-presenting cell surface. This simplified assay immobilizes the either protein to a gold chip, which will allow us to directly measure if molecules **3**–**5** are capable of binding and/or inhibiting from both the perspective of the immune cell surface (PD-1 immobilized) and from the perspective of the cancer cell surface (PD-L1 immobilized).

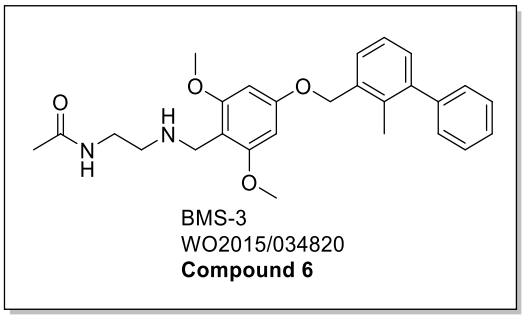

Figure 2.6. Positive control compound from Bristol-Myers Squibb (BMS) known to dimerize solubilized PD-L1. This was used as a positive control.

Surface Plasmon Resonance and Our Binding Assay:

Surface plasmon resonance (SPR) is a powerful characterization technique in determining binding affinities between two moieties.[223–227] The effect itself occurs when a light source is reflected on a noble metal surface that causes oscillation in the electrons (plasmon wave). As molecules are bound to the surface, there is a change in the refractive index that reaches the detector that reports a signal (response, RU). As more molecules adsorb to the surface, there is a larger change in the refractive index as more electrons are present to oscillate, which leads to a change in response observed in real-time resulting in a *sensorgram.*

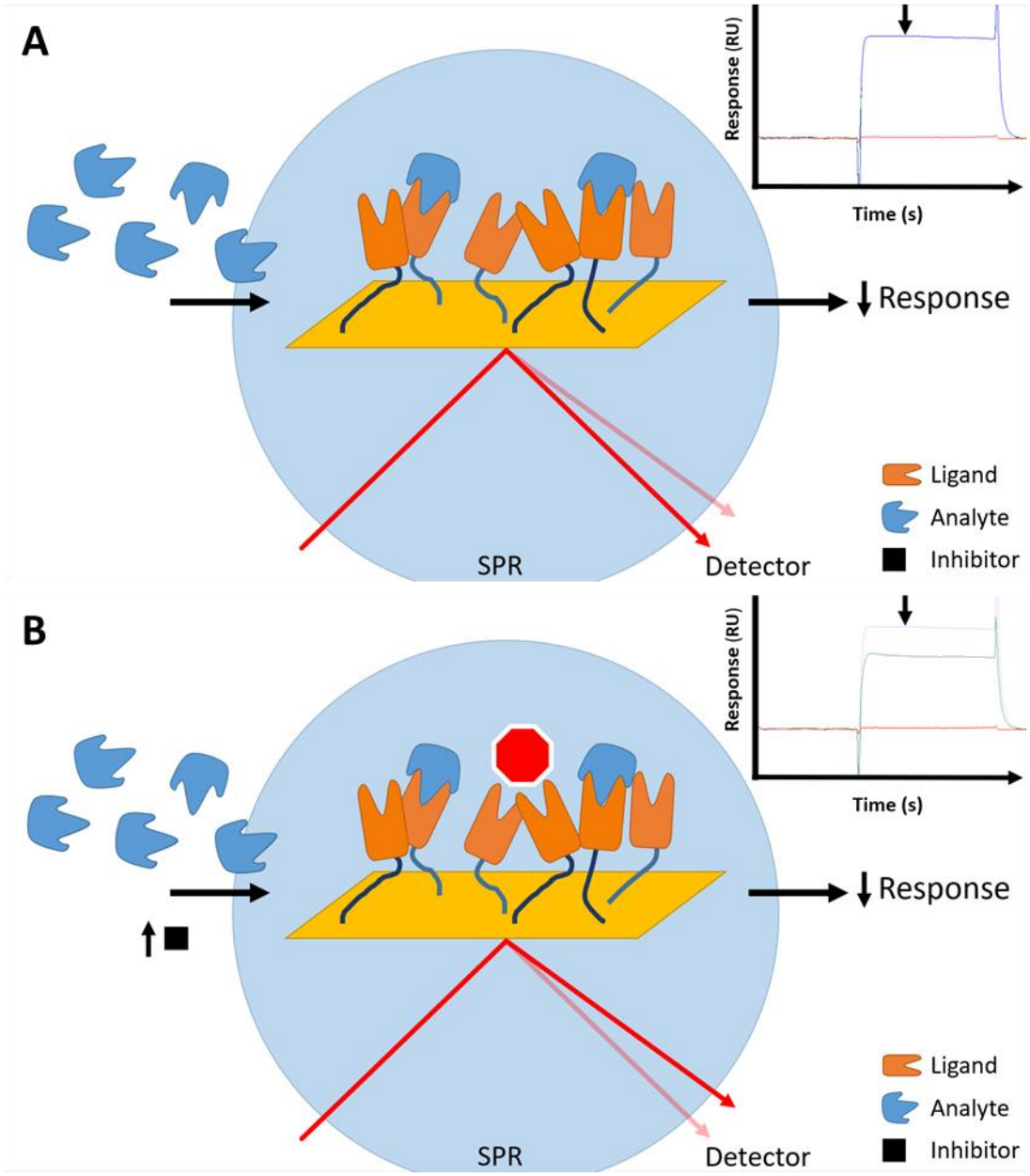

Scheme 2.2. Titrating the inhibitor should lower the interaction between analyte and ligand. **A**. Analyte is freely flowed across a ligand-coated gold surface. Binding instances cause a change in the refractive index to the detector, which results in the

sensorgram in the top right with a blue trace. **B**. As an inhibitor is titrated, we expect to see a decrease in response in the sensorgram with the lower green trace.

The sensorgram is a real-time readout of binding events between flowed analyte binds to the adsorbed ligand as they change the refractive index of an incidental light beam on the gold surface (Scheme 2.4). The molecules adsorbed to the gold surface are known as the *ligand* and species flowed across is called the *analyte*. A sensorgram is a composite image of all binding events occurring in real-time as the ligands approach saturation (associative). When all binding sites are occupied, we obtain equilibrium of an on (k_{on}) and off rate (k_{off}) that reveals the dissociation constant (K_D) (Equation 1). Ideally, when the analyte is stopped flowing, the dissociation should recover the ligand surface.

$$\mathrm{K}_D = \frac{k_{off}}{k_{on}} \tag{1}$$

The intensity of the response at equilibrium can be correlated with the concentration of the analyte to also reveal the activity of binding. Using Equation 2, we can reveal how active the ligand bound to the chip is by comparing the expected maximal response to the observed. The only dependent variables are the molecular weights and valence of the ligand and analytes.

$$R_{ligand} = \frac{R_{max} * MW_{ligand}}{MW_{analyte}} \tag{2}$$

The largest benefit of performing an SPR-based technique is that it is considered label-free.[225] This means that we may directly observe protein-protein interactions, or in our case, the lack thereof due to titrating the prospective inhibitors. Ideally, our work should corroborate what is being described by the patents in the splenocyte recovery assay, where titrating any of compounds **3**–**5**, will result in a lower response as they are expected to disrupt the binding (Scheme 2.4B).

Using SPR, we performed an inhibition-assay that detects the binding between the extracellular domains of PD-1 and PD-L1, and how they are affected in the presence of the Aurigene compounds, **3**–**5**. In the first binding assay, biotinylated-PD-L1 (BPS Bioscience) was adsorbed to a streptavidin-coated gold surface (SA Chip, Cytiva), and varied concentrations (ranging from 30 nM to 30 µM) of compounds **3**–**5** were flowed across in triplicate (Figure 2.5). The compounds were independently titrated over the flow cell of PD-L1 while in the presence of recombinant solubilized PD-1 (corresponding residues P34–E150 of the native protein).

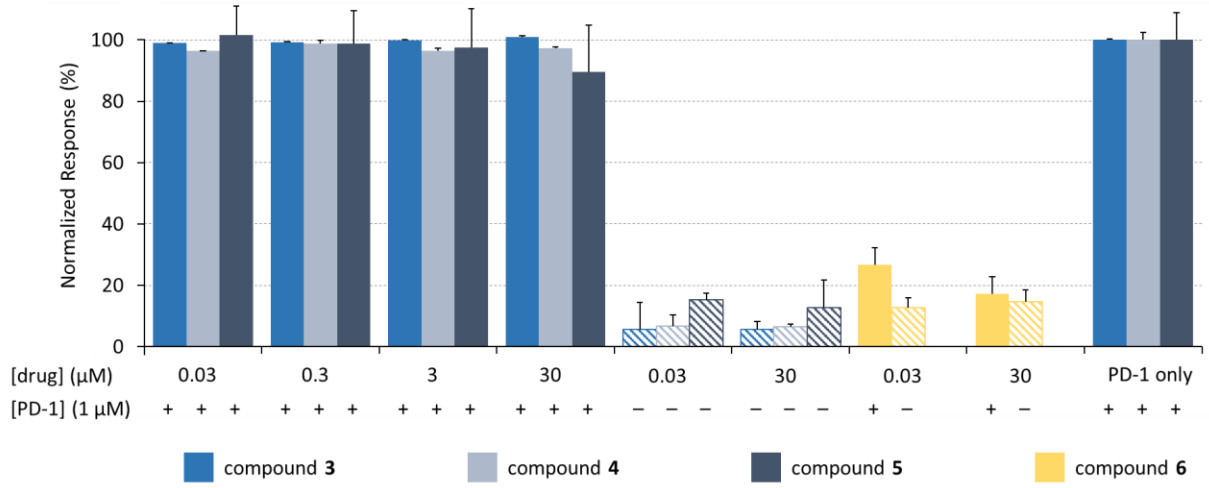

Figure 2.7. The Aurigene compounds **3**–**5** show no inhibition between 30 nM and 30 μM for PD-1 flowing over PD-L1. Soluble PD-1 was flowed across surface-bound PD-L1 with and without test compounds at varying concentrations. The response was normalized to the control protein (PD-1 only). Hashed data signifies small molecule sample in the absence of PD-1. Samples were measured in triplicate and normalized to the protein only control. Error bars indicate standard deviation. No statistical analysis was performed as there was no evidence of disruption or binding during the titration.

The binding responses were normalized to the native protein interaction between PD-1 and PD-L1, in the absence of any of the Aurigene species. Inhibitive compounds are expected to decrease this binding response relative to the control series. To validate the assay, we used a known PD-1/PD-L1 inhibitor from another pharmaceutical company, Bristol-Myers Squibb (BMS), as a positive control in compound **6** (Figure 2.6).[220] Previous studies have demonstrated that **6** induces a dimerization between extracellular PD-L1, effectively shutting down the PD-1 binding domains, preventing binding.[175,200,228] As expected, **6** showed effective inhibition at the low (30 nM) and high (30 μM) concentrations. For the titration data associated with **6**, see supplementary Figures S2.3 and S2.4.

When compounds **3**–**5** were evaluated in this assay, we observed no change in binding between the two proteins (Figure 2.7, left four columns). Moreover, in the absence of PD-1 protein (hashed data) the Aurigene compounds also elicited little signal variance between the two extreme concentrations (30 nM and 30 μM), indicating that there were non-specific binding events (i.e., adsorption and mass transfer), suggesting there was no directly observable binding to the immobilized protein (PD-L1, ligand). While a very small signal was likewise observed in **6** in the absence of PD-1, this is consistent with the known 2:1 stoichiometric binding mode previously reported between **6** and PD-L1.[228] Such behaviour would effectively the double the molecular weight of the receptor (since **6** binds to PD-L1 forming a homodimer, rather than monomeric PD-L1), while reducing the density of the receptor on the surface of the chip (since not all surface-bound protein would be capable of dimerizing). The result would be a very weak signal since SPR response is proportional to both the molecular weight *and* the valency between ligand and analyte – in this case PD-L1 and our small molecules – as well surface density.

The converse inhibition experiment was performed to validate potential binding to PD-1 (Figure 2.8). This was done using a fresh SA chip and adsorbing biotinylated-PD-1 (BPS Bioscience) on its surface and flowed recombinant solubilized PD-L1 protein (corresponding residues A18–T239, chosen to represent both extracellular domains present in the native protein) across the chip along with various concentrations of

3–**6**. This type of reciprocal binding assay serves as an important control for binding artifacts in SPR experiments. Once again, the positive control molecule (**6**) was observed to inhibit the interaction (in yellow), although in this case higher concentrations of **6** were required because of the high concentration of PD-L1 required in the experiment. These data provide additional support for the earlier study determining PD-L1 as the biological target for **6**.[200]

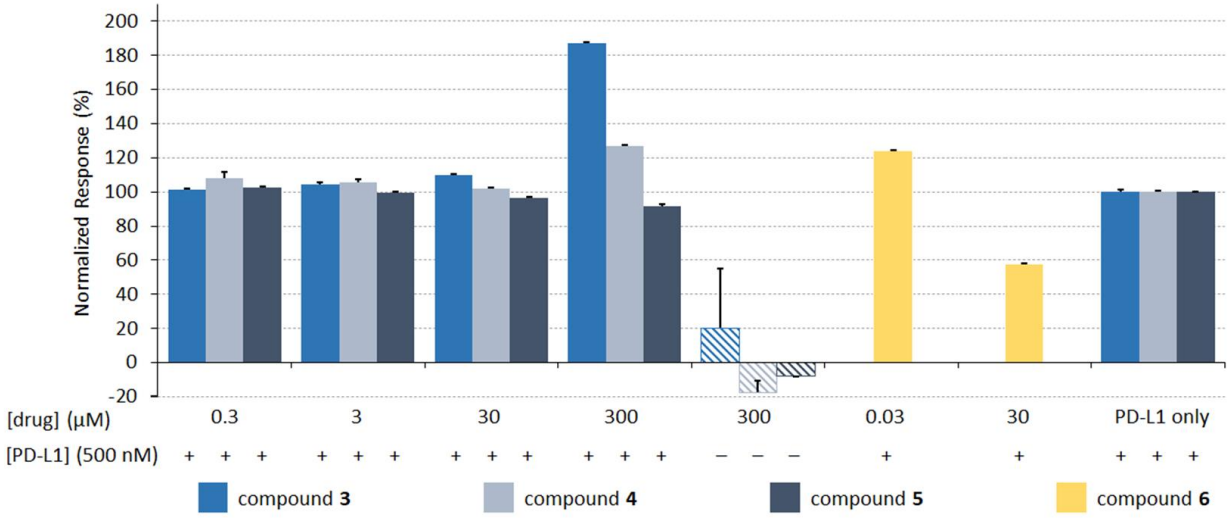

Figure 2.8. The Aurigene compounds (**3**–**5**) show no inhibition between 300 nM and 300 μM for PD-L1 flowing across a PD-1 surface. Soluble PD-L1 was flowed across surface-bound PD-1 with and without test compounds at varying concentrations. The response is normalized to the binding response of protein control samples (PD-L1 only). Hashed data signifies small molecule sample in the absence of PD-L1. Samples were measured in triplicate and normalized to the protein only control. Error bars indicate standard deviation. No statistical analysis was performed as there was no evidence of disruption or binding during the titration.

As in the previous assay, however, the Aurigene compounds, **3**–**5**, showed no inhibition of the PD-1/PD-L1 interaction nor did they elicit any statistically significant binding to the adsorbed PD-1. At very high concentrations (300 μM/0.3 mM), compounds **3** and **4** had showed an increase in response (i.e., "negative inhibition"), but this is likely attributed to the molecules nonspecifically adsorbing to the surface or possibly aggregating/precipitating.

Although the PD-1/PD-L1 blockade is more prominently discussed, PD-1 and PD-L1 are capable of interacting with other proteins in an non-redundant manner of immune suppression.[145,149,229] To try and validate that maybe the Aurigene molecules were disrupting other immunosuppressive groups, we titrated the molecules again but across a surface of PD-L2 (Figure 2.9). With no change in response relative to the control (PD-1 only) it was concluded that compounds **3**–**5** were not disrupting this other pathway. Compound **6** was also shown not to inhibit the PD-1/PD-L2 interaction, nor directly bind to PD-L2, highlighting its specificity to PD-L1.

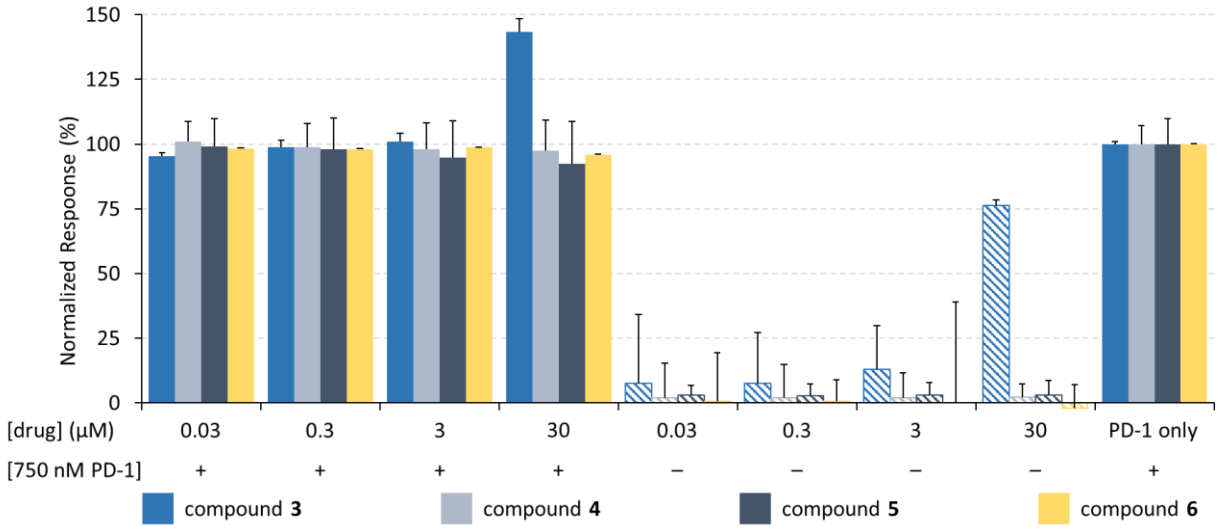

Figure 2.9. The Aurigene compounds (**3**–**5**) show no inhibition between 30 nM and 30 μM when flowed with PD-1 across a PD-L2 surface. The response was normalized to the binding response of protein control samples (PD-1 only). Hashed data signifies small molecule sample in the absence of PD-1. Samples were measured in triplicate and normalized to the protein only control. Error bars indicate standard deviation. No statistical analysis was performed as there was no evidence of disruption or binding during the titration.

Previous work established by Dr. Ronan Hanley had confirmed that **3** was unsuccessful at mitigating a blockade between PD-1/PD-L1 through commercial ELISA with a reported IC_{50} > 3 μM. This was run in parallel with **6** which had maintained consistency as a positive control with an IC_{50} = 33 nM. This data can be found in the supplementary materials (Figure S2.8) of the published work and their thesis.[172,200]

As previously described, Aurigene characterized the efficacy of their lead compounds using a phenotypic cell-based assay built around splenocyte inhibition and recovery as a proxy for the immune system.[194–196,221,222] Compounds **3**–**5** triggered high recovery and potency in their experiments (68%, 93%, and 92%, respectively, relative to an uninhibited positive control) at 100 nM of compound.[194–196] The limited experimental detail in Aurigene's patents (including controls with PD-L1 in the absence of small molecules) suggest the phenotype was PD-L1 specific. But as we have demonstrated above the results from Aurigene's cell-based assay cannot be attributed to direct inhibition of the PD-1/PD-L1 interaction, nor do our results suggest that compounds **3**–**5** directly interact with either protein. Instead, an alternative mechanism must be responsible for their observed effects.

Despite the recent appearance of a number of papers related to small molecule modulation of the PD-1/PD-L1 interaction, there is little explanation of how the Aurigene compounds exert their function.[64,67,143,176,189,201,230] However, a close reading of Aurigene's patent portfolio provides some insight into the development of this class of small molecules (peptidomimetic immunomodulators). Aurigene's earlier patent filings claimed large peptides that mimic a significant portion of the PD-1 extracellular domain.[221] This includes much of the PD-L1 binding interface, and so it is likely that these large peptides would be competitive inhibitors of the PD-1/PD-L1 interaction. Attempts to achieve more drug-like properties, however, led to the subsequent filings describing the development of macrocyclic peptides that mimic the 7-residue BC-loop (Figure 2.5B).[222] The more recent patents refined the structure (and, presumably, improved the pharmacokinetic properties) by developing some small tripeptide-like

analogues that mimic the central serine-asparagine-threonine tripeptide of this loop (Figure 2.5C).[194–196] This is the iterative development that ultimately led to compounds **3**–**5**.

Critically, however, the BC-loop (and particularly the region mimicked by compounds **3**–**5**) is regionally distal to the PD-L1-binding interface, and so it is unclear why these molecules would be expected to be *direct* binding inhibitors, notwithstanding their apparent potency in cell-based assays and the fact they are referred to (with little supporting data) in Aurigene's patents and subsequent reviews[67,143,231] as inhibitors of the PD-1/PD-L1 interaction.

Although it is possible that there is some key difference (e.g., glycosylation state) between our *in vitro* system and the "real-life" PD-1 and PD-L1 proteins expressed on the surface of T cells and antigen presenting cells, a more likely scenario is that the compounds do mimic the PD-1 surface as intended but that this serves not to directly disrupt binding with the PD-L1. These peptidomimetic species are disrupting a potential other immunosuppressive PD-1 binding partner beyond PD-L2. Both PD-1 and PD-L1 are thought to participate in regulatory binding interactions with other proteins (of the B7 superfamily) and we hypothesize that one or more of these might be the true target of **3**–**5** (Figure 2.8C).[144,145]

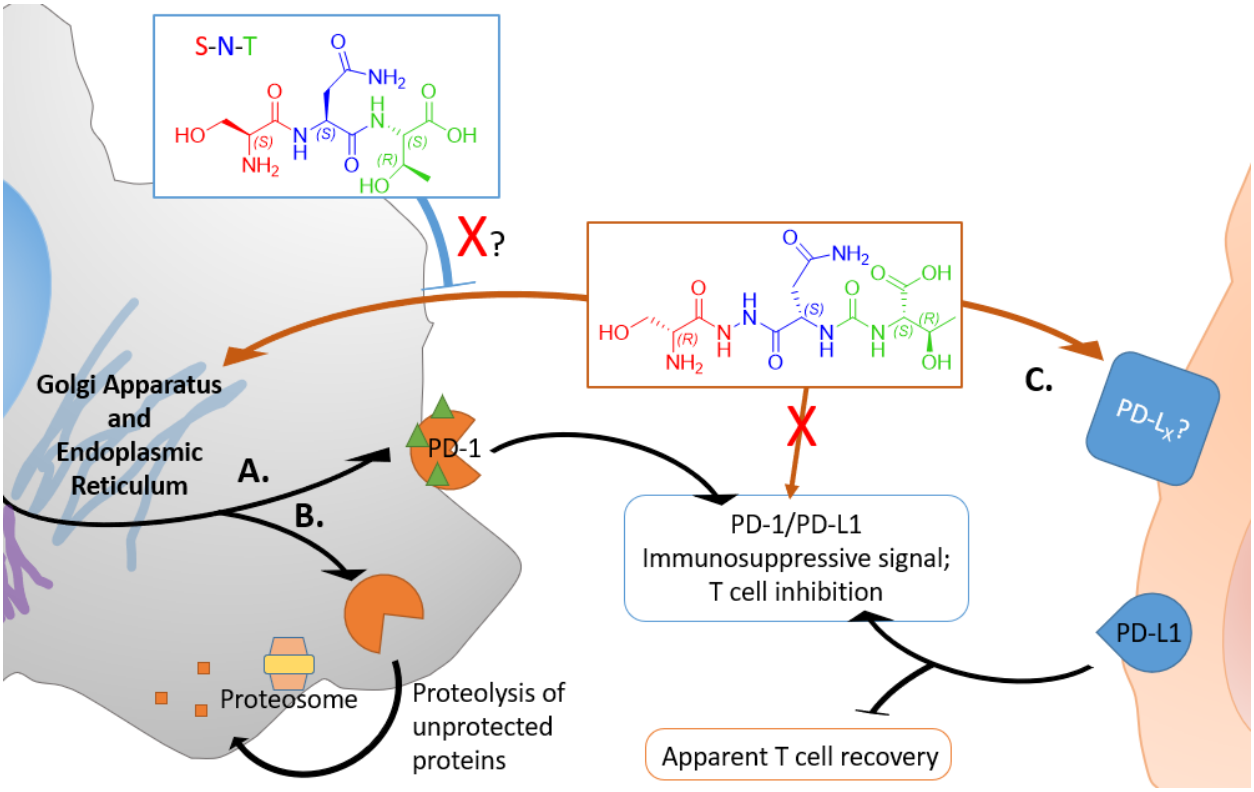

Figure 2.10. The Aurigene molecules do not blockade the PD-1/PD-L1 interaction as displayed by our SPR data. **A**. Under native conditions translated proteins are folded and modified through the Golgi apparatus and endoplasmic reticulum to protect from degradation. **B**. The Aurigene small molecules may be blocking upstream post-translational modification enzymes (i.e., glycosyltransferases) leading to proteolysis by the proteosome and thus removing the immunosuppressive signal with PD-L1. **C**. Alternatively, PD-1 is capable of binding with other ligands beyond PD-L2 and VISTA, however the lack of inhibitive evidence with these proteins may suggest some other binding event that the Aurigene molecules target, allowing for the phenotypic recovery observed in their cell data.

Lastly, in 2015, Curis Inc. initiated some clinical trials with a small molecule from Aurigene known as CA-170.[199] The exact structure of CA-170 was not disclosed at the time that our experiments were conducted, but this lead candidate had emerged from a focused library of hit compounds that was designed to exploit hot spots within the PD-1/PD-L1 complex.[142] In a recent review by two of the inventors of the Aurigene molecules,[67] they claim that CA-170 was designed to target one or more conserved pockets shared between in PD-L1 and VISTA (V-domain Immunoglobulin Suppressor of T Cell Activation), another nonredundant immunosuppressing protein that belongs with B7-superfamily like PD-L1 and PD-L2.[232,233] These authors were careful not to indicate whether CA-170 is structurally related to their earlier disclosed compounds. One of these recent reviews asserts that CA-170 is an oxadiazole (akin to **4** and **5**),[178] while another describes CA-170 as a molecule capable of PD-1/PD-L1 complex.[55] The existence of a clinical candidate that is likely related to compounds **3**–**5** and that is thought to function though direct blockade provides motivation to better understand the function for this series of small molecules.

In this study, we performed SPR-based assays to test the hypothesis of direct protein binding inhibition and found that none of the compounds assessed can disrupt the interaction between soluble PD-1 and adhered PD-L1 or between soluble PD-L1 and adhered PD-1. Beyond PD-1 and PD-L1, we investigated whether compounds **3**–**5** would have any potential inhibitory effects with other immunosuppressive proteins such as PD-L2 (Figure 2.7) or VISTA (Figure S2.7).

Preliminary testing confirmed that compounds **3**–**5** did not interact with surface-bound VISTA (Figure S2.7). Based on these data and an analysis of structural features of the PD-1/PD-L1 interaction (and particularly the region of the PD-1 BC-loop from which Aurigene's lead compounds were derived), we hypothesize that this family of small molecules may regulate the function of some other PD-1 binding partner or an upstream enzyme and they observed the downstream effects.[233]

Proposed Rationale for the Apparent Phenotypic Effects Observed from the Aurigene Molecules

Our SPR-based assays resulted in a confirmation that compounds **3**–**5** do not exhibit any inhibitory effects of the PD-1/PD-L1 complex, nor do they bind to either protein. We also found that these molecules do not disrupt or bind other described complexes and their respective individual components with PD-L2 and VISTA. Although we never saw any direct binding from any of the Aurigene compounds, the data from the splenocyte recovery assay indicate these molecules undergo a different mode of action that results in the apparent recovery in T cell activity.

Compounds **3**–**5** all share a common pharmacophore (Figure 2.4, box) which is comprised of serine, asparagine, and threonine (SNT motif). This motif in particular is attributed to the post-translational modification that decorate proteins with bulky protective sugars that will increase the longevity of protein half-lives.[137,204] Glycosylation is a protein modification that covalently binds large oligosaccharides to protect from protease degradation and other metabolic recycling. Although experimental specifics of how long the Aurigene compounds are incubated are not disclosed, these compounds intuitively resonated as inhibitors of a potential upstream glycosyltransferase. To elaborate, during T cell activation there is an upregulation in PD-1 expression, however this is disrupted when a ligand, PD-L1 or PD-L2, binds and that causes the suppressive elements observed. Potentially, these compounds may be taken-up by the cells and recognized by other upstream proteins such as glycosyltransferases, and effectively shutting down their activity (Figure 2.10B). With the glycosyltransferases inhibited, there would be less proteins

protected from proteolysis, thus leading to the lower inhibition events observed in Aurigene's comingling assay, rather than a direct binding.

In 2021, following the publication of the data presented above, the inventors on the Aurigene patents published a thorough article about the synthesis and development of CA-170, and its effects with PD-1, PD-L1, PD-L2, and VISTA.[234] In brief, this paper contextualizes the characterization data to determine why CA-170 is a useful molecule – as an orally available selective small molecule for PD-L1. The paper highlights that it does not disrupt the PD-1/PD-L1 interaction directly, but in the presence of CA-170 T cell activation is maintained regardless of the PD-1/PD-L1 complex, indicating that the molecule causes some allosteric interaction that prevents the immunosuppressive signal. The authors allude that there is noticeable difference in effect for CA-170 when the proteins of interest were expressed natively (in their work) or recombinantly (comparing to other published data), and this difference highlights the efficacy of CA-170 and its dependence on post-translational modifications, which may reinforce the glycosylation hypothesis. Although this is speculative, these reports indicate that Aurigene's molecules have more of an effect on upstream regulation than directly as immunomodulators.

Antibodies, a Necessary Evil?

Despite the promise in the literature, compounds **3**-**5** from Aurigene are **not** suitable candidates for targeting PD-L1. Thus, an alternative targeting candidate would be needed to conjugate to the gold surface. Although **6** showed excellent selectivity for PD-L1 in the previous SPR assays (Figure S2.4). It was not chosen as the targeting agent as it is unlikely it would be able to directly disrupt the PD-1/PD-L1 interaction to recover lymphocyte cytotoxicity, due its mode of action requiring dimerization of the PD-1 binding interface. This expected 2:1 stoichiometry of **6**:PD-L1 may be insufficient to warrant a blockade and therefore show no immunotherapeutic effect. We speculate that development of a library of **6** analogs with varied tethers and tether sites would be needed to validate the conjugation and defer the nanoparticle synthesis, and characterized before actually being used as a targeting agent. We saw this effort was out of the scope of the project and began investigating a commercially available mAb that was on-hand (Chapter 4).

To date, monoclonal antibodies are the only clinical form of targeting agent for the PD-1/PD-L1 complex and despite their progress in clinical treatments, there is still a large risk attributed to their use – immunogenicity.[189,192] Antibodies are used mostly as targeting agents to improve the selectivity of other payloads (i.e., nanocarriers of cytotoxic agents via ADCs or nanoparticles), however their prevalence is limited by their size and accessibility to tissues.

3. Cell Culture Conditions Can Cause Premature Release in Ester-Linked Traceless Disulfide Linkers

The following chapter was adapted from the manuscript published in Journal of Drug Delivery Science and Technology.[235]

Blevins, D. J., Nazir, R., Dabiri, S. M. H., Akbari, M., Wulff, J. E. *J. Drug. Deliv. Sci. Tech.* **2022**, *78*, 103950.

*This was a collaborative effort between the Wulff and Akbari groups in determining where and why we observed premature turn-on fluorescence from disulfide-tethered compounds. The fluorogenic disulfide tethers were proxy reagents intended for tumour-specific triggerable release. However, they showed low selectivity and high background release in cells. The premature release of the dye was mitigated by installing methyl groups at the α-position to the carbonyl carbons as to limit any ester hydrolysis induced by the FBS, a necessary cell culturing component. Dr. Hossein Dabiri performed the cellular studies monitoring dye release. Dr. Rashid Nazir finalized and scaled up the synthesis of compound **9** for molecule reactivity studies in MilliQ water. Derek Blevins developed the real-time assay to monitor the dye release, provided the synthesis of compounds **7** and **8**, and determined how to mitigate esterase-specific release. The relevant supplementary data are found starting on page 173.*

Foreword

Alongside targeted delivery, controlled release is especially helpful in mitigating off-targeting adverse effects caused by cytotoxic drug molecules in chemotherapy regimens. We wanted to develop a suitable linker for our dual-functional AuNPs, such that they may actively block PD-1/PD-L1 on the cancer cell surface as well as internalize to sensitize them. While previous efforts of targeting nanoparticles to PD-L1 with small molecules were not fruitful, targeting with an αPD-L1 antibody was still a viable strategy. However, by conjugating large biomolecules to the gold surface, these potential drugs grow in volume further limiting their deliverability throughout the tumour. To circumvent the possibility of the AuNPs being limited to shallow penetration when treating TNBC, we investigated some methods of controlled release that may improve uptake of the gold core for future radiosensitization assays (see Follow-up 3C, Figure 6.8). For our nanocarriers there is potential for non-specific internalization (i.e., lysosome-directed endocytosis), but we aimed at developing a tether to release the particle from the surface. This method of environmentally stimulated degradation is currently employed in delivering potent chemotherapeutics, where the chemotherapeutic agents are tethered to the targeting agent (e.g., ADCs), and use expected environmental phenomena to help liberate the active drug.

Many chemotherapeutics with high potency for cell death may not be delivered directly for two reasons.[163,236] The first is an incompatibility with aqueous environments where the compounds may aggregate due to their high hydrophobic character. Secondly, the compound alone may not have desired selectivity which makes them difficult to dose without triggering adverse effects (i.e., unwanted cell death outside disease site).

Nanomedicine can overcome these barriers to improve delivery for these toxins by compartmentalizing the chemotherapeutic agents in hydrophobic domains (e.g., polylactic acid (PLA) in polymer nanoparticles).[163] This compartmentalization allows for other targeting agents to help direct the drug, improving selectivity, as well as retaining a high drug potency and mitigating off-targeting.

While nanocarrier compartmentalization gets the drug into the body, it might not leave the carrier as the hydrophobic drug could remain in the hydrophobic core. To overcome this barrier, controlled release employs environmental triggers to disassemble the core and effectively release the drug into the bulk, ideally only at the disease site. We wanted to employ a similar trigger system, which is selective for the tumour microenvironment (TME), where our nanoparticles were not limited to the surface of TNBC cells, nor limited to non-selective uptake for possible radiosensitization (Figure 6.8).

Abstract

Disulfide acids are important for traceless release mechanisms in prodrugs and drug delivery applications. Their ability to self-immolate and release cargo due to environmental stimulus is invaluable. However, complex reactivity patterns may be overlooked as assays increase in complexity or are conducted in media of increasing biological relevance. Conclusions drawn from preliminary characterization in simple phosphate buffers are often applied to *in vitro* studies in which more complex media are used (e.g., containing glucose, amino acids, FBS, and the cell surface). We developed a model disulfide incorporating a fluorogenic dye as a reporter group in order to explore the generality of the disulfide prodrug system, and used this to explore the stability of disulfide esters in various contexts of increasing complexity. We found that our reporter molecules prematurely released cargo in a series of cell-containing and cell-free assays. We systematically reverse-engineered the components of a complex cell medium and found that FBS was capable of interfering with disulfide-based prodrug linkers, triggering the release of conjugated 4-methylumbelliferone (4-MU) from representative reporter molecules. FBS consistently induced premature 4-MU release in complete media (i.e., DMEM and RPMI 1640), minimal essential media, and in pure water indicating some form of thiol exchange or hydrolysis was occurring due to the sera contributing to the release of the dye. The premature fluorescence was mitigated when FBS was subjected to intense heat (> 100 °C) or esterase-specific protease inhibitor cocktail (PIC), indicating that esterases from the sera were capable of triggering cargo release using a hydrolysis mechanism that is separate from the desired reductive cleavage pathway. These findings are important because they show that variance in models may hide unexpected results, which calls for more meticulous consideration of control experiments when developing stimulus-release agents for biological applications.

Introduction

Self-immolation is frequently used in drug delivery systems to facilitate the release of a drug by controlled disassembly of the vehicle or a prodrug form.[37,54,91,94,96,188,237–244] In controlled drug delivery systems, the triggered release of a drug is attributed to intentional deconstruction of the vehicle by an external factor or stimulus, which releases the active drug moiety. Stimuli may be intrinsic environmental factors such as changes in pH, temperature, irregular concentration of redox reactive species, or external factors like light or ultrasound.[95,187,245,246]

The TME is reported to be more acidic and highly reductive, making it a prime target for stimulus-based drug delivery.[37,62,96,103,242,247–249] The irregular environment (relative to basal cell conditions) is caused by an imbalance in metabolites. One frequently associated metabolite with the TME is reduced glutathione (GSH), a common thiol-containing tripeptide; it is reported at unusually high concentrations surrounding tumours.[248] The abnormal concentration of GSH consequently introduces an immediate reducing extracellular matrix relative to healthy tissues, making it an excellent focus for stimulated release via disulfide-based prodrugs or nanoparticle release mechanisms.[182,188,248]

Disulfides are an important moiety in nanomaterials for drug delivery due to their redox capability for controlled deconstruction.[37,94,239,244,250–253] Dithiodiacids are useful as prodrug linkers with their two carboxylic acid handles for potential asymmetric conjugation, and the disulfide bridge which is reactive with a reducing environment. Upon reduction of the disulfide, the free thiol (or thiolate) is capable of nucleophilic addition to the nearby carbonyl group, resulting in the formation of a thiolactone and releasing the active drug species (Scheme 3.1). Disulfides are a traditional approach to redox-responsive nanocarriers selective for a reducing environment.[37,54,96,254–261] Their response to the environment may induce swelling or shedding of the hydrophilic component of a vehicle, releasing the payload into the bulk. Disulfides have also been used as chemodosimeters to discriminate various thiols.[262,263] Bohn *et al.* used a series of asymmetric disulfide–linker prodrugs to discriminate and decrease esterase degradation, effectively improving the half-life of the molecules; the increased hydrophobicity also helped the molecules cross the blood-brain barrier.[260]

In this work, we employed dithiodiacids as a means of selective and controlled release for the reducing character of the TME using turn-on fluorescence from liberated 4-MU as the primary readout.[103,241,242,260,264,265] However, we found an incompatibility with common cell culturing techniques when transitioning from molecular-based studies to cellular. Herein we emphasize how common biological reagents were used to discriminate the stability of our compounds, and how cell culturing techniques and conditions affected our controlled release studies when transitioning into more complex systems.

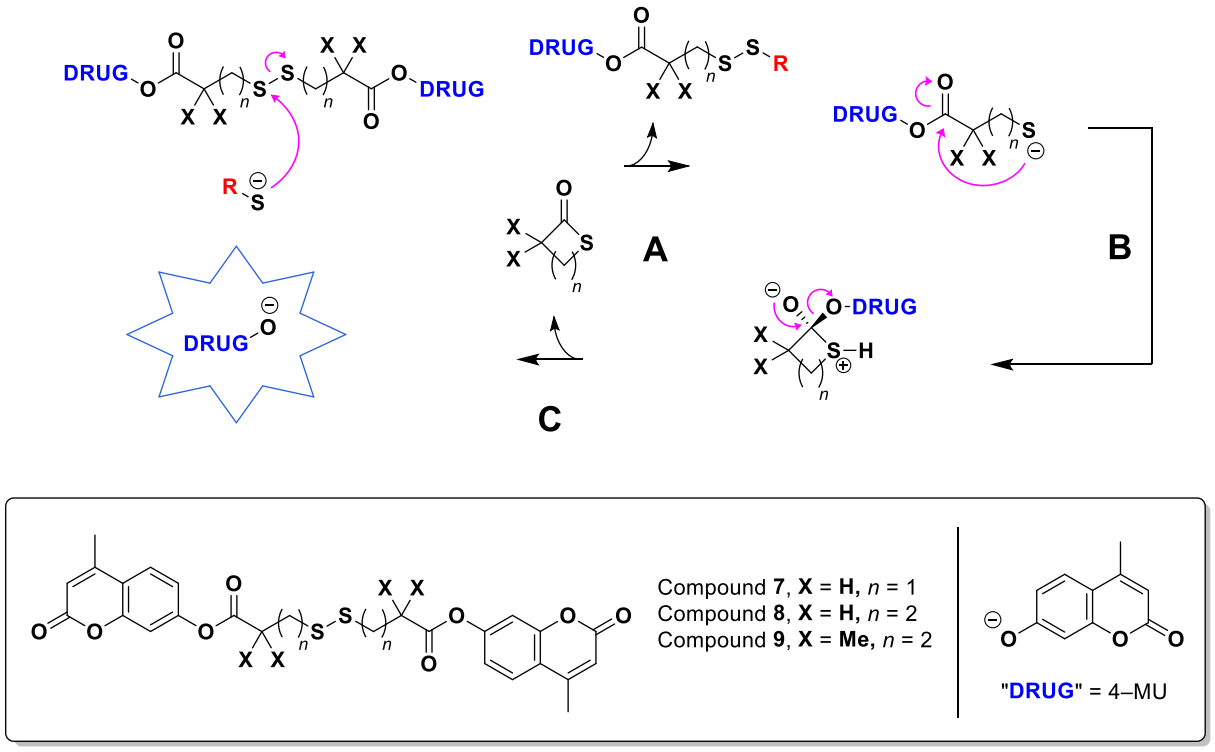

*Scheme 3.1. General mechanism of disulfide-induced release of 4-MU anion from fluorescently quenched bis-esterified prodrugs **7–9**. **A**. Exchange or reduction of the disulfide with another thiolate-species is expected to form the free thiolate. **B**. The reduced thiolate undergoes an intramolecular nucleophilic substitution cyclization forming an unstable intermediate. **C**. The intermediate species collapses favouring formation of the thiolactone, which releases the drug into the bulk. 4-MU behaves as a surrogate drug*

*with turn-on fluorescent properties when in the anionic form. The inset presents the structures of the 4-MU anionic fluorophore and the variation between traceless prodrug linkers in compounds **7–9**. The complete structures are found in Figure S3.1.*

Materials and Methods

1. Materials

3,3'-dithiodipropionic and 4,4'-dithiodibutyric acid, EDC, 4-MU, DMAP, DCM, MeOH, oxidized glutathione (GSSG), reduced glutathione (GSH), cysteine (Cys), *meta*-chloroperoxybenzoic acid (*m*CPBA), Na_2S, NaSH, Tris-HCl, and acetonitrile were obtained from Sigma. TCEP was obtained from ChemImpex. All culturing media (DMEM, RPMI 1640, DPBS, and MEM) were purchased from ThermoFisher, 100x Protease Inhibitor Cocktail Set I purchased from Calbiochem®, and Fetal Bovine Serum (FBS) One shot purchased from GibCo™.

2. Instruments

1.1.1. NMR

^{1}H NMR spectra were either recorded at 500.27 or 300.27 MHz, respectively, on a Bruker AVANCE NEO 500 spectrometer equipped with a BBF probe or a Bruker AVANCE 300 spectrometer equipped with a 5 mm PABBO BB-1H/D Z-GRD probe. ^{13}C NMR spectra were recorded at 125.81 MHz on a Bruker AVANCE NEO 500 spectrometer equipped with a BBF probe. ^{1}H chemical shifts (δ) are reported in parts–per–million (ppm) relative to tetramethylsilane and referenced to the solvent peak ($CDCl_3$, δ 7.27). The NMR data is presented as follows: chemical shift, multiplicity (s = singlet, d = doublet, dd = doublet of doublets, dt = doublet of triplets, qt = quintet, app = apparent, m = multiplet), coupling constants (J, reported in Hz), integration. All ^{13}C NMR spectra are proton-decoupled (^{13}C{1H}). ^{13}C chemical shifts (δ) are reported in parts-per-million (ppm) relative to tetramethylsilane and referenced to the solvent peak ($CDCl_3$, δ 77.2)

1.1.2. Fluorescence Monitoring

All subsequent fluorescence experiments monitored release of 4-MU with fixed excitation and emission wavelengths of 315 nm and 445 nm, respectively. Any observed release of the fluorophore from compounds **7** and **8** were normalized with respect to 2 mol eq. 4-MU in the appropriate medium, expressed as a percentage described in Equation 4. The fluorescence intensity of 4-MU release in cell–free media was kinetically monitored using a SpectraMax M5 (Molecular Devices LLC, US) by reading every 180 s for compounds **7** and **8**, and every 300 s or 600 s for compound **9**. The fluorescence intensity of cell supernatant was measured using an Infinite M Nano plate reader (Tecan, Switzerland). Plates were incubated at 37 °C.

1.2. Molecular Characterization

Stock solutions of prodrugs **7** and **8** were made in 100% acetonitrile and were dilute to a working concentration of 200 µM (20x) with 30% MeCN / 70% Tris buffer, pH 7.4. Two Tris buffers stocks was prepared using Tris-HCl, the first (Tris buffer A) was a working stock at 71.4 mM, such that it would have a final concentration of 50 mM when 30% (v/v) MeCN was added. Tris buffer B was prepared at 50 mM Tris-HCl and used as the solvent for preparing reagent stocks. Both Tris buffers had their pH adjusted to 7.4 with 6 M NaOH. The reagent stocks used in Figure 3.1 were prepared at 31.6x concentrate, such that the final concentration would be 30 mol eq. relative to the traceless linkers. In a 96-well plate, the 20x compound solution (3:7 MeCN/Tris buffer A) were further dilute with 31.6x reagent solution (Tris buffer B) making a 1x compound, 30x reagent, and 1.5% v/v MeCN.

The spectrophotometer detected fluorescence of 4-MU by exciting at 315 nm and detecting the emission at 450 nm. This was performed either in a quartz cuvette with a 1 cm pathlength or in a 96-well plate with a with 1 cm pathlength. The fluorescent release profile of "high" concentration acetonitrile was 5% v/v – by preparing 20x stocks of compound in acetonitrile (100% v/v) and performing 1:19 dilution with the 30 mol eq. reactive species in Tris buffer.

1.2.1.1. Cell–Free Plate Assay

The subsequent cell–free plate assays had the molecule dissolved in the above mixture as a stock solution and diluted into the appropriate media, treated with either 30 mol eq. TCEP and/or FBS. With untreated media serving as a negative control. The plate was excited at 315 nm to stimulate emission of 445 nm photon from released 4-MU every five minutes.

Synthesis and characterization of compounds **7**–**9** is provided in the Supplementary Material Chapter on pages 173–175, and 191–201.

3. Molecular-Release Study Characterization

3.1.1. Fluorescence Spectroscopy

A SpectraMax M5 plate reader was used to monitor release of 4-MU. Measurements were made using 96-well flat-bottom plate (Corning Costar). 4-MU was excited at 315 nm, and emission measured at 450 nm. Upon conjugation, the emission peak of the coumarin was suppressed, but this quenching was shown to be reversible upon addition of at least 30 mol eq. TCEP. Time–dependent release of 4-MU from the model prodrugs was normalized relative the intensity of 2 mol eq. free 4-MU using equation 3 as described below:

$$Release\ (t) = \frac{F(t)-F_0}{F_{4-MU}-F_0} * 100\% \quad (3)$$

Where "*Release (t)*" is the normalized release represented as a percentage, "*F(t)*" is the observed fluorescence at a given time point, "F_0" is fluorescence intensity of media, and "$F_{4\text{-}MU}$" is the intensity of the total 4-MU (2 mol eq. relative to the traceless linker). Time was set to 0 s when the prodrugs were added to their respective well.

3.1.2. Turn-On Fluorescence of Model Prodrug Compounds

Compounds **7** and **8** were screened for selective turn-on fluorescence with a plethora of reducing agents, oxidizing agents, and sulfur exchanging species (Figure 3.1, Figure S3.3, Figure S3.4). In a 96-well plate, 10 µM compound was treated with 30 mol eq. TCEP, glutathione (GSH), oxidized glutathione (GSSG), cysteine (Cys), H_2O_2, or *m*CPBA and monitored for 4-MU release with the previous conditions.

Compounds **8** and **9** were screen for selective turn-on fluorescence as described above (Figure S3.5).

4. Cell-based Studies

4.1.1. *In vitro* culture of U-87, U-251, and HNDF cells

Human-derived glioma cell lines, U-87 (ATCC® HTB–14™) U-251 (Creative Bioarray, CSC–6321W) and Human primary normal dermal fibroblast (ATCC® PCS-201-212™) were cultured according to the standard protocol provided by the supplier. Briefly, cells (Passage 3-8) were initially grown in the Corning 25cm² Rectangular Canted Neck Cell Culture Flask using Dulbecco's modified Eagle's medium (DMEM, Gibco™ by

Life Technologies™, USA) treated with 10% FBS (Gibco™ by Life Technologies™, USA) and 1% penicillin-streptomycin (10 000 unit/mL, Gibco™ by Life Technologies™, USA) as the growth medium. Cells were incubated in an atmosphere of 5 % CO_2 at 37 °C.

When cells were 85% confluent, they were detached from the surface of culture flask when growth media was replaced with 3 mL trypsin-EDTA (Gibco™ by Life Technologies™, USA) and incubated at 37 °C for 5 minutes. After, 6 mL of growth media was added to the detached cells to deactivate trypsin activity, followed by centrifuging the cell suspension at 300x g to make a cell pellet. The supernatant was discarded, and 1 mL of fresh growth media was added to the cell pellet to suspend the cells by gentle pipetting.

The next step was seeding cells in Corning 96-well plate at the density of 3 000 cells/well and incubating the well plate at 37 °C in an atmosphere of 5 % CO_2. After 24 hours, the cell culture media in each well was replaced by the 300 µL of prodrug solution (10 and 20 µM of compound **7** or **8** dissolved in growth medium) and incubated for 24 hours. A control solution of free 4-MU was prepared to monitor "full" release (20 and 40 µM, respectively).

4.1.2.Kinetic Compound **7** Release Study with U-87 Glioma Cells

U-87 cells were seeded in 96-well plate at the density of 3 000 cells/well as described above. After 24 hours the cell growth media was replaced with 300 µL of different release media. To obtain different release media containing 10 µM of compound **7**, a stock series was diluted in several media such as DPBS, DPBS+Glucose, DPBS+Glucose+Glutamine, and DPBS+Glucose+Glutamine+FBS. The concentrations of glucose, glutamine, and FBS were 4.5 g/L, 0.584 g/L, and 10% (v/v), respectively. Also, the standard release medium was prepared by dissolving equivalent concentration of 4-MU (20 µM) in the same series of buffers. After 24 hours, cell media was removed and replaced with appropriate release medium and standard release medium. After predetermined time points, the fluorescence intensity was measured as described before and the obtained intensity was normalized with respect to the intensity of the equivalent concentration of 4-MU cultured in the same release medium. The experiment was conducted with 6 replicates.

4.1.3.Cell Viability Assay

To identify the effect of release media and compound **7** on the cell viability, U-87 cells were seeded in a Corning 96-well plate at the density of 3 000 cells/well as previously described. After 24 hours, the cell media was removed and replaced with different release media containing 10 µM compound **7**. Moreover, cells cultured with cell media and Milli-Q water were considered as the positive and negative controls, respectively. At specific time points (namely 12h, 24h, 48h, and 72h), the release media was removed and replaced with 110 µL of cell media containing 10% (v/v) PrestoBlue reagent (Invitrogen, USA). After 30 minutes of incubation at 37 °C, 100 µL of supernatant was taken from each well and the fluorescent intensity of supernatant was measured at excitation wavelengths of 560 nm and emission of 590 nm by the plate-reader. The results were normalized with respect to the positive control to obtain relative viability. The experiment was conducted with 6 replicates.

4.2. Cell-Free Thiol Release Assays

A 96–well plate, as visualized in Figure S3.9, monitored fluorescent release from model prodrug compounds under various conditions with various media to assess what was causing reduction of the

disulfide linker. Any turn-on fluorescence observed from either compound was normalized to a control series of wells with 2 mol eq. 4-MU. Each subsequent experiment contained a background series of simply media absent of compounds **7** and **8** or 4-MU. The plate was monitored for turn-on fluorescence every five minutes up to 1 hour with same excitation and emission wavelengths mentioned above. The media investigated were DMEM, RPMI 1640, MEM, and MilliQ water. Each sample replicate was measured from at least three wells.

A final assay was performed using MilliQ alone treated with or without 10% FBS. With a fresh FBS shot, the serum was either heat-treated at > 110 °C for at least 1 hour in a water bath prior to mixing with MilliQ water or treated normally by incubating at 37 °C. To determine if there was esterase activity, an additional 1% PIC was also added. The plate was assayed under the same conditions as above: monitoring turn-on fluorescence of 4-MU from the prodrugs, where the intensity was normalized to 2 mol eq. of 4-MU, reading the emission wavelength at 445 nm every 5 minutes for 1 hour.

4.3. Statistical analysis

Time-dependent analysis was performed using One-way ANOVA between at least three replicates, comparing averaged intensity at time initial with averaged intensity at one hour. This was done to determine if background hydrolysis of 4-MU was significant in buffer control, and the determine the reagent effects after one hour.

Time-independent analysis was performed using Two-way ANOVA between at least three replicates, comparing averaged intensity at one hour between reagents. This test allowed us to compare intensities induced by reagent to background hydrolysis.

Results and Discussion

Compound Synthesis and Screening of 4-MU Release

Compounds **7** and **8** were synthesized as models of selective payload release for the tumour microenvironment, by turn-on fluorescence of the conjugated fluorophore 4-methylumbelliferone (4-MU; Scheme 3.1). The fluorescence of 4-MU is quenched when the dye is esterified through the phenol group (Figure S3.2). Previously, Zou *et al*. reported compound **7** as a chemodosimeter for endogenous H_2S.[262] Zou's findings suggested that H_2S exchanges with the disulfide, forming an asymmetric nucleophilic persulfide, which causes release of one 4-MU molecule. Zhang *et al*. noted a similar mechanism with benzodithiolane released alongside the liberated fluorophore.[263]

The two reporter molecules, **7** and **8**, were first screened for reactivity (at 10 µM) with various biologically relevant oxidizing and reducing agents (30 molar equivalents; 300 µM) in Tris buffer containing 1.5% v/v acetonitrile (MeCN). The concentration of stimulant was selected to match the previous studies by Zou,[262] and to be consistent with the expected concentration of GSH in biologically relevant tissue.[266,267] The emission intensity observed from each experiment was normalized to that of 2 molar equivalents of free 4-MU as shown in Equation 3. In buffer alone, a low rate of background hydrolysis was observed, such that < 5% release of 4-MU occurred from **7** or **8** within the first hour of incubation (Figure 3.1), while approximately 15% release of 4-MU was observed following a 24 h incubation (Figures S3.3–S3.4). To confirm that disulfide reduction was capable of initiating 4-MU release, we employed a non-thiol-containing reducing agent, *tris*-carboxyethyl phosphine (TCEP), as a positive control.[268,269] As expected,

TCEP triggered significant 4-MU release from both **7** and **8** within one hour ($P < 0.0001$; Figure 3.1 and Table S3.1).

$$Release\ (t) = \frac{F(t)-F_0}{F_{4-MU}-F_0} * 100\% \quad (3)$$

Thiol-containing biological reducing agents (e.g., GSH and cysteine (Cys)) were similarly effective at triggering 4-MU release from compound **7**, leading to a statistically significant increase in fluorescence within 1 hour ($P < 0.0001$; Figure 3.1A and Table S3.1). In both cases the rate of 4-MU production was significantly larger than that of background hydrolysis ($P = 0.024$ for GSH; $P < 0.001$ for Cys; Table S3.2). As expected, a negative control molecule that lacks free thiol groups (glutathione disulfide; GSSG) did not lead to a significantly greater release of 4-MU than was observed in the buffer-only samples ($P = 0.92$; Table S3.2).[270]

Interestingly, the oxidants hydrogen peroxide (H_2O_2), potassium peroxymonosulfate (Oxone), and *meta*-chloroperoxybenzoic acid (*m*CPBA) were also effective at liberating 4-MU from compound **7** within 1 hour ($P < 0.0001$ for each oxidant; Figure 3.1A and Table S3.1). For H_2O_2 in particular, the rate of production of 4-MU was significantly greater than that observed in the buffer-only samples ($P < 0.0001$; Table S3.2). Indeed, H_2O_2 induced a greater degree of 4-MU production than did glutathione, cysteine, or even TCEP. This is a remarkable result given that disulfides (including dithiodiester motifs) are often assumed to be predominantly sensitive to *reductive* cleavage conditions. Clearly their equivalent sensitivity to oxidative conditions is important to bear in mind when designing drug-releasing small-molecule or nanoparticle constructs.

Compound **8** was likewise found to be sensitive to the positive control molecule (TCEP) and to be insensitive to the negative control molecule (GSSG). In the case of TCEP, a statistically significant production of 4-MU was observed from **8** within one hour ($P < 0.0001$; Figure 3.1B and Table S3.1), and this rate of increase in fluorescence was significantly greater than that observed in the buffer-only vehicle control samples ($P < 0.0001$; Table S3.2). In the case of GSSG, no significant increase in fluorescence was observed, relative to that of the vehicle control samples ($P = 0.42$; Table S3.2).

Interestingly, however, compound **7** was generally less sensitive to the presence of either oxidants or reducing agents. Within 1 hour, cysteine triggered no statistically significant release of 4-MU relative to the rate of background hydrolysis ($P = 0.88$; Table S3.2), while the rate of GSH-triggered 4-MU production was modest ($P = 0.0034$ after 1 hour; Table S3.1) and was not statistically significant when compared to the rate of hydrolysis in the vehicle control samples ($P = 0.19$; Table S3.2). Intriguingly, H_2O_2 was the only agent tested (other than the TCEP positive control) which led to a rate of 4-MU production from compound **8** that exceeded that of background hydrolysis to a statistically significant degree ($P = 0.022$; Table S3.2). This once again reinforces the need to consider *oxidative* release mechanisms for disulfide systems alongside reductive mechanisms. At the same time, it must be recognized that hydrogen peroxide can promote ester hydrolysis as well as disulfide oxidation; this alternative mechanism of 4-MU liberation is discussed in more detail below.

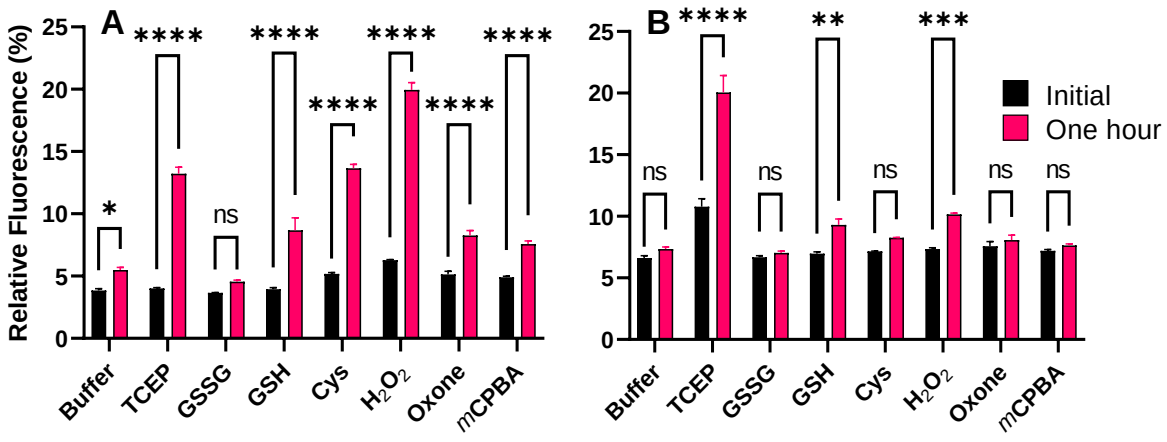

*Figure 3.1. Compounds **7** (**A**) or **8** (**B**) at 10 µM were monitored for reactivity with 30 mol eq. (300 µM) of various reducing and oxidizing agents by a means of turn-on fluorescence from liberated 4-MU in Tris buffer containing 1.5% MeCN. A two-way ANOVA analysis was used between 4 replicates to compare intensities between time points, and a one-way ANOVA analysis was used to investigate time-dependent release. The bars represent standard error of mean (SEM) (* : P < 0.05, ** : P < 0.01, *** : 0.001, #: P < 0.0001). The complete statistical comparison is found in Table S3.1. Data from longer incubation times (24 h) are found in Figure S3.3 and Figure S3.4 for compounds **7** and **8**, respectively.*

When the release reaction was allowed to proceed for 24 h (Figures S3–S4), a further increase in 4-MU production was observed from compounds **7** and **8** in the positive control experiments that used TCEP as the reducing agent (up to *ca.* 50% conversion in both cases), while the negative controls using GSSG once again showed no greater amount of 4-MU production than was found in the vehicle control samples. In the 24 h measurement, cysteine, hydrogen peroxide, Oxone and *m*CPBA all elicited a statistically greater amount of 4-MU release than was observed in the vehicle control samples (Table S3.3), while for compound **8** only hydrogen peroxide triggered 4-MU release at a rate that was higher than that of background hydrolysis.

Bohn *et al.* reported that increased hydrophobicity in the disulfide-containing reagent corresponded to a slower rate of reduction.[260] This observation was consistent with our finding that compound **8** appeared to react less efficiently with both oxidants and reducing agents than did compound **7**, but we wondered whether the reason behind the reduced reactivity was due to decreased solubility (or increased aggregation) for the marginally more lipophilic **8**, or whether it might simply be due to differences in the rate of attack of the thiol (or thiolate) nucleophile at the electrophilic carbonyl group (Scheme 3.1), given that the aliphatic linkers in **7** and **8** were of different lengths. To probe whether solubility was a factor, we repeated the 4-MU release experiments using an increased concentration of MeCN in the Tris buffer (5% instead of 1.5%).

No differences were observed in the UV/Vis spectra of **7** and **8** when the concentration of MeCN was increased (Figure S3.2), and the production of 4-MU from compound 8 remained slower than the release observed from compound **7**, no matter which chemical trigger was employed (Figure S3.6). We therefore conclude that aggregation likely does not play a role in the reduced reactivity of **8**, and that instead the

reduced rate of production of 4-MU from this reporter reagent was either due to the intrinsic lipophilicity of the compound itself (as suggested by Bohn) or was due to differences in the release rate that stem from the use of the longer linker group.

Inadequate Selectivity between Different Cell Types

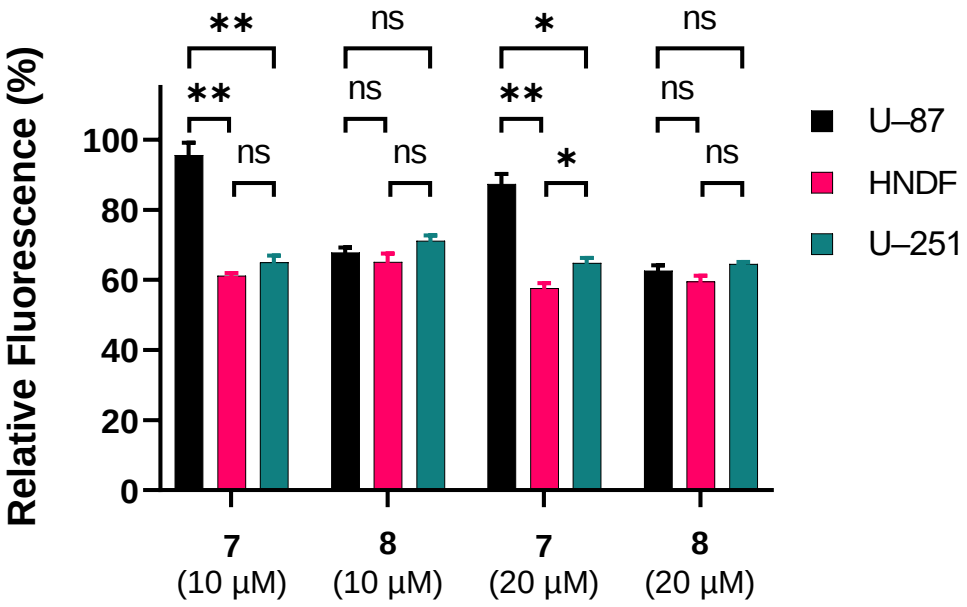

*Figure 3.2. Compounds **7** and **8** were incubated at either 10 µM or 20 µM with human glioblastoma cells (U-87, U-251) and normal dermal fibroblasts (HNDF) to validate TME selectivity, and we observed no selective release. The cells were treated under typical growth conditions, incubating 24 h in DMEM treated with 10% FBS at 37 °C. The fluorescence intensity was normalized to that of 2 mol eq. free 4-MU. The bars represent SEM, and n = 3. The complete statistical analysis is found in Table S3.6.*

Following the above confirmation that GSH was inducing 4-MU release from our traceless linkers, we wanted to investigate how the compounds **7** and **8** would react when presented with varied endogenous levels of the metabolite, in the context of a cellular model system (Figure 3.2). From previous reports, U-87 glioblastomas have consistently higher levels of GSH than do U-251 cells, and this empirical data was used as the baseline for selectivity.[123,271–273] Human normal dermal fibroblasts (HNDF) cells were used as a negative control.

GSH-positive U-87 glioblastoma cells promoted a significant release of 4-MU from compound **7**, relative to both HNDF and U-251 ($P < 0.01$, Table S3.6). When the concentration of compound **7** was doubled to 20 µM, the intensity of 4-MU fluorescence remained constant in U-87 and HNDF cells, whereas only at 20 µM did compound **7** display significant release of 4-MU in U-251 compared to HNDF ($P < 0.05$, Table S3.6). Consistent with the data from our molecular assay, which showed that **8** was less sensitive to GSH-triggered immolation than **7**; 4-MU release from compound **8** was not affected by cell type.

The above data indicated some degree of correlation between the cell-based experiment and the earlier release assays performed in Tris buffer. Once again, compound **7** proved to be a superior reporter to compound **8**, and a modest selectivity for release by the GSH-rich U-87 glioblastoma cells was observed. At high concentrations of **7**, a greater degree of 4-MU release was observed in the second tumour cell (U-251) than in the healthy control cells, which once again was consistent with expectation. By far the most

striking observation, however, was the large rate of background 4-MU release observed in the cell-based experiment: regardless of the cell type, > 50% of the reporter dye was liberated within 24 hours. This was a surprising result, given the frequency with which disulfides are employed in controlled release systems using cytotoxic payloads.[37,50,91,241,243]

We tested cell viability to determine that the emission observed was not caused by cell death (Figure S3.7), since it is known that 4-MU possesses modest anticancer properties, and there was a concern that apoptosis may have contributed to further release.[124] However, upon starving the cells for up to three days to compare the viability in the presence of the compounds, we found that the concentrations of either compound had no significant effect on cell viability (Figure S3.7), and the total amount of cell death was low, in both starved controls cells and in cells treated with either compound. This led us to believe there was something in the culturing media or culturing conditions that were causing release rather than the cells alone.

The data collected in Figure 3.2 suggest the linkers are not stable in complex matrices, since all cell types caused 4-MU release. However, our initial characterization (Figure 3.1) had been performed in a much simpler model. To probe whether the effects were induced by the cells or by some other factor in the media itself, we monitored the emission intensity of 4-MU from compound **7** with U-87 cells in a simple salt solution, Dulbecco's phosphate-based saline (DPBS), and added components that are commonly found in a complete medium (e.g., DMEM) to determine if they were contributing to the unwarranted release. We monitored 4-MU production for up to 2 hours in the presence or absence of U-87 cells to isolate which of the major components could be causing the unwarranted release of the fluorophore (Figure 3.3). By incubating compound **7** and U-87 cells in un-supplemented DBPS, we saw that the cells did have a significant impact on 4-MU release from the traceless linker (Figure 3.3A), presumably as a result of disulfide cleavage. When glucose or glutamine were added to the media there was no change in intensity unless the U-87 cells were present (Figure 3.3B–C). The concentrations of the additives were comparable to what are found in the formulation of the complete medium, DMEM, at 4.5 g/L glucose and 0.5 g/L glutamine, respectively.[274] Since the glucose and glutamine did not elicit higher intensities of 4-MU emission than in Figure 3.3A, they were therefore not contributing to the 4-MU liberation.

However, when 10% v/v fetal bovine serum (FBS) was added to the media there was a substantial increase in 4-MU release over 2 hours, even without any U-87 cells present (Figure 3.3D). This FBS-promoted release was much faster than the rate of cell-promoted release observed in panels A–C. As such, no statistically significant differences could be observed in the rate of reaction in the presence vs. absence of cells, when FBS was present. When the cells were incubated for 3 days, a similar pattern of emission intensity was observed (Figure S3.8). Once again, when FBS was present there was no significant difference in fluorescence intensity caused by the presence of cells (Figure S3.8D). Interestingly, the total fluorescence emission from the released 4-MU reporter observed in DPBS supplemented with FBS (with or without U-87 cells; Figure 3.3D) was similar to that observed in the cell-culturing experiments described in Figure 3.2. These data clearly implicate fetal bovine serum as the factor contributing to premature release of the molecular cargo — a surprising result given the ubiquity of FBS in tissue culture work.

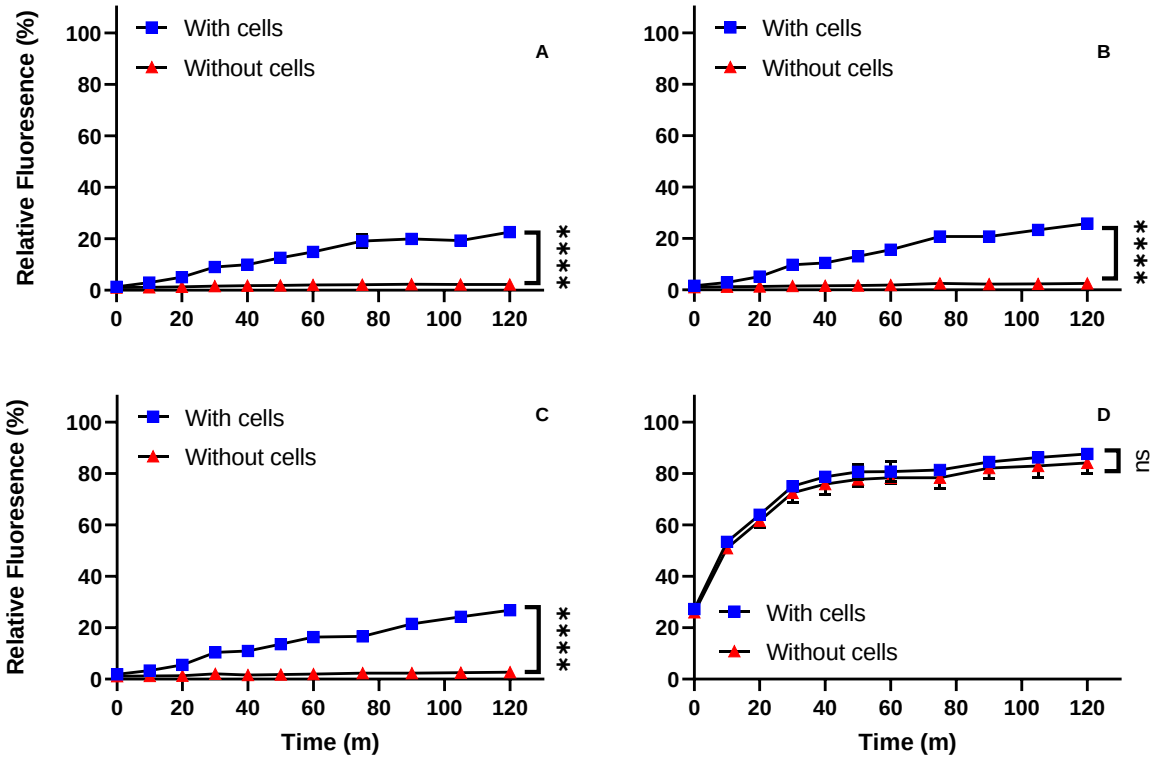

*Figure 3.3. Compound **7** showed significant release from U-87 glioma cells within two hours, except when media was supplemented with FBS. **A**. The traceless disulfide linker **7** was incubated with or without U-87 glioma cells in pure DPBS. **B**. The DPBS was supplemented with 4.5 g/L glucose. **C**. The DPBS was supplemented with 4.5 g/L glucose and 0.5 g/L glutamine. **D**. The DPBS was supplemented with 10% FBS (v/v) in addition to glucose and glutamine. Error bars represent SEM of three replicates and statistics were measured at the 2 h timepoint. Compound intensity was normalized to 2 mol eq. 4-MU, expressed as a percentage. The full statistical analysis can be found in Table S3.8.*

Next, the U-87 cells were removed to isolate how the components in the actual complete media, DMEM, could affect the traceless disulfide linkers (Figure 3.4). The DMEM was supplemented in one of three ways: either with TCEP (30 mol eq.) to confirm disulfide reduction and 4-MU release, or with 10% v/v FBS (a common supplement added to complex media), or with both. In all cases, significant release of 4-MU from compound **7** was observed when comparing time points at zero minutes and one hour; some of this release could be attributed to background hydrolysis, as seen in the black trace. Compound 8 displayed a similar trend, except that the rate of background release in native DMEM was reduced, possibly due to a greater degree of hydrophobicity present in compound **8** vs. compound **7**. Regardless, the presence of TCEP and/or FBS had a significant impact on the release of 4-MU from both traceless linkers after an hour, and the intensities were significantly higher than observed from background hydrolysis in DMEM (Table S3.9). When performed again in another complete media, RPMI 1640, we saw a similar trend in release intensity, where FBS had a significant effect of 4-MU emission (Figure S3.9). Interestingly, when either compound was incubated with both FBS and TCEP, there was no increase in emission intensity compared to the individual reagents alone.

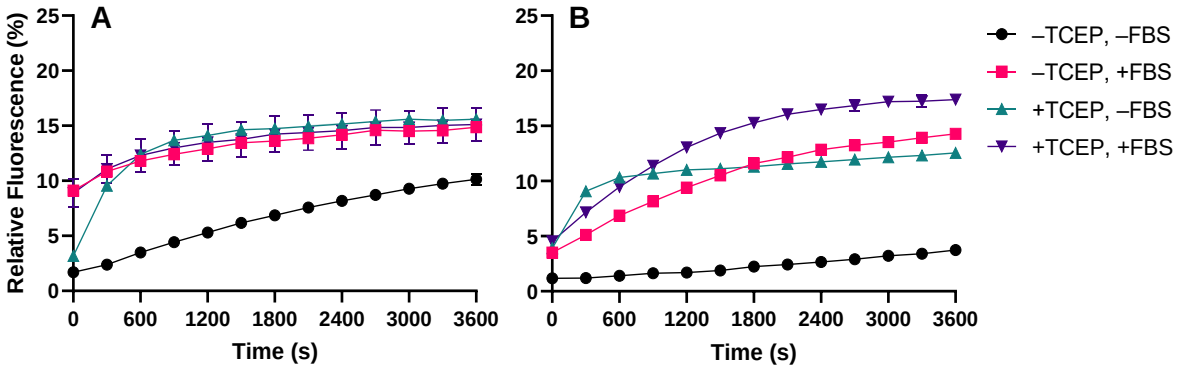

*Figure 3.4. The release of 4-MU was monitored from traceless disulfide linker **7** (**A**) or **8** (**B**) at 10 µM in DMEM over one hour. Wells were treated with either 30 mol eq. TCEP (green), 10% FBS (pink), or Both (purple). Compounds in DMEM alone were used as a control to assess background hydrolysis (black). Intensities are normalized to 2 mol eq. 4-MU and the bars represent SEM and n = 3. The complete statistical analysis is found in Table S3.9.*

To offset the possible effects of cysteine found in complete media affecting release of 4-MU and to focus more on the FBS-induced release, we repeated the measurements in minimum essential media (MEM) (Figure S3.10). In these experiments, we observed a noticeable decrease in emission intensity in the untreated MEM (black trace), relative to previous complete media. MEM is expected to have around half the concentration of Cys, relative to DMEM and RPMI 1640.[274–276] Therefore, the decrease in intensity could be attributed to the reduced thiol content. For both compounds **7** and **8**, FBS additives still induce significant release of 4-MU relative to untreated media ($P < 0.0001$), meaning that thiol-exchange was not a major source of unwarranted release. The same pattern was observed when MilliQ water was used as the media (Figure S3.11).

Assessing if the Release is Enzymatic and Mitigated by Denaturation

FBS is an essential additive for preparing complete media to sustain cellular growth.[277,278] However, it is a complex serum on its own, with growth factors and other proteins.[278,279] Therefore we wanted to assess if the sera effects were enzymatic and if they may be mitigated by denaturation and inhibitors.[277–279] To this end, we explored the effect of thermal denaturation of sera proteins (by incubation at 100 °C for 60 min) and also incorporated a protease inhibitor cocktail (PIC) using aprotinin, to deter any esterase activity on compounds **7** and **8** (Figure 3.5).

As anticipated by the experiments described above, the addition of FBS to a solution of compound **7** in water led to a significant release of 4-MU within 1 hour (Figure 3.5A; $P < 0.0001$, Table S3.13). Addition of 1% PIC did not immediately affect the release rate, but when the FBS was thermally denatured prior to addition, the rate of 4-MU production was significantly reduced (Figure 3.5A, red vs. purple; $P < 0.01$). Combining the two treatments (i.e., adding 1% PIC to thermally denatured FBS) reduced the rate of 4-MU release still further (Figure 3.5A, purple vs. violet; $P < 0.01$).

Compound **8** showed a similar pattern to compound **7** with respect to 4-MU release, albeit with a smaller difference in emission intensity between the test samples and vehicle control (Figure 3.5B). When incubated with 37 °C FBS, with or without PIC, there was a significant increase in 4-MU production, compared to the background control (Figure 3.5B, red vs. black, green vs. black; $P < 0.0001$, Table S3.13). Once again, however, thermal denaturation of the FBS reduced the amount of release, and addition of

PIC to the denatured serum further reduced the amount of 4-MU production. Together, these data indicate that the premature release of the 4-MU reporter group that was observed in the earlier experiments is likely to be due to esterase activity rather than disulfide reduction (Scheme 3.2).

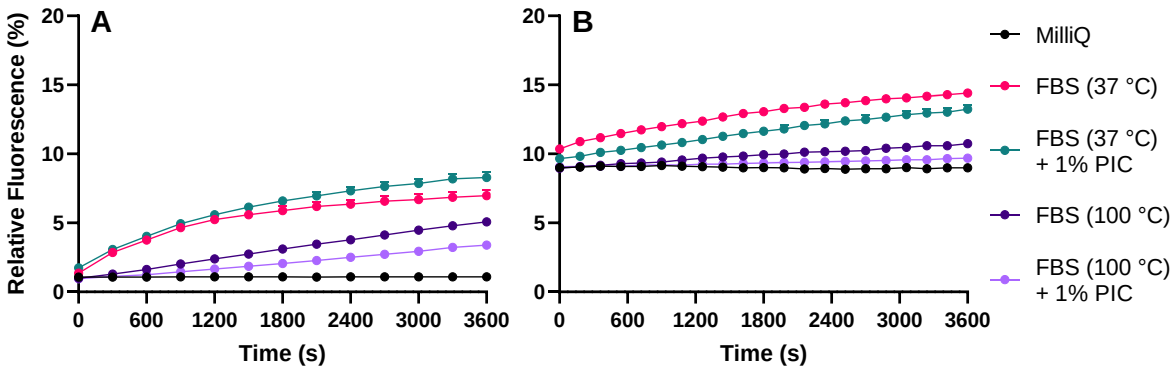

*Figure 3.5. The enzymatic effects causing the release of 4-MU from compounds **7** (**A**) or **8** (**B**) were mitigated by denaturing FBS and incorporating a protease inhibitor cocktail (PIC) in water. FBS was treated normally by incubating at 37 °C (Pink), FBS treated with PIC (Green), FBS subjected to > 100 °C without PIC (Purple) or with PIC (Violet). Error bars are SEM of n = 3. The complete statistical analysis is found in Table S3.13.*

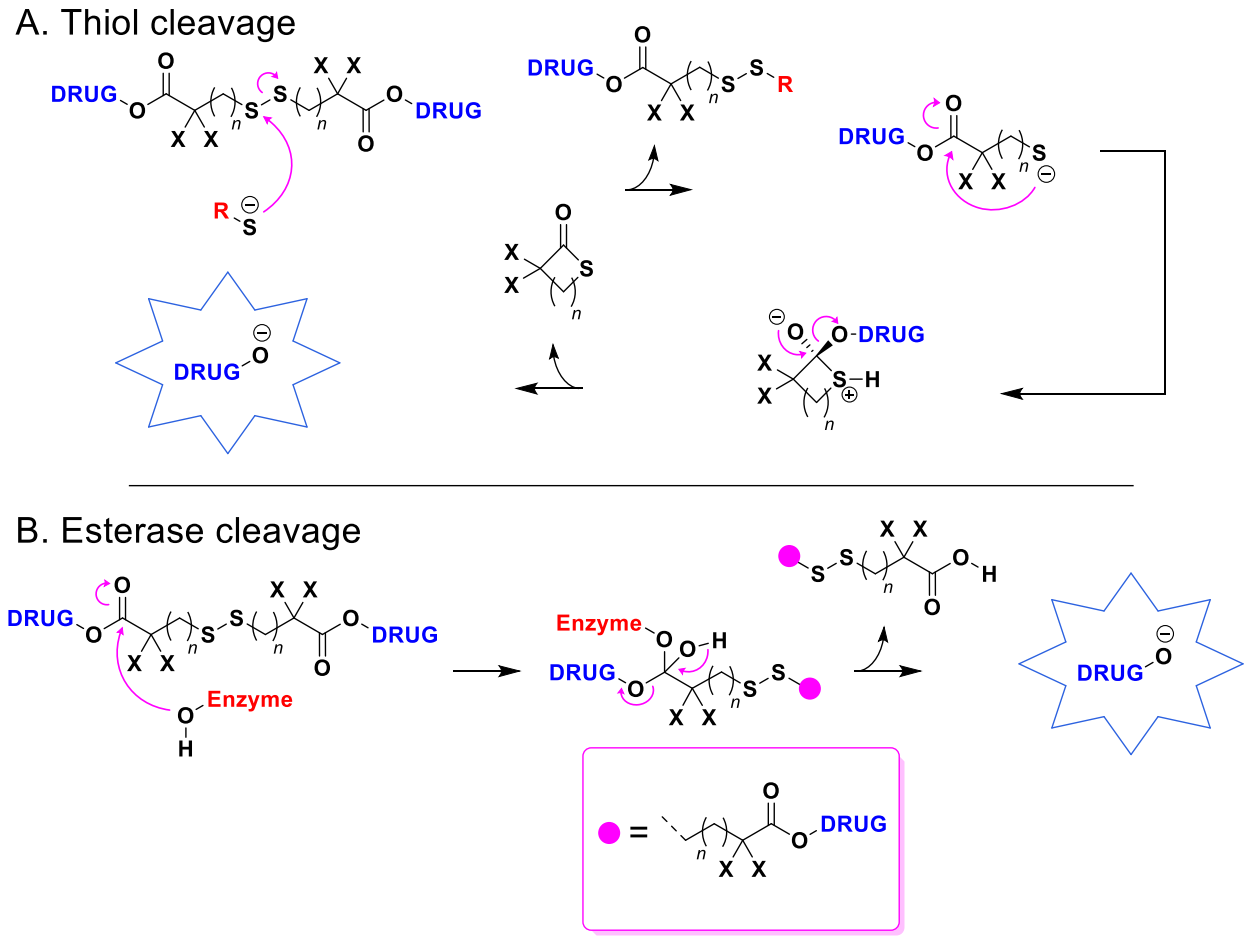

*Scheme 3.2. Two competing mechanisms of cargo release from functionalized dithiodiacid frameworks. The fact that FBS-promoted release of 4-MU from compounds **7** and **8** can be blocked by thermal denaturation and through the use of a protease inhibitor cocktail indicates that esterase-mediated hydrolysis is a dominant mechanism. To reduce the susceptibility of the reporter molecule toward esterase activity, additional steric bulk can be added adjacent to the carbonyl group.*

To further prove the hypothesis that premature cargo release from **7** and **8** was due to esterase activity, and to demonstrate a ready solution to the problem of premature liberation of the active agent from disulfide diacid drug-releasing constructs, we designed and synthesized compound **9**, which incorporated two methyl groups adjacent to each carbonyl group (Figure S3.1, Figure 3.6). Inspired by previous studies from Bohn *et al.*,[260] the addition of extra steric bulk at this position was expected to deter enzymatic cleavage reactions.

As expected, compound **9** liberated 4-MU when treated with TCEP (employed as a positive control reducing agent; Figure S3.5) and did not release 4-MU when treated with GSSG (employed as a negative control). A statistically significant increase in 4-MU release (relative to background hydrolysis) was observed when **9** was treated with GSH ($P = 0.0091$) or H_2O_2 ($P = 0.0067$) for 1 hour (Table S3.2). Consistent with the earlier point that increased hydrophobicity appeared to reduce the rate of reaction, the average rate of 4-MU production from **9** was less than that observed for **7** or **8** (Figure S3.3–S3.5). Nevertheless, when the incubation time was increased to 24 hours, we observed statistically significant 4-MU release

(relative to the rate of background hydrolysis) promoted by TCEP, GSH, Cys, and H_2O_2 ($P < 0.0001$ for all four compounds; Table S3.3). Once again, the use of a higher concentration of acetonitrile (5% instead of 1.5%, Figure S3.6) did not significantly alter the emission intensity, suggesting that solubility was not a limiting factor for compound **9**.

Most importantly, we found that compound **9** had improved stability in FBS-treated media, such that only very minimal hydrolysis was observed when non-denatured serum was added to a solution of **9** in water (Figure 3.6A). As expected, this minimal rate of hydrolysis could be further reduced by denaturing the FBS or by adding a protease inhibitor cocktail, or both (Figure 3.6B). These data indicate that while the addition of methyl groups adjacent to the ester groups in **9** did not completely block esterase activity, it did protect the compound from unwanted enzymatic cleavage.

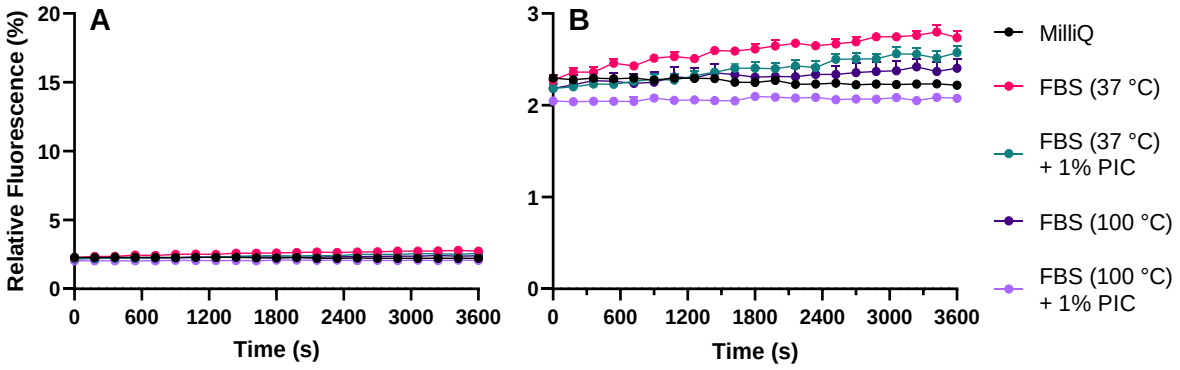

*Figure 3.6. Compound **9** suffers substantially less FBS-promoted enzymatic cleavage, as a result of the incorporation of addition steric bulk near the carbonyl groups. Panel (**A**) shows the data on the same scale as that used for Figure 3.5. Panel (**B**) uses an expanded Y-axis to display the decrease in 4-MU intensities between treatments. Error bars are SEM, n = 4. The complete statistical analysis is found in Table S3.13.*

Conclusions

Traceless disulfide linkers are valuable for controlled release studies but must be appropriately characterized prior to use in *in vitro* experiments. Upon systematic removal of the complex variables between cellular studies and our initial reagent screening, which had been conducted in a simple buffer matrix, we found that the common, but necessary, tissue culture additive, FBS, was a major factor in premature release of our 4-MU reporter from our disulfide constructs. When the serum was denatured by thermal treatment to inactivate enzymatic components, there was a significant decrease in release rate, and when PIC was added, the rate further decreased indicating that the cleavage observed was enzyme-induced cleavage at the ester rather than the reduced disulfide immolation (Scheme 3.2). This competitive (and undesirable) enzymatic release pathway could be almost completely blocked through the addition of extra steric bulk at the position adjacent to the ester groups that were used to conjugate the reporter molecule to the disulfide.

The use of FBS (or a similar serum additive) is a requirement for most tissue culture protocols, and of course all animal studies will necessarily involve exposing the agents under study (whether small molecules, polymers, or nanoparticles) to enzymes present within the organism. The present study shows that typical disulfide diacid constructs are much more sensitive to endogenous hydrolase enzymes than might be predicted based upon a survey of the literature, which reveals these types of linkages to be used in a broad array of applications. As such, we strongly recommend that release studies be carried out using at least 10% of non-denatured FBS (rather than simply using PBS or Tris buffers, which has been the norm). Moreover, we recommend that investigators consider installing quaternary centers beside the carbonyl group that links the 'cargo' to the disulfide motif. Doing so should provide improved selectivity for triggered release over background hydrolysis.

4. Development of the First Formulation of Gold Nanoparticles Functionalized to Target PD-L1

Foreword

With the findings from the Aurigene publication (Chapter 2), we continued to push forward with targeting experiments and characterization around a commercial monoclonal antibody from BioXCell. Although antibodies as drugs are not revolutionary, this is certainly an appropriate step forward as a targeting agent. Prior to this series of experiments, we needed to characterize whether the antibody was suitable for selectively targeting PD-L1 and, hopefully, blockading the PD-1/PD-L1 interaction. We anticipate that the following methods of optimization and characterization for these gold nanoparticles may be pursued with future formulations, including those delivering other payloads (i.e., SN-38 or doxorubicin), in a similar fashion to antibody-drug conjugates, to both improve efficacy and mitigate potential off-targeting adverse effects. The relevant supplementary data are found starting on page 202.

EDC/NHS Peptide Coupling and Mechanism

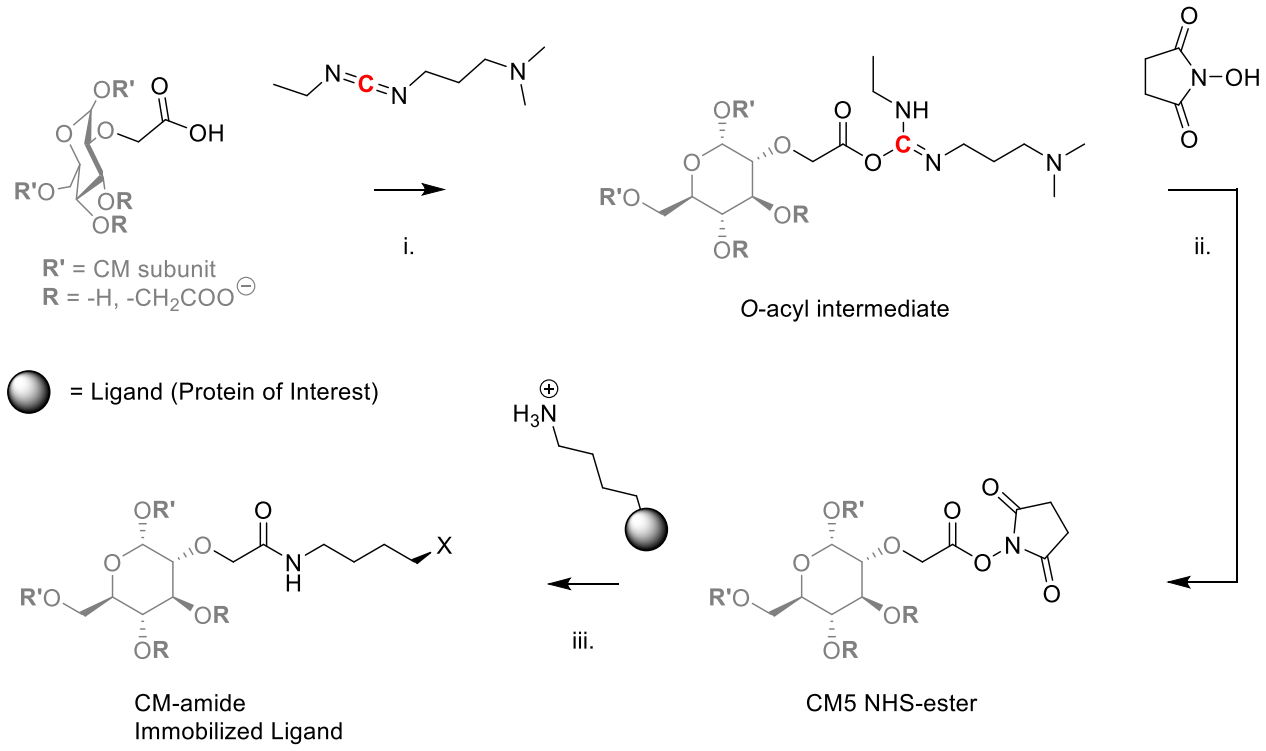

Scheme 4.1. Demonstrating how carboxymethyl dextran (CM) is primed for ligand immobilization with the lysine residues of any given protein using EDC/NHS peptide coupling. The mechanism of each step is described more thoroughly in Scheme 4.2. The CM oligomer is coated onto the gold surface prior to immobilization, although not explicitly mentioned in the Cytiva manufacturing, it is likely through the self-assembled monolayers through the gold-sulfur interaction. Another image of the gold chip is found in Figure 4.1.

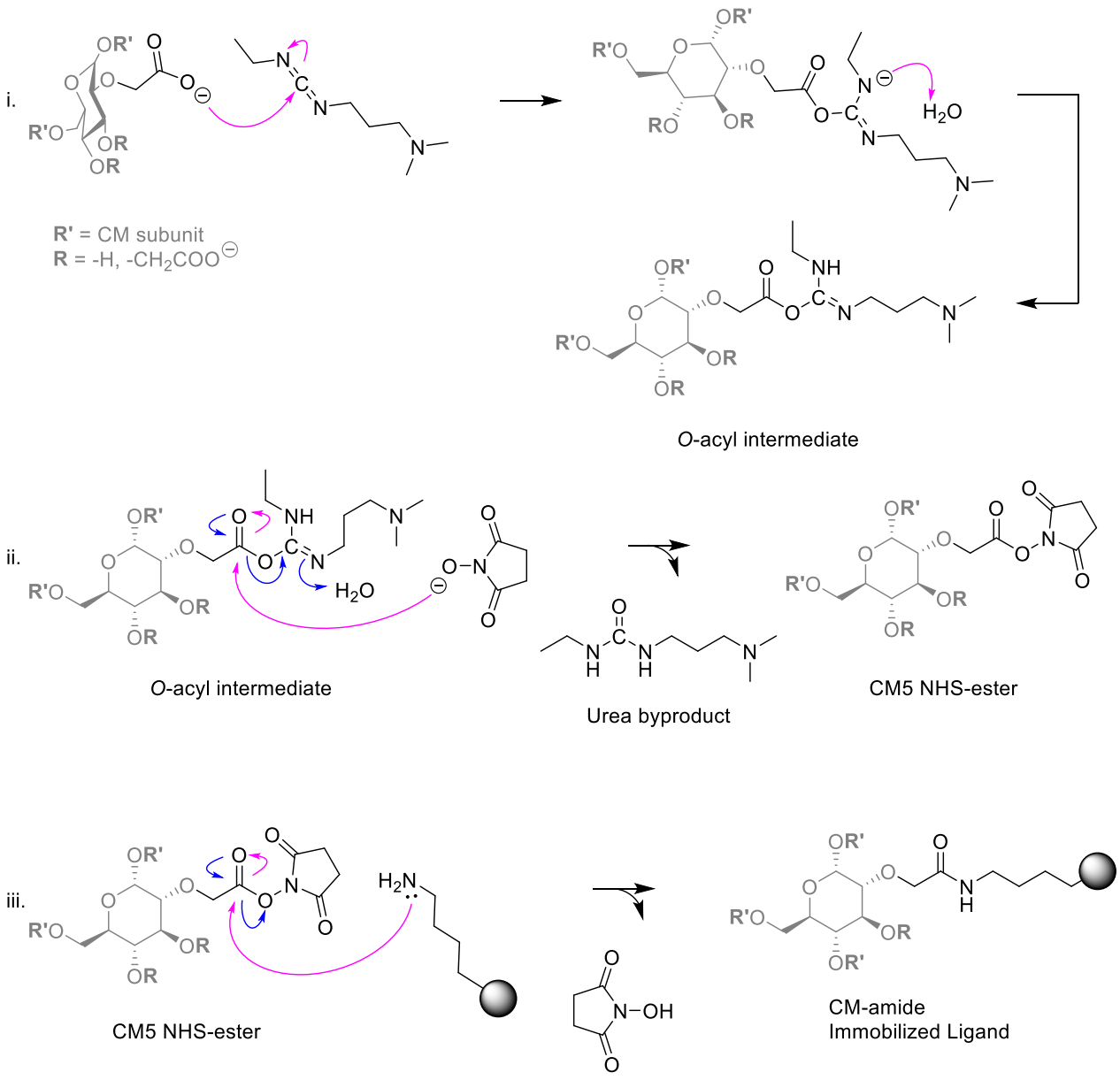

Scheme 4.2. Example mechanism of carboxymethyl dextran (CM) undergoing EDC/NHS peptide coupling to immobilize a ligand onto a gold chip. i. Nucleophilic carboxylate moieties of CM readily undergo nucleophilic addition to the carbodiimide center of EDC forming an *O*-acyl intermediate. ii. Nucleophilic NHS undergoes a nucleophilic addition (pink) and elimination (blue) at the carbonyl carbon in two steps, resulting in an NHS-ester and the urea byproduct. iii. Nucleophilic amine of lysine residues on our protein ligand perform a similar nucleophilic addition at the carbonyl center, and eliminating the NHS, resulting in a covalent ligation of protein to the CM gold surface. For simplicity, a single subunit of CM was shown, where **R** functional groups may be a free alcohol or carboxymethyl moiety, and **R'** represents another CM subunit.

The Flavours of Ligation for SPR Chips

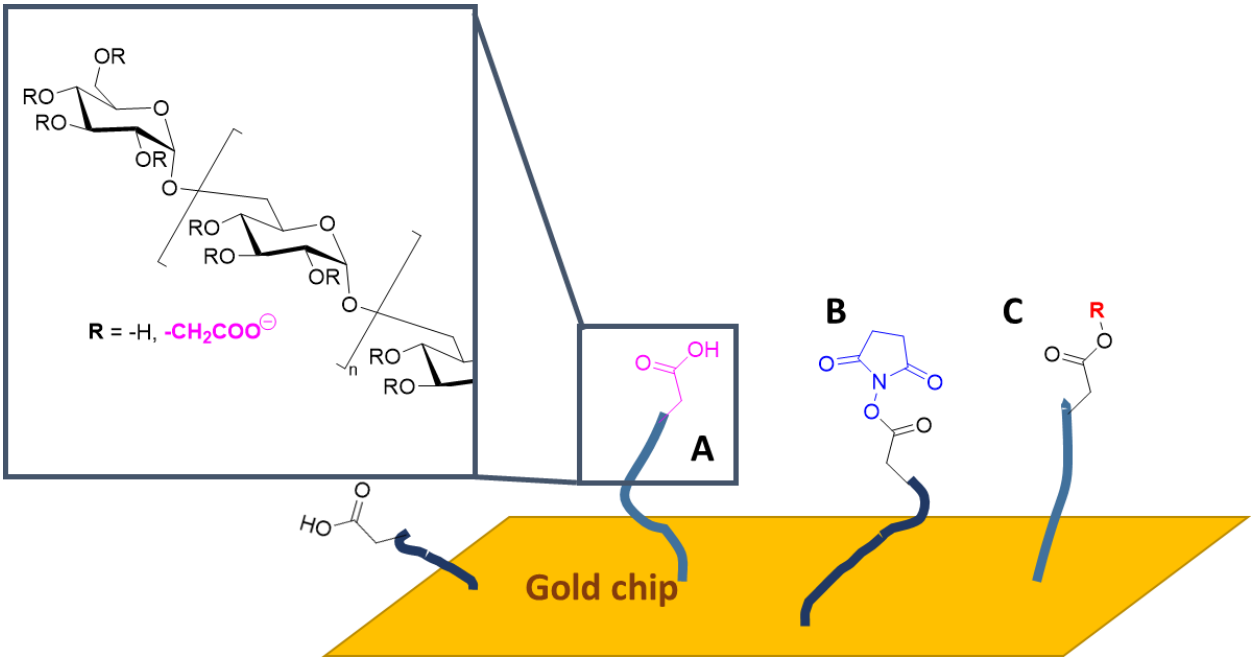

Figure 4.1. The protein of interest is covalently bound to a surface of carboxymethyl dextran (CM) via EDC/NHS conjugation to immobilize proteins onto the gold surface. **A**. The native carboxylic acid moiety (pink) of CM is shown and the inset displays the full polymer bound to the gold surface. **B**. After reacting with the EDC as described in Scheme 4.2, the gold surface is coated in stable NHS-esters. **C**. The ligand of interest is flowed across the gold chip, and nucleophilic residues (i.e., lysine) will react with the NHS-esters covalently binding (immobilizing) our protein of interest (**R**) to the gold surface for subsequent surface plasmon resonance analysis.

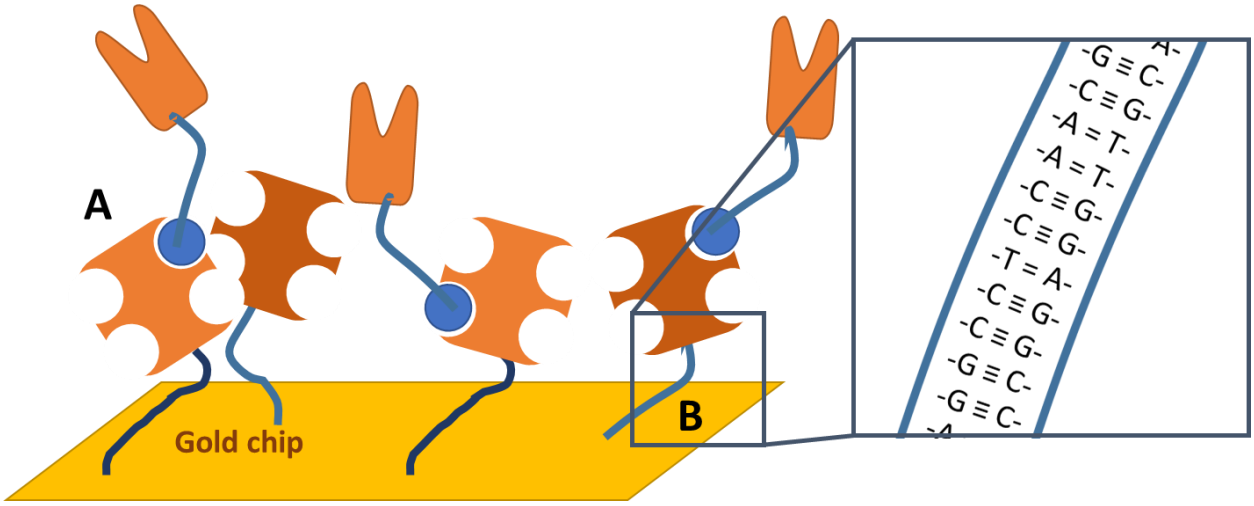

Figure 4.2. The differences of ligand capture in two similar streptavidin-coated (SA) gold chips, which immobilize biotinylated protein (blue circle) to the SA surface. **A**. The SA chip is commercially available with SA previously bound to the surface, and ligand will immobilize readily with the high specificity of biotin to streptavidin. **B**. In a more sophisticated setup using a CAP chip, prior to immobilization of ligand, the chip is coated in a DNA-oligomer that spontaneously anneals to a complementary-conjugated commercially available SA protein. The inset highlights that the SA is immobilized to the CAP gold chip by nucleotide base pairing.

Surface plasmon resonance (SPR) is a powerful label-free binding technique for characterizing affinity of protein-protein interactions as previously addressed in Chapter 2. Prior to any binding assays, one of the

proteins (or molecules) of interest must be bound to the surface of the gold chip, defined as the *ligand*. There are many options on how to immobilize the ligand, where most commercially available options will use *in situ* peptide conjugation using EDC/NHS coupling on a negatively charged polymer coating of carboxymethyl dextran (CM) as described in Schemes 4.1 and 4.2. CM chips are commonly used in SPR experiments for their relative ease at forming peptide bonds with the ligand of interest using EDC/NHS peptide coupling, where the polymer is primed as an NHS-ester (Scheme 4.2.ii, Figure 4.1B), and the extracellular lysine residues may readily react forming an amide to the polymer (Scheme 4.2.iii, Figure 4.1C). The benefit of covalent immobilization is that the surface ligand is reusable under certain conditions. Despite how easy immobilization is, the orientation of the ligands may not be entirely uniform. This will reduce the overall activity of binding as the analyte is flowed across the ligand surface as not all binding sites may be available. Additionally, the binding activity of the ligand and chip reusability will vary from subsequent and frequent exposure to denaturing agents that are used to regenerate the surface, which will lead to the unfolding of the ligand. To account for degradation between cycles, we validated our results by performing a reciprocal assay to determine if the initial calculated affinity claims hold true, as we would expect similar k_{on} and k_{off} rates, which *should* result in a similar dissociation constant (K_D).

$$\mathrm{K}_D = \frac{k_{off}}{k_{on}} \tag{1}$$

Other methods are also available for covalent immobilization of proteins, but they may suffer from similar heterogenous orientations that result in lower overall activity. To pursue more uniform ligand immobilization, there are more sophisticated gold surfaces which are available that employ biotin and streptavidin (Figure 4.2). Commercially available biotinylated proteins (e.g., BPS Bioscience) help assure that the binding events observed are in uniform orientation. Streptavidin and biotin have strong non-covalent affinity in the low femtomolar range (fM, 10^{-14} magnitude), this affinity makes them difficult to desorb from each other. The advantage of using biotin over conventional covalent linkages is that there are fewer variables required to optimize ligand immobilization (e.g., there are only two molecules, instead of four reagents to optimize reaction conditions – temperature and acidity). In other words, the strong affinity of biotin and streptavidin is orders lower than that of typical protein-protein interactions (~low µM), and in antibodies (~low nM), making biotinylated proteins easier to immobilize with higher efficiency than conventional peptide coupling. However, the problems in surface regeneration are still a major factor, where pH change and protein unfolding/refolding may result in less activity of the ligand.

To fully overcome the problem of ligand denaturation, there is a more sophisticated SPR SA chip known as a CAP (capture) chip. This method assures full activity of binding by re-immobilizing the ligand within each cycle. These kits use a proprietary DNA oligomer that coats the chip, and a modified streptavidin with the complementary strand to anneal and immobilize the SA. The biotinylated ligand is captured by the SA, the analyte binds to the ligand, and then the surface is reset to perform another measurement.

To regenerate the surface, the double-stranded DNA is torn by disrupting the H-bonding of the base pairs, removing the SA/biotin/ligand complex, and allowing for a fresh immobilization to occur in the next cycle (Figure 4.2B). The process of regeneration uses denaturants to disrupt the hydrogen-bonding of the DNA tethering the SA to the gold, using guanidinium hydrochloride and sodium hydroxide (pH > 10) to unfold and strip the complementary oligomers. This kit was chosen as most appropriate for characterizing our commercial antibody as we required native PD-L1 for every cycle, as to not lose activity and mis-characterize the affinity between our analyte and ligand.

Materials and Methods

1. HBS-EP$^+$ Running Buffer for SPR and Sample Preparation

HBS-EP$^+$ was produced in house using materials from Sigma-Aldrich using the final concentrations as described by the manufacturer (Cytiva). The 10X concentrate buffer is 1.5 M NaCl, 0.1 M HEPES, 30 mM EDTA, and 0.5% v/v P20 (a.k.a. Tween 20), that upon dilution will have a final pH ~ 7.4. Both the concentrate and active buffer are filtered and degassed through a 0.22 µm PES filter. The techniques and instruments were used as described in Chapter 2.

2. Gold Nanoparticle Synthesis and Characterization

Synthesis

Our AuNPs were synthesized as described by Xia *et al.,* using a citrate salt reduction-based method to form stable, 15 nm AuNPs, in aqueous conditions similar to the Turkevich method.[33] In brief, a 2..5 mL "pre-mix" solution was made in two steps. The first step had 500 µL 1% w/v $HAuCl_4$ (14.7 mmol) mixed with 42.5 µL 0.1% $AgNO_3$ (2.5 µmol). This mixture was then given 1.1 mL 1% (w/v) tribasic sodium citrate (cit^{3-}; 58.2 mmol), and the remaining volume (876 µL) of deionized water (MilliQ) to make a 2.5 mL "pre-mix" solution. This solution was stirred at room temperature for 4.5 min, then transferred quickly via syringe to refluxing and vigorously stirred deionized water (47.5 mL). The 50 mL solution began to turn dark grey, then deep purple, and eventually the ruby red associated with < 20 nm cores within 3 minutes post-transfer. The mixture is then taken off reflux after 30 minutes of stirring and cooled. The AuNPs are sized using TEM, DLS, and UV-vis spectroscopy. The glassware and stir bars were cleaned with neat nitric acid (35%) to remove any dust or other possible nucleation sites, which may contribute to higher dispersity.

Nanoparticle Characterization

Gold cores were characterized by transmission electron microscopy (TEM), where images of the gold cores were acquired using a JEOL JEM-1400 microscope, operating at an accelerating voltage of 80 kV, and equipped with a Gatan Orius SC1000 CCD camera. An aliquot (10 µL) of gold particles was deposited on a Formvar/carbon-coated 500-mesh copper TEM grid and dried under ambient conditions. The grid was imaged at least three times in separate quadrants at 100 000× – 150 000× magnification to image at least 1500 particles in total. These images were processed using ImageJ with a calibrated scale to determine the area of the cores. Particles were binarized by a threshold to differentiate the core from the Formvar background and analyzed cores with a measured radius between 5–50 nm, omitting sizes greater than 50 nm as aggregates. The average core size was determined from the three images and used to calculate the average molar mass of the cores, described below, for functionalization via surface plasmon resonance (SPR). Reported uncertainties σ were calculated from the standard deviation *s* of average dimensions taken from the three images: $\sigma = s/\sqrt{3}$.

The hydrodynamic radius was measured by dynamic light scattering (DLS) to observe any discretions of the core volume size in suspension in real-time to corroborate with values measured by TEM. The DLS samples of AuNPs were prepared in triplicate and read thrice in clean silica cuvettes. The cuvettes were cleaned by rinsing with 15 mL 95% EtOH dispensed over 2 mL aliquots and vortexed, and then washed similarly with deionized water, and then the sample is added to be measured. An aliquot of particles was diluted between 1:7 and 1:10 from stock suspension (< 10 nM, < 62 mg/L $AuNP_{15\ nm}$) in HBS-EP$^+$ buffer or deionized water in clean silica cuvettes. The low concentrations were to mitigate any potential aggregation between particles, so the populations observed were individual cores.

The DLS experiments were performed on a Brookhaven Instruments photocorrelation spectrometer equipped with a BI-200SM goniometer, a BI-9000AT digital autocorrelator, and a BI-Mini-L30 30 mW red (636 nm) compact diode laser, at a scattering angle of 90° and a temperature of 25 °C. For each AuNP dispersion, mean effective hydrodynamic sizes and dispersities were determined from three measurements of the autocorrelation function using cumulant analysis. Representative intensity-weighted size distributions were determined from CONTIN analysis. Reported mean effective hydrodynamic sizes and dispersities for each condition were determined by averaging values from triplicate preparations. Standard errors (σ) on hydrodynamic sizes and polydispersity were calculated from the standard deviation (*s*) of triplicate values: $\sigma = s/\sqrt{3}$.

Gold core diameter was also measured by UV-visible (UV-vis) spectroscopy as described by Haiss *et al*. Where an aliquot of AuNP was diluted in HBS-EP$^+$ buffer and measured for absorbance between 440 – 540 nm. The ratio of absorbance between the Lambda max (SPR wavelength) and absorbance at 450 nm, was used to quickly evaluate the mean core size described in the tabulated data by Haiss *et al*. Samples were measured in at least duplicate prior to direct measurements by TEM and DLS. This method of core size evaluation was used to qualitatively assess success of core synthesis. After direct measurements were acquired, UV-vis was used to standardize samples for SPR using Beer–Lambert Law of absorbance. Samples were either prepared in a Quartz cuvette cleaned as described in the DLS section with a fixed pathlength of 1 cm, or prepared in a 96-well plate (Corning COSTAR™) where the sample volume dispensed in the well resulted in a 1 cm pathlength from the top of the sample to the bottom of the well.

Calculating the Molar Mass of the Gold Nanoparticles

The molar mass of the AuNPs was determined using previously acquired metrics: the radius of a single Au atom is 144 pm ($1.44 \cdot 10^{-10}$ m), the measured diameter of the AuNPs core, (i.e., 15 nm ($7.5 \cdot 10^{-9}$ m)), and the Au atoms have a face-centered cubic packing efficiency of 74% (Table 4.1) were all used in Equation 3. The molar mass was corrected according to the mean size of the core determined by TEM.

Table 4.1. Approximate volumes of Au atoms and AuNPs to achieve a theoretical MW of particles.

Species	Radii (m) [respective size]	Volume (m^3)
Au Size atom	$1.44 \cdot 10^{-10}$ [144 pm]	$1.25 \cdot 10^{-29}$
AuNP (15 nm)	$7.5 \cdot 10^{-9}$ [7.5 nm]	$1.77 \cdot 10^{-24}$

$$\frac{vol.AuNP}{vol.Au} * 0.74 * 196.97 \frac{g\ Au}{mol\ Au} = MW_{AuNP} \quad (3)$$

This calculation is adjusted per batch of AuNP synthesized, after the particles have been sized by TEM. For 15 nm AuNPs the MW_{AuNP} is 20.6 GDa ($2.0 \cdot 10^7$ g/mol), but assumes low dispersity of perfect spheres. This value is 137-fold greater than the average MW_{IgG} = 150 kDa ($1.5 \cdot 10^5$ g/mol), and this is our given estimate for characterization as a "Golden Ratio". This value will change depending on how large the gold core is (i.e., 237-fold for AuNPs with a core diameter of 18 nm). More details of particle synthesis and characterization are in Table S4.1.

3. General Conjugation of αPD-L1

25 mg αPD-L1 (BioXCell) are reconstitutionalized in HBS-EP$^+$ buffer and dilute for peptide conjugation to (0.5 mg/mL) in excess (> 100-fold) reagents of EDC, NHS, and GSSG. The following day, ethanolamine is

added to quench any unreacted NHS-esters, and the small molecules were removed by either spin-column chromatography or dialysis. Disulfide dimers were reduced using 5 mol eq. TCEP. Final protein concentration was remeasured using Pierce™ BCA Protein Assay kit as directed to determine how much protein was lost during the process. The molar absorptivity of a typical 150 000 g/mol IgG is 210 000 $M^{-1}cm^{-1}$. More thorough purification is described in the supplemental materials on pages 203–206.

Characterizing the Monoclonal Antibody

An antibody from BioXCell was chosen as our primary targeting agent after our prior findings with small molecules had proven fruitless (Chapter 2).

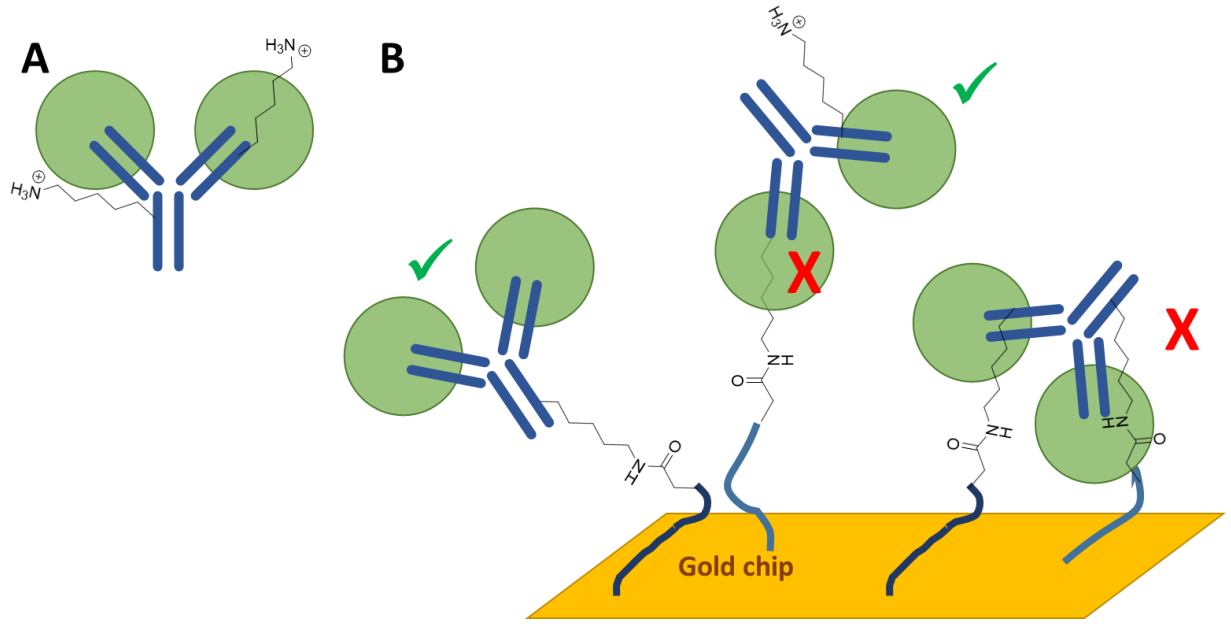

Figure 4.3. The monoclonal antibody was characterized using SPR under two assumptions regarding the selectivity of its antigen, PD-L1. **A.** We assume that the monoclonal antibody has two epitope binding sites (green circles) and at least one lysine residue for peptide conjugation. **B**. Due to the uncertainty of where the lysine residues may conjugate, we expect random orientations of varied epitope availability; the most optimal (left, both epitopes available) to least optimal orientation (right, no epitopes available).

Proper characterization went into investigating whether the antibody would be a suitable targeting agent, which were inspired by a handful of assumptions of the protein (Figure 4.3). First was that both epitopes are capable of targeting and binding PD-L1. The second assumption described the presence of lysine residues available for peptide coupling, , and if conjugating these residues will affect epitope recognition activity. We expect that the upon formation of an amide bond, under random orientation, would have some effect on disrupting epitope recognition of PD-L1. If nonspecific peptide coupling greatly removes selectivity, this antibody would be inappropriate as a targeting agent to conjugate onto the AuNPs.

We characterized the antibody using similar methods to our previous small molecule published work using SPR as the primary technique. Initially, the antibody was flowed across a surface of immobilized PD-L1, to characterize the affinity of the antibody to its antigen. Most antibody epitopes have a binding affinity with a low nanomolar (nM) potency, which is much stronger than most native molecular interaction (between

high nM – low µM) by at least two orders of magnitude. However, we needed to affirm that peptide coupling would not be detrimental to selectivity.

Test 1: Flow αPD-L1 across a surface of PD-L1 – CAP.

Unfortunately, due to the high affinity of antibodies we could not use normal separation techniques to regenerate the PD-L1 surface without denaturing the ligand beyond recognition (change in pH and incorporation of detergents). When characterizing affinity of an antibody we require a fresh surface of PD-L1 every time to overcome the high affinity of the antibody and its antigen. To overcome this, we used an SPR CAPture kit, which uses oligomeric nucleotides to anneal a complementary strand conjugated with streptavidin (Figure 4.2B). The streptavidin (SA) layer immobilizes the biotinylated conjugate of our protein of interest, PD-L1. The use of the nucleotides is important for regeneration, as it is easy to disrupt annealed DNA consistently with chaotropes, which completely removes all bound protein each cycle. This whole surface regeneration allows full activity binding measurements without risking the loss in activity.

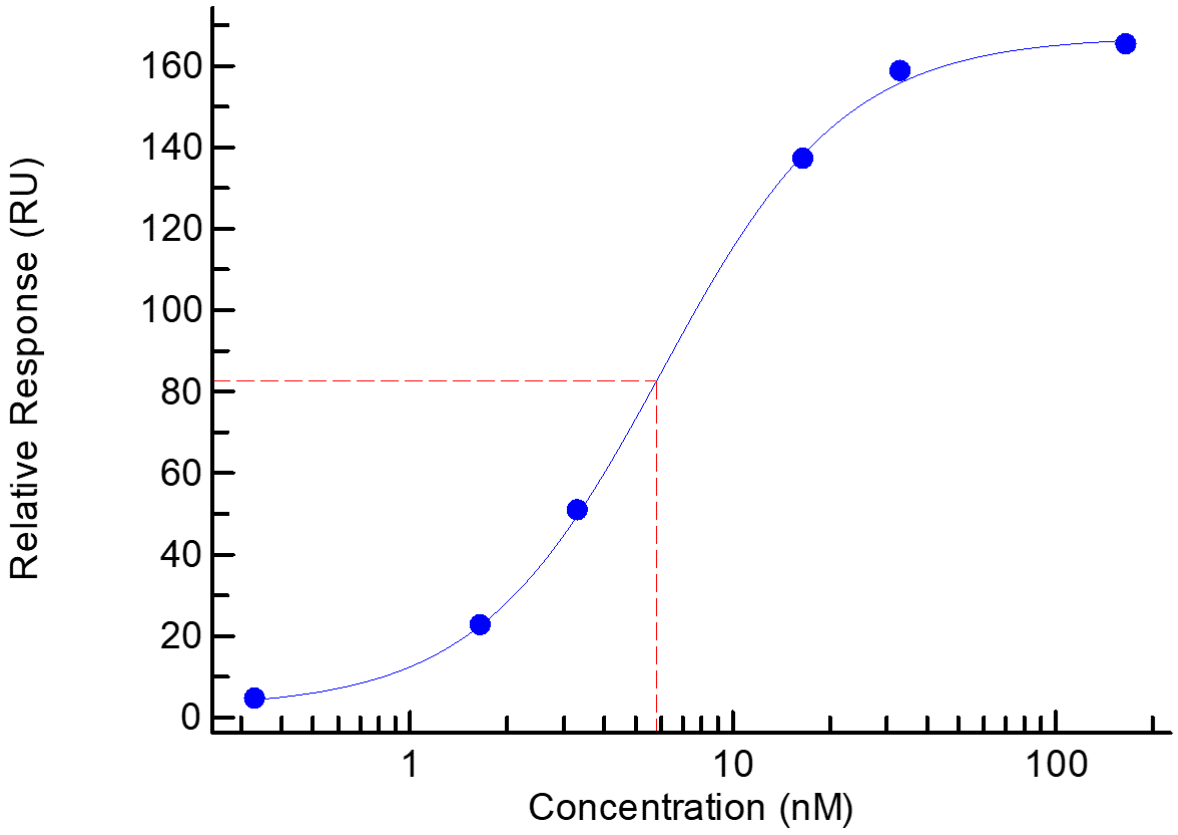

Figure 4.4. The antibody had a measured dissociation constant of 5.79 nM determined by SPR. 100 nM biotinylated-PD-L1 (BPS BioScience) was immobilized to a streptavidin (CAP) chip, and the antibody was titrated across the PD-L1 surface. Each cycle, the antibody:PD-L1 complex was stripped away using guanidinium hydrochloride and NaOH to regenerate the surface, and new PD-L1 was immobilized. Error bars represent the relative error of two replicate cycles to visualize binding consistency. The error in the current experiment is too small for the error bars to be visualized outside of most of the data points.

The values from the titration were normalized as the binding events approached saturation (250 nM) across a PD-L1-immobilized surface with an expected concentration of 100 nM. The true responses were normalized with respect to the highest binding response. The values were fit to a binding event curve and the 50% response was evaluated as the K_D, which was found to be 5.79 nM (Figure 4.4). This technique is,

however, resource intensive due to needing fresh ligand material at each cycle and was chosen with careful deliberation as the best course for characterizing the affinity and selectivity of the antibody.

Test 2: Flow PD-L1 across a surface of αPD-L1 antibody – CM5.

This is a reciprocal assay to validate the specificity of binding events observed previously. Herein, we covalently bound the antibody to the gold chip surface by direct peptide conjugation as described in Scheme 4.1 and Figure 4.1.

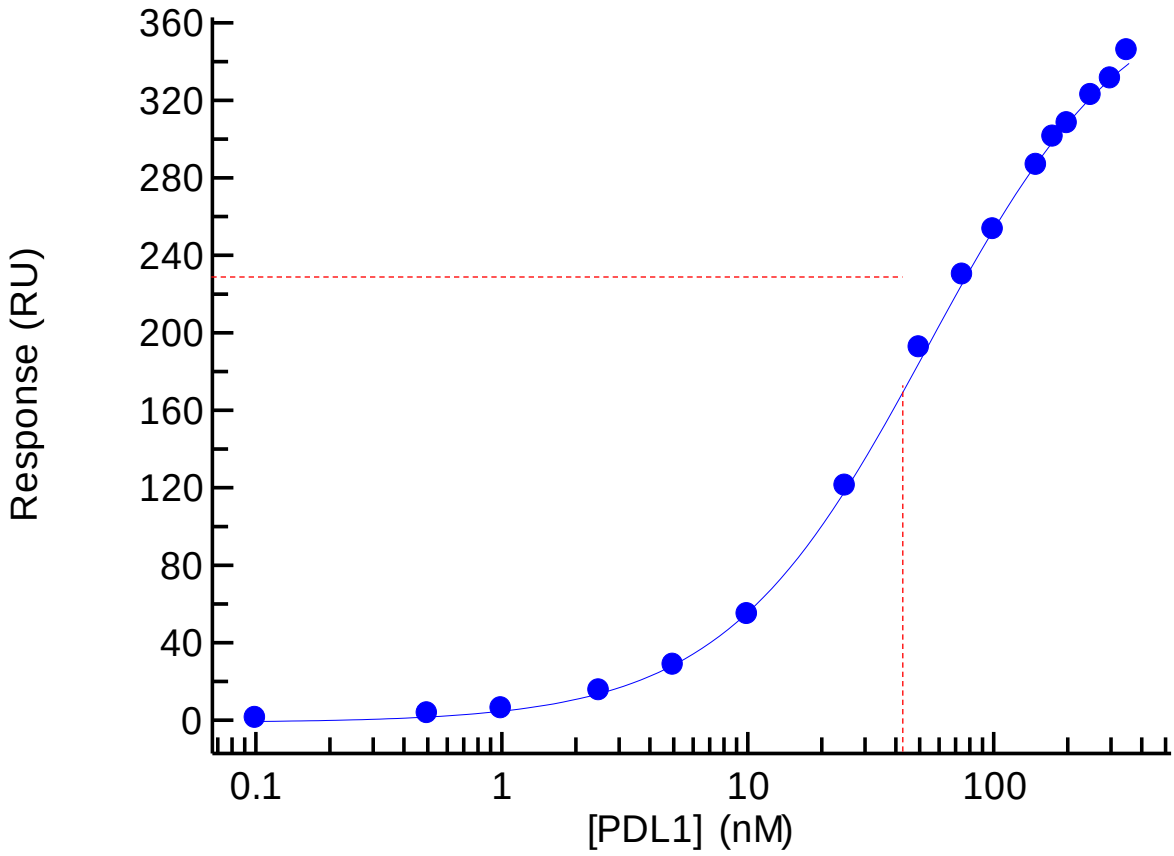

Figure 4.5. When the αPD-L1 was covalently immobilized to a CM5 chip using peptide coupling, and soluble PD-L1 was flowed across to validate the prior K_D. This reciprocal assay determined the K_D as 43 nM. Error bars represent the relative error of two replicate cycles. The error in the current experiment is too small for the error bars to be visualized outside of most of the data points.

The purpose of this experiment was to investigate if the random orientation of peptide conjugation would disrupt activity of epitope recognition. As we do not know how many lysine residues are present on the antibody, and we also do not know if these residues are present in the epitope binding site, it is possible the random orientations may reduce binding activity upon conjugation. This information would be afforded to us by seeing an increase in the affinity constant – indicating a decrease in affinity overall, due to steric blocking the epitope as shown in Figure 4.3.

This series also demonstrated the resilience of mAbs, as these proteins were subjected to harsh regenerative conditions, but managed to still show remarkable binding in PD-L1 each cycle. The binding surface was regenerated by subjecting the αPD-L1/PD-L1 complex to denaturants (i.e., chaotropes to

unfold, and extreme pH change to disrupt electrostatics) such that the less robust solubilized PD-L1 would unfold and no longer be bound to the surface. Due to the tight binding between antibody and antigen, it is unlikely that all the PD-L1 will dissociate freely within a reasonable amount of time. After each analyte flow cycle, we regenerated the αPD-L1 surface by effectively unfolding the PD-L1 by increasing the pH from 7.4 to ~12 and incorporating the chaotropic agent, guanidinium hydrochloride. We expect the antibodies are resilient to withstand these unfolding conditions, where they maintain most of their shape and therefore epitope activity. However, after 10+ cycles there is some loss in binding activity. This may be one of reasons as to why we never achieved saturation in the response curve as the [PD-L1] concentration begins to exceed 300 nM in Figure 4.5. This titration resulted in an affinity constant of 43 nM, which is slightly worse than in the reciprocal assay (Figure 4.4), but still quite strong relative to native PD-1/PD-L1 affinity of 8 μM.[145]

Although we did not observe true saturation between the antibody and antigen in this reciprocal assay, we did observe a similar affinity constant. These assays also confirmed that random peptide conjugation should not totally deter mAb activity, indicating that there are lysine residues present, and that the epitope is not blocked. Although the affinity constant is not identical between the assays, the discrepancy is attributed to those nonselective amide formations. We do recognize that the random orientation and inability to achieve proper saturation may also increase the apparent K_D further away from sub-nM orders. However, this assay also affirmed the resilience of these antibodies, as they were capable of still recognizing PD-L1 after 10+ cycles of intense denaturation conditions. This commercial mAb from BioXCell is a suitable targeting agent.

Test 3: Competitive Inhibition of the PD-1/PD-L1 interface with αPD-L1 antibody – SA Chip

The previous two tests afforded the crucial information about how we may process the antibodies moving forward when functionalizing them onto our gold core. A final experiment was performed to evaluate whether the antibody could competitively disrupt the PD-1/PD-L1 interaction. This is a key factor as it could highlight the potential immunotherapeutic benefit that we may observe when transitioning into the more complex systems of cell- and animal-based studies. Current immunotherapies rely heavily on antibodies that disrupt these protein-protein interactions to reinstate immune activity.[81,115,203] However, as described in Chapter 2, antibodies are not universal drugs despite their high specificity, but are excellent as targeting agents. The previous two tests show that this antibody from BioXCell is selective for PD-L1 and a robust targeting agent but does not describe or forecast any immunotherapeutic benefit.

To test whether the αPD-L1 antibody *could* be an immunotherapeutic agent, we used a simplified competitive-based assay with immobilized PD-1 and a fixed concentration of 500 nM PD-L1 (Figure 4.6). We then titrated αPD-L1 from 10 nM to 1 μM which resulted in a negative binding curve.

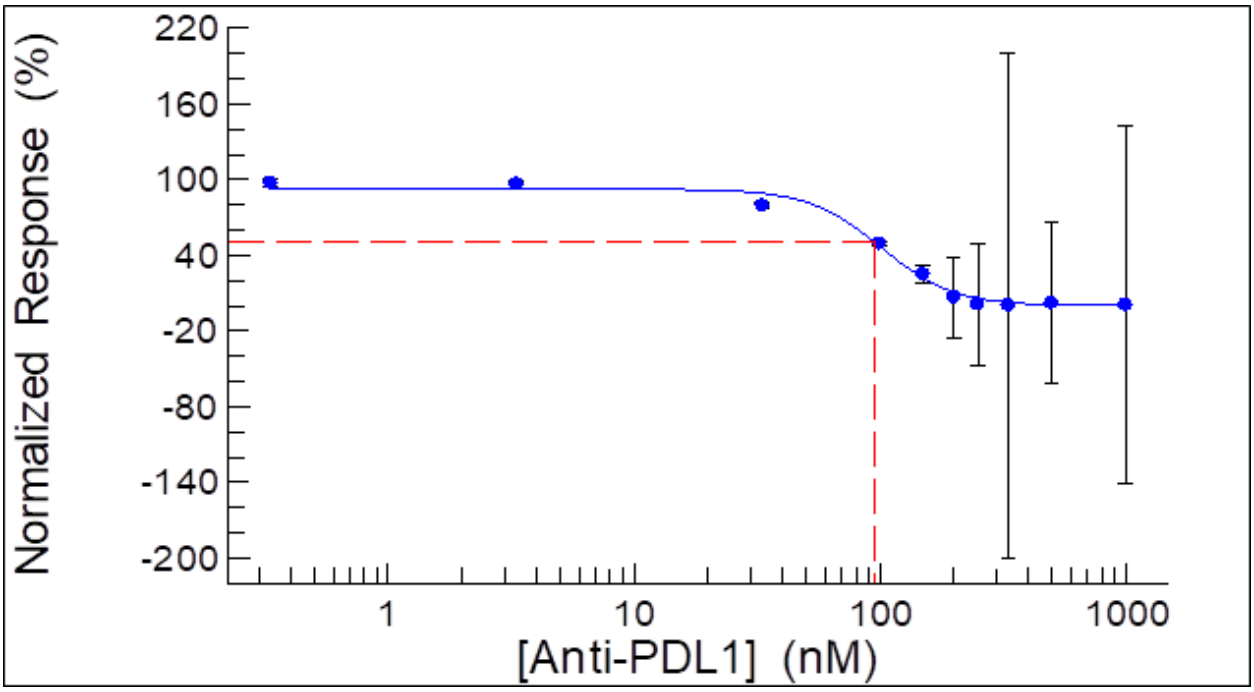

Figure 4.6. A semi-log plot characterizing the inhibiting effects of the monoclonal antibody targeting PD-L1 (αPD-L1) as characterized using a competitive SPR assay, where a fixed concentration of PD-L1 (500 nM) was flowed across a surface of biotinylated-PD-1 and the αPD-L1 was titrated to observe any disrupting effects. The responses were normalized with respect to uninhibited binding response between PD-1 and PD-L1. The bars represent relative error between two replicate sample cycles. As the concentration approaches 250 nM αPD-L1, there is no observable binding of PD-L1. This highlights the 2:1 valency of antibody and indicates that both epitopes are available for targeting. 50% activity was achieved with 95.7 nM mAb.

There are two important takeaways from Figure 4.6. First, the antibody has full activity for its antigen and second, it can achieve full inhibition of binding between PD-1 and PD-L1. As the concentration of the antibody approaches 250 nM, we achieve no response in binding between PD-1 and PD-L1, which highlights the 2:1 valence of the antibody and indicates that both epitopes are active for targeting PD-L1. The lack in response as the mAb concentration increases indicates occlusion between PD-1 and PD-L1. This highlights not only selectivity between the mAb and the antigen, but potentially alludes to immunotherapeutic benefit of preventing the signal. Otherwise, if we were to observe an increase in response it would be due to an antibody:PD-L1 complex that can still recognize the PD-1 surface. The importance of having a PD-1/PD-L1 competitive agent over targeting these proteins alone, returns to immunotherapy. We hope that the inhibition of activity could result in T cell recovery. Regardless, both outcomes achieve PD-L1-targeting for delivery of the gold core.

These three SPR tests were sufficient to characterize the commercial antibody as an appropriate targeting agent for our gold nanoparticles, with promising *in vitro* results that indicate our antibody could have an immunotherapeutic effect alongside selective targeting.

Direct *In Situ* Peptide Conjugation was not a Suitable Method for Functionalizing Gold Particles

Previously stabilized particles from Devika Chithrani's group were prepared using a Turkevich-based reducing method.[280] Our intent was to repeat the conjugation process that was observed via SPR but on a curved surface instead of flat one. We intended to use the carboxylic acid moiety on an internalization

peptide to conjugate the antibody to the AuNPs (Figure 4.7). This RGD internalization peptide was previously shown by the Chithrani group to improve uptake of particles into cells by binding with integrin receptors.[98,167] This peptide conjugation method has been previously reported for functionalizing particles.[12,110,281] However, we did not observe any indication that particles were conjugated or functionalized, and an alternative method of conjugation was needed to functionalize the AuNPs (Figure 4.8).

We used SPR as a direct means of characterizing the functionalization of the AuNPs by directly comparing the response of the functionalized particles, as they were flowed across a chip of biotinylated-PD-L1, to the relative binding response observed with the equivalent amount of free antibody (e.g., the concentration needed to functionalize the AuNPs). From our previous characterization studies, we can assume that functionalized particles should have a non-zero valence (i.e., if particles have one antibody each, the valence is still an average near "1" to account for the random orientation of the epitopes, where some are unfavourable for binding). This assumption in valence allows for a more straightforward estimated SPR response of the particles, where the direct comparison relies solely on the magnitude of responses which is proportional to the molecular weight between the particles and the antibodies. If no binding is observed from the particles, then no conjugation has occurred.

In initial attempts of peptide conjugation to functionalize our particles, we thought to directly conjugate to a peptide known to improve gold uptake in cells.[167] The full structure of the "RGD" peptide shown in Figure 4.7, it contains a lot of positively charged lysine residues and uses the cysteine residue to adsorb and stabilize to the gold surface. We aimed to form the NHS-ester at either of the carboxylic acid sites (Figure 4.7, red) of either the aspartate (**D**) or the carboxyl terminus. Unfortunately, these first iterations resulted in binding responses similar to the antibody alone, indicating overall poor conjugation. This led to an alternative development of functionalization where the antibody was conjugated to a thiolated agent, and then this conjugate was used to functionalize the AuNPs (Figure 4.8).

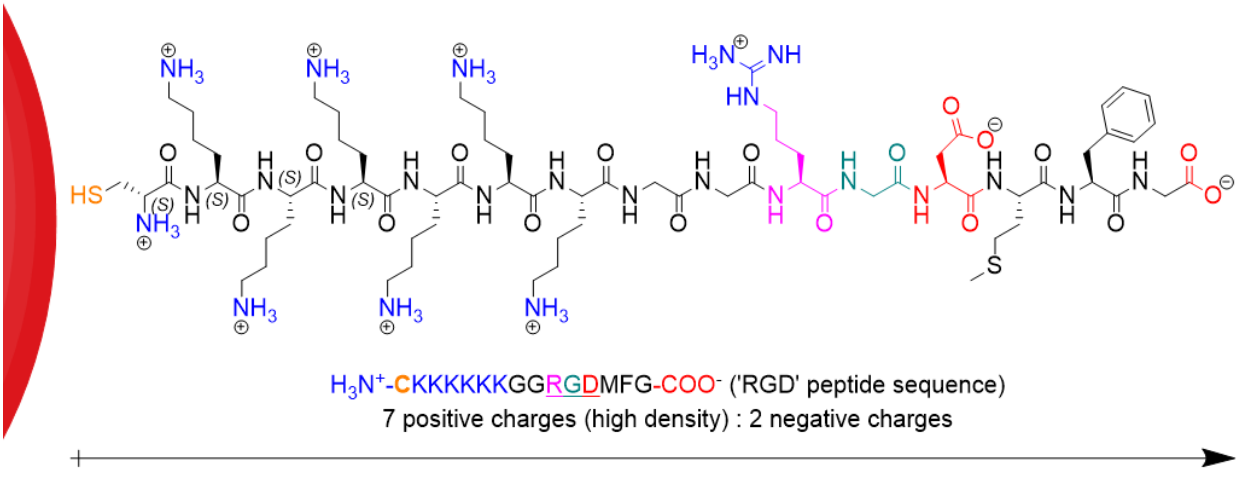

Figure 4.7. Full structure of RGD peptide, highlighting viable conjugation sites for NHS ester (red), as well viable amines for intramolecular nucleophilic substitution (blue). The "RGD" residues are highlighted accordingly and underlined.

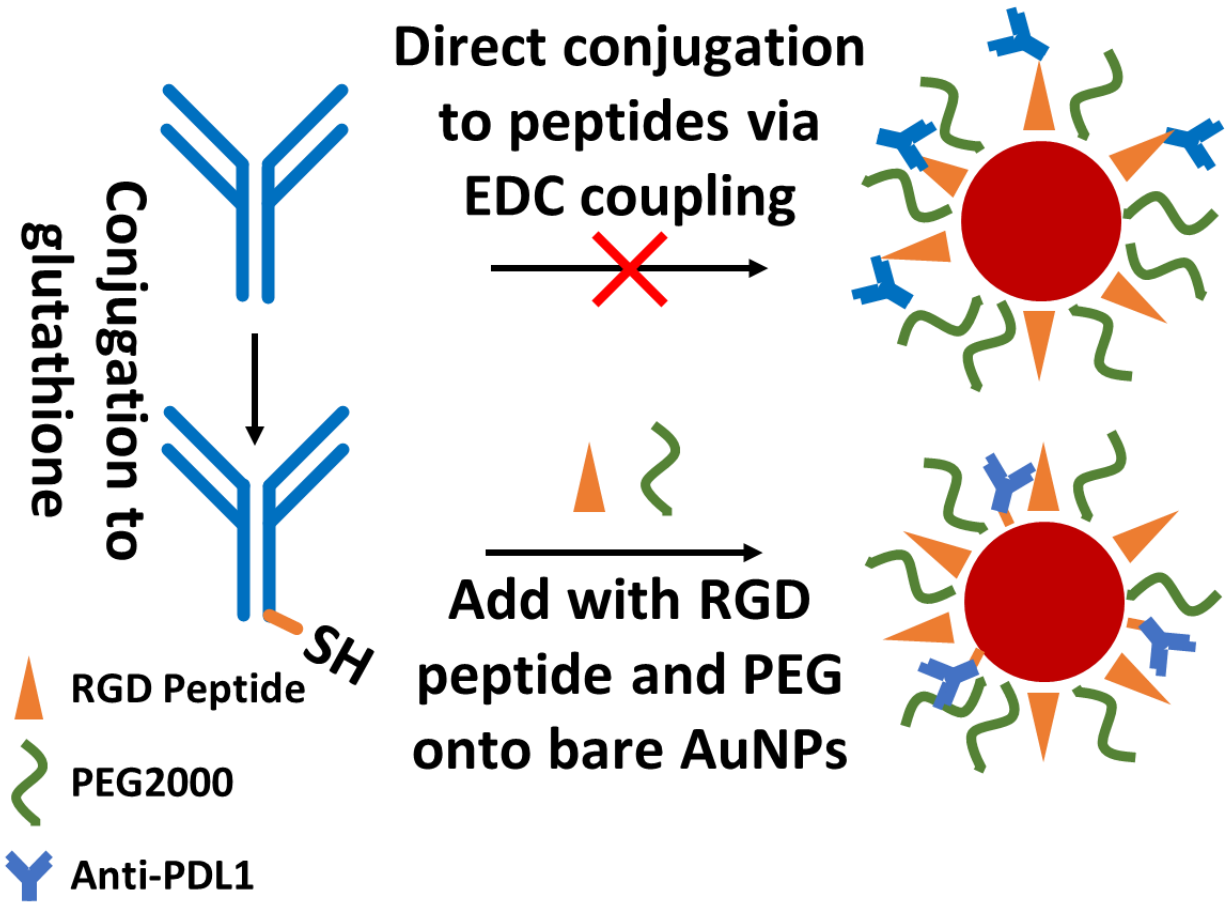

Figure 4.8. Intent to functionalize gold nanoparticles with αPD-L1 antibody. We found that direct peptide coupling to pre-formed, stabilized particles was ineffective, and therefore we sought to create thiol-conjugated antibodies to functionalize and stabilize the gold core.

There are a few reasons as to why the RGD conjugation may have failed, even with high molar ratios of 300 mol RGD : 600 mol PEG_{2000} per 1 mol AuNP. First is steric hindrance caused by the other stabilizing molecule, $mPEG_{2000}$-SH (PEG_{2000}), a biocompatible polymer. This molecule is a spacer that prevents core aggregation, and upon formulation is used in greater excess than the RGD peptide. The lower concentration coating the cores could have less conjugation available for the antibodies to functionalize the particles. If the formulation were to increase the concentration of the RGD peptide, there is an increase in conjugation opportunities, but this will change the polarity of the particles entirely. Too much of the "RGD" internalization motif could result in large off-targeting of particles, which would nullify the intent of our targeting agent.

Another possibility of the poor conjugation could be due to intramolecular polymerization of the peptides. Given the highly positively charged backbone, any NHS-ester intermediates formed on the RGD peptide may have had circumstances that favoured intramolecular nucleophilic substitution where the RGD peptide was cyclizing and preventing antibody conjugation. Alternatively, the high RGD density per particle may have also favoured polymerization between peptides; regardless, both result in the poor conjugation of the mAbs to the core.

Glutathione-Antibody Conjugates for Gold Nanoparticles Functionalization

Rather than conjugating the peptide to previously stabilized gold nanoparticles, we aimed to stabilize the gold with our targeting agents by thiolating the antibody. Due to the risk of intramolecular polyamidation, we chose not to pursue the EDC/NHS conjugation on the RGD peptide prior to stabilization. Our rationale was based on how much positive charge is present in the peptide relative to the carboxylic acid sites (Figure 4.7) where our conjugation conditions would result in mostly cyclization or polymerization of the peptide rather than conjugating to the antibody. Instead, our initial thiol conjugate was the tripeptide glutathione, which is comprised of glutamine, cysteine, and glycine (Figure 4.9). This molecule is ubiquitous and biocompatible and was deemed appropriate for pushing forward with antibody conjugation.

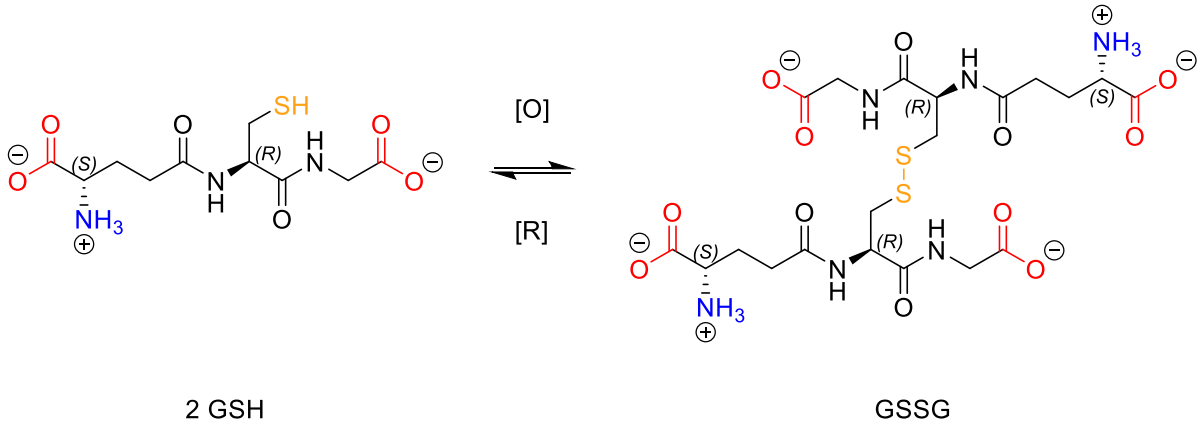

Figure 4.9. Glutathione in both its reduced (GSH) and oxidized (GSSG) states. With the higher number of negative charges per molecule and no opportunity of steric hindrance from surrounding PEG, we expected better peptide conjugation to the antibody.

Thiolation and Purification of the Antibody

The antibody was the limiting reagent in a one-pot reaction with excess EDC, NHS, and GSSG (> 100 mol eq.) and was left to react overnight. Any unreacted NHS-esters formed *in situ* were quenched with ethanolamine – also in excess (Figure 4.10A). This crude reaction was then purified by spin column filtration with a molecular weight cutoff (MWCO) filter of 3 000 g/mol, such that *only* the antibody and antibody-conjugates would reside in the retentate after the pull-down (Figure 4.10B).

Spin-column filtration was chosen initially over dialysis such that we could quickly scout the conjugation parameters of thiolating mAbs onto AuNPs. However, using such small volumes and specialized plastics was short-lived due to being too expensive. Once the purification conditions were established, subsequent thiolated antibody purification used dialysis.

The columns were spun at 10 000×g for 7 min, these conditions were required to concentrate the reservoir in the retentate from a marked 500 µL to 100 µL. Unreacted small molecules like GSSG and EDC were removed by centrifugal force. The retentate was resuspended in a HEPES-based saline (HBS-EP$^+$) running buffer and was expected to be mostly antibody and its peptide-coupled conjugates. This volume was returned to the marked volume of 500 µL to exchange the antibody-GSH conjugates into an SPR-compatible buffer and maintained the effective concentration of the antibody. This spin-down was repeated at least five times, such that the small molecules were diluted a total of 3 125-fold (where the antibody is now expected to be 31-times more concentrated with respect to the small molecules) (Table S4.3).

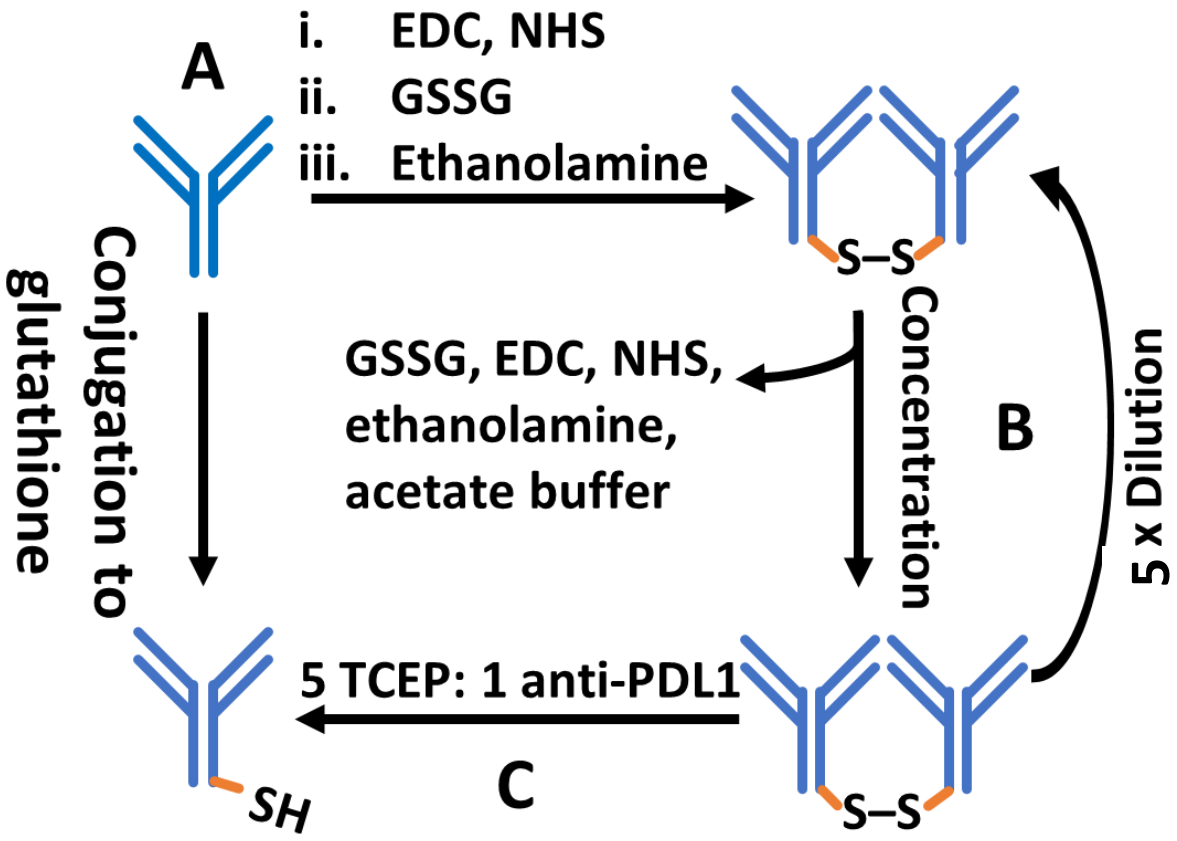

Figure 4.10. GSH-thiolation and processing of αPD-L1 antibody. **A**. 417 nM αPD-L1 is reacted with excess (> 100 mol eq.) EDC, NHS, and GSSG to create NHS-ester *in situ*. After an overnight incubation, the reaction chamber is given excess ethanolamine to quench any unreacted NHS-esters. **B.** The small molecules are removed by spin-column centrifugation through five iterations of concentration and resuspension. **C**. 5 mol eq. TCEP reduced the GSSG-conjugates resulting in free thiols for gold core functionalization.

To assure that antibodies were not conjugated as dimers, we found that adding 5 mol eq. TCEP to reduce GSSG to 2 GSH had the most activity overall (Figure 4.10C).

Although peptide conjugation of glutathione was done with the oxidized dimer, we wanted to assure that adsorption was occurring only with the thiol and not potential dimers. The antibody conjugates were screened in functionalizing gold nanoparticles with various conditions used in forming the thiolated antibody (Figure 4.11). The concentration of the antibody-GSH conjugates was determined using a NanoDrop A_{280}/A_{260} absorbance reading with a previously calculated molar absorptivity coefficient for IgGs. We wanted to monitor the concentration before and after conjugation to ascertain that the processing was not detrimental to protein stability (e.g., if the antibodies were embedded in MWCO membrane, aggressive resuspension may unfold the protein lowering activity). In most cases, the concentration did not change drastically, staying within the original 0.5 mg/mL concentration (Table S4.3).

Figure 4.11 shows how the optimization in thiolating the antibody led to more functionalized AuNPs. The trend observed was that more spins and higher amounts of reducing agent resulted in an overall higher

response (with respect to the equivalent amount of free antibody), which indicates that the small molecules could contribute to poorer functionalization. Although the thiol in cysteine adsorbs strongly with gold, GSH/GSSG alone are not suitable as spacer agents alone, and these smaller molecules may be contributing to gold particle aggregation. Their removal increases the likelihood of antibody adsorption – as shown by the increase in response, and this increase in response is therefore indicative of more *functionalized* particles. If we used SPR to measure change in activity post-processing in the antibodies alone, we would expect a lower overall response – indicative of epitope unavailability. However, upon *functionalization*, we are seeing an increase in response of the AuNPs, indicating there are more *active* antibodies are present on the particles.

SPR as a Form of Characterizing Functionalization of AuNPs – Biochemical Assay "Golden Ratio"

To characterize by SPR, a handful of assumptions need to be characterized prior to normalizing responses attributed to functionalized AuNPs. Primarily are the molecular weights of the binding species of interest (i.e., analytes and ligand). To characterize whether the particles are functionalized, we need to be able to accurately compare how the analytes are expected to bind. In the simplest case of 1:1 binding, it is a comparison of molecular weights between unbound free mAbs and the AuNPs as described in Equation 2. One given is that immunoglobulin gamma proteins have a universally accepted average MW of 150 000 Da ($1.5 \cdot 10^5$ g/mol) and a valence of 2 for their antigen, which for ligand, PD-L1, the valence is reciprocated to ½ in Equation 2.

$$R_{max} = \frac{R_{ligand} * MW_{analyte} * Valence_{ligand}}{MW_{ligand}} \quad (2)$$

To accurately size the particles is more involved, as each batch of cores will never truly uniform, so we characterize the mean core size and distribution to acquire a molecular weight for SPR characterization, with an intended size and limitations. We measure core sizes and a sample distribution directly through TEM, and orthogonally validate the dispersity using DLS. We can compare the intended size to what is measured to determine if the core synthesis was successful prior to any functionalization.

The molecular weight of the gold cores Is determined by the relationship of face-centered cubic packing density efficiency (0.74) of metallic gold atoms expected to fit within the measured mean size by TEM (Equation 3).The intended 15 nm diameter nanospheres are expected to have a molecular weight of the expected of 20 600 000 g/mol ($2.06 \cdot 10^7$ g/mol); assuming they are all uniformly spherical. Although this molecular weight will vary based on core size and dispersity, these measurements act as a starting point for assessing the expected response in the SPR experiments. Additionally, the coating agent molecular weights were negligible to the total molecular weight (< 1.1% MW increase; Table S4.2), which allowed for direct comparison between functionalized core to the equivalent amount of mAb. If core synthesis failed to meet the criteria during TEM and DLS characterization (i.e., d >> 15 nm and/or, PDI > 0.15), then a fresh series of particles was created. By maintaining a constant core volume, this allowed us to prioritize optimizing coating functionalization rather than the physical core variables. These criteria became more stringent with each iteration of synthesized particles.

Although the antibodies have two epitope binding sites, our assumption is that thiolated antibodies have a binding valence to PD-L1 of < 2, due to the non-specific peptide conjugation with the thiolating agents. The extracellular domain of our protein of interest, PD-L1, has a molecular weight around 25 000 g/mol when considering only the external domain residues 19–238; our commercially biotinylated

PD-L1 contains this same domain as well as the mono-biotinylated tag, resulting in a total MW of 54 000 g/mol (BPS Bioscience) allowing for uniform binding with our analytes.

Using Equation 2 and substituting the appropriate values in for both analytes, the equations can be simplified to represent the magnitude response expected between those two analytes. Continuing the example with 15 nm AuNPs, the expected intensity of the particles should be 137-fold greater than the binding response of the free antibody. This magnitude is our "Golden Ratio" and is a ceiling value representative of 100% activity assuming all particles are functionalized with at least one antibody. If the value is not achieved, then we can assess the degree of which the particles are functionalized.

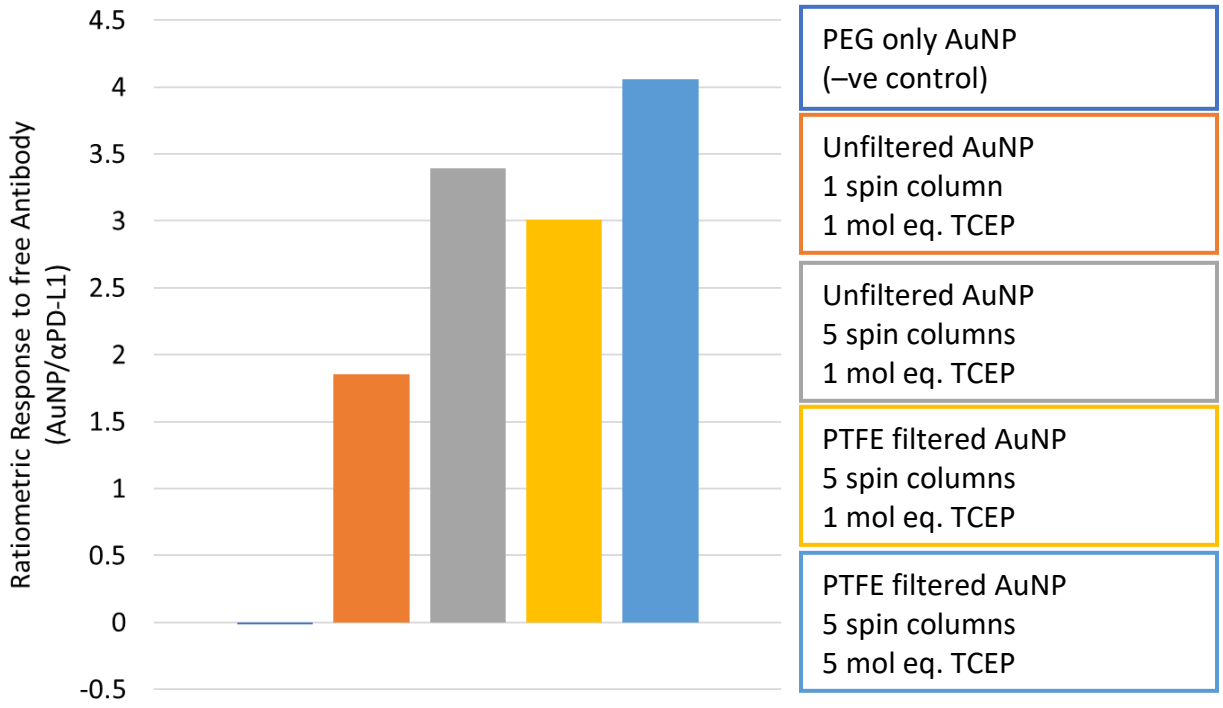

Figure 4.11. Initial optimization process when synthesizing GSH-mAb conjugates for AuNPs. These initial SPR experiments primarily investigated the parameters surrounding removal of unwanted small molecules while retaining the concentration of the antibodies – looking how many spins to remove small molecules, and how much TCEP was needed. The general trend shows an increase in response of binding as the antibodies were processed to remove the small molecules for thiol conjugation, indicating better functionalization of the particles. The formulation of these AuNPs uses 15 mol eq. GSH-αPD-L1 (and 300 mol RGD: 600 mol PEG_{2000}) – assuming the particles are uniform and using the concentration described by Haiss *et al*.

However, these assumptions are not taking into consideration that antibodies could be on opposing hemispheres of one gold particle. This bridging effect could be detrimental as it reduces opportunity for other AuNPs to bind, while also *decreasing* the valence of the ligand, which could thereby reduce the ceiling of activity (e.g., valence of 1 analyte binding to 2 ligands reduces the expected R_{max} in half).

As previously mentioned, the general trend shows an increase response from the AuNPs when the antibodies are more processed and expected to have better purification in isolated thiolated mAbs. There is an increase in binding response (1.8-fold to 3.4-fold binding response relative to the equivalent mAb concentration, Figure 4.11) when the number of spins was increased from 1 to 5 (10 000 x g for 7 min), the removal of unconjugated GSH. Similarly, the binding responses increases when the reducing agent, TCEP was present. The addition of a reducing agent removes any GSH polymer conjugates that may

also be coating the AuNPs, preventing mAb functionalization. TCEP reduction also ensures a free thiol is present on the antibody to conjugate to the gold. These positive trends in binding response indicate that more processing with the intent of purifying of mAb conjugates is needed to functionalize the nanoparticles. However, due to this conjugation forming *in situ* there are many possible side reactions, making it difficult to characterize how much GSH is present per antibody. Therefore, by processing to remove the side reactions, we saw higher binding responses overall as there were more antibody conjugates present to functionalize. Regardless of the positive trend in response attributed to a higher purity of thiolated mAbs to functionalize the particles, the overall degree of activity is quite low. The highest achieved response (4-fold binding response relative to the equivalent mAb concentration) is < 3% of the expected magnitude of the 137-fold "Golden Ratio", indicating that this method of conjugation is quite poor.

How Many Antibodies per AuNP?

The expected maximum was calculated by considering the AuNP core as a sphere and solving for the number of mAbs of a given dimension that could fit on the surface of that sphere (Table 4.2, Figure 4.13).This was used to assess the "degree of functionalization" and calculate the ceiling concentration required to wholly coat the particles (expressed as percentage). To calculate the total surface area of the cores in a given sample, we needed an accurate sizing of the particles – which was measured by TEM and DLS. These techniques were used to directly measure the core size and to confirm whether there is low dispersity of the core sizes (they may be considered "acceptable" if the dispersity < 0.15).

For the TEM, sample photos of the gold core are measured using a calibrated imaging software, ImageJ, with at least four separate images from one of the quarters of the TEM grid, viewed at 150 000x magnification (example shown in Figure 4.12). From measuring at least 2 000 AuNPs in one sample over at least three images, we can directly measure the core size of the batch using TEM.

DLS was used to measure the hydrodynamic volume of the particles in real-time, as well as characterize their dispersity and visualize stability. Three samples of AuNPs (1:7 dilution from stock < 62 g/mL concentration) are measured independently, three times. The volumes are often slightly larger than observed by TEM due to DLS observing the hydrodynamic radius (hydration shell). The TEM image yields a 2-D image of the widest circumference of the particles in the absence of solvent. Both characterization techniques yield similar results to ascertain the size of the particles. Our particles are synthesized with an expected core size of 15 ± 1 nm in diameter as described by Xia *et al*.[33] and Table S4.1 shows the characterization data of each batch of AuNPs that were synthesized.

Additionally, we measure the core size by UV-vis spectroscopy as described by Haiss *et al*.,[19] where the maximum absorbance wavelength is correlated with AuNP size, and using Beer–Lambert absorptivity coefficients (ε) of the fixed core volume, we may now describe the concentration of the AuNPs in molarity. Although this may only be used qualitatively as it assumes all the particles are uniform.

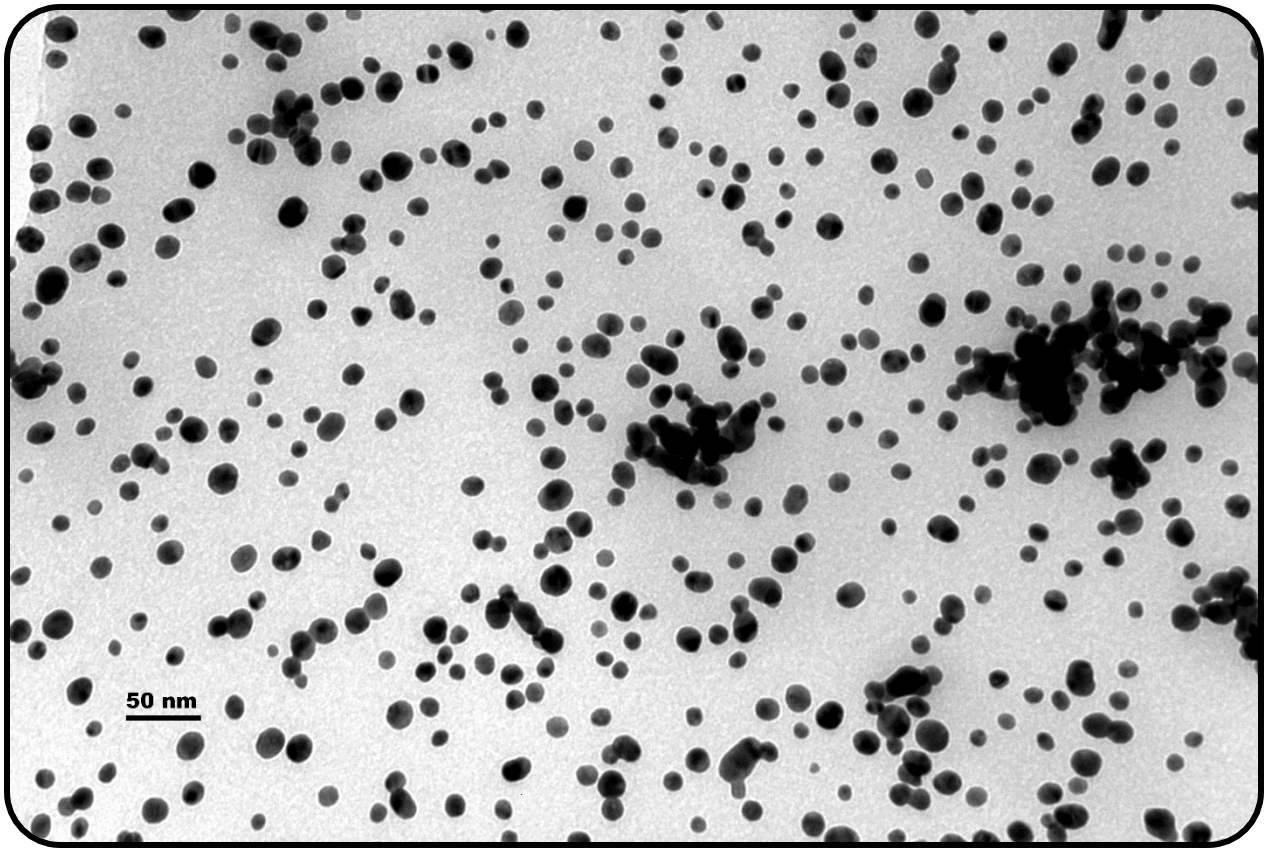

Figure 4.12. Sample TEM image of citrate-coated "bare" AuNPs synthesized using an alternative Frens method described by Xia *et al*.[33] The average size of the particles was calculated over three images of at least 1500 individual particles. These particles were synthesized to have an expected core size of 15 nm. They were analyzed by TEM and found to have a mean core diameter of 12.9 ± 1.5 nm with respect to the standard error. The error value is representative of the standard error of the mean within three images.

Similar to how the MW of the core was determined, we use a similar packing optimization to model how many antibodies could be expected to functionalize the AuNP surface. We chose the empirical values measured from Tan *et al*. where they measured the dimensions of immunoglobulin gamma (IgGs) 15 nm x 8.5 nm x 4.5 nm using atomic force microscopy.[174] These dimensions were used to obtain estimated volumes for the antibody ranging from a trigonal planar-sized minimum (319 nm^3) to a spherical maximum (1 767 nm^3) (Table 4.2).

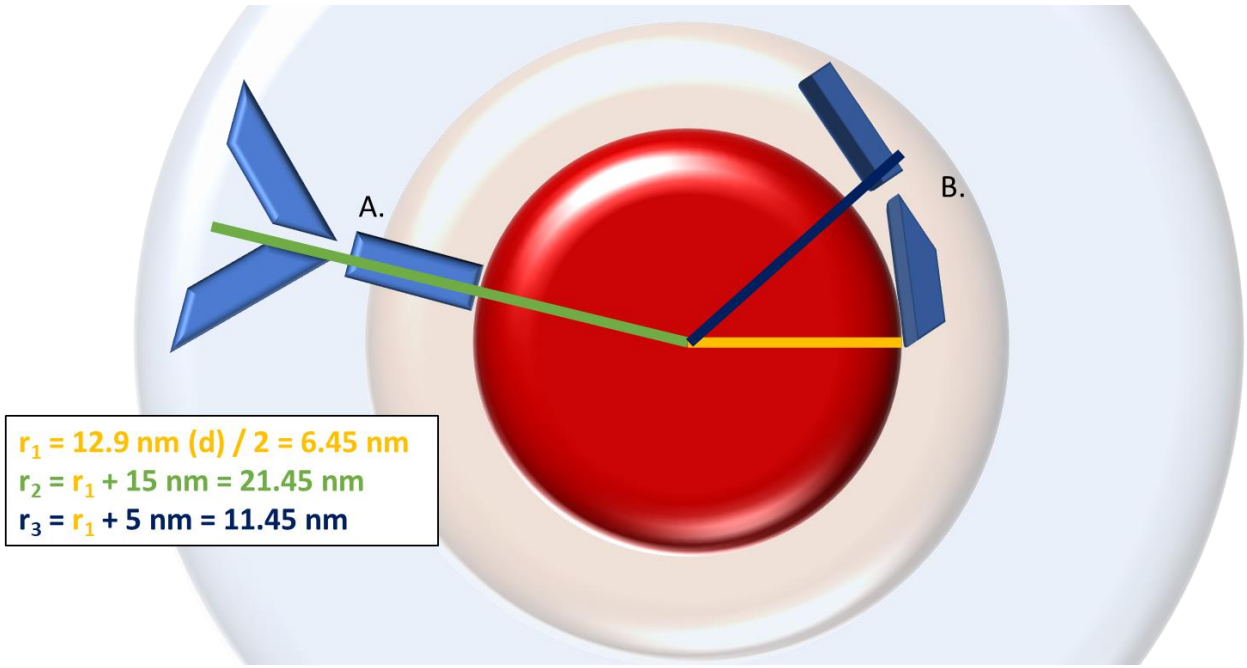

Figure 4.13. Two extreme orientations that the mAb behave upon functionalizing the AuNP core. **A**. The ideal orientation that maximizes the radius with the additional 15 nm length. **B**. A non-ideal extreme where the antibody is laid flat around the gold core, adding an additional 5 nm to the expected radius. These radii were used to estimate the shell volumes to calculate how many GSH-mAb conjugates per AuNP.

As the thiol-conjugation was performed in excess, we expect a variety of orientations that the mAbs may be in, we chose two extreme orientations to determine the theoretical "functionalized AuNP" volumes (Figure 4.13). When the antibodies adsorb to the gold cores in an optimal lengthwise orientation, the radius becomes r_2 with full epitope availability (Figure 4.13A). The non-optimal extreme (r_3) uses an ineffective *flat* orientation, adding the width of the IgG to the core (Figure 4.13B). Both orientations were used to determine the volume shells of "functionalized" particles that the antibodies may occupy by removing the core volume, yielding the shell volumes of 6 414 nm^3 (orange, B) and 45 946 nm^3 (blue, A), respectively.

The maximum number of antibodies required to coat the nanoparticles was calculated by looking at the ratio of the volumes between the shells and various volumes of IgGs (Table 4.2). From the shape volumes chosen, spheres were the most reasonable with an expected maximum of 26 antibodies. This maximum does not account for orientations that may hinder activity, however with such high coverage numbers, it is unlikely that a large population of antibodies will show non-selective activity, as the previous peptide coupling experiments showed reasonable selectivity despite the expected random orientations. Using a more accurate, although extreme minimum occupancy shape like a columnar trigonal prism, the expected number of antibodies increases; these volumes now account for tessellation where the epitopes will be sterically hindered by adjacent mAbs. Using the spherical model volume was much simpler when functionalizing nanoparticles in future formulations, where 25% mAb coated the nanoparticles with an expected four and six antibodies per AuNP, rather than 30–40.

Table 4.2. Volumes calculated to determine the how many antibodies may fit on the surface of a gold nanoparticle. Highlighted in green was the chosen as "most reasonable" and was carried forward.

Shell B (flat antibody)			**Total Antibodies within Shell**	**Shell A** (tall antibody)			**Total Antibodies within Shell**
V_mAb (trigonal)	319	nm^3	20.1		319	nm^3	144.1
V_mAb (cuboid)	638	nm^3	10.1		638	nm^3	72.1
V_mAb (Sphere)	1767	nm^3	3.6		1767	nm^3	**26.0**
V_mAb (Cone)	549	nm^3	11.7		549	nm^3	83.7

Change the Formulation – Following the Wheel of Functionalization (and some Future Work)

Given our current processing had shown some success in functionalization, we investigated other parameters to functionalize the particles that might improve the overall binding response in a "fail-fast" manner using SPR as the main instrument of characterization. Our current purpose was to maintain the simple particle consisting of the targeting agent and a stabilizing agent and determine which formulation can maximize the overall activity of targeting before moving the particles into cellular studies.

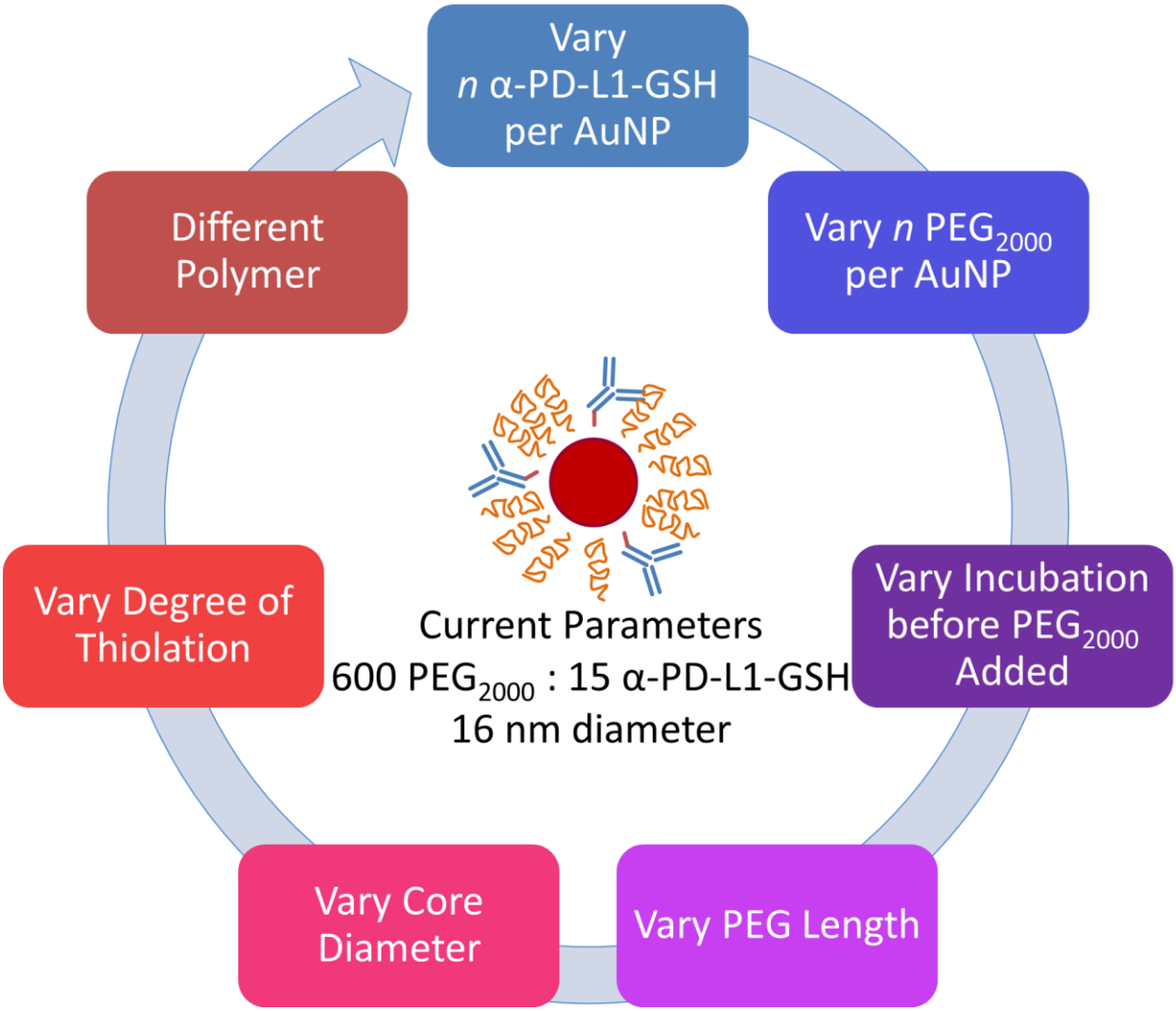

Figure 4.14. A wheel of functionalization, these are the various parameters that were investigated to develop the AuNPs that target PD-L1. These parameters were optimized using SR as the primary means of characterization, where the response values were compared to the expected 100% activity (the Golden Ratio). The given molar formulation in the center was used with respect to previous particles stabilized in the Chithrani group.[167,280] These molar ratio coverages were converted to a mass-based ratio of molecules needed to coat the total surface area, they are equivalent to 67% mAb and 217% PEG_{2000}, respectively. The wild excess of PEG may have also had negative impact on functionalization. In all experiments, AuNPs were flowed across a CAP chip with biotinylated-PD-L1 for uniform characterization of binding, and responses were compared to the response of equivalent amount of free antibody.

Increasing GSH-mAb per AuNP – we found that formulations with increasing concentrations of mAb and a fixed concentration of PEG had no effect of saturation. We had hoped to achieve some form of *f*-AuNP saturation curve, indicating the point where all effective antibody was adsorbed to all the particles. However, our results yielded a linear curve with respect to the concentration, determining that our functionalization method was poor (Figure 4.15).

The responses observed were quite low with respect to the equivalent unbound antibody, indicating overall poor efficiency in functionalization, which may be attributed to poor conjugation conditions for the antibody to the glutathione. The responses when plotted with respect to the molar amount of mAb used per AuNP results in a linear curve. Although there is a positive correlation in binding response in

AuNPs with higher mAb concentrations (Figure 4.15A, blue), the respective response of equivalent unbound antibodies still did not reflect the Golden Ratio (Figure 4.15A, red). This indicates relatively poor functionalization of the AuNPs, however at it is difficult to assess whether it is due to poor conjugation efficiency between glutathione and the antibodies, or the processing that functionalizes the particles.

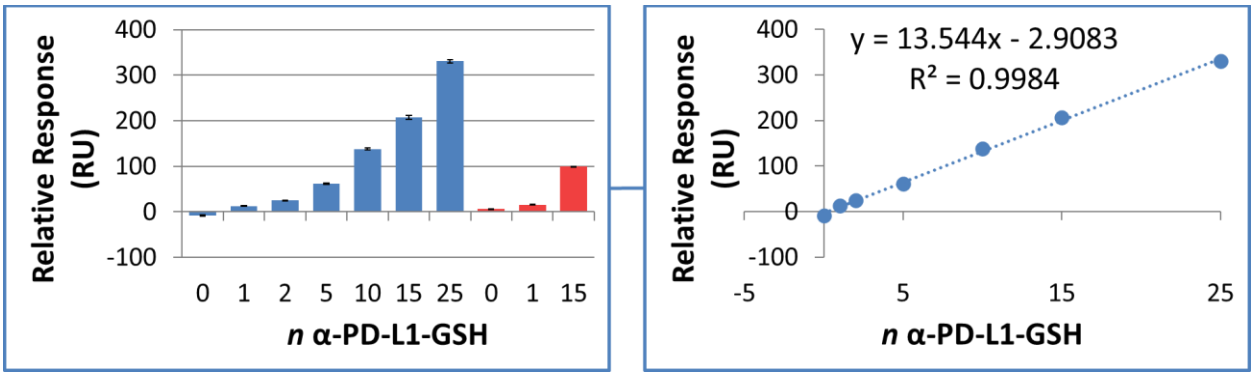

Figure 4.15. Varying the amount of GSH-mAb per AuNP, when functionalizing the AuNPs. We maintained a fixed concentration of 600 mol eq. PEG_{2000} per particle. **A**. AuNPs with varied amounts of GSH-mAb (*n* mol eq.), with fixed 600 mol eq. PEG_{2000} (blue), and the observed responses of free GSH-mAb of 1 mol eq. and 15 mol eq., respectively (red). **B**. The *f*-AuNP responses were plotted with respect to the mol eq. GSH-mAb, which resulted in a linear curve.

Decreasing the PEG per AuNP – one hypothesis as to why GSH-mAb was not functionalizing was due to an imbalance of coverage, and the excess PEG was potentially desorbing our antibody. The current molar ratio of 600 PEG per AuNP was near the upper limit, expected to coat 85% of the surface of the AuNPs in polymer (values in Table 4.3). Previously described in the literature, Rahme *et al*. characterized the PEG_{2000} of 15 nm AuNPs by thermogravimetric analysis and determined the molecular occupancy of 700 PEG_{2000} molecules to totally coat their particles.[282] This value was chosen as our upper limit to proportionally coat the particles where antibodies could not.

By reducing the PEG amount, we expected to limit the excess polymer present and therefore reduce the exchangeability between bound and unbound coating agents. However, our results showed no difference at lower levels of polymer, and therefore no correlation with this formulation between antibody and stabilizer (Figure 4.17).

Note, despite the overall high responses of each particle (between 6–8-fold greater than free antibody (red), Figure 4.16), these particles were unsuitable for cellular work. The concentration of the *f*-AuNP formulations was measured immediately post-functionalization by UV-vis spectroscopy and are reported in Table 4.3. The high binding responses of the formulations with the low concentrations indicate poor stability of the particles, prone to plaque aggregation. This is more apparent when the expected surface coverage of polymer becomes < 50%, and the concentration of the particles decreases, and plaque formation is more prominent during purification. In the cases of high binding, we are likely observing particles with antibody present, but not in sufficient concentrations nor formulations suitable for clinical work.

Post-functionalization, the unbound thiol molecules were removed by centrifugation or dialysis, and the remaining functionalized particles were measured by UV-vis spectroscopy to determine the concentration of the sample. This was done using the data collected by Haiss *et al*., who characterized the Lambda max of various AuNP sizes, attributed to surface plasmon excitation, to determine the molar absorptivity

coefficients (ε) of any given core diameter.[19] They characterized ε for various core sizes by evaluating the relationship of absorbance intensity between the Lambda max (SPR wavelength) and 450 nm.

UV-vis spectroscopy was used as a method to quickly evaluate successful synthesis of AuNPs and functionalization of the cores. The former would measure the absorbance between 440–560 nm, specifically investigating the intensity of the SPR wavelength and 450 nm. If the ratio of absorbance was A_{spr}/A_{450} ~1.62 and A_{spr} was 518 nm, this would indicate that most of the cores were 15 nm in diameter. This would be corroborated by directly measuring the core samples by TEM and DLS. Once the core sizes were measured, the tabulated molar absorptivity coefficients (ε) described by Haiss *et al*. were used to standardize the samples for SPR binding by describing them as a molar concentration (M) in accordance with the Beer-Lambert law (Table 4.3).

During the functionalization process, the SPR wavelength should remain constant. If the particles were not sufficiently coated with either mAb or PEG, they become unstable and aggregate, and the overall concentration of that sample decreases. Additionally, the post-functionalization supernatants were measured for any unbound protein using a BCA protein assay kit (Pierce™) to corroborate for successful conjugation to the AuNP surface.

The maximum number of PEG_{2000} or thiol-mAbs expected to coat the 15 nm AuNPs were calculated independently, where we expect ~700 PEG molecules or 26 mAbs, respectively. By knowing these maximum values and describing them "100% coated", we can then appropriately dilute those coating concentrations for subsequent formulations as to functionalize with minimal excess of either reagent. Furthermore, the increase in molecular weight between a functionalized and non-functionalized AuNPs is negligible (< 1.1%, Table S4.2), which allowed us to focus on the magnitude of response between AuNPs and the dependent variable (equivalent amount of mAb) and correct those responses with the expected valency of the AuNPs (0.5 per mAb per AuNP with respect to binding PD-L1).

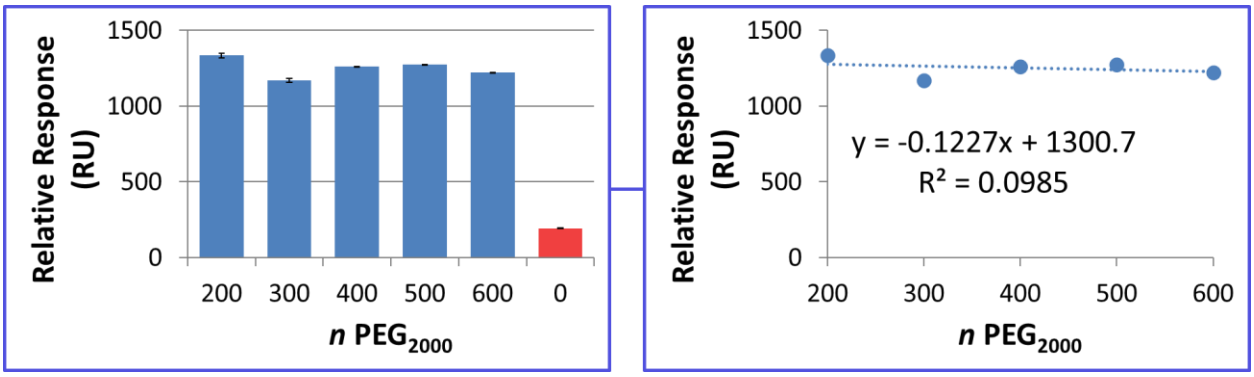

Figure 4.16. Varying the amount PEG_{2000} per AuNP, when functionalizing with a fixed 25 mol eq. GSH-mAb. The""0" sample is the response of unbound GSH-mAb at the same concentration used to functionalize the particles. Each sample of particles was measured by UV-vis correlating the A_{spr} peak with concentration and diluted in HBS-EP+ to 3.61 nM, such that the responses could be compared.

Table 4.3 Concentration of AuNPs determined by UV-vis spectroscopy. The particles are functionalized with PEG_{2000} of varying amounts and a fixed concentration of GSH-MAB to determine if the polymer concentration was deterring mAb accessibility. These particles were then concentrated and resuspended in 500 µL fresh HBS-EP$^+$ running buffer and then diluted to the lowest appropriate concentration (3.6 nM) such that all samples could be compared by SPR as shown in Figure 4.16. The number of PEG_{2000} molecules to coat 15 nm AuNPs was described previously by Rahme *et al*. and was used as the upper boundary to wholly coat AuNPs.[282]

Sample	*n* PEG_{2000} (%-Coating)	A_{spr} (nm)[b]	[C] (nM)[19]
1	0 (0%)	528	0.00972[a]
2	100 (14%)	522	0.565
3	200 (29%)	522	1.39
4	300 (43%)	522	3.61
5	400 (57%)	522	5.33
6	500 (71%)	522	5.41
7	600 (85%)	519	5.42

Notes: When polymer amount was greatly reduced, more gold aggregates (plaques) had formed during the centrifugation resulting in visibly less AuNPs. Similarly, the observed 9.7 pM "f-AuNPs" (0 PEG, 25 mAb) is considered 100% mAb only, which also resulted in plaques of gold with no function. [a]These particles had little absorbance intensity and mostly plaques on the bottom on the centrifuge tube.[b] The absorbance intensity of the SPR peak is correlated with the size of the core, and assumes all particles are uniform as described by Haiss *et al*.

Pre-mixing Times Do Not Affect Functionalization – with the growing concern that PEG-SH was desorbing GSH-mAb (Figure 4.17), we investigated whether the stabilization period and order of addition affects functionalized particles (i.e., PEG first or mAb first). By allowing the AuNPs to exchange citrate with GSH-mAb and *then* PEG, we thought that this would reduce desorption. However, our results indicated that PEG does not appear to affect adsorption of GSH-mAb (Figure 4.18). We compared both a high and low concentration of PEG_{2000} (600 mol eq. and 300 mol eq. respectively) and let the mAbs incubate for up to 3 h before adding the stabilizing agent, and still observed no difference in response. Interestingly, this series also yielded the highest overall activity in all previous batches. The sample not shown in Figure 4.18 (300 mol eq. PEG_{2000} added 30 min the mAb) could not be measured in this series as the SPR instrument was at capacity.

These SPR runs are still only individual samples and the bars shown are representative of the noise in a sample. To evaluate the missing sample, the experiment would need to be re-run entirely. One sample flowed across multiple surfaces shows the average binding of the sample, but this does not show the robustness in the formulation. The significance of binding could be determined by independently reproducing the synthesis of the particles and their functionalization. As these were scouting conditions with the intent to maximize antibody-binding and particle stability, these averaged sensorgrams were sufficient to indicate if functionalization/desorption was occurring. Future formulation work will be more closely monitored, as then we could assess the consistency in the formulation more confidently, rather than just assessing if functionalizing is occurring qualitatively.

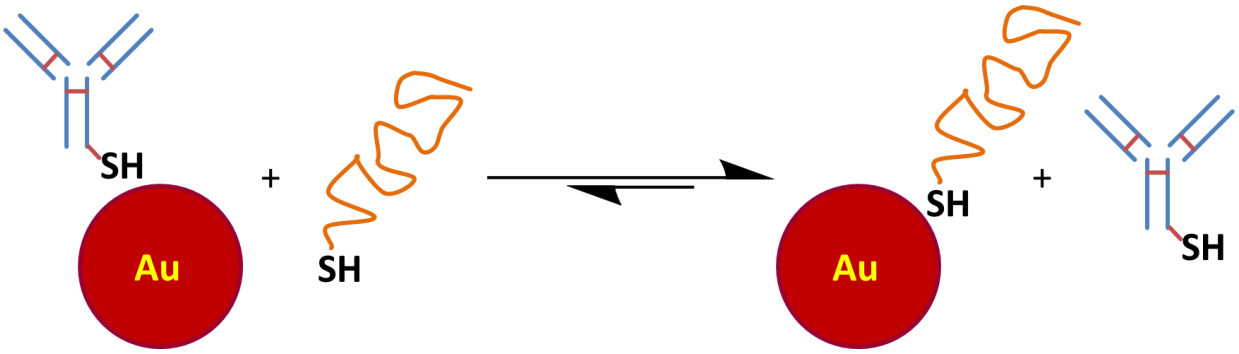

Figure 4.17. Adsorbed thiol exchange on gold core surface. We were concerned that the PEG-thiol could be desorbing the thiolated antibodies, due to higher concentration, which is why we were not observing proper functionalization. The smaller PEG, relative to the bulky protein, at higher concentrations could have negative effects of desorbing the antibodies. This led to the development of increasing thiol content on the mAbs. Higher thiol per mAb could reduce desorption by PEG-SH.

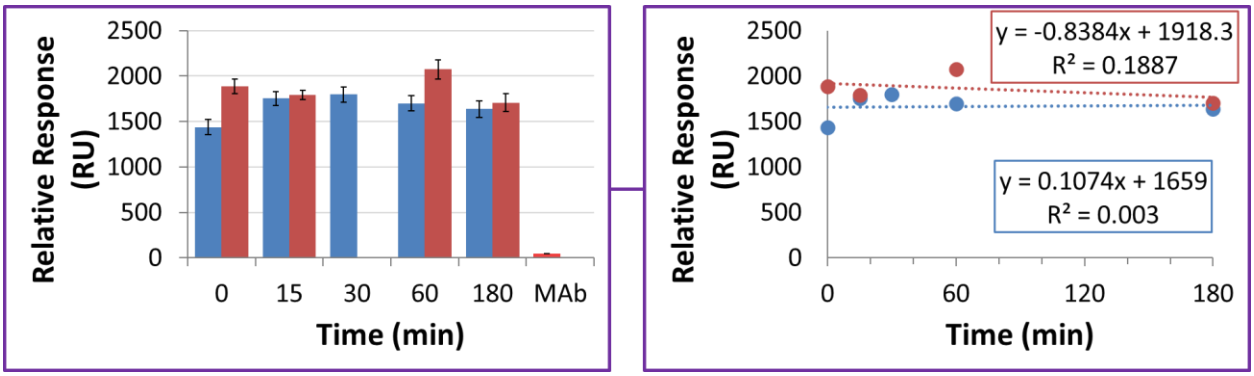

Figure 4.18. Two sets of *f*-AuNPs were investigated for GSH-mAb stabilization, where 25 mol eq. GSH-mAb was allowed to exchange with citrate-coated particles for a fixed duration before adding 300 mol eq. (red) or 600 mol eq. (blue) PEG_{2000}, indicative of 48% and 97% coating, respectively. The responses of the particles are in respect to the equivalent amount of free antibody (mAb).

Changing Polymer Length – increasing the polymer length should increase stability of particles by physically increasing the distance between gold cores to prevent aggregation. However, this may also reduce antibody activity as the longer polymer size can occlude the surface availability for the antibody to functionalize the particles. However, when trying to investigate these conditions by synthesizing new particles, we saw "negative" binding occur (Figure 4.19).

Despite not observing any response in the SPR experiments, we maintained the use of PEG_{2000} in the formulation, but this may be subject to change in future work as these variables have still not been investigated for optimization. Using smaller PEG chain lengths should improve activity of the antibody, by having the targeting agent be more accessible and would show higher binding response in the SPR approaching the Golden Ratio. Conversely, reducing the spacer length between cores there would be more reliance on the antibodies to prevent aggregation rather than the spacer, where mAbs were previously found to be poorer stabilizing agents at higher coating concentrations (Samples 1–4 in Table 4.3).

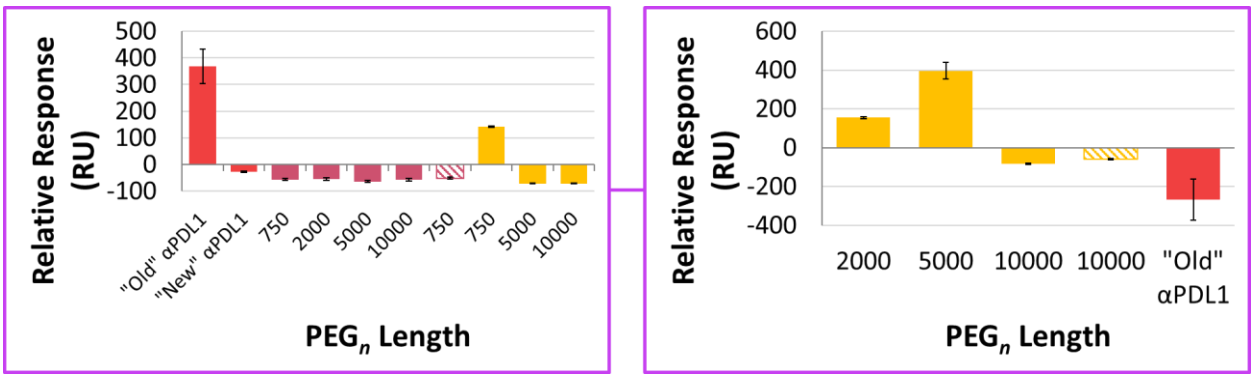

Figure 4.19. Fixed formulation of two *f*-AuNP particle sets with 25 mol eq. GSH-mAb with either 600 mol eq. (purple/red) or 300 mol eq. (yellow) PEG of varied chain lengths to indicate if chain length affects mAb activity post-functionalization. Hashed data are AuNPs only covered in polymer to display non-specific binding events. The apparent negative response is based on the instrument subtracting the reference and the sample response. However, non-specific binding events, and differences in the buffer can cause a large change in the refraction indices, thus resulting in the negative response. The "old" and "new" αPDL1 are two different batches of GSH-mAb conjugates.

The primary purpose for PEG in our system is to provide a biocompatible steric barrier to prevent gold core aggregation. We use a modified version of this polymer that contains a thiol to adsorb to the gold. When adsorbed onto the surface, it has a relatively tight packing footprint that also precludes other thiols from adsorbing. By reducing the chain length, we are reducing the volume of capacity the polymer has on the surface, requiring an increase in the amount of PEG needed to stabilize the gold surface, which would also occlude other molecules from adsorbing. The trends depicted by Sebby *et al*.; Xia *et al*.; and Rahme *et al*. had shown that smaller PEG lengths had more efficient packing densities, and conversely larger PEGs had worse packing efficiency.[282–285] We found that based on these values, we can estimate that the total number of PEG per AuNP is ~700 PEG to totally cover 15 nm AuNPs and this was used proportionally.

Unfortunately, when the response is "negative" it is often indicative of an incompatible buffer (red bars, Figures 4.19, 4.20) attributed to a difference in refractive indices between the flowed sample and the reference. The SPR is sensitive enough to detect discrepancies in composition between the two flow cells, where an additive like DMSO may affect the attenuation that reaches the detector. We saw no trend between AuNPs using 600 mol eq. PEG and 300 mol eq. PEG at varied lengths. There is increase in response when comparing 300 mol eq. PEG_{5000} AuNPs to the PEG_{2000} formulation, however this is more likely due to the overall change in mass of the particle rather than an increase in the degree of AuNP functionalization (Figure 4.19B, 4.20). Therefore, because we did not see any improvement or change in response when the PEG length was varied, *it indicated that conjugation was still the limiting step to functionalizing the particles.* To reiterate, the primary purpose for the polymer in our system is to provide

a biocompatible steric barrier to prevent gold core aggregation, but the formulation is not limited to strictly PEG alone and future batches may investigate other biocompatible polymers (e.g., PLGA, PCL).[39,43]

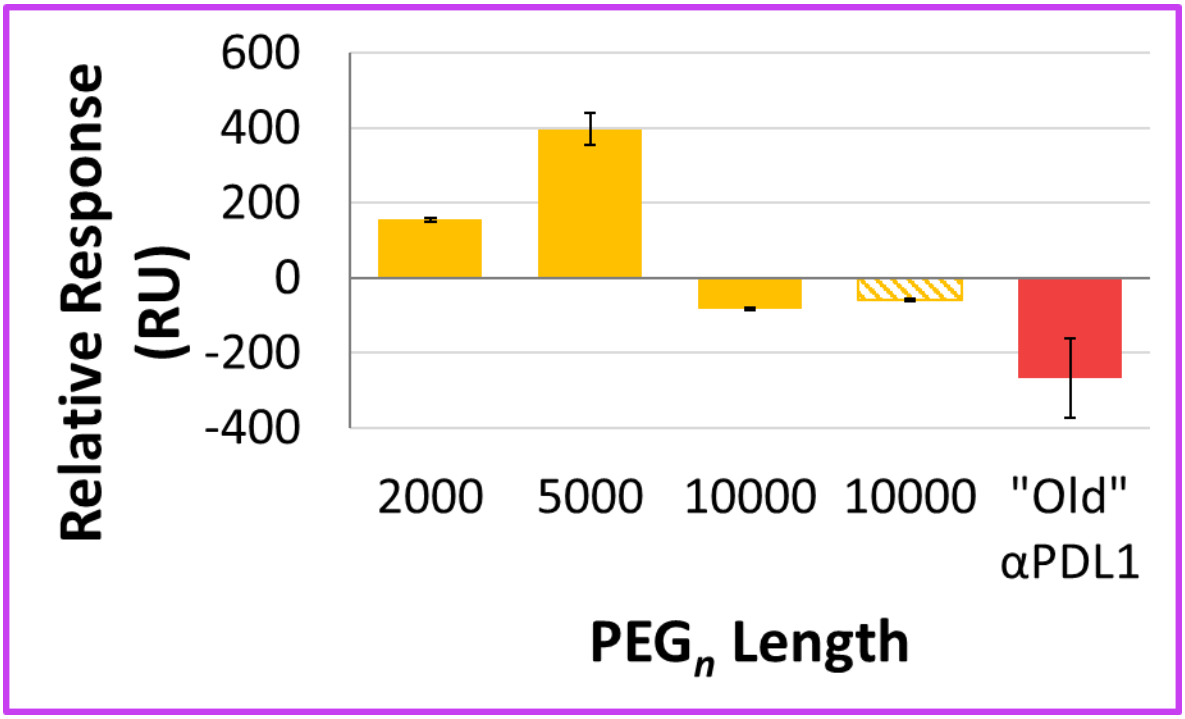

Figure 4.20. Expansion of Figure 4.19, where GSH-αPD-L1 functionalized AuNPs were flowed across a surface of PD-L1. Each sample had a different average PEG MW. All samples expected to have 48% coverage of polymer (300 mol eq.). Hashed data are AuNPs only covered in polymer to display non-specific binding events. The "old" antibody was used as a positive control to assure binding despite showing no binding.

Varying the Core Diameter – increasing the volume of the gold increases the surface area and reduces curvature, which will vary functionalization efficiency. Using a less complex and broader surface could yield better functionalization but will require more materials, which will also scaleup when moving into more complex studies. Of course, the particles are not limited to being delivered as spheres, and other shapes could be investigated for delivery (i.e., nanorods, nanostars).[31,71] For simplicity, we kept using spheres and focused more on optimizing the functionalization.

Increasing the core diameter will increase the resources needed to sufficiently coat the particles, but there is a physiological limit of 200 nm. This ceiling helps establish the restrictions for other formulations to abide by, such as optimization of spacer length and core diameter. Consequently, using smaller polymers to coat reduces the distance between cores and thereby those formulations may be less stable. Future particles should not exceed a core size of 50 nm so that they are well below the 200 nm ceiling when functionalized and may be taken into the tumour; this way, formulation optimization can be more target-focused.[10,51,184]

Reducing the Opportunity for Polymerization – the GSH formulation relied on random peptide conjugation between lysine and the two carboxylic chains of GSH (Figure 4.9, 4.21). However, GSH contains an amine which is also capable of self-conjugation and potential polymerization. Strategically simplifying the reaction, by removing the ability for the thiol-containing molecule to polymerize, we

expect better conjugation efficiency to the antibodies. This increase in thiolated antibodies will be reflected by higher binding activity of functionalized particles, and the response should begin to approach the Golden Ratio as more particles bind to the PD-L1 surface.

Increased Thiol Content – one concern associated with stabilization using thiolated molecules to functionalize the gold surface with adsorbed thiols is their state of equilibria, where the greater concentration of unbound thiols will exchange and desorb the previously adsorbed thiols, favouring the species with the smaller footprint (Figure 4.17).

We wanted to improve functionalization of the AuNPs by increasing the thiol content conjugated to the antibody without surrounding the antibody in thiols. By increasing the local thiol content, we expect that the adsorbed antibodies will be less likely to desorb by exchanging with the monothiolated polymer. This should improve stability of the particles post-functionalization.

If the thiol desorption was problematic, we would see less activity of PD-L1 targeting at much higher concentrations of PEG_{2000}. However, we saw no apparent change in activity (Figure 4.16). Similarly, allowing a pre-incubation of GSH-mAb showed no major difference in stability or activity when added at the same time as the polymer or if the polymer was added 3 h later (Figure 4.17). Regardless, by increasing the local thiol content of the mAb, we remove the concern of desorption entirely, as we would expect the higher concentration of adsorbed thiol per molecule would favour remaining adsorbed and less likely to exchange with monothiolated species.

We expect that the equilibrium between adsorbed and desorbed thiols would favour adsorption of non-adsorbed GSH-mAb over desorption and rely on size as the determining factor of stability.[285] Tsai *et al*. found that smaller thiol molecules (e.g., mercaptopropionic acid) were more likely to desorb PEG-SH,[286] and this similar effect of PEG-SH desorbing the larger mAb maybe be occurring too. Therefore, by increasing the local thiol-content on the antibody we can improve the stability of the functionalized particle-conjugate without fear of desorption by the smaller thiol species (i.e., PEG-SH desorbing mAbs).

The reason for why this could be a concern is that formulation coats our particles in slight excess (e.g., 110%-coating = 35% mAb + 75% PEG) with respect to the total AuNP surface area. This is done to assure that every particle is sufficiently coated. The upper boundaries of each molecule to wholly cover 15 nm AuNPs in PEG_{2000} or mAb are 700 and 26, respectively (determined earlier in Table 4.1). These upper limits are then scaled to accommodate the remaining surface area. Once a more stable mAb conjugate is developed, it would be suitable to try re-optimizing the formulation to wholly characterize the distribution of functionalized particles, rather than using this generalized method. This could also establish if there was a desorption problem.

Increasing Sulfur per Antibody

By increasing the thiol content per mAb we could provide a stronger affinity to the gold surface during functionalization, and less likelihood of destabilization due to desorption of our antibodies. The synthesis of a novel *tris*-thiol compound **21** was proposed (Scheme 4.3), but unfortunately was not pursued. A commercially available disulfide was sought as a successor for the thiolation of mAbs.

α-Lipoic Acid Conjugation of αPD-L1

As the efforts to achieve installation of three sulfur atoms were proving difficult, we also looked towards conjugating to simpler molecules. The criteria we hoped to achieve were the following:

1. Biocompatible and generally non-toxic – we intend to make a drug for clinical use, toxic compounds should be avoided as much as possible.
2. Capable of peptide conjugation, but not polymerizable – ideally a molecule only one site for EDC/NHS peptide coupling.
3. More than one thiol – polythiols are expensive, but disulfide bridges are quite stable when adsorbed to Au surfaces.[287,288]
4. Easier to process – no longer requiring the additional reduction step in conjugate processing and purification.

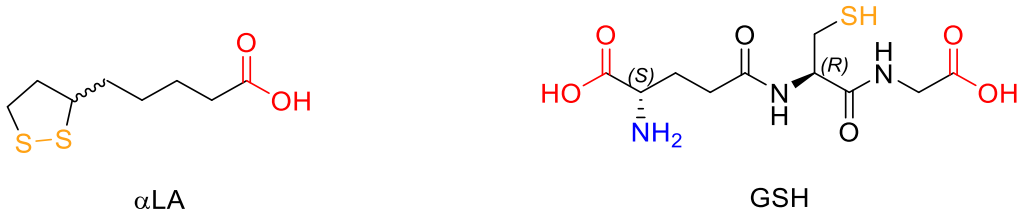

Figure 4.21. Structures α-lipoic acid (αLA) and glutathione (GSH). The sites of conjugation with EDC/NHS are highlighted in red, sites of self-conjugation are highlighted in blue, and thiols are highlighted in yellow. This highlights the simplicity of αLA compared to GSH with one conjugation site and higher thiol content.

Interestingly, due to points 3 and 4, we were not limited to processing/producing thiols and that disulfides would be a suitable alternative. One molecule that met all the above criteria was alpha-lipoic acid (αLA), a hydrophobic metabolite, which required reoptimizing the conjugation conditions to the mAb.[283,289] Initial trials investigated the *in situ* conjugation to maintain the processing and compare activity directly between GSH and αLA conjugates, still using the same 25 mol eq. mAb and 600 mol eq. PEG_{2000} formulation. However, we saw slight variation in coupling efficiency between *in situ* formation of the NHS ester with either molecule. We aimed to rectify this by isolating the αLA-NHS ester (**22**) to simplify the conjugation conditions, where a more reactive intermediate reacts directly with the commercial antibody, rather than expecting to generate the intermediate under the previous conditions (Scheme 4.2).

Compound **22** was synthesized as described by Shi *et al*., where we obtained 78% in high purity (observed by ^{1}H NMR and ATR-IR lacking characteristic carboxylic acid peaks in their spectra; Materials & Methods).[290] Purification of the conjugates was also simplified at this stage, where larger batches of mAb conjugates were dialyzed with the same 3 000 MWCO to remove any unbound αLA and NHS. The conjugates would then be used to coat AuNPs, expecting that the higher purity mAbs would result in a

greater success of achieving saturation when characterized by SPR, resulting in a response emulating only the magnitude between the MW of the *f*-AuNPs and the equivalent amount of mAbs, the Golden Ratio.

We found that by isolating the NHS ester (**22**) we could obtain better coupling and therefore better functionalization overall (Table 4.4). In the end, a stock solution of αLA-NHS (**22**) between 1–5 mg/mL dissolved in anhydrous DMF was most appropriate for long-term stability and solvation, which may be diluted further into compatible buffers for protein conjugation. This process is also inherently safer from a drug development perspective, as it removes the peptide sensitizers (e.g., EDC, HATU) and their urea byproducts as risks, and still achieves the intended outcome while being a fully characterizable and isolatable intermediate for other work.

The αLA-mAbs were prepared by mixing a solution of αPD-L1 (0.5 mg/mL) in excess αLA-NHS (20% v/v DMF). The reaction was then dialyzed to remove the small molecules by using a semi-porous 3 000 MWCO membrane with a 1:400, twice for an effective 160 000× dilution. This dilution is necessary to reduce the amount of organic solvent. After one dialysis, the %v/v DMF is expected to be 0.5%, but to reduce the high concentration of αLA and derivatives, more dialysis is required to help dilute and exchange the mAb conjugates into appropriate buffers while removing the smaller molecules. The concentration of the antibodies is measured using nanodrop A_{280}/A_{260} with the same absorptivity coefficient for general IgGs and this concentration was used to proportionally coat the gold cores.

The αLA-mAb was used to functionalize AuNPs, with a similar 25% coating formulation as described before, where the concentration of mAb needed is used to coat all particles sufficiently (assuming 100% conjugation), and the remaining 75% of all surface area was PEG_{2000}. We investigated the processing of various forms of αLA-conjugates (Table 4.4) and observed the following binding responses by SPR to characterize their activity.

Table 4.4. Varied modes of conjugation to improve thiolation content on our αPD-L1 antibodies (initial concentration 0.5 mg/mL). The response was measured by SPR in two separate cycles across a surface of biotinylated-PD-L1. The responses were normalized with respect the response of unmodified (fully active) mAbs at the same effective concentration. The particles were formulated under the assumption of "25%" coating which is equivalent to ~5 mAb per AuNP with our previous theoretical maximum. The core size of this batch 16.5 nm as measured by TEM in Table 4.6. The total maximal response expected for 100%-coated functionalized AuNPs is 183-fold, therefore 25% should be 46-fold.

αLA-Conjugation Mode	Response Relative to Equivalent Free mAb measured by SPR.	% Activity (if all particles were considered active)	Expected %Coating of mAb-thiol
In situ (One pot)	0.48 ± 0.05	0.26	25
2300 mol eq. αLA-NHS	**40 ± 0.1**	22	25
1100 mol eq. αLA-NHS	24. ± 0.06	12	25
Unreacted (non-thiolated mAb)	27. ± 0.05	15	25
Sulfo-NHS ester (*in situ*)	7.5 ± 0.08	4.1	25
PEG Only	0.08 ± 0.3	0.044	0

Due to the solubility problem that αLA imposes relative to GSH, as it possesses much more aliphatic character, we looked at whether our *in situ* conjugation was remotely effective. The response being less than the equivalent of free mAb affirmed poor conjugation, likely due to insolubility of the acid. The negative control AuNPs (PEG only) showed a limited response indicative of nonspecific binding between the polymer and PD-L1. Both sets of isolated αLA-NHS esters (rows 2 and 3) had shown significant binding responses, nearly an order magnitude higher than our previous best (~4-fold). Both of these cases where compound **22** was conjugated with antibodies had responses that reflect a large population of the AuNPs are functionalized with the thiolated antibodies. For row 2 it is 87% of the expected maximal response, and 52% of the total response expected from the formulation in row 3 of Table 4.4.

The unreacted mAbs (Row 4, Table 4.4) also showed a respectably high response (27-fold greater than free antibody alone; 59% activity), however these particles were unstable and had a much shorter shelf-life. This could be attributed to the binding occurring on the AuNP surface, where without the thiols, there is a weaker carboxylate adsorption on the surface, which may freely exchange with other molecules. We suspect that we saw a large but short-lived response, due to the mAbs likely desorbing from the particles, which then began to agglomerate. This was noticed by seeing the concentration of the *f*-AuNPs decrease over time as small black plaques formed near the bottom of the Eppendorf tubes.

Using a more hydrophilic analog, the sulfo-NHS ester (which was also generated *in situ*) did result in a nominal higher response compared to row 1. This highlights that αLA solubility was a problem for successful conjugation to the mAbs. Both rows 1 and 5 also relied on peptide coupling agents, where these additional parameters hindered successful formation of conjugates, thus the lower binding responses.

In both cases of isolated NHS-esters (rows 2 and 3) the response is quite high, and the particles were stable without any visible aggregation or plaque-formation in the tubes for up to 6 months. The overall expected response for these particles, still assuming 100% coating of all particles, was 183-fold that of unbound antibody. In these series, our AuNPs are formulated assuming that 25% of the total surface area is functionalized with antibody. The highest response our particles exhibited was 40-fold higher than equivalent antibody, which is just short of 25% of 183, indicating a high degree of functionalization and antibody activity using this NHS-ester method. In the lower stoichiometry sample (row 3), there is still a respectable response (24-fold greater than free mAb; but it half as efficient overall). This lower overall response could be due to poorer conjugation efficiency, and further optimization may be required.

Conclusions and Future Work

Regardless, the 25%-coating formulation using αLA-NHS to conjugate the mAb achieving responses that were 88% of the expected maximum, indicating a high degree of successful particle binding to PD-L1. This formulation was transitioned into cellular studies to elucidate whether the inhibition of PD-1/PD-L1 observed in Figure 4.6 would be selective in cells and capable of possible recovery for immune exhaustion.

While not all variables on the Wheel of Functionalization were fully investigated, the high degree of functionalization indicated our current formulation was appropriate and stable to move into cellular work to determine the selectivity and possible recovery from T cell exhaustion. Some variables may not be investigated until full cellular work has been done to establish a baseline of toxicity, selectivity, and efficacy of the current formulation.

5. Preliminary T Cell Recovery with Functionalized Gold Nanoparticles and Proposed Future *In Vitro* Endeavours for our Nanoparticles

Foreword

After determining an appropriate formulation for the AuNPs to target PD-L1, we sought to determine whether the competitive activity of the antibody, when functionalized onto the core, could be used to recover exhausted T cells, allotting an immunotherapeutic function. This chapter discusses the development and characterization of naïve lymphoblasts, Jurkat cells (ATCC® TIB–152™), and their artificial stimulation with PHA, their apparent suppression of stimulation with PD-L1, as well as their apparent recovery when the PD-L1-targeting AuNPs are present. These *in vitro* experiments are used to reinforce the potential immunotherapeutic efficacy of the *f*-AuNPs, rather than just a deliverable platform, as the particle may be blockading the PD-1/PD-L1 interaction, thus removing the immunosuppressing effects. The relevant supplementary data are found starting on page 209.

The intent of this chapter was to investigate the immunotherapeutic effect of the PD-L1-targeting AuNPs by directly measuring T cell recovery in a simple and controlled environment. Further investigation would use the observed effects as guidelines to elucidate T cell recovery in a more biologically relevant scenario such as co-mingling the Jurkat cells with a PD-L1-presenting cancer cell line similarly described by Aurigene in Chapter 2.

Immunostimulation is used to induce the transcription of pro-inflammatory genes by stimulants emulating antigen-presenting cells (APCs), which then activates certain naïve white blood cells into mature killer cells. We attribute the evidence of T cell maturation to a high cell density, indicative of induced proliferation and the presence of pro-inflammatory cytokines.[291,292] When in the presence of checkpoint proteins, such as PD-L1, this pro-inflammatory activity is noticeably suppressed.[202,203] We employed Jurkat cells as surrogate naïve white blood cells that upon stimulation will mature accordingly to express PD-1,[145,293] and proinflammatory cytokines (i.e., IL-2 and IL-6).[294,295] We expect stimulants, such as PHA, PMA, or αCD3/αCD28, will induce proliferation and will reflect the higher cell activity with a much greater cell density when measured the following day with a hemocytometer, with respect to their unstimulated cohorts.

Jurkat cells were chosen to model the immature immune cells, where previously shown in the literature they may produce proinflammatory cytokines (i.e., IL-2, IL-6) upon exposure to stimulating agents like PMA/ionomycin or PHA.[291,295,296] These lymphoblasts are imperative to modeling T cell recovery as they do not produce PD-1 unless in a proinflammatory state. Therefore, we wanted to investigate potential immunotherapeutic recovery from PD-L1-induced inhibition, by measuring the cell densities attributed to these on/off states and showing their respective recovery due to the presence of *functionalized* AuNPs.

Although we could not directly detect proinflammatory cytokines by ELISA indicative of T cell activation and maturation, we monitored the cell densities under stimulating and basal growth conditions and eventually adding PD-L1 to prevent stimulation. Then by introducing functionalized AuNPs to these conditions, we thereby allowed for continuous PHA-induced proliferation in the presence of PD-L1, indicating the prospective value of the functionalized particles as immunotherapeutic agents. Furthermore, non-functionalized particles were used as a control to elucidate whether the sub-pM concentrations may be intrinsically toxic to the cells, but yielded no significant effect on the proliferating cell densities.

Much of this work revolved around the optimization of stimulating naïve Jurkat cells so that we could observe immunosuppression by PD-L1. This resulted in three control populations *prior* to any characterization with our *f*-AuNPs. The controls are unstimulated basal growth, to determine the baseline of "regular" cell division; stimulated growth, which should show a significantly higher cell density; and immunosuppressed, where addition of PD-L1 turns down stimulation, to demonstrate that the checkpoint protein (PD-1) prevents the proinflammatory response, which results in a lower cell density. To validate recovery, we anticipate that the presence of PD-L1-targeting AuNPs will have cell densities similar to the uninhibited stimulated growth control, and conversely, non-targeting AuNPs should no show difference in the cell density to the inhibited stimulate3d growth control. However, if these populations were significantly lower it may indicate toxicity of the core,[11,297] and if the cell density was much greater it may indicate some form of immunogenicity.[298]

We did not perform the control of non-functionalized particles incubated with naïve Jurkat cells. We expect this population would have no significant difference in cell density compared to basal growth. This would otherwise indicate that the gold core is itself antigenic to the white blood cells and its own possible stimulant. This control was ignored as the "stealth" polymer PEG-coated AuNPs should not warrant any immunogenic response.[24,44,98]

Materials and Methods

1. T Cell Growth Conditions

Jurkat E6.1 cells (ATCC® TIB-152™) were grown in RPMI 1640 (Gibco) media supplemented with 10% FBS (Gibco), and 1% Penicillin/streptomycin. Passages were seeded with a final density between 50 000 – 100 000 cell / mL every two or three days at 37 °C, with 5% CO_2. The day before stimulation, cells were passaged as normal and then topped up with an additional 5 mL complete growth media and grown to a density of 5 000 000 cell/mL. If the density was much below 5 000 000 cell/mL, cells are concentrated using Allegra X-12R centrifuge at 400 rpm for 10 min, removing the supernatant and resuspended in complete growth media to the expecting concentration, and validated by counting using a hemocytometer under a light microscope.

2. T Cell Stimulation Conditions

Jurkat cells (ATCC® TIB–152™) were seeded at $5{\cdot}10^5$ cells per well in a 24-well tissue culture plate. An aliquot of 10X PHA (50 µg/mL) with a final concentration of 4.5 µg/mL was added to all wells, except the basal growth control (RPMI 1640, 10% FBS, 1% Pen/Strep) which was complete media to accommodate the volume of the stimulant so that all wells had the same volume and initial cell density. The cell culture plate was incubated overnight at 37 °C, with 5% CO_2.

Naïve white blood cells have an endogenous expression of PD-1 and PD-L1 to reduce auto-immunogenic effects (i.e., self-attack). The Jurkat T cells were primarily activated by PHA, which binds to the T cell receptor (TCR), emulating stimulation from antigen-presenting cells (APC) as to upregulate expression of PD-1, as well as pro-inflammatory cytokines.[232,299,300] Upon activation, naïve lymphoblasts become more specialized and begin proliferating rapidly. Alongside the higher expression of immune response checkpoint proteins, T cell activation induces the proliferation of recognition proteins like cytokines.[100,301] Therefore upon stimulation, we expect to see higher rates of cell division through cell counts and this stimulation can be validated by the presence of pro-inflammatory cytokines (i.e., IL-2, IL-6).

Common methods of stimulation *in vitro* are through targeting the T cell receptor (TCR) or downstream kinase cascade. The three methods of T cell activation that were investigated to optimize stimulation were an αCD3/αCD28 antibody cocktail[145,292,299] or phytohemagglutinin (PHA),[292,298] both of which target the TCR directly, and PMA (palmitoyl myristyl acetate), which is a diacylglyceride mimic that induces the downstream signal transduction.[291,292,295] Each of these methods have been shown to induce T cell activation in Jurkat cells (a human lymphoblast cell line) and should therefore also co-induce production of cytokines, if the white blood cells are truly "activated". Under stimulation, the white blood cells proliferate rapidly, indicating a higher overall cell density when measured the following day.

Through optimization, we found that PHA was most consistent at eliciting higher cell density attributed to T cell activation when measured the following day by hemocytometer. We therefore expect higher expression of PD-1 upon maturation from T cell activation. Although we never measured PD-1 expression directly, we established that the cells were "stimulated" due to their apparent inactivity when immunosuppressing PD-L1 is present. More optimization details involving T cell culturing and stimulation conditions are described in the Supplementary section on starting on page 209–212.

3. Measuring T Cell Activation by Hemocytometer

After treating the cells with their respective stimulant and incubating overnight, samples were read the following day via hemocytometer. A micropipette was used to perturb and homogenize wells before aliquoting onto the hemocytometer. At least two sample reads were required, which consisted of at least 5 large squares, ideally one from each quadrant. If a large square was counted and exceeded 100 cells, the smaller squares in the center were counted to save time.

Unfortunately, there is no viability data, as classic staining technique for cell counting (i.e., Trypan Blue™) induces cell osmolysis as described by Chan, Rice, and Qiu, and therefore we must assume that all cells are alive.[302]

Once cell count conditions were optimized, seeding and stimulation of two or three wells per cell line per stimulant were counted to obtain biological replicates of our populations.

4. Synthesis of αLA-αPD-L1-conjugates

Commercially available α-lipoic acid (αLA, Sigma) was esterified with NHS using DCC conjugation as reported by Koufaki and Detsi.[289] In brief, αLA (300 mg, 1.5 mmol) and NHS (1.6 mmol) were dissolved in anhydrous DCM, and 2.2 mol eq. DCC solution was added dropwise via syringe pump (150 µL/sec) to the reaction mixture. The reaction, initially on ice, was stirred overnight at room temperature. Then, the solute was filtered, and the solvent was removed by vacuum. The colourless NHS-ester product was washed with Et_2O with a yield of 86% and analyzed by ^{1}H and ^{13}C NMR, and ATR-IR.

The antibodies were thiolated with the NHS-ester and used to functionalize the gold particles. The NHS-ester was dissolved in DMF as a stock solution at 3 mg/mL. This stock solution was further dilute in DMF to 25 µg/mL, and this was added to the antibody stock with a final concentration of 5% DMF (v/v). From our previous peptide-coupling experiments, the αPD-L1 (BioXCell) can conjugate with minimal loss in activity. The DMF and excess small molecules were removed by dialysis such that the final concentration of the DMF was < 0.05% (v/v).

The αLA-NHS ester was serially dilute in DMF to a working concentration of 25 µg/mL, and this solution was then diluted in HBS-EP^+ running buffer to 2.5 µg/mL (1.8 mol eq.) in the presence of αPD-L1 (1 mg/mL;

6.6 µM). The reaction mixture was incubated overnight stirring at room temperature. The following day the solution was dialyzed in 200 – 300 vol eq. HBS-EP$^+$ buffer with a 3K MWCO to remove the excess small molecules (e.g., NHS, unreacted αLA-NHS, and DMF). Ideally, there should be minimal change in volume post-dialysis, but the thiolated antibody concentration was determined by A_{280}/A_{260} absorbance and the Pierce™ BCA Protein Assay kit, and validated for binding by SPR.

5. Functionalized Gold Nanoparticle Synthesis and Characterization

Citrate-coated "non-functionalized" particles of an expected diameter of 15 nm were synthesized using the methods described by Xia *et al.*[33] Bare particles were sized by TEM (JEOL 1400) and this size was used to calculate the total surface area in a batch of particles. The core volumes were cross validated for dispersity using DLS (Zetasizer II), by measuring at least three reads of three samples.

To stabilize and functionalize the gold cores, citrate was exchanged with αLA-conjugated αPD-L1 antibody and PEG_{2000}-SH (Nanocs) with an assumed 33% αPD-L1 surface coverage on all particles. The *f*-AuNPs were subjected to 15 000 x g for 20 min, after which the supernatant was removed, and the particles were resuspended in HBS-EP$^+$ running buffer. This operation was performed twice more to remove any unbound molecules by aspirating the supernatant. The particles were validated for functionalization by SPR, comparing the relative response of *f*-AuNPs to the effective concentration of free antibody used to functionalize the particles. Using the MW difference between the theoretical MW of the gold core to the typical MW of an IgG (150 000 g/mol), we confirmed that the particles were appropriately functionalized by comparing the binding response between *f*-AuNPs and free mAbs, and using a non-functionalized AuNP (coated only in PEG) as a negative control to account for non-specific interactions between PD-L1 and the gold core.

The concentration of the *f*-AuNPs was determined by UV-vis as described by Haiss *et al.*[19] using the relation between the measured size by TEM and appropriately associated molar absorptivity coefficient (ε) to attain the concentration in nM, under the assumption the particles are homogenously disperse.

PD-L1-targeting *f*-AuNPs are Capable of T Cell Recovery as Measured by Hemocytometer

Given the success of purposefully inhibiting stimulated Jurkat cells with solubilized PD-L1 shown in Figures S5.15 and S5.17, we attempted to directly reverse these effects by introducing the αPD-L1 antibodies functionalized onto AuNPs and monitoring the apparent recovery over multiple passages (Figures 5.1–5.3).

Each of the following experiments employed αPD-L1 functionalized particles (*f*-AuNPs) to PHA-stimulated Jurkat cells in the presence of PD-L1. We expect that the Jurkat cell densities would remain stimulated when the antibody is present, on a particle or freely in solution, regardless of the presence of PD-L1. This would indicate that the antibody is overriding the immunosuppressive response induced by the PD-L1 protein. We also employed PEG-only particles at similar concentrations as a vehicle control both in the presence and absence of PD-L1. This was done to determine if the gold core has any negative effect on the Jurkat cells during a state of immunosuppression (PD-L1 present), and if the core could be inherently toxic to the Jurkat cells (PD-L1 absent), respectively. Unbound antibodies were used as a positive control for recovery at the concentration expected on the surface of the particles to determine if there is a noticeable decrease in activity. The cell densities were measured the following day, where the wells were mixed with a micropipette before using transferring to count on the hemocytometer. Each treatment condition was prepared independently in three tissue culture wells and measured at least twice by hemocytometer to obtain triplicate data for statistical analysis of the AuNP impact on the stimulated cells.

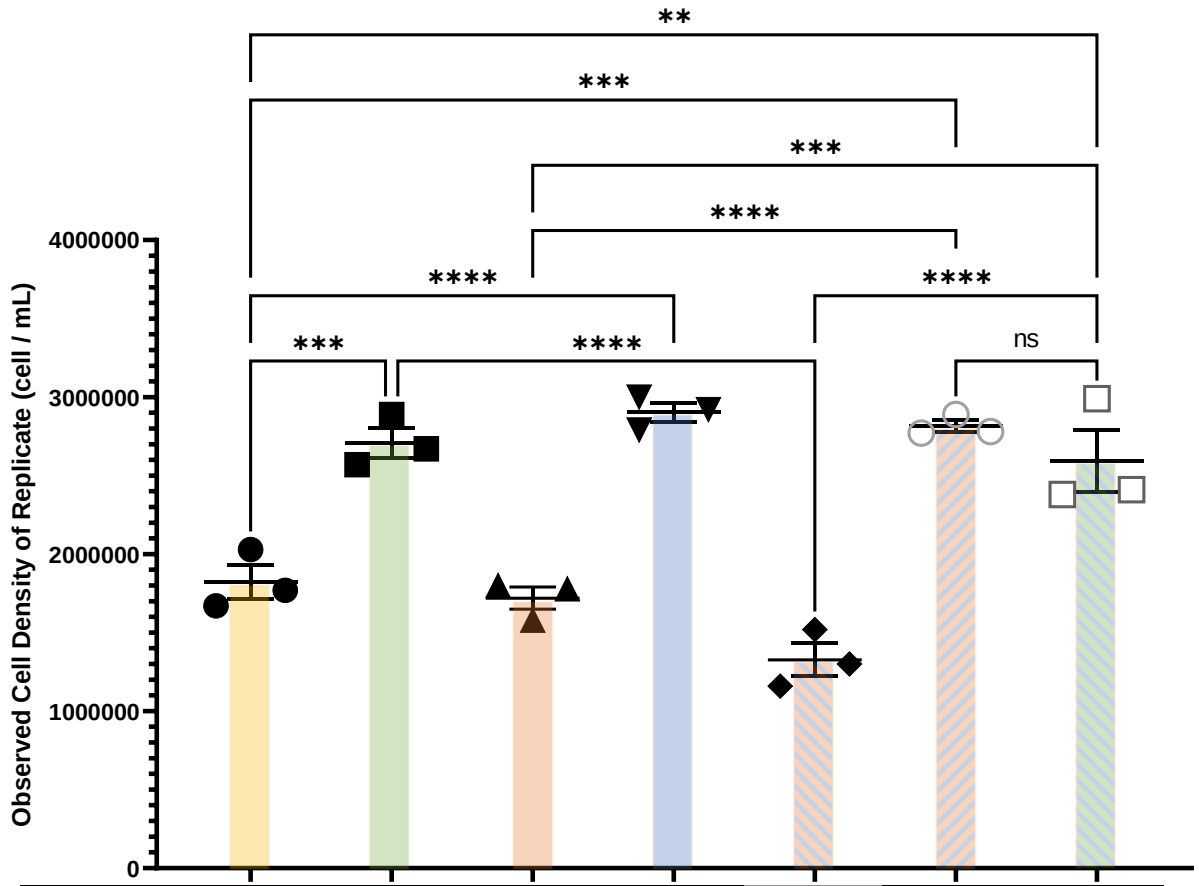

	Basal growth	Stimulated growth	Inhibited growth	Blockade with *f*-AuNPs	PEG NPs (–ve control)	Blockade with αPD-L1	PEG NPs* (core toxicity)
+ PHA	–	+	+	+	+	+	+
+ PD-L1	–	–	+	+	+	+	–
+ *f*-AuNPs	–	–	–	+	–	–	–
+ PEG NPs	–	–	–	–	+	–	+
+ αPD-L1	–	–	–	–	–	+	–

Figure 5.1. Jurkat cells (P6) show promising recovery in the presence of *f*-AuNPs (blue) when stimulated with PHA and inhibited with PD-L1 (32 nM). The table describes the conditions of each column, and each point displayed was the observed cell densities of each well from at least three hemocytometer reads. Hashed columns indicate an isolated variable with respect to the *f*-AuNPs (left: PEG NPs used, gold core only; right: only αPD-L1, no core). The concentrations of the particles were 1.3 nM (*f*-AuNPs), 0.38 nM (PEG NPs), and 0.38 nM (PEG NPs*, –PD-L1). PEG NPs* were gold cores incubated with stimulated Jurkat cells in the absence of PD-L1, to determine if the core had any intrinsic toxicity on the cells. The mAb concentration was 5.7 nM. Bars indicate SEM, *n* = 3. * : P < 0.05, ** : P < 0.01, *** : P < 0.001, **** : P < 0.0001. All comparisons not shown were not significant (ns). All relevant statistical data can be found in Table S5.4.

Despite being unable to detect cytokines by ELISA, the consistently higher cell density indicative of the stimulants constituted strong phenotypic evidence suggesting T cell activation (Figure 5.1, yellow vs. green; Table S5.4, P = 0.0007). This proliferation was also consistently suppressed when the stimulated cells were co-incubated with PD-L1 resulting in cell densities not significantly different from the basal growth control (yellow vs. orange), as was previously observed in Figures S5.15 and S5.17. Upon addition of the *f*-AuNPs (blue), the cell density was not significantly different from the stimulant only cells (green), indicating that the functionalized particles were disrupting the PD-1/PD-L1 interaction and the Jurkat cells

remained stimulated. The same result was observed when the Jurkat cells were recovered using the equivalent amount of unbound antibody (blue and orange hashed bar, right), where there was no significant difference in cell density, indicating that the antibody does inhibit the PD-1/PD-L1 interaction, preventing T cell exhaustion. Moreover, the antibody alone did not significantly decrease the cell density under these "recovered" conditions. This suggests that the antibody was also not intrinsically toxic on the white blood cells at these concentrations. All cases where antibody was used, either in solution or on a particle, resulted in a cell density similar to stimulant-only incubation (green), which was always significantly greater than the densities observed in basal (yellow) and inhibited growth (orange) conditions.

Non-functionalized PEG NPs were used as a vehicle control and had no significant impact on exhausted T cells (Figure 5.1, blue and orange hashed bar, left) when compared to the basal growth control (yellow). Conversely, the PEG NPs similarly had no significant impact on proliferating T cells (blue and green hashed bar) when compared with the stimulated growth control (green). Both experiments indicate that the gold core had no overall impact on the cell density, which would also indicate the gold core is not intrinsically toxic to the white blood cells at these concentrations. There was also no significant difference in cell density between 1.3 nM *f*-AuNPs and 0.38 nM PEG NPs despite the large variance in concentration, which reinforces the biocompatibility of the particles as the core.

The *f*-AuNPs were able to overcome the inhibitory effects of PD-L1 at relatively low concentrations. The concentration of PD-L1 (32 nM) is nearly 6-fold greater than the *f*-AuNPs (calculated from SPR activity and concentration, and the valency of the 25%-coated formulation is expected around ~5, ergo ~6 nM αPD-L1 was the effective concentration used). The PD-L1 concentration was 24.6x higher than the particles, and 2.8x higher than the unbound αPD-L1 (with both epitopes available). Yet both experiments managed to sustain stimulated levels of growth. The cell density of apparent recovery was also not significantly different from uninhibited stimulation indicating that the core is not intrinsically toxic to the white blood cells.

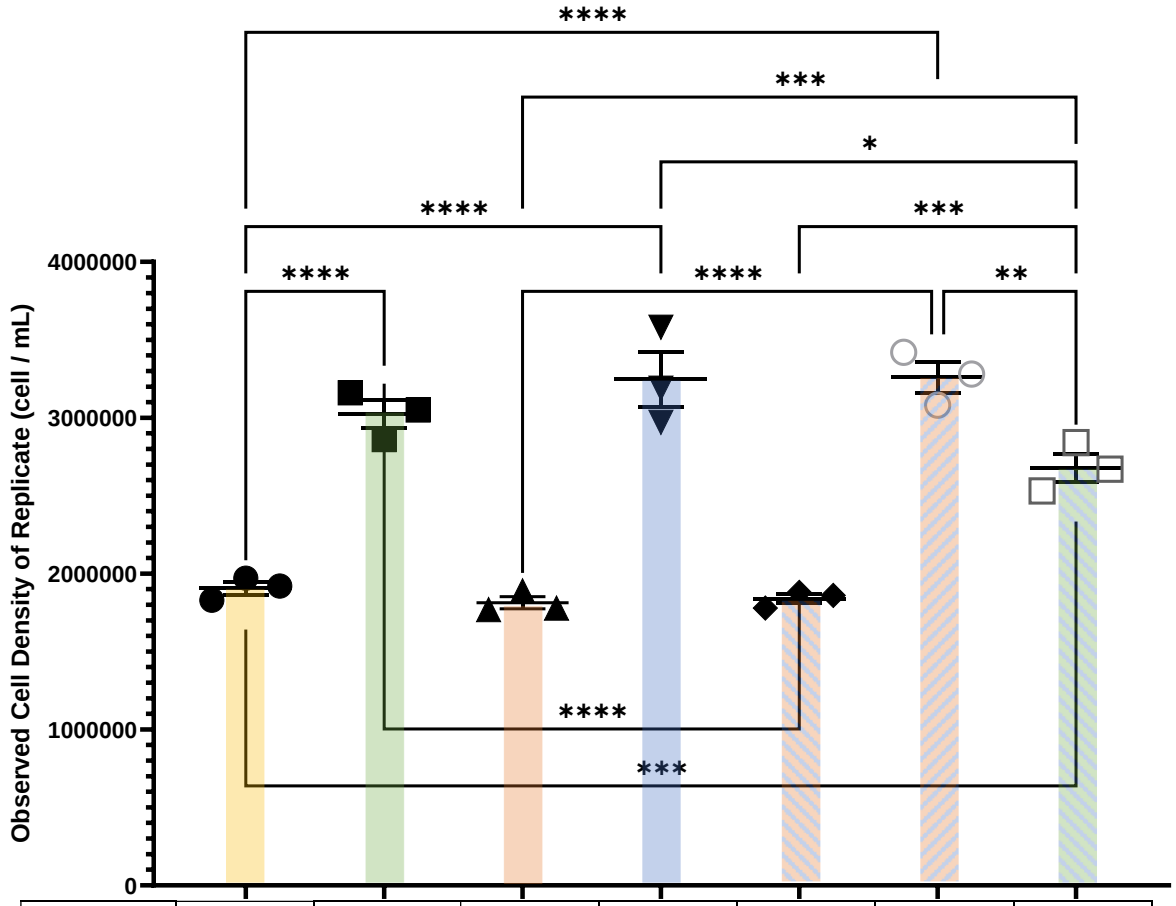

	Basal growth	Stimulated growth	Inhibited growth	Blockade with *f*-AuNPs	PEG NPs (–ve control)	Blockade with αPD-L1	PEG NPs* (core toxicity)
+ PHA	–	+	+	+	+	+	+
+ PD-L1	–	–	+	+	+	+	–
+ *f*-AuNPs	–	–	–	+	–	–	–
+ PEG NPs	–	–	–	–	+	–	+
+ αPD-L1	–	–	–	–	–	+	–

Figure 5.2. Jurkat cells (P9) continue to show promising recovery with *f*-AuNPs (blue) when stimulated with PHA and inhibited with 32 nM PD-L1. At a relatively high concentration, the PEG NPs shown a significant effect at reducing the proliferation of stimulated Jurkat cells (left hash, blue and green) indicating possible toxicity. The table describes the conditions of each column, and each point displayed was the observed cell densities of each well from at least three hemocytometer reads. Hashed columns indicate an isolated variable with respect to the *f*-AuNPs (left: PEG NPs used, gold core only; right: only αPD-L1, no core). The concentrations of the particles were 0.46 nM (*f*-AuNPs), 0.61 nM (PEG NPs), and 1.8 nM (PEG NPs*, –PD-L1). The mAb concentration was 5.7 nM. Bars indicate SEM, $n = 3$. * : $P < 0.05$, ** : $P < 0.01$, *** : $P < 0.001$, **** : $P < 0.0001$. All comparisons not shown were not significant (ns). All relevant statistical data can be found in Table S5.5.

This pattern remained consistent when the experiment was performed again at a higher passage number (P9) as shown in Figure 5.2. In this case, we used approximately 3-fold fewer *f*-AuNPs and still observed the cell densities equivalent to the stimulated growth control (green). This continues to highlight the potency of the AuNPs disrupting the PD-1/PD-L1 interaction, even in relatively high PD-L1 concentrations. To complement the varied concentration comparison with varied particles, we varied the vehicle control

concentrations to scout for possible core incompatibilities. We omitted the experiment using *0.61 nM* PEG NPs (+ PHA, – PD-L1), as we expected this would result in a cell density not significantly different than with stimulant alone (green), and with the limited resources chose to scout for possible toxicity. By using a relatively higher concentration under those same stimulating conditions, we may observe if the cell density was impacted.

The observed cell densities of stimulated Jurkat cells incubated with PEG NPs (Figure 5.2, blue and orange hashed bar, left) was significantly lower when compared with experiments that used αPD-L1 to disrupt the PD-1/PD-L1 interaction (vs. blue, P = 0.0104; vs. orange and blue hashed bar, right P = 0.0087; Table S5.5), and these lower densities were not significantly different from the basal (vs. yellow) and PD-L1 inhibited (vs. orange) controls. This indicated that the gold core was not toxic at sub-μM concentrations. However, there was a significant decrease in cell density in all cases when the core concentration was increased to 1.8 nM (Figure 5.2, blue and green hashed data). This could suggest that the higher concentration of gold could be negatively affecting the T cell proliferation.

The 3-fold increase in concentrations of PEG NPs was used to scout whether the higher concentration of particles could have debilitating effects on stimulated growth. Instead of a comprehensive titration, which is resource intensive, we focused on the "fail-fast" approach to scout for effects of toxicity. By omitting experimental controls that are safely anticipated (i.e., expecting that 0.61 nM PEG NPs will *not* significantly impact proliferation, regardless of PD-L1 presence), there is more opportunity to focus on the variable itself (e.g., "could *this* concentration effect proliferation", rather than "at *which* concentration is proliferation effected"). As the higher concentration did impact the cell density, this would be imperative to investigate further and characterize the concentration at which the AuNPs do affect stimulated cells.

However without a comprehensive titration to characterize the Jurkat cell viability with and without functionalized cores, it is difficult to determine if the core was truly toxic or impacting the proliferative signal of the PHA.[302] Furthermore, the previous *f*-AuNPs recovery (1.3 nM; Figure 5.1) did not show any significant change in cell density to the stimulated Jurkat populations (green). This may suggest that concentrations > 1.5 nM AuNPs per 100 000 cells may be problematic in future pharmacodynamic studies, and caution should be taken if bioaccumulation may lead to these higher effective concentrations.

The higher concentration of AuNPs (1.8 nM) resulted in significantly lower cell density of stimulated Jurkat cells (blue and green hash bar) when compared to other stimulated but recovered Jurkat cells (*f*-AuNPs or αPD-L1 alone). Despite the apparent lowered cell density, this was not significantly different compared with the cell density of Jurkat stimulated in PHA alone (vs. green, P = 0.1998; Table S5.5). Conversely, the cell density of the Jurkat cells treated with PEG NPs* (+ PHA, –PD-L1) remained significantly higher compared to the PD-L1 suppressing (vs. orange, P = 0.0002) and basal growth (yellow, P = 0.0007) controls. From these data, the core concentration does have a significant impact on cell densities, which may indicate the potential toxicity. This limit should be characterized *in vitro* with a more comprehensive titration, and then can hopefully be characterized in higher order, more complex systems. Prior understanding and characterization of an LD_{50} in various tissues in a controlled environment will be easier to recognize than retroactively determining from a more complex and resource heavy animal study.

To further validate the potency of T cell recovery with *f*-AuNPs, the stimulation experiment was performed a third time with even more matured Jurkat cells (P11), which resulted in the same overall pattern of cell density (Figure 5.3). In summary, PHA significantly increases the Jurkat cell population (yellow vs. green; Table S5.6, P < 0.0001). Introducing solubilized PD-L1 (orange) results in a "basal-like" cell growth

phenotype with no significant difference in cell density to the basal control (yellow vs. orange; Table S5.6, ns). When *f*-AuNPs (blue) or αLA-αPD-L1 (blue and orange hashed bar, right) are added to the PD-L1-inhibited Jurkat cells, the cell density is not significantly different to the cell density of Jurkat cells treated with stimulant alone (vs. green), indicating that proliferation continues regardless of PD-L1. Conversely, the cell density of these "recovered" Jurkat cells are significantly higher than both basal (vs. yellow) and PD-L1-induced inhibited (vs. orange) growth controls (all cases, $P < 0.0001$).

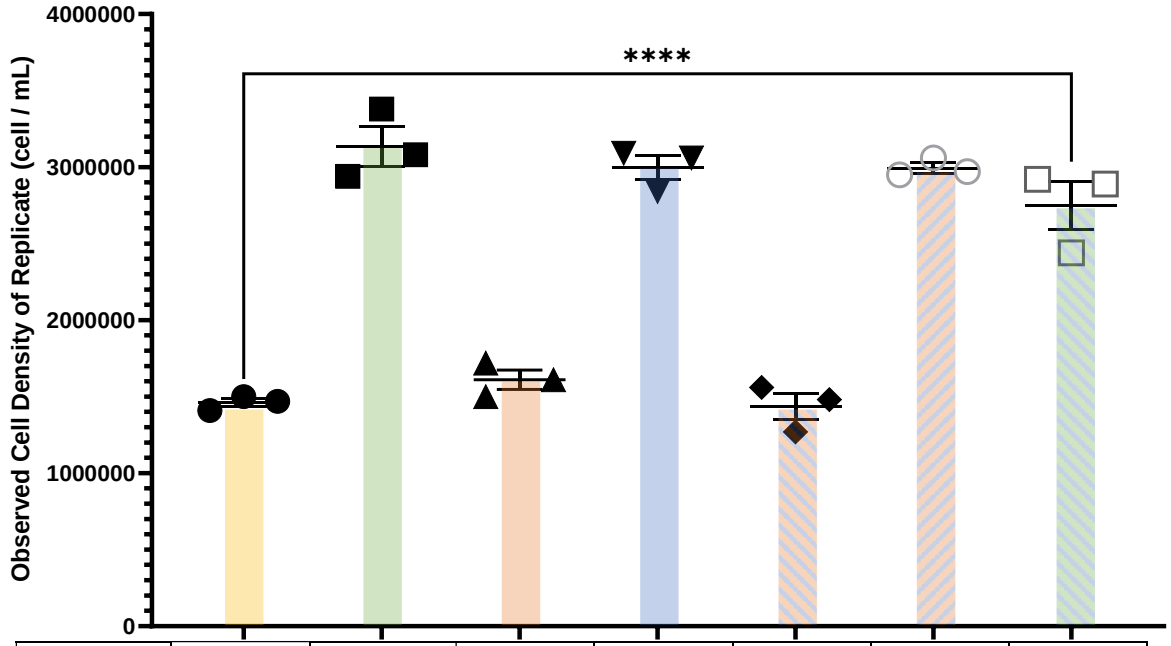

	Basal growth	Stimulated growth	Inhibited growth	Blockade with *f*-AuNPs	PEG NPs (–ve control)	Blockade with αPD-L1	PEG NPs* (core toxicity)
+ PHA	–	+	+	+	+	+	+
+ PD-L1	–	–	+	+	+	+	–
+ *f*-AuNPs	–	–	–	+	–	–	–
+ PEG NPs	–	–	–	–	+	–	+
+ αPD-L1	–	–	–	–	–	+	–

Figure 5.3. Jurkat cells (P11) maintain promising recovery with *f*-AuNPs (blue) when stimulated with PHA and inhibited with 32 nM PD-L1. The table describes the conditions of each column, and each point displayed was the observed cell densities of each well from at least three hemocytometer reads. Hashed columns indicate an isolated variable with respect to the *f*-AuNPs (left: PEG NPs used, gold core only; right: only αPD-L1, no core). The concentrations of the particles were 0.53 nM (*f*-AuNPs), 0.49 nM (PEG NPs), and 0.49 nM (PEG NPs*, –PD-L1). The mAb concentration was 5.7 nM. Bars indicate SEM, $n = 3$. * : $P < 0.05$, ** : $P < 0.01$, *** : $P < 0.001$, **** : $P < 0.0001$. All comparisons not shown were not significant (ns). All relevant statistical data can be found in Table S5.6.

Figures 5.1–5.3 show a promising pattern that the PD-L1-targeting *f*-AuNPs are disrupting the immunosuppressing effects of the PD-1/PD-L1 interaction between stimulated white blood cells and PD-L1. This resulted in cell densities equivalent to Jurkat cells stimulated by PHA alone, which were both significantly greater than the basal growth controls, indicating recovery from exhaustion induced by PD-L1. Furthermore, this recovery was successful at relatively low concentrations the particles, which consistently resulted in this proliferative cell density and may signify the immunotherapeutic properties

when carried forward into animal studies. However, this experimental model is limited. Our focus on the recovery of T cell activity occurred in an isolated system, which may not be congruent as more variables are added in higher order systems. This formulation should be carried forward to scope out toxicity in other immediately relevant cells expected at the tumour site, including PD-L1-presenting cells and non-PD-L1-presenting tissues, to determine if the immunotherapeutic properties occur selectively and at concentrations below any toxicological events to indicate the efficacy and safety of the particles.

Other future work should prioritize comingling the Jurkat cells with PD-L1-presenting cells to investigate and characterize the *f*-AuNPs and their effects in a more complex system, which will more appropriately approximate a biological environment. Unfortunately, using the hemocytometer as a readout would no longer be suitable as the Jurkat cell population would be nearly impossible to differentiate from the PD-L1-presenting cells, and another readout method would be necessary. Under ideal conditions, the splenocyte recovery assay described previously by Aurigene could be a suitable alternative. However, given the past poor sensitivity to detect cytokines, further optimization is necessary.

Currently, the commercial antibody from BioXCell shows promise as a useful PD-L1 inhibitor for potential immunotherapeutic applications. Its further conjugation to the gold core has given it practical use as a targeting agent to deliver gold for future radiosensitivity experiments.

Returning to the Wheel of Functionalization, other variables in future formulations may be selected in future iterations of this project (more thoroughly described in Chapter 4). This work mostly focused on the development and characterization of functionalized AuNPs to target PD-L1 using SPR. Despite these efforts, there is still a lot of work to be done before these particles may be afforded the title of "dual-functionalized."

The blockading of PD-1/PD-L1 by the antibody observed by SPR was still present in cellular work, although not measured directly. This effect was maintained in cells and is expected to yield some recovery from PD-1/PD-L1 T cell exhaustion. The presence of the *f*-AuNPs (or the antibodies) removed the apparent immunosuppression from soluble PD-L1, highlighting that the particles can blockade the PD-1/PD-L1 interaction and T cell activity remains. However, we have not measured any immunotherapeutic benefits (i.e., Jurkat cells become cytotoxic). The immune system is complex and relying on one checkpoint protein oversimplifies the problem.

Models are a good indicator to explain and rationalize processes that we may adjust and test in a white room before exploring *in vivo*. By starting simple and testing for selectivity and competitivity of the antibody (i.e., SPR), we would expect that it can successfully prevent the activity of the immunosuppressing proteins (i.e., cells remain stimulated). However, this binary metric becomes less accurate when more variables are incorporated and does not accurately reflect immune checkpoint proteins. Fortunately, other immune checkpoint proteins were not problematic, and resulted in a simple drug formulation of αLA-mAbs on a gold nanosphere (*f*-AuNPs) that can selectively bind and disrupt the PD-1/PD-L1 interaction. Furthermore, this cellular recovery model abided by the predicted outcomes and by blocking the PD-1/PD-L1 interaction resulted in the recovery from T cell exhaustion induced by PD-L1 alone. Upon addition of a cell membrane independently expressing PD-L1 (and other proteins) by co-mingling with the Jurkat cells, the perceived T cell proliferation may not be present as other immune suppressing signals will also be present as the two cells crosstalk.

However, it would be interesting to try for recovery with subsequent AuNPs formulations with mixed targeting for the other immune checkpoint proteins (i.e., CTLA-4, PD-L2), with prior αPD-L1 conjugates. With more immunosuppressing signals, it may be suitable to test if the Jurkat cells are remaining anergic or truly recovering by measuring for changes in cellular activity (i.e., cytokines or whole cell mass-spectroscopy).

Lastly, the gold cores show promise to selectively deliver to PD-L1-presenting tumour cells with a high potency upon functionalization with the αLA-thiolated αPD-L1 antibody. This means future experiments may investigate how the current formulation performs for uptake and radiosensitization studies in ionizing and non-ionizing radiation therapies to characterize the secondary function of the platform as a selective radiosensitizer, and eventually branching into other formulations that improve selectivity of TNBC tissues over other PD-L1-presenting tissues, which would reduce the overall gold exposure.

6. Concluding Remarks and Prospective Works

The gold core is a sufficient vehicle platform for targeted drug delivery, and it has promise to not be intrinsically toxic to human white blood cells. We would like to continue investigating these AuNPs as a platform for personalized nanomedicines to wholly characterize these effects (both intended clinical as well as toxicological screening and selectivity) prior to investigating them *in vivo*. Although we are not limited to using antibodies as the only targeting agents, nor is the specific formulation that was used for *in vitro* work limited to treating TNBCs. The Wheel of Functionalization should be used to further optimize the formulation by continuing to investigate the other variables (e.g., different polymers, mAb-conjugate linker lengths, increased thiol content).

While targeting with antibodies is a step forward for promising immunotherapeutic effects using endogenous means, they are quite limited as drugs. Industrial scaleup is a common bottleneck for their commercial use, and the homogeneity of these large proteins is entirely dependent on the fidelity of the polymerases that transcribe and translate them. These factors can contribute to batch variance and needs more stringent characterization to overcome. In addition, the biocompatibility of mAbs allows for longer circulation times, which makes them difficult to dose as they may not clear the patient in an effective manner. Furthermore, the long retention time of a foreign entity can contribute to inducing immunogenic effects, and all of these factors should be the driving force to continue pursuing the investigate small molecule biologics. Although we performed no toxicological assays with the αLA-mAb AuNPs, future work should characterize whether the particles could have any detrimental effects on other tissues, and use these as a benchmark when formulations that use small molecule targeting agents are designed.

While we did not directly characterize immunotherapeutic efficacy such as the PD-1/PD-L1 disruption with TNBC and Jurkat cells *in vitro*, Figures 5.1–5.3 show compelling evidence suggesting that the αLA-mAb AuNPs can disrupt the PD-1/PD-L1 interaction and recover PHA-stimulated Jurkat cells from PD-L1-induced immune suppression. The remainder of this chapter describes other avenues of drug delivery to explore with the gold nanoparticles (i.e., small molecule targeting and triggered release) well as other pre-clinical characterization methods to determine their safety prior to performing *in vivo* experiments. Moreover, the scope of this work is not limited to targeting PD-L1, nor treating specifically TNBCs. With the proposed subsequent future work, we expect to further expand and characterize the proposed functions (e.g., determining selectivity of radiosensitivity, uptake, and co-mingling) as well as their safety. With these, gold particles may be more broadly used in clinical applications, from theragnostic imaging to controlled delivery. The remainder of this chapter expands on how future experiments could integrate the learned knowledge from Chapters 2 and 3 and how those formulations may affect PD-L1-targeting particles. Where our work was predominantly focused on a simple AuNP, composed of monoclonal antibodies and PEG spacers at a relatively fixed concentration (sub-pM), it would be interesting to investigate other drug loadings (i.e., varied concentrations of mAb per AuNP, and varied concentrations of cores) to optimize immunotherapeutic efficacy and characterize any intrinsic toxicity from the core to finally remove this cloud of uncertainty that is preventing broad clinical applications of gold nanoparticles.

Follow-Up Experiments for Small Molecule Binding and Characterization (Chapter 2)

The small molecules from Aurigene showed no evidence of interacting with PD-1, PD-L1, PD-L2, nor VISTA proteins as determined by SPR. However, according to the literature, their mechanism of action may be affecting some upstream effector protein, which results in the immunomodulation observed in the splenocyte recovery assay. Herein our proposed future work to try to determine where the small molecules are targeting and how they could be incorporated into future nanoparticle formulations.

Follow-Up 2A: Detecting Proteosome Degradation by Incubating Transfected HEK293 Cells with PD-L1-GFP conjugates with the Aurigene Compounds

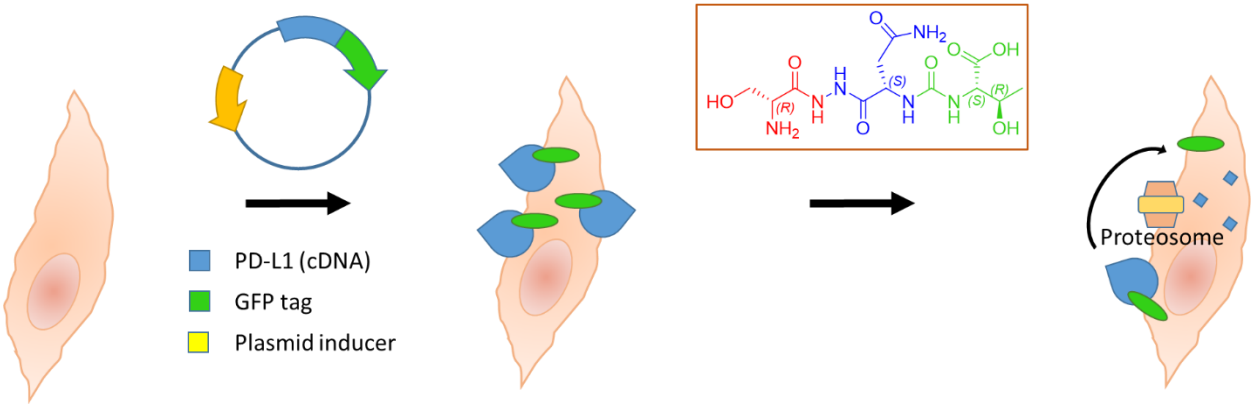

Figure 6.1. Schematic to validate the hypothesis that the Aurigene compounds are glycosylation inhibitors, using transfected HEK293 cells.

Earlier, in Chapter 2, we proposed the hypothesis that the Aurigene compounds **3**–**5** were competing with the upstream post-translational mechanism that protects proteins, glycosylation, due to the pharmacophore resembling the SNT motif. Figure 6.1 illustrates an experiment to characterize and validate that claim by using the methodology described by Li *et al.*, where HEK293 (PD-L1^{-}) cells were transfected to endogenously express human PD-L1 with a GFP tag.[204] Ideally, the plasmid would have an inducible vector that produces a fluorescent signal indicating the induced expression of PD-L1. The successfully transfected cells would then be further incubated with the Aurigene compounds at a similar concentration (100 nM), and hopefully there would be a decrease in fluorescence intensity, indicative of protein degradation by the proteosome. This experiment would validate the claim that the Aurigene compounds directly impacted *N*-linked glycosyltransferase activity, which contributed to less immunosuppressing protein overall, and resulted in the apparent T cell recovery that Aurigene observed in their splenocyte recovery assays.

Initial optimization begins with transfection and seeding of the human cells to express the plasmid, which could be validated through an antibiotic resistance factor on the plasmid. After successful transfection, cells should become fluorescent by incubating them with an induction factor that stimulates expression of the plasmid. The degree of fluorescent intensity may be optimized by monitoring incubation times, where incorporating the putative inhibitors should result in a lower emission intensity.

To overcome experimental biases in this biochemical assay, a variety of plasmids would need to be optimized for successful transfection and inducible expression (Table 2.2). Using the full structure of PD-L1 as a conjugate may result in some misfolding with the tether, by also using just the soluble

extracellular fraction, we may see if the tether is disrupting possible downstream activity. Similarly, by using the PD-1 equivalents expressing a different fluorescent protein (e.g., red, RFP) we could overlay and see any possible disruptive outputs (i.e., less green indicative of protein degradation).

This proposed assay could provide orthogonal evidence to characterize the mechanism of action of Aurigene's compounds. The objective is to measure if Aurigene's small molecules, which contain the core SNT-pharmacophore, are affecting some upstream enzyme in protein stabilization. We would expect that upon incubation of the Aurigene compounds, there is some inhibitory activity of a glycosyltransferase, such that new proteins are not being protected by glycosylation, and therefore display less fluorescent signal due to higher protein degradation. Although this assay is quite qualitative, using chimeric protein expression and apparent changes in fluorescent emission as the output of inhibition, it should help in characterizing the mechanistic effects of compounds **3–5**. Cells incubated with the small molecules would be expected to have more proteasome activity, and therefore less emission. This could be corroborated with a mass-spectrometry study for higher amounts of ubiquitinylated PD-L1-fragments present in the sera; stimulated cells without the small molecules would show other post-translational modifications.[303]

Table 6.1. Some proposed plasmids that are expected to be useful in measuring whether the Aurigene small molecules are contributing to upstream inhibition of glycosyltransferases. By expressing PD-L1 endogenously in eukaryotic cells, we expect the presence of post-translational modifications. Plasmids expressing PD-L1 or PD-L1 with a chimeric reporter protein (i.e., green- and red-fluorescent proteins) would be expected to have a lower fluorescent output, indicating proteolytic degradation.

Gene of Interest	Plasmid Variant	Plasmid
PD-L1 (full)	PD-L1 (full) GFP	1
PD-L1 (extracellular)	PD-L1 (extracellular) GFP	2
PD-1 (full)	PD-1 (full) RFP	3
PD-1 (extracellular)	PD-1 (extracellular) RFP	4
Control	GFP only	5

As we had shown that compounds **3**–**5** do not directly interact with PD-1, PD-L1, PD-L2, or VISTA we could expect that any plasmid variants using the full or extracellular fractions of these proteins would be suitable alternatives, as this is to address any upstream glycosyltransferases.

Follow-Up 2B: Diazirine-Analogs Determining the Binding Site of Aurigene Compounds by Mass Spectrometry

Alternatively, a proteomic approach would be appropriate to determine where compounds **3**–**5** are binding in cells. Synthesizing diazirine-containing analogs would be suitable for mass spectrometry (Scheme 2.3). The Aurigene compounds would be expected to be in any binding pockets behaving as substrates to the SNT motif, then could be activated with UV light to covalently bind the molecule to the target proteins.[304,305]The fragments which were positive for the compounds would then be sequenced as to determine the most frequent binding site in the proteome.

These two follow-up experiments would be able to orthogonally validate and more accurately describe how Aurigene's peptidomimetic compounds behave *in vivo*.

Scheme 6.1 is a proposed synthesis to make a diazirine-analog of compound **5**, where the secondary alcohol of the threonine-like residue is transformed into a diazirine species in five steps. The diazirine moiety is crucial proteomic studies because upon near-UV activation it will release nitrogen and form a reactive carbene. This species will covalently form a new bond via C–H insertion. After incubation and activation, the cell particulate is subjected to peptide digestion to fragment the proteins making them more accessible for mass spectrometry. The major takeaway being fragments that are hits with the initial mass of the compound would be indicative of the binding pockets the molecule can access. Furthermore, fragments are sequenced to determine the selectivity of the compound. If our hypothesis about these molecules competing for glycosylation is correct, we would expect to see most peptide fragments associated with glycosyltransferases. This assay will showcase the "specificity" of the molecule, or lack thereof, as well as finalize where these molecules bind within the cells.

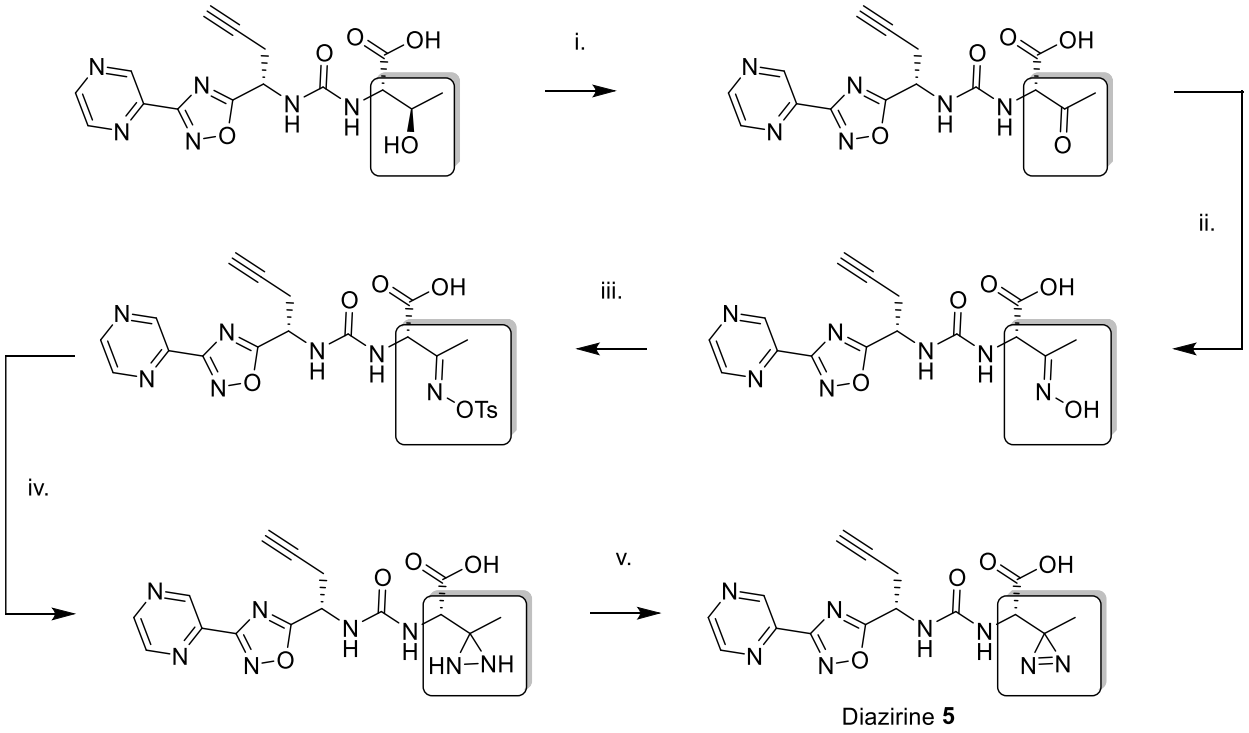

Scheme 6.1. Proposed synthesis of diazirine analog of Aurigene compounds using **4** as an example. i. Oxidation of the secondary alcohol to a ketone. ii. Formation of the oxime. iii. Activation of the oxime by tosylation. iv. Converting to diaziridine species by reacting with ammonia. v. Oxidation to an expected diazirine.

Follow-Up Experiments for Characterizing Controlled Release of the Tumour Microenvironment (Chapter 3)

Triggering release mechanisms are becoming more commonplace amongst nanomedicines for their desirable application to greatly remove off-targeting effects from non-selective interactions between the patient and drug. The methyl groups installed at the α-position of our fluorogenic compound blocked unwanted esterase release, but further cellular release studies should be performed with **9** to establish its TME selectivity (Follow-Up 3A). We expect that these disulfide linkers will improve the delivery of an anti-tumour agent by incorporating a triggerable release mechanism that is selective for the tumour microenvironment, either as a *bis*-dimer prodrug, similar to **9** (Follow-Up 3B), or through an asymmetric tether from its precursor, **15** (Follow-Up 3C), which may be employed in future AuNP formulations. Additionally, precursor **15** could be used as a linker for the targeting mAb to maintain the PD-1/PD-L1 disruption on the cell surface, while allowing uptake of the gold core for radiosensitization studies.

Follow-Up 3A: Complete Cell Incubation and Selectivity Studies with 9

Reproducing the cellular release experiment described in Figure 3.2, but with compound **9**, should reveal the degree of GSH-sensitivity between the glioma cell lines and normal fibroblasts to validate the initial claim of redox-triggered release. We would expect a much lower background fluorescence intensity, ideally none in the HNDF cells. By retaining the U-87 and U-251 cell lines, this could validate the initial claim of "high" and "low" reducing activity proposed from the empirical data and validate the claim for TME-selective release. Our *in vitro* control study, which incubated **9** in MilliQ with denatured FBS and protease inhibitor cocktail, had **9** shut down the esterase activity (Figure 3.6); however, we did not incubate **9** with the various cell lines to establish their selectivity to the TME.

Introducing the more hydrophobic **9** into the cellular release experiment from Figure 3.2 should elucidate the disulfide exchange mechanism of "turn-on" fluorescence by reducing the esterase cleavage, previously implicated in the high overall background fluorescence – as shown in Scheme 3.2. We would expect that background release would be greatly reduced and any fluorescent intensity would be attributed to disulfide exchange triggering the fluorescent release of 4-MU. Both cancer cell lines are anticipated to have higher fluorescence emission to the control HNDF cells, and we would expect a significantly higher emission intensity attributed to the higher GSH concentration. After an overnight incubation, the emission intensity would be normalized to the intensity of the corresponding 4-MU control.

Similarly, reproducing this cellular experiment with 1% PIC-treated media should further remove esterase activity. We should be able to identify distinct basal cleavage/release from HNDF cells and ideally see a significant difference in fluorescent intensity between U-251 and U-87 due to their respective GSH concentrations. Similarly, we could spike the cells or cell media (control) with 30 mol eq. TCEP to induce the disulfide-based release of 4-MU from **9** in cell culture conditions, this would reinforce the trends observed between **7** and **8** when we were determining where the release activity was originally occurring.

Following the incubation with cells, we would be able to accurately address if the disulfide tether would be suitable for further prodrug release studies, or if other immolation-based tethers should be pursued. Disulfides are often the first motif that comes to mind for their bioavailability and biocompatibility, but there are other environmentally reactive moieties.[244,251,306]

Follow-Up 3B: Synthesize SN-38 Esters for Turn-On Fluorescence and Cytotoxicity

Interestingly, the 4-MU conjugates (**7**–**9**) were made as a safer analog to a known cytotoxic species, SN-38.[182,307] Despite its potency as an antitumour agent, SN-38 is difficult to deliver due to its labile/sensitive lactone and its insolubility to aqueous environments.[308] Previous works overcome these barriers through hydrophobic encapsulation; however other post-delivery barriers still need to be overcome (i.e., targeting).[182,307,308] By harnessing TME-selective immolation, we could expect controlled release in dosing of SN-38.

Both SN-38 and 4-MU share the phenol moiety capable of ester conjugation (Figure 3.7), and both lose fluorescence upon conjugation. We expect that the SN-38 analogs (**10**–**12**) should perform similarly to our initial findings with compounds **7**–**9**, especially with the presence of cells, where sterically-hindered **12** should only indicate turn-on fluorescence via thiol exchange. Additionally, a follow-up cell viability assay with proposed compounds **10**–**12** would establish the uptake of cytotoxic SN-38. Of these, *bis*-esterified SN-38 conjugate to DTDPA was synthesized (**10**) (Figures 6.2–6.3). However, the poor yield and complex purification made it difficult to isolate for the reagent-based screening that had been used previously with compounds **7**–**9** (Figure 3.9).

The basic conditions used to synthesize compound **10** were chosen to selectively esterify SN-38 at the phenol position rather than the tertiary alcohol (Figure 6.4). Since the acidity of the phenolic proton (pK_a ~9) is higher than the tertiary alcohol (pK_a ~17), it is more likely to be deprotonated by N,N-diisopropylethylamine (DIPEA, pK_a ~11) and react with acyl chloride **16**. By ^{1}H-NMR analysis of the product, there was no visible change in the chemical shift and integration of the tertiary alcohol (6.48 ppm), and a downfield shift in the doublets of the protons at the *ortho*-position to the new ester group was observed (Figure 6.5).

In previous literature precedence, selective esterification of SN-38 on the tertiary alcohol requires installing a Boc protecting group on the phenol which is removed shortly after. This allows for the coumarin-like moiety to remain fluorescent (Boxed, Figure 6.2) in the conjugate product.[182,185] Regardless of where SN-38 is conjugated for drug delivery, there is difficulty in achieving delivery of its lactone-*stabilized* form.[307,309,310] This will be a problem for future preclinical studies that focuses on characterizing SN-38 release from *bis*-products (**10**–**12**) for tumour-specific release attributed to the tumour microenvironment, as shown with the 4-MU analogs. Using **10**–**12**, we would expect a similar “turn-on” fluorescence output as well as cytotoxic activity when implemented with cells.

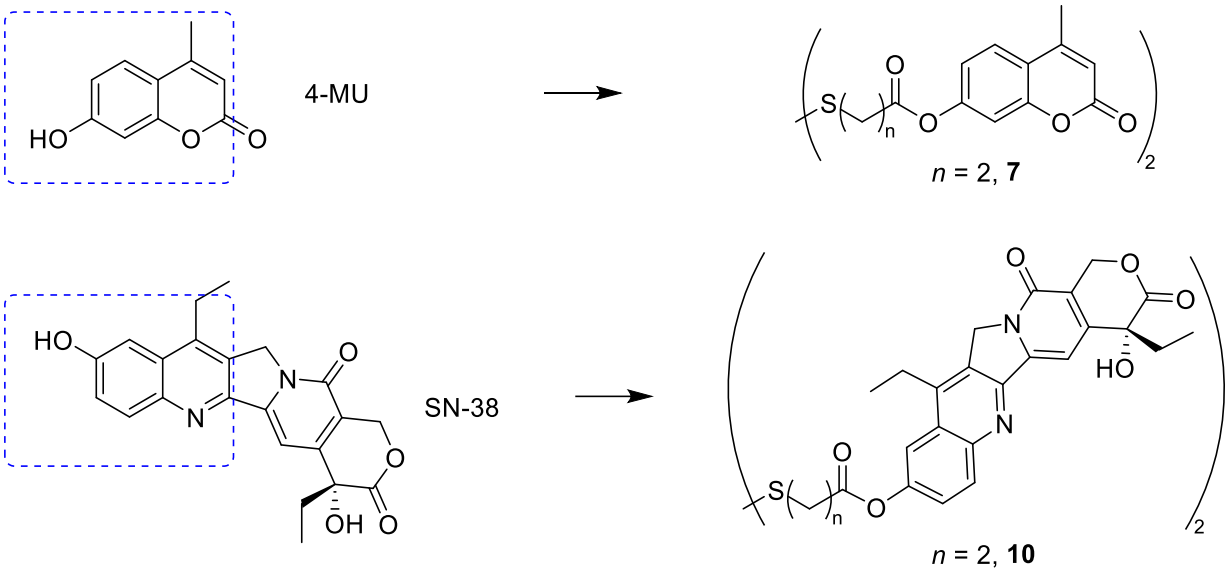

*Figure 6.2. Highlighting the aromatic systems responsible in both 4-MU and SN-38 that""turn-of"" fluorescence upon esterification. Both compounds are bis-ester conjugated to dithiodipropionic acid (DTDPA, **17**). However, SN-38 conjugates, **11** and **12**, would use dithiodibutyric acid (DTDBA, **18**) and our α,α'-dimethyldithiodibutyric acid (**15**) as their respective tethers.*

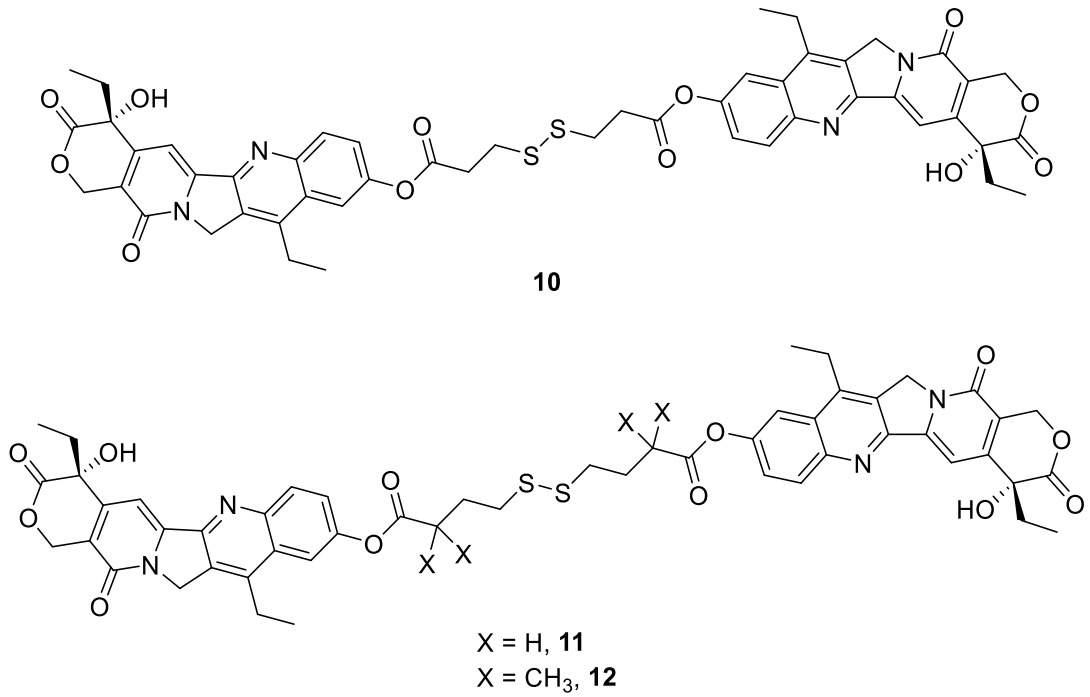

*Figure 6.3. Full structures of proposed bis-SN-38 conjugates, **10**–**12**.*

These conjugation reactions were attempted. The determination of successful conjugation relied on diagnostic peaks in ^{1}H NMR found in the crude spectra; however, the reactions did not prove fruitful (Scheme 6.2). Overall, carbodiimide reactions (EDC, DIC, and DCC) were initially chosen to mimic the synthesis of compounds **7**–**9** but showed poor conversion.[311,312] Using more robust coupling agents like HATU and HBTU showed no change in conversion, but were not followed through due to risk of

sensitization.[311,313] A Mitsunobu esterification was also attempted to esterify SN-38,[314,315] and similarly showed poor conversion of product **10**.

Synthesis of **10** was moderately successful by conjugating SN-38 to the diacyl chloride derivative of DTDPA (**16**, Figure 6.4). Compound **16** was synthesized by reacting oxalyl chloride quantitatively with DTDPA in anhydrous DCM under vacuum as described by Makarova *et al*.[316] The starting material was initially characterized by ^{1}H and ^{13}C NMR to observe any distinct changes in the chemical shifts upon acylation.

Firstly, in the ^{1}H NMR, the upfield triplets at 2.87 ppm and 2.62 ppm are representative of the methylene protons, which do not shift post-acylation. There is a third peak in the starting material where a singlet at 12.36 (1H) is absent in the acyl chloride indicative of successful exchange of the -OH with -Cl. Although the chemical shifts are similar in the ^{1}H, the change becomes more apparent in the ^{13}C NMR where the observed peaks were 172.89 ppm, 33.69 ppm, and 33.15 ppm, are slightly further downfield with respect the starting material (i.e., 172.64 ppm, 33.54 ppm, and 32.97 ppm). The success of **16** is further affirmed when the molecule is analyzed by ATR-IR, where characteristic broad -OH stretching of carboxylic acids is absent, and the C=O stretch goes from 1687 cm^{-1} to 1785 cm^{-1} (Figure S3.20).

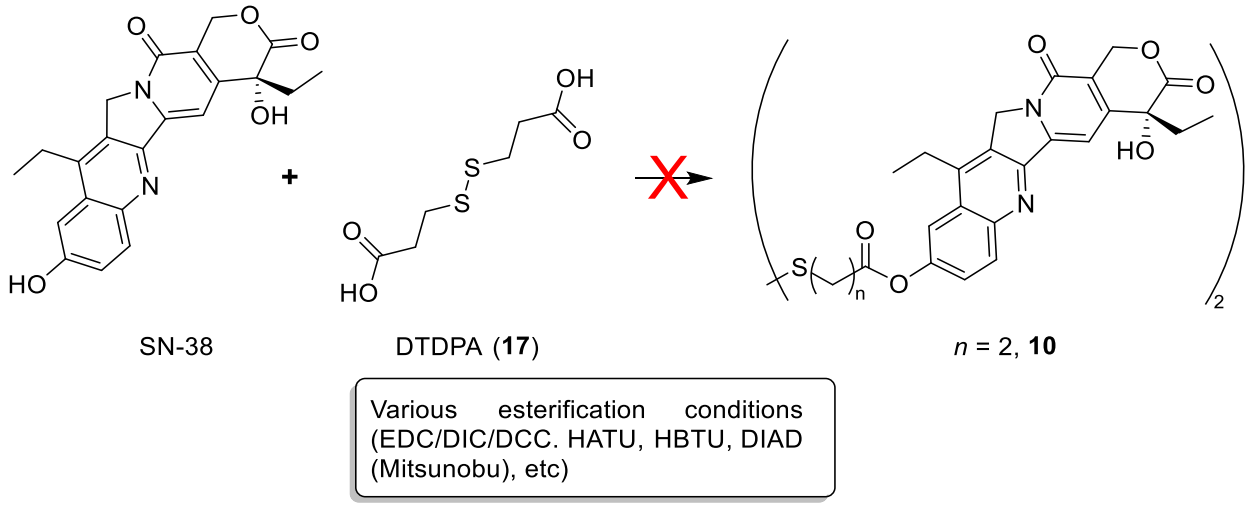

*Scheme 6.2. General reaction scheme of failed esterification conditions to synthesize compound **10** with SN-38 and dithiodipropionic acid (**17**).*

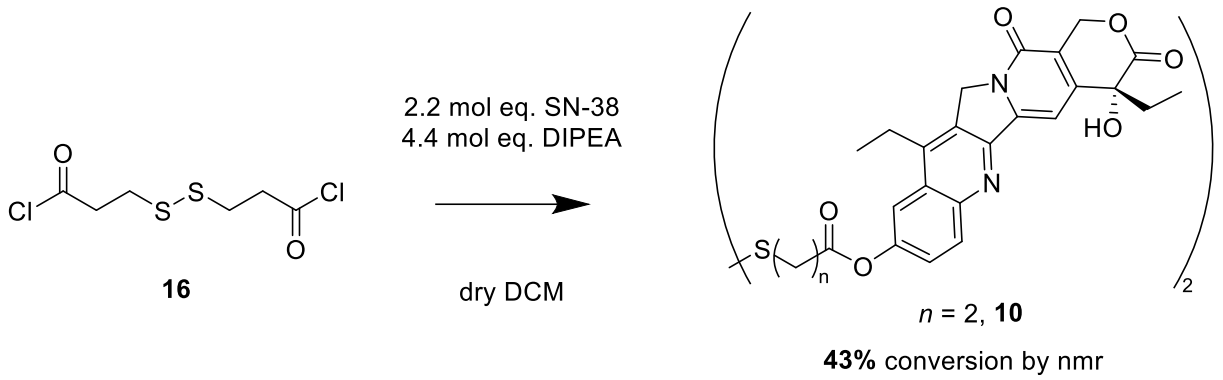

*Figure 6.4 Reaction conditions for the synthesis of compound **10**, the bis-SN-38 conjugate from diacyl chloride **16**. We anticipate similar reaction conditions would be suitable for the synthesis of a steric analogs for future cell data, shown in Figure 3.10.*

The presence of conjugate product **10** was determined by diagnostic ^{1}H NMR peaks (Figure 6.5). More specifically, a reference spectrum of SN-38 (top, green) and product **10** (red, middle), and the crude spectrum in blue on the bottom. We identified that the doublet at 8.03 ppm was the *ortho* position proton of the free SN-38 (determined by HSQC), highlighted by the green arrow, and upon esterification becomes more downfield shifted to 8.15 ppm. Similarly on the other side of the phenolic proton, the *ortho* and *meta* coupling aromatic protons also become a more prominent doublet of doublets shifting downfield from 7.40 ppm to 7.62 ppm. Both populations can be clearly observed in the crude mixture.

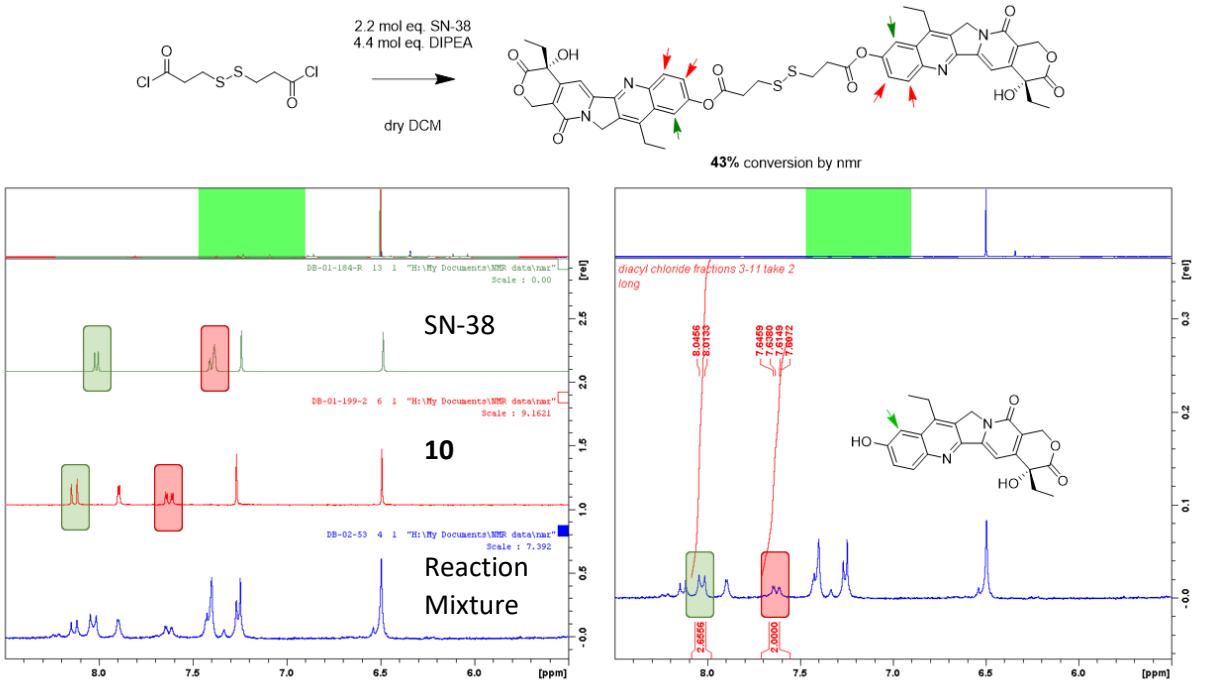

*Figure 6.5. Diagnostic aromatic peaks in ^{1}H NMR spectra in synthesis of compound **10**, where **16** was reacted with 2.2 mol eq. SN-38 and diisopropyl ethanolamine (DIPEA) under anhydrous conditions. The crude reaction mixture was purified using column chromatography with a gradient-based eluent (19:1 Hex/EtOAc → 1:1 Hex/EtOAc), where after 1.5 column volumes the polar fraction was increased by 5. **Left.** Aromatic diagnostic signals in ^{1}H NMR spectra are highlighted to show presence of starting materials and product **10** (blue), using reference spectra of SN-38 (green spectrum, top), and previously isolated **10** (red spectrum, middle). The highlighted proton regions correspond with the respectively coloured arrows in the starting material and product. **Right**. Highlighting the same diagnostic peaks in the crude mixture, where the green signal is indicative of unreacted SN-38 (structure inset), and the red signal is indicative of compound **10**.*

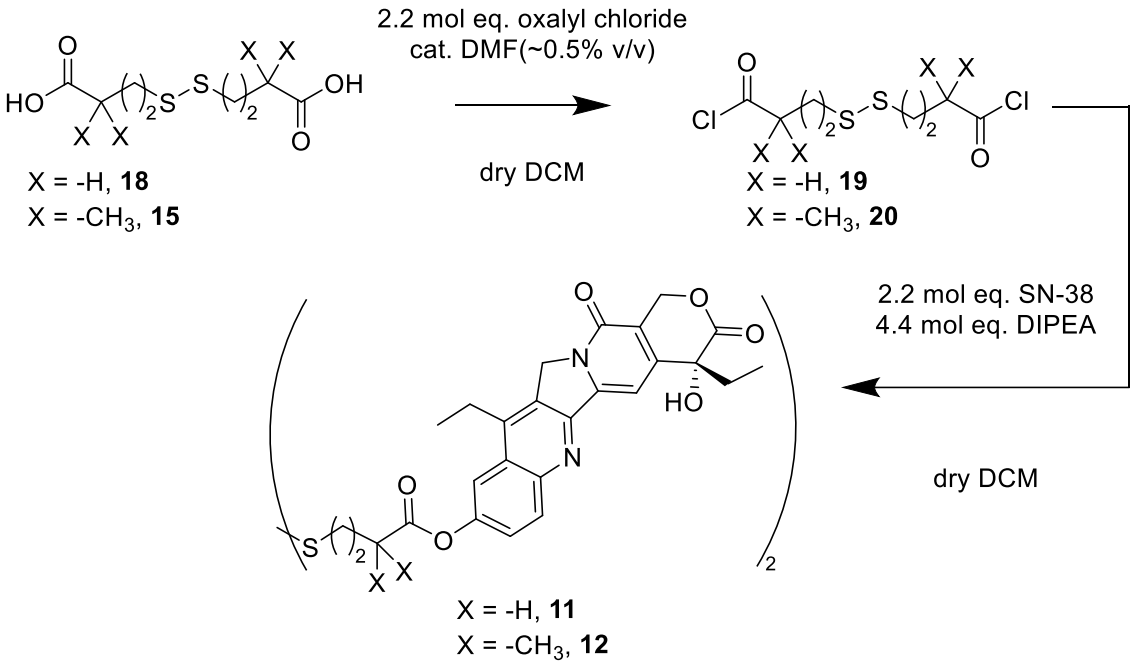

*Figure 6.6. Proposed synthesis of SN-38 conjugates for future cellular studies, in two steps. First, formation of acyl chloride derivatives from **18** and **15**, and then a nucleophilic substitution at the carbonyl with SN-38 and diisopropyl ethylamine (DIPEA).*

The scope of synthesis for this project was quite limited and there are still multiple avenues to be explored for the synthesis of target compounds **10**–**12**. As the acyl chloride **16** showed most promise in conversion of product **10**, it would be suitable to try and synthesize similar acyl chloride derivatives from dithiodibutyric acid (**18**) and its steric analog (**15**) using the similar method as described by Makarova *et al.*,[316] which may then further react with SN-38 as a nucleophilic substitution reaction to make compounds **11** and **12**, respectively (Figure 6.6).

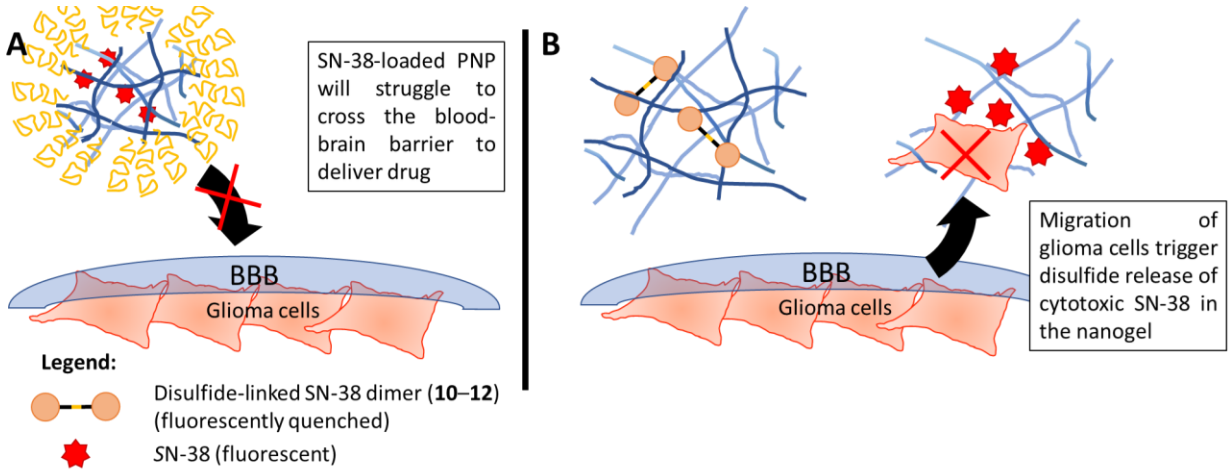

*Figure 6.7. Comparison of SN-38 delivery between an encapsulated PNP (**A**) and the proposed impregnated gel system (**B**) in the treatment of gliomas. **A**. Traditional delivery using PNPs would use a hydrophobic block of a co-polymer to encapsulate the drug, however transient delivery across blood-brain barrier (BBB) may prove difficult for the hydrophilic shell. **B**. The bis-SN-38-loaded nanogel is expected to reduce adverse effects, like leeching of SN-38, by increasing its hydrophobic character as a reduction-triggered disulfide-tethered dimer. In addition, The challenge of crossing the BBB is reduced by "fishing" for metastatic tumour cells that will release the drug upon entering the gel, resulting in cell death attributed to TME.*

Once compounds **10**–**12** are successfully synthesized and characterized, we may continue the research of controlled release in the dosing of SN-38 in the proposed nanogel system (Figure 6.7). By incorporating a cytotoxic agent into the system there is a new reading output, not solely fluorescent but cell viability, where cell death can be attributed to disulfide reduction and SN-38 release. We would expect a high fluorescent signal associated with cell death, selective for gliomas, where the higher concentration of GSH *should* elicit the most cell death and fluorescence intensity. This would be done by impregnating the compounds into a slightly hydrophobic nanogel, and incubating with the same glioma cell lines, U-87 and U-251.

Follow-Up 3C: Employ Disulfide Tethers for Targeted Uptake of AuNPs

Furthermore, with pursuits of controlled release, we propose to use this selective immolation with our AuNPs to hopefully improve the uptake of the gold core after targeting, as well as maintain the PD-1/PD-L1 blockade for immunotherapeutic recovery (Figure 6.8). Using compound **15** (α,α'-methyl disulfide precursor of compound **9**) in an asymmetric synthesis to conjugate αLA to αPD-L1 would allow for this selective controlled release (Figure 6.9D). We expect that these asymmetric αLA-tether-mAb-conjugates would allow the dual-modality of treatment predicted, where the targeting mAb remains blocking PD-1, and reduction of the tether will allow for gold core internalization as two independent mechanisms (Figure 6.8B), whereas the current simple formulation has both occurring concurrently which *may* impede success. The proposed controlled release formulation should yield higher internalization for radiosensitization, but would require scaleup to characterize and confirm this prediction, given that no radiosensitizing studies were performed.

Alternatively, the proposed asymmetric linker in Figure 6.9C would be suitable in conjugating other drugs for improved selectivity and controlled release with cytotoxic moieties such as SN-38. However, this will ultimately result in more complexity between batches. These expected formulations are similar in build to current ADCs, which use tethers to deliver chemotherapeutic agents, but instead of tethering directly to the mAb, they would be conjugated to the AuNP surface.

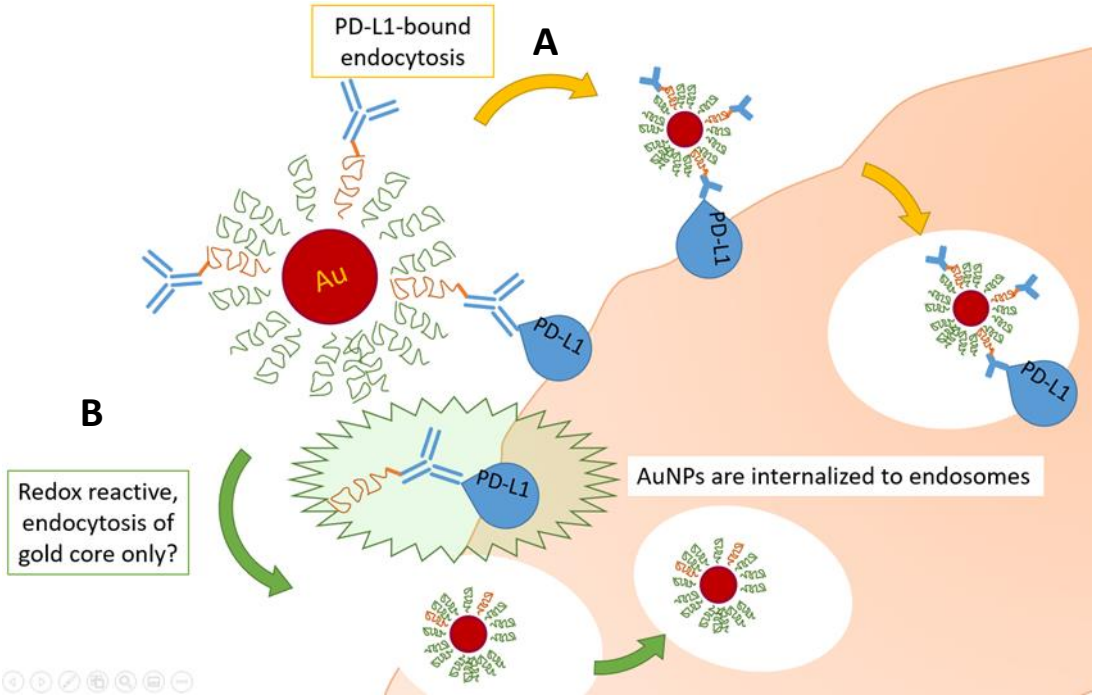

*Figure 6.8. Proposed formulations for dual-functionalized gold nanoparticles targeting PD-L1 and their possible methods of internalization upon binding. **A**. PD-L1-targeting AuNPs are likely bound to surface of PD-L1-expressing cells, where internalization is dependent on endosomal formation internalization whole carrier. **B**. Using a redox reactive controlled release system would be able to implement dual-axes function where the bound targeting agent retains immune recovery activity, and liberation of gold core may improve uptake and internalization. Future AuNPs could have a chemotherapeutic cargo and/or surfactant that releases core from endosome, improving radiosensitization.*

Future studies would require characterizing degree of selective uptake and optimize pathways for internalization, rather than relying on passive uptake alone via endocytosis,[52,317] using a cleavable linker could have benefits on improving uptake of the gold core. Selectively increasing the degrees of freedom for the core, using TME-triggered release upon binding to the tumour cell surface, should increase the likelihood of particle internalization via phagocytosis, pinocytosis, endocytosis, active transport. The former three would likely still have the gold bound to the cell surface (via PD-L1). However, the endosomes formed will likely not transfer the cargo to the nucleus, where we would want the gold to be for radiosensitization experiments.

While formation of radical oxygen species (ROS) in the cytoplasm is destructive to cells, containment within the endosomes may not be useful. Ultimately radiotherapy is most effective when it destroys the cellular machinery of DNA replication, or it destroys the DNA substrate.[1,318] By allowing the targeting agent and delivery of the gold to the cell, the selective release of the core may have higher uptake as there are more axes of internalization, which should yield selective radiosensitivity.

Although literature suggests passive internalization will occur to the bound particles, it is not guaranteed.[34,110,280,319] Predominant internalization of the core will likely occur via endosome formation, which are expected to drop the pH from 7 to 3 and isolate our core from the cellular machinery. To liberate the AuNPs, it would be suitable to investigate acid-labile linkers for the drug-conjugate payload but not necessarily targeting tethers.[320]

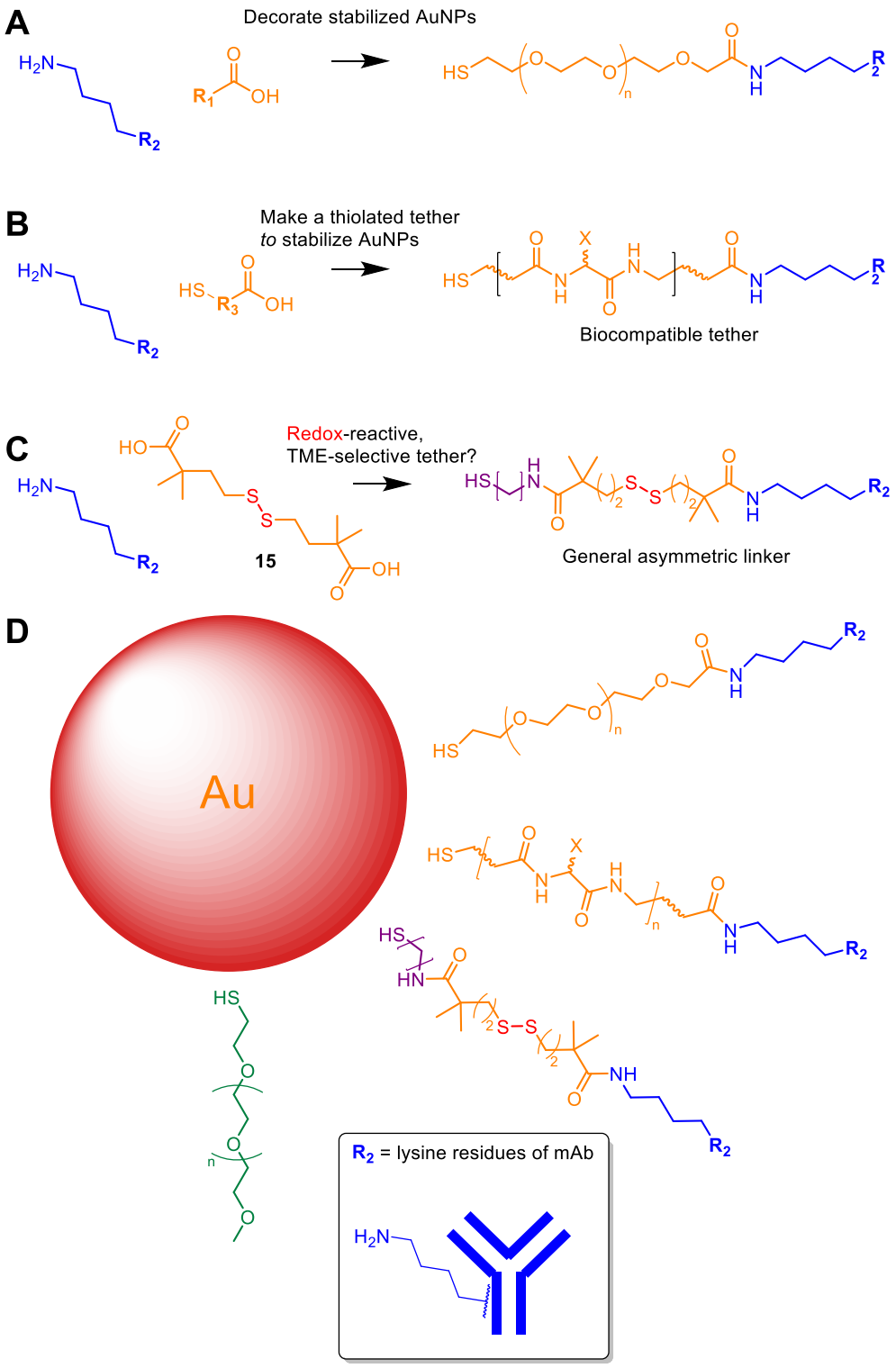

*Figure 6.9. Previous methods (**A, B**), and proposed methodI), of functionalizing the gold core for future AuNP formulations. **A**. The antibody is directly ligated to a carboxylic acid using EDC/NHS coupling on previously stabilized AuNPs – these are often large polymers. **B.** The antibody is conjugated to a thiol source, and this is used to coat and stabilize the particles. **C**. One proposed controlled release tether using **15** that employs asymmetric conjugation, where the antibody (blue) and a different biocompatible polymer (purple) surround the disulfide (red) which expects TME-selective release. **D**. Schematic of tethers on surface; the green polymer is PEG.*

Unfortunately, more variables could lead to more variety between batches, and therefore simplicity is better. Similar to ADCs, the AuNPs are not limited to employing direct drug-conjugates as a payload and using these disulfide tethers to help release the payload could improve efficacy (Figure 6.9D). However, optimization on drug-conjugation and quantifying the average drug per particle may be difficult. Herein, we wanted to keep the overall vehicle of delivery simple, such that current directions in nanomedicine may be used in future iterations with these active drug-loaded analogs. With the primary goal of targeting PD-L1, it was unnecessary to continue the pursuit of controlled release until we had achieved targetability and selectivity of the AuNPs, as this would increase the inherent complexity of the particles.

Eventually we want to characterize whether with our gold carrier is capable at innovating either radio- or immunotherapy via radiosensitization and immune recovery, respectively. As current clinical pursuits are more focused on combination-based therapies, as they are showing success in patient survivability.[319,321] By increasing the avenues of treatment accessibility on one platform, we would expect a similar beneficial outcome.

Follow-Up Experiments and Formulations of Functionalized Particles (Chapter 4)

Although most of the work in Chapter 4 revolved around synthesis and conjugation of the mAb to the AuNP cores for functionalization, one of the more interesting variables to improve stability was taking advantage of the gold-sulfur interaction. The following steps describe the intent to synthesize a *tris*-thiolated linker for mAb-conjugation (Follow-up 4A) and which other variables should be investigated when it comes to optimizing future iterations of AuNPs for targeting therapies via The Wheel of Functionalization (Follow-up 4B).

Follow-Up 4A: Synthesis of *Tris*-Thiol

From our work exploring formulation parameters, we found that the concentration of PEG was much too high and needed to be reduced – and the two-fold decrease from 600 mol eq. to 300 mol eq. (< 50% coating) was most appropriate. Our other intended goal was to potentially create a *tris*-thiolated antibody derived from Tris, a common buffer reagent comprised of one primary amine, and three alcohols (Scheme 6.3). This proposed work was inspired by work of Wojckykowski *et al*. where they worked with *tris*-alkane thiol sulfur gold monolayers (SAMs);[322] we wanted to create a hydrophilic *tris*-thiol conjugate (**21**) for the same purpose – improving stability for our antibody tethered to the gold core.

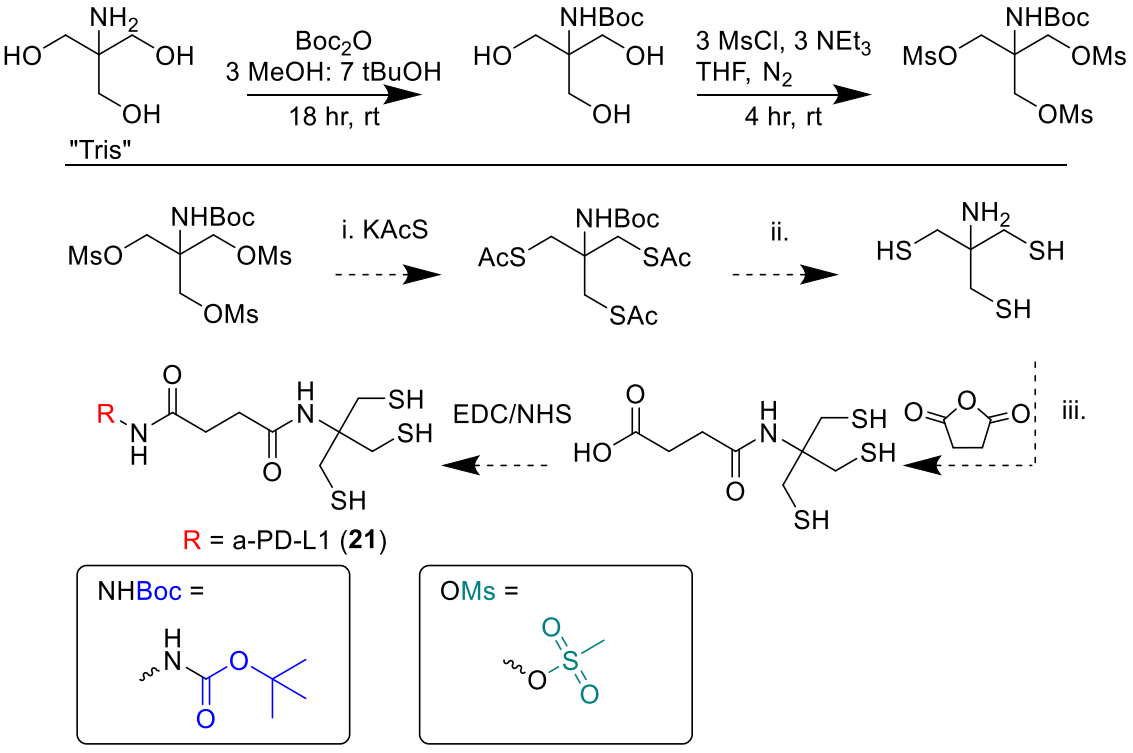

Scheme 6.3. Proposed *tris*-thiolate for mAb conjugation from Tris buffer starting material (Tris). The species in the top row were synthesized and characterized, but subsequent thiolation was unsuccessful. i. Installation of the thioacetate from the mesylate is described by Bennett *et al*.[323] ii. Reduction of the thioacetate to the thiol is previously described by Brackmann, where potassium carbonate in methanol is used to form the free thiol, optimizing would be required to achieve *tris*-thiolation and characterize the distribution.[324] An acidic workup using HCl would be requiring to deprotect the carbamate back into an amine for subsequent conjugation to a tether species such as succinic anhydride (iii).

Unfortunately, we did not successfully prepare the *tris*-thiol, due to incomplete conversion at the mesylation step to form the *tris*-mesyl intermediate. This work had the intent of making a *tris*-thiol species, although the proposed synthesis is not limited to strictly thiols. It may be useful to attempt

synthesis of the Tris-derived thioethers, **21b** and **21c** (Scheme 6.4), as the thioether is also quite stable when adsorbed to gold and less likely to dimerize/exchange with itself as the free thiol analogs.[322,325,326] Both reactions should result in an asymmetric *tris*-thioether where the sulfur atoms are in close enough proximity to still afford the Au–S handle without possible bridging between particles.[287,325]

However, there was no selectivity when conjugating the mAb to GSH or αLA, nor characterization of how many peptide conjugates were present per antibody. The random *in situ* conjugation (Figure 4.5) showed a slight decrease in antigen activity relative to the free binding initial characterization (Figure 4.4). The conditions of Figure 4.5 were much shorter relative to the bulk conjugation method used to make thiolated antibodies. This may result in batch variation, especially when the peptide reagents are in excess, as over-thiolated mAbs could now be "functionalizing" the gold core non-productively, favouring more flat orientations of r_3 due to much higher degree of valency (Figure 4.13B) and showing less binding overall via SPR.

Future optimization efforts with other thiolate conjugates should focus on the conjugation conditions that prioritize selectivity and activity. Empirically we have seen that by increasing the effective thiol concentration (i.e., 1 → 2 per conjugate when changing from GSH to αLA) and reducing the processing (i.e., removing spin down, removing disulfide reduction), we remove opportunities that may hinder activity and improve the degree of functionalization. Using SPR-based characterization can quantify the degree of functionalization, and this should effectively reduce batch-to-batch variability for these particles moving forward. Ideally, by increasing the effective thiol concentration per mAb, we would expect higher stability of the particles and less likelihood of desorption from other thiol-species.

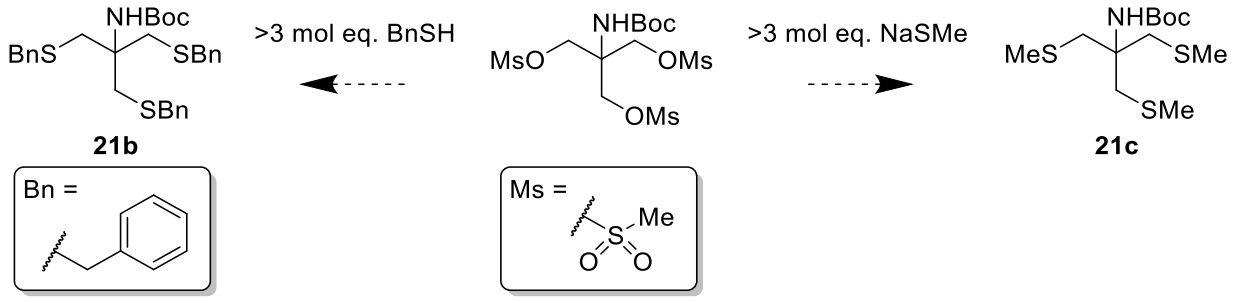

Scheme 6.4. Alternative *tris*-thiol intermediates for AuNP functionalization to make compound **21** contingents **21b** and **21c**.

Follow-Up 4B: Further Optimizing the Formulation – Future Iterations of AuNPs

As presented in Figure 4.14, not all of the variables were thoroughly investigated. However, now that a baseline formulation has been established, it would be practical to continue investigating other particle formulations.

Firstly, would be to reproduce the experiment in Figure 4.19, where AuNPs with varied spacer lengths were expected to show epitope availability as to optimize the space between cores without blocking the mAb epitope. It would be interesting to compare the binding responses of the similarly functionalized particles with varied lengths of steric barriers and using this to optimize grafting of mAbs. Using smaller linkers, it should be easier to detect anisotropic changes attributed to antibody grafting. This is expected because IgGs are of similar volume to the 15 nm core size. This would be invaluable characterization data to help determine how many mAbs per AuNPs for dosing experiments. However, reducing the spacer between cores increases the likelihood of aggregation and unstable particles.

Upon corona functionalization, there is an expected increase in hydrodynamic volume as well as overall shape. This large change in geometry was expected as the mAbs are similar in size to gold particles (15 nm) and to be detectable through DLS. We expected that functionalized particles would cause a large shift in the hydrodynamic radius, and major broadening in the dispersity. This is due to the limited surface area available *for* functionalization of the S–Au interaction, and not every particle will have the same number or distribution of PEG or mAb bound to their surface. The presence of the antibody functionalizing onto the AuNP surface should broaden the dispersity of the particles, causing an obvious size shift by increasing the radius overall. Upon functionalization of a single mAb to our 15 nm AuNPs, the diameter nearly triples from 7.5 nm to 22.5 nm, which increases the volume at a greater rate. However, in the current formulation, by using a relatively long PEG polymer length (2 000 g/mol, 44 units) these size changes to differentiate between functionalized and not may not be as obvious in DLS, as the *stretched* polymer length is of comparable size to the mAb height (~12 nm). We used SPR to confirm the functionalization by measuring the direct binding to PD-L1 and comparing the responses with the equivalent amount of free antibody. Using smaller spacer polymers, we would expect that DLS would be able to distinctly show *functionalized* AuNPs because of the more prominent change in the overall volumes (i.e., mAb-bound to the AuNPs), and PEG only motifs would have distinctly smaller size. However, doing so reduces the steric barrier between particles, relying on the mAbs to space between cores, and may risk core aggregation in tissues.

Similarly, we maintained a relatively small core size of particles (~15 nm) which we expect is capable of hosting 26 mAbs per AuNP (according to the predicted maximum occupancy model). By increasing the core size, this should make functionalization data via SPR and DLS data more compelling. In the SPR data, we expect larger responses observable in the SPR sensorgrams due to the increased MW of the cores. In the DLS data, the AuNPs would display a nominal shift in an increased hydrodynamic radius attributed to grafting of mAbs to core, and any unbound protein would result in a second, smaller, population around 15 nm. However, increasing the volume of functionalized particles may risk reducing uptake in the tumour tissues,[319] and warrant further investigation with smaller targeting agents to offset the increased volume. Smaller cores are also an option, where the change in size between pre- and post-functionalization would be more obvious by DLS.[110] However, using a smaller core will reduce the ability to characterize the degree of functionalization by SPR; the larger this molecular weight difference is between the ligand and the analyte, the more distinct the response is in the sensorgram. When reducing the overall size, we reduce the capacity of the core to carry our targeting agents, and thus reduce the sensitivity of the SPR experiments overall. Changing the core size will also vary gold uptake into cells, so what tradeoffs are made in the manufacturing phases may not be justified in more complex conditions.[77] This current αLA-formulation is the current baseline formulation aimed at 15 nm with 25% coating should be investigated for particle uptake and targeting efficacy alongside 5 nm and 50 nm core variants, prior to looking at other polymer lengths. Increasing the overall volume of the core will increase the carrying capacity of the particles, but with the caveat of likely reducing uptake and internalization due to size limitations with the tumours.[319,327]

We are not limited to working with PEG exclusively. Although formulations using other biocompatible polymers (e.g., polyurethane or polylactic acid) would be expected to target similarly to our baseline formulation, the downstream effects of changing to a chemically different system may not be noticeable until more complex assays are performed (i.e., cell- and animal-based measurements). The current formulation is a suitable “standard” to compare with when looking into these alternative polymer AuNPs.

In future particle iterations it would be interesting to investigate selective release studies. While briefly alluded to in Chapter 3, investigating redox reactive tethers could improve the degree of freedom and efficacy of the drug (Figure 3.20). Ultimately, future iterations of our AuNPs would use pH- and/or redox-reactive tethers to liberate the cargo from the carrier in a selective manner. More specifically, using cleavable tethers that trigger the removal of the delivered chemotherapeutic from the gold core. However, incorporating a new variable such as a third stabilizing agent (i.e., redox-reactive polymer with a chemotherapeutic conjugate), would require another series of optimization experiments and determining the chemo-capacity.[110,184]

Similarly, functionalization of the AuNPs involved thiolating the antibodies and directly adsorbing them to the gold, where increased thiol content resulted in better activity. However, more optimization in thiolation efficiency could be investigated where possibly other spacer lengths may be used with varying degrees of thiol content.

Follow-Up Experiments for Evaluating Clinical Efficacy with 2-D *In Vitro* Models (Chapter 5)

Much of Chapter 5 focused on immunostimulation and maturation of Jurkat cells, and their subsequent recovery of proliferation from PD-L1. The results from Chapter 5 were inherently limited at providing evidence of *immunotherapeutic efficacy* with our current formulation of particles. However, this relatively "simple" *in vitro* model was inspired by the splenocyte recovery assay from Aurigene. I want to propose how the recovery assay may be further evaluated by repeating the co-mingling studies described earlier by Aurigene in Chapter 2.

Once a baseline of 2-D cellular experimentation is standardized to characterize both immunotherapeutic recovery and radiosensitization, then other formulations may be investigated. This would include looking at anti-tumour agents integrated into the formulation, optimizing tethers for controlled release, and potentially expanding a library for targeting. Provided below are ways to orthogonally evaluate these characteristics of the AuNPs prior to performing animal studies, allowing for *in vitro* optimization as we transition from 2-D to 3-D models (Scheme 1.1)

Follow-Up 5A: Evaluating Immunotherapeutic Efficacy by Co-mingling Cell Culture of Stimulated T Cells and Triple-Negative Breast Cancer Tissue

The formulation successfully targeted and disrupted the PD-1/PD-L1 interaction, which resulted in the sustained proliferation of stimulated Jurkat cells in excess PD-L1. This is, however, an incomplete model, which suggests if no other immune checkpoint proteins are present, T cell activity is recovered. To ascertain if the particles are immunotherapeutic, it would be interesting if the higher cell density phenotype is maintained in the presence of whole cells that express PD-L1. While previous characterization studies provided evidence of interruption between solubilized protein-protein interactions, and that the *f*-AuNPs can recover lymphocyte stimulation while inhibited by the presence of solubilized PD-L1, we have not measured any direct recovery of T cellular activity between two cell lines (Scheme 6.5).

As mentioned earlier, while the cell count suggests recovery is plausible with this model, it is not sufficient. Future work should prioritize the optimization and scaling up of AuNP synthesis, such that a co-mingling assay (akin to Aurigene's splenocyte recovery assay) can be performed and used to properly characterize the proposed immunotherapeutic effects.

A follow-up comingling assay would model the effects in the immediate surrounding breast tissue, to continue to characterize potential off-targeting effects. Using stimulated Jurkat cells co-incubated with normal epithelial breast tissue cells (i.e., MCF-10A), we could observe any potential adverse effects the particles may present in the surrounding tissue prior to an investigation in animals. This will demonstrate the higher targeting function of the gold particles and determine if they have any adverse effects in the peripheral breast tissue near the tumour sites. The *f*-AuNP selectivity could also be characterized using a clonogenic assay for radiosensitization (Follow-up 5C).

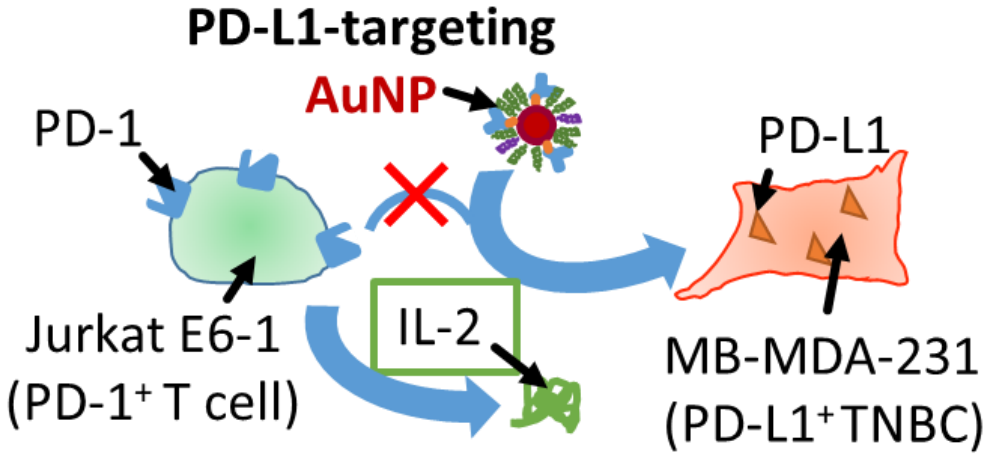

Scheme 6.5. Comingling immune cells with PD-L1-presenting TNBC cells such that PD-L1-targeting AuNPs may compete to bind and recover T cell exhaustion.

Other Methods Validating Maturation of Jurkat Lymphoblasts

Monitoring secretion of IL-2 post-stimulation – ELISA

Although we observe a higher cell density of Jurkat cells when they are incubated with PHA and other immune stimulants as recorded by hemocytometer, the populations are assessed assuming all cells were alive. It is difficult to accurately measure cell viability of Jurkat cells as common staining reagents used in hemocytometry are toxic, resulting in real-time cell death on the instrument.[302] Regardless of whether consistently higher cell density was observed comparing stimulant presence/absence, we will never know how many cells were alive and how many are anergic in the presence of PD-L1 using the hemocytometer alone.

Directly measuring cytokines would be invaluable to upholding the claim that the Jurkat cells are stimulated by PHA, and that stimulation is suppressed by PD-L1, but moreover that the stimulation is recovered due to the AuNPs. This type of monitoring would be more useful in co-mingling assays as it would be difficult to differentiate between Jurkat cells and other cells on the hemocytometer directly, and help reinforce the claim that the AuNPs do have immunotherapeutic properties like other ICIs.

Following optimization of Jurkat cell stimulation and staining, it is expected there will be an increase in cytokine production. One of the immunostimulant products assumed to be present under T cell activation is interleukin-2 (IL-2), a cytokine which will upregulate cytotoxic activity and maturation of T cells. We expect that IL-2 will be readily exported into the matrix; however, cytokines are too small to be detected by flow cytometry directly. To minimize subjection of the cells to further modification and molecules, it would be best to isolate the IL-2 rather than internalize it. Previous attempts to measure IL-2 production using kits from ThermoFisher (Cat. No. EH2IL2) or Sigma-Aldrich (Cat. No. RAB0296), where the absorbance intensity is correlated with the concentration of IL-2, did not prove fruitful.

Validating Stimulation by Detecting a Change in PD-1 Surface Expression – Flow Cytometry

T cell activation will also result in a change in protein expression between naïve and mature Jurkat cells.[207] We expect that upon T cell activation, not only will there be an increase in Jurkat cell density, but also higher overall expression of PD-1 on the Jurkat cell surface.[328] To evaluate this claim of maturation, it

would be useful to detect that intensity by flow cytometry. Using a fluorescent-conjugated antibody selective for PD-1, and then co-incubating with a secondary constitutively expressed protein (i.e., CD28 or CD3) could confirm targeting and create a baseline indicative of basal expression levels. Using non-specific isotypes will quantify how many events were false positives due to non-specific binding events with respect to the fluorophore. Then lastly, upon stimulation our Jurkat cells as described above with 1 µg PHA per $1 \cdot 10^6$ cells, we would expect a large increase in PD-1-associated events. This would corroborate the findings attributed to stimulation and T cell activation previously described only by hemocytometer. This could be taken further by including soluble PD-L1 to prevent the experimental stimulation, and if PD-1 expression remains "basal" on the Jurkat cells.

Validating Stimulation by Detecting a Change in PD-1 Surface Expression – Mass Spectrometry

Using protein fingerprints and the expected post-translational modifications, we would expect an increase in glycosylated SNT motifs,[303,329] indicative of more PD-1 and PD-L1 present on the mature cell surface.[293,328]

Assessing Selectivity of the AuNPs – Flow Cytometry

A more comprehensive test of binding would determine how selective the particles are and assess whether the particles are still as effective in much noisier, but biologically relevant environments. Similar to a cell viability assay, the AuNPs will be titrated into wells of cells. However, instead of assessing cell death and toxicity, the intent would be to quantify the proportion of AuNPs bound to PD-L1-presenting cells over other cells of varied PD-L1 expression. We would expect that particles selective for PD-L1 should have a greater likelihood of being associated with cells presenting the antigen, whereas cell lines with a much lower PD-L1 expression would result in only non-specific uptake events of AuNPs. By incorporating a fluorophore on the AuNPs, we could quantify the direct interactions and uptake of the particles with various cellular surfaces.

We would expect that cell surfaces with lower PD-L1 expression *should* have no AuNPs, and the non-specific binding events would be quantified using non-functionalized PEG NPs also with the same fluorophore. The cell lines will be tagged with an appropriate antigen (Table 6.2) and to simplify, all antigens will have the same fluorophore (except PD-L1-targeting AuNPs). This should make it easier to determine when PD-L1 binding events are competing. The proposed fluorophores for each target cell should have minimal overlap and should each be independently excited by a separate laser to minimize fluorescent overflow/bleeding.

Similarly, monitoring the SPR absorbance wavelength in supernatant after incubating in various cell lines could constitute a suitable method for determining the selectivity of the particles, as cells with lower PD-L1 expression should have higher SPR absorbance in their supernatant. To detect for high selectivity, we would expect a high population of PD-L1 targeting AuNPs on PD-L1-expressing surfaces, and conversely more particles in the supernatants of cell lines with no PD-L1. Under highly selective conditions we would expect a larger decrease in the SPR absorbance intensity with respect to the initial concentration, since most of the AuNPs are bound the cells. As SPR occurs in the visible light spectrum (520–550 nm), it would be best to avoid cell reporter fluorophores that are excited near those wavelengths (i.e., APC) to prevent bleed-through. Non-specific uptake could be detected by using the non-functionalized PEG NPs and still measuring the SPR in the cellular fraction. These uptake and selectivity studies could be corroborated with each other.

Table 6.2. Flow cytometry proposal with expected targets with fluorescent conjugates, their excitation and emission wavelengths, intended laser, and bandpass filter.

Cell Line	Target	Fluorophore
MB-MDA-231	PD-L1 (mark TNBC cells)	BV605 (violet 610/20)
MCF-10A	EGFR (mark noncancerous breast tissue cells)	V500
Jurkat E6-1	CD3 (induce stimulation; mark lymphoblasts)	AF700 (red 712/25)
Fluoro-PEG-NPs	None (these will demonstrate nonspecific uptake of AuNPs)	Cy5 (blue 525/40)
Fluoro-*f*-AuNPs	PD-L1 (be found predominantly in TNBC cells)	Cy5

Measuring Competitivity – Flow Cytometry

PD-L1-expressing MB-MDA-231 cells will be co-incubated with fluoro-*f*-AuNPs and another fluorescent protein (fluoro-mAb, commercially available or fluoro-PD-1). The AuNPs and fluorescent protein are expected to selectively bind PD-L1. The intent is to titrate the AuNPs with the fluoro[1]-mAb at a fixed concentration with respect to the cells. The two antigens for PD-L1 will result in disruption of the PD-1/PD-L1 interaction, and more AuNP occupancy on the cell surface at higher concentrations (e.g., [fluoro[2]-*f*-AuNPs] will displace the [fluoro[1]-mAbs:PD-L1] complex resulting in [fluoro[2]-*f*-AuNPs:PD-L1] complex and unbound [fluoro[1]-mAbs]). The disruption should decrease the observed populations attributed to fluoro[1]-mAb binding events indicating the success that the particles compete for a similar domain as our surrogate "PD-1".

Alternatively, using a chimeric fluorescent PD-1 protein could model the disrupting activity of the *f*-AuNPs by actively displacing more relevant proteins. Although, using a more transiently binding protein like PD-1 may be difficult to observe through flow cytometry. Conversely, by repeating this using cell lines with low PD-L1 expression, PD-L1-targeting isotypes, and vehicle control PEG NPs, we would be able to elucidate the degree of non-specific events the particles exhibit which could be useful in predicting and discussing the biodistribution data collected with *in vivo* studies.

To further validate the claim that the particles are competing to bind for PD-L1, we would expect T cell activity to return. This proliferative activity would result in higher concentrations of IL-2 present in the supernatants of co-mingled Jurkat and TNBC cells (Scheme 6.5). We would expect that at higher particle concentrations, the particles are more likely to inhibit the immunosuppressing pathway, and this will allow the expression of pro-inflammatory cytokines. Although previous attempts to measure the IL-2 and IL-6 in stimulated Jurkat cells were undetected (Figure S5.9).

Furthermore, this experiment may be expanded to characterize the selectivity of AuNP formulations, by repeating with varied cell lines of differing PD-L1 expression levels. This would help determine how other

tissues may be affected by particles adversely during their time in the circulatory system. Wholly characterizing the non-specific interactions would be useful in predicting where the particles might pool in the body prior to entering an animal with *in vivo* studies, and coinciding that data with the toxicological studies (i.e., AuNP titration), we may develop a more thorough avenue when dosing those particles in a clinical setting. This would mitigate the concern of toxicity via bioaccumulation and help remove one of the largest barriers in the drug discovery and development cycle.

For example, by co-incubating the T cells with "normal" (MCF-10A) cells, there is expected to be a "normal" or uninhibited expression level of IL-2. Effectively, upon incubation the T cells should remain "stimulated" as they are not interacting with PD-L1-presenting cells, and have cell densities and IL-2 levels similar to the respective monoculture of lymphoblasts. Conversely, when the stimulated Jurkat cells are co-incubated with a TNBC cell line such as MB-MDA-231, where the PD-L1 expression level is higher, we expect that IL-2 expression is hindered. However, in the presence of the *f*-AuNPs, if they do disrupt the PD-1/PD-L1 interaction, we expect some degree of recovery in IL-2 production. These experiments will focus on characterizing the selectivity and specificity of the particles and monitoring the ability to disrupt the PD-1/PD-L1 interaction between stimulated T cells and the TNBC cells *in vitro*.

Investigating AuNP Toxicity and Selectivity

Despite the promising effects observed in Figures 5.1–5.3, the concentration of the AuNPs is quite low (sub-nM), and without a titration there is not enough information to describe the particles as non-toxic. To address this, it would be appropriate to perform a titration with PEG particles and determine concentrations where AuNPs are exhibiting a detrimental effect on cell density. Furthermore, expanding that titration to cell lines beyond the immediate drug model (i.e., hepatocytes for accumulation in the liver; other PD-L1 privileged tissues) will be useful in assessing the safety of the particles prior to using animals.

Regardless, to characterize selectivity of the particles in various tissues to prepare for whole animal studies, the synthesis and functionalization of the particles would require overcoming scaleup challenges of samples requiring nearly 30 mg/mL ($AuNP_{15\ nm}$ 14 μM) per cell line per replicate.

Our results of sustained proliferation at sub-nM concentrations of *f*-AuNPs indicate the potency of the particles, however when Jurkat cells were treated with nearly 2 nM, there was a negative impact on proliferation (Figure 5.18). This could indicate that are higher cumulative concentrations of gold may be harmful on white blood cells. We expect that PEG-coated particles will carry relatively long circulatory half-lives, and non-specific uptake in peripheral tissues. As stated earlier, by determining these values prior to entering animals, it will be useful help ease the uncertainty of the safety of the particles.

Follow-Up 5B: Continuing Along the Wheel of Functionalization (and Establishing the Cellular Baseline)

By wholly characterizing the scope of the current series of particles, we achieve a more comprehensive understanding of how the particles may behave *in vivo.* These experiments would investigate other formulations based on the intrinsic physical differences and characterizing whether those attributes effect selectivity relative to the αLA-mAb formulation described in Chapter 5. The purpose is to overall optimize selectivity and reduce potential off-targeting without overengineering the platform.

Establishing the current formulation required omitting the exploration of variables, such as particle size. The particle size was maintained at 15 nm to address the expected drastic change in the size when

conjugating the antibodies by DLS (Figure S4.1). By maintaining the core size, it was easier to focus on improving the activity and functionalization of the core with the thiolated mAbs. Now, as the status quo of functionalized particles is established, it would be useful to explore other core sizes, as studies begin to focus on radiosensitization and particle internalization and validate whether the 15 nm core is the best for delivery.

DLS becomes less sensitive to characterize *f*-AuNPs with larger cores, as the change in volume upon functionalization will be become less noticeable (i.e., where functionalization of 15 nm AuNPs will have an expected 10-fold growth in volume, whereas 50 nm AuNPs will only grow ~3-fold). These changes in volume would likely be reflected with a Stokes shift, but the latter core size is also more likely to broaden overall. By increasing the size of the particles, we decrease the sensitivity of conjugation observable by DLS by effectively reducing the larger change in volume expected. Thereby making functionalized particles too similar in size to non-functionalized. However, the larger core will result in a drastic increase in molecular weight which will much more noticeable by SPR. By increasing the core size, or changing the shape, we exponentially increase the surface area, which also increases the theoretical maximum (ceiling) of antibodies for targeting. Similarly, this size increase could broaden the distribution of functionalized particles, making the SPR ceiling of binding activity more difficult to observe as higher valency in the analyte (the particles) decreases the response. With a current 15 nm diameter, the maximum number of mAbs estimated were at 26 per AuNP (assuming 100% coating per AuNP). To characterize the distribution, further optimization studies would investigate the partitioning of particles with varying degrees of antibody, such as an HPLC. These 1-D techniques can be used orthogonally to characterize the functionalization of the AuNPs, and used to monitor their batch variability during scaleup processes.

Previous attempts to characterize the distribution of mAb per AuNP, used the theoretical maximum occupancy of PEG and mAb molecules required to coat the total surface area of AuNPs in a given volume (%-coating). The control cases of 100% PEG and mAb, resulted in the latter being unstable, and each variable was proportionally adjusted to remain at “100%” coating of AuNPs. We found that between 10–50% mAb coating is where particles were stable to submit for binding response evaluation by SPR. However, as the mAb content increased, we did not obtain any form of binding response saturation, indicating that not all particles are functionalized equally. By increasing the core size, this may further broaden the degree of non-functionalized particles.

Alternatively, changing the stabilizer length will have large effects on stability, but it is unknown if these larger particles will be beneficial for delivery or efficacy. Having increased PEG length reduces the likelihood of core aggregation by increasing the steric bulk between the cores. However, that increased PEG length could equally reduce selectivity by precluding the antigen-binding sites. Each variable of nanomedicine has an apparent trade-off. Conversely, by reducing the PEG length, there should be higher instances of binding effects for the antibody (at the cost of potential core aggregation).

The previous chapter had optimization favour increasing thiol content to improve the grafting of the targeting mAbs, prioritizing activity and stability of the antibody as a strategic advantage to prevent over-PEGylation of the core. This relatively simple formulation of αLA-mAb and PEG_{2000} on a gold core has established a suitable baseline for T cell recoverability and targeting of PD-L1, but as described in other future work sections more complex formulations would be the next step, such as controlled release tethers (Follow-up 3C), integrating other reagents such as SN-38 to the particle for delivery (Follow-up 3B), and trying to optimize synthesis of a *tris*-thiol grafting agent (Follow-up 4A). Other particle

formulations should continue to investigate what linkers would be suitable to maintain targetability of the cores, while also considering which formulation would be appropriate for animal studies. Despite the promising immunotherapeutic effects observed *in vitro,* there are other factors that have yet to be characterized – selectivity for uptake and toxicity. Future directions with these AuNP should prioritize PK/PD studies and optimize scaleup for animal studies.

Follow-Up 5C: Radiosensitization and Emulating Pharmacokinetic Experiments (Predicting Tolerance Beyond the Tumour Site)

Lastly, one of the intentions of using gold particles was their value of sensitizing tumours for radiotherapy. Herein is a proposed clonogenic assay to characterize the non-specific and specific uptake of the cores for radiological studies. Simple models would focus on immediately relevant tissues to determine how much selectivity the cores have compared to a non-targeting vehicle.

Using a clonogenic assay, we can predict how much gold would be required to effectively sensitize a tumour. For the immediately relevant tissue, a series of experiments should focus on sensitizing both TNBCs and epithelial breast tissues (e.g., MCF-10A) as well as stimulated lymphoblasts (e.g., Jurkat E6-1), as these cell lines would be best representative of the environment we intend to treat. Each experiment would titrate the gold particle concentration, both with and without targeting, as to determine the specificity of the particles and measure the effective concentration required to enter and sensitize the cells. These assays are intended to characterize the selectivity of the particles as deliverable sensitizers to treating PD-L1 presenting cancer cells. We expect that high PD-L1 expression would result in less overall survivability, when treated with targeted AuNPs, and the vehicle controls would help characterize the degree to which the particles that are being taken elsewhere.

One caveat of these proposed series of experiments is that they look at the cell lines individually, whereas an actual tumour environment is much more complex.[90,330,331] Future work may consider performing a co-mingling assay, similarly discussed by Aurigene and in Follow-up 5A, emulating the complexity of the tumour environment *in vitro* via 3-D printing.[332] By creating an artificial tumour surrounded by other relevant epithelial tissues, we may directly observe the effects of uptake and radiosensitization and predict to what extent the collateral tissue damage would occur prior to entering animals.

Furthermore, the conclusion from Figures 5.1–5.3 suggest that the *f*-AuNPs can restore T cell activity in Jurkat cells when stimulation is exhausted in the presence of PD-L1, and therefore the particles may have potential immunotherapeutic benefit. However, if this cannot be detected in more complex systems, there is still promise of the particles as a delivery platform for other chemotherapeutic reagents and selective delivery core for future radiosensitization studies, indicating there are other avenues these particles may take as a therapeutic agent.

References

(1) Hainfeld, J. F.; Dilmanian, F. A.; Slatkin, D. N.; Smilowitz, H. M. Radiotherapy Enhancement with Gold Nanoparticles. *J. Pharm. Pharmacol.* **2008**, *60* (8), 977–985.

(2) Hainfeld, J. F.; Lin, L.; Slatkin, D. N.; Avraham Dilmanian, F.; Vadas, T. M.; Smilowitz, H. M. Gold Nanoparticle Hyperthermia Reduces Radiotherapy Dose. *Nanomedicine Nanotechnology, Biol. Med.* **2014**, *10* (8), 1609–1617.

(3) Vines, J. B.; Yoon, J. H.; Ryu, N. E.; Lim, D. J.; Park, H. Gold Nanoparticles for Photothermal Cancer Therapy. *Front. Chem.* **2019**, *7* (167), 1–16.

(4) Papaioannou, N. E.; Beniata, O. V.; Vitsos, P.; Tsitsilonis, O.; Samara, P. Harnessing the Immune System to Improve Cancer Therapy. *Ann. Transl. Med.* **2016**, *4* (14), 261–276.

(5) Dimitriou, N. M.; Tsekenis, G.; Balanikas, E. C.; Pavlopoulou, A.; Mitsiogianni, M.; Mantso, T.; Pashos, G.; Boudouvis, A. G.; Lykakis, I. N.; Tsigaridas, G.; Panayiotidis, M. I.; Yannopapas, V.; Georgakilas, A. G. Gold Nanoparticles, Radiations and the Immune System: Current Insights into the Physical Mechanisms and the Biological Interactions of This New Alliance towards Cancer Therapy. *Pharmacol. Ther.* **2017**, *178*, 1–17.

(6) Drasler, B.; Sayre, P.; Steinhäuser, K. G.; Petri-Fink, A.; Rothen-Rutishauser, B. In Vitro Approaches to Assess the Hazard of Nanomaterials. *NanoImpact* **2017**, *8* (March), 99–116.

(7) Shi, J.; Kantoff, P. W.; Wooster, R.; Farokhzad, O. C. Cancer Nanomedicine: Progress, Challenges and Opportunities. *Nat. Rev. Cancer* **2017**, *17* (1), 20–37.

(8) Sani, A.; Cao, C.; Cui, D. Toxicity of Gold Nanoparticles (AuNPs): A Review. *Biochem. Biophys. Reports* **2021**, *26*, 100991.

(9) Libutti, S. K.; Paciotti, G. F.; Byrnes, A. A.; Alexander, H. R.; Gannon, W. E.; Walker, M.; Seidel, G. D.; Yuldasheva, N.; Tamarkin, L. Phase I and Pharmacokinetic Studies of CYT-6091, a Novel PEGylated Colloidal Gold-RhTNF Nanomedicine. *Clin. Cancer Res.* **2010**, *16* (24), 6139–6149.

(10) Sykes, E. A.; Chen, J.; Zheng, G.; Chan, W. C. W. Investigating the Impact of Nanoparticle Size on Active and Passive Tumor Targeting Efficiency. *ACS Nano* **2014**, *8* (6), 5696–5706.

(11) Arvizo, R.; Bhattacharya, R.; Mukherjee, P. Gold Nanoparticles: Opportunities and Challenges in Nanomedicine. *Expert Opin. Drug Deliv.* **2010**, *7* (6), 753–763.

(12) Hatoyama, K.; Kitamura, N.; Takano-Kasuya, M.; Tokunaga, M.; Oikawa, T.; Ohta, M.; Hamada, Y.; Tada, H.; Kobayashi, Y.; Kamei, T.; Gonda, K. Quantitative Analyses of Amount and Localization of Radiosensitizer Gold Nanoparticles Interacting with Cancer Cells to Optimize Radiation Therapy. *Biochem. Biophys. Res. Commun.* **2019**, *508* (4), 1093–1100.

(13) Zhang, C.; Yan, L.; Gu, Z.; Zhao, Y. Strategies Based on Metal-Based Nanoparticles for Hypoxic-Tumor Radiotherapy. *Chem. Sci.* **2019**, *10* (29), 6932–6943.

(14) Mi, X.-J.; Xu, X. Y.; Choi, H. S.; Kim, H.; Cho, I. H.; Yi, T.-H.; Kim, Y.-J. The Immune-Enhancing Properties of Hwanglyeonhaedok-Tang-Mediated Biosynthesized Gold Nanoparticles in Macrophages and Splenocytes. **2022**.

(15) Dykman, L. A.; Khlebtsov, N. G. Gold Nanoparticles in Chemo-, Immuno-, and Combined Therapy: Review [Invited]. *Biomed. Opt. Express* **2019**, *10* (7), 3152.

(16) Lee, J.; Yang, J.; Ko, H.; Oh, S. J.; Kang, J.; Son, J. H.; Lee, K.; Lee, S. W.; Yoon, H. G.; Suh, J. S.; Huh, Y. M.; Haam, S. Multifunctional Magnetic Gold Nanocomposites: Human Epithelial Cancer Detection via Magnetic Resonance Imaging and Localized Synchronous Therapy. *Adv. Funct. Mater.* **2008**, *18* (2), 258–264.

(17) Shao, J.; Griffin, R. J.; Galanzha, E. I.; Kim, J. W.; Koonce, N.; Webber, J.; Mustafa, T.; Biris, A. S.; Nedosekin, D. A.; Zharov, V. P. Photothermal Nanodrugs: Potential of TNF-Gold Nanospheres for Cancer Theranostics. *Sci. Rep.* **2013**, *3* (1), 1–9.

(18) Singh, P.; Pandit, S.; Mokkapati, V. R. S. S.; Garg, A.; Ravikumar, V.; Mijakovic, I. Gold Nanoparticles in Diagnostics and Therapeutics for Human Cancer. *Int. J. Mol. Sci.* **2018**, *19* (7).

(19) Haiss, W.; Thanh, N. T. K.; Aveyard, J.; Fernig, D. G. Determination of Size and Concentration of Gold Nanoparticles from Extinction Spectra. *Anal. Chem.* **2007**, *79* (11), 4215–4221.

(20) Albanese, A.; Tsoi, K. M.; Chan, W. C. W. Simultaneous Quantification of Cells and Nanomaterials by Inductive-Coupled Plasma Techniques. *J. Lab. Autom.* **2013**, *18* (1), 99–104.

(21) Jazayeri, M. H.; Amani, H.; Pourfatollah, A. A.; Pazoki-Toroudi, H.; Sedighimoghaddam, B. Various Methods of Gold Nanoparticles (GNPs) Conjugation to Antibodies. *Sens. Bio-Sensing Res.* **2016**, *9*, 17–22.

(22) Khlebtsov, N.; Dykmana, L. Biodistribution and Toxicity of Engineered Gold Nanoparticles: A Review of in Vitro and in Vivo Studies. *Chem. Soc. Rev.* **2011**, *40* (3), 1647–1671.

(23) Zhang, X. D.; Wu, H. Y.; Wu, D.; Wang, Y. Y.; Chang, J. H.; Zhai, Z. Bin; Meng, A. M.; Liu, P. X.; Zhang, L. A.; Fan, F. Y. Toxicologic Effects of Gold Nanoparticles in Vivo by Different Administration Routes. *Int. J. Nanomedicine* **2010**, *5* (1).

(24) Owens, D. E.; Peppas, N. A. Opsonization, Biodistribution, and Pharmacokinetics of Polymeric Nanoparticles. *Int. J. Pharm.* **2006**, *307* (1), 93–102.

(25) Kumagai, M.; Sarmat, T. K.; Cabral, H.; Kaida, S.; Sekino, M.; Herlambang, N.; Osada, K.; Kano, M. R.; Nishiyama, N.; Kataoka, K. Enhanced in Vivo Magnetic Resonance Imaging of Tumors by PEGylated Iron-Oxide-Gold Core-Shell Nanoparticles with Prolonged Blood Circulation Properties. *Macromol. Rapid Commun.* **2010**, *31* (17), 1521–1528.

(26) Blanco, E.; Shen, H.; Ferrari, M. Principles of Nanoparticle Design for Overcoming Biological Barriers to Drug Delivery. *Nat. Biotechnol.* **2015**, *33* (9), 941–951.

(27) Yeh, Y. C.; Creran, B.; Rotello, V. M. Gold Nanoparticles: Preparation, Properties, and Applications in Bionanotechnology. *Nanoscale* **2012**, *4* (6), 1871–1880.

(28) Tripathi, K.; Driskell, J. D. Quantifying Bound and Active Antibodies Conjugated to Gold Nanoparticles: A Comprehensive and Robust Approach to Evaluate Immobilization Chemistry. *ACS Omega* **2018**, *3* (7), 8253–8259.

(29) Sperling, R. A.; Parak, W. J. Surface Modification, Functionalization and Bioconjugation of Colloidal Inorganic Nanoparticles. *Philos. Trans. R. Soc. A Math. Phys. Eng. Sci.* **2010**, *368* (1915), 1333–1383.

(30) Moraes Silva, S.; Tavallaie, R.; Sandiford, L.; Tilley, R. D.; Gooding, J. J. Gold Coated Magnetic Nanoparticles: From Preparation to Surface Modification for Analytical and Biomedical

Applications. *Chem. Commun.* **2016**, *52* (48), 7528–7540.

(31) Yang, W.; Liang, H.; Ma, S.; Wang, D.; Huang, J. Gold Nanoparticle Based Photothermal Therapy: Development and Application for Effective Cancer Treatment. *Sustain. Mater. Technol.* **2019**, *22*, e00109.

(32) Liu, S.; Lämmerhofer, M. Functionalized Gold Nanoparticles for Sample Preparation: A Review. *Electrophoresis* **2019**, *40* (18–19), 2438–2461.

(33) Xia, H.; Xiahou, Y.; Zhang, P.; Ding, W.; Wang, D. Revitalizing the Frens Method to Synthesize Uniform, Quasi-Spherical Gold Nanoparticles with Deliberately Regulated Sizes from 2 to 330 Nm. *Langmuir* **2016**, *32* (23), 5870–5880.

(34) Manson, J.; Kumar, D.; Meenan, B. J.; Dixon, D. Polyethylene Glycol Functionalized Gold Nanoparticles: The Influence of Capping Density on Stability in Various Media. *Gold Bull.* **2011**, *44* (2), 99–105.

(35) Moser, F.; Hildenbrand, G.; Müller, P.; Al Saroori, A.; Biswas, A.; Bach, M.; Wenz, F.; Cremer, C.; Burger, N.; Veldwijk, M. R.; Hausmann, M. Cellular Uptake of Gold Nanoparticles and Their Behavior as Labels for Localization Microscopy. *Biophys. J.* **2016**, *110* (4), 947–953.

(36) Martínez Rivas, C. J.; Tarhini, M.; Badri, W.; Miladi, K.; Greige-Gerges, H.; Nazari, Q. A.; Galindo Rodríguez, S. A.; Román, R. Á.; Fessi, H.; Elaissari, A. Nanoprecipitation Process: From Encapsulation to Drug Delivery. *Int. J. Pharm.* **2017**, *532* (1), 66–81.

(37) Xu, C.; Song, R. J.; Lu, P.; Chen, J. C.; Zhou, Y. Q.; Shen, G.; Jiang, M. J.; Zhang, W. PH-Triggered Charge-Reversal and Redox-Sensitive Drug-Release Polymer Micelles Codeliver Doxorubicin and Triptolide for Prostate Tumor Therapy. *Int. J. Nanomedicine* **2018**, *13*, 7229–7249.

(38) Grossen, P.; Witzigmann, D.; Sieber, S.; Huwyler, J. PEG-PCL-Based Nanomedicines: A Biodegradable Drug Delivery System and Its Application. *J. Control. Release* **2017**, *260*, 46–60.

(39) Bernabeu, E.; Gonzalez, L.; Legaspi, M. J.; Moretton, M. A.; Chiappetta, D. A. Paclitaxel-Loaded TPGS-b-PCL Nanoparticles: In Vitro Cytotoxicity and Cellular Uptake in MCF-7 and MDA-MB-231 Cells versus MPEG-b-PCL Nanoparticles and Abraxane® *J. Nanosci. Nanotechnol.* **2016**, *16* (1), 160–170.

(40) Ilkar Erdagi, S.; Yildiz, U. Diosgenin-Conjugated PCL-MPEG Polymeric Nanoparticles for the Co-Delivery of Anticancer Drugs: Design, Optimization, in Vitro Drug Release and Evaluation of Anticancer Activity. *New J. Chem.* **2019**, *43* (17), 6622–6635.

(41) Dong, Q.; Yang, H.; Wan, C.; Zheng, D.; Zhou, Z.; Xie, S.; Xu, L.; Du, J.; Li, F. Her2-Functionalized Gold-Nanoshelled Magnetic Hybrid Nanoparticles: A Theranostic Agent for Dual-Modal Imaging and Photothermal Therapy of Breast Cancer. *Nanoscale Res. Lett.* **2019**, *14* (1), 235–251.

(42) Primard, C.; Poecheim, J.; Heuking, S.; Sublet, E.; Esmaeili, F.; Borchard, G. Multifunctional PLGA-Based Nanoparticles Encapsulating Simultaneously Hydrophilic Antigen and Hydrophobic Immunomodulator for Mucosal Immunization. *Mol. Pharm.* **2013**, *10* (8), 2996–3004.

(43) Pandita, D.; Kumar, S.; Lather, V. Hybrid Poly(Lactic-Co-Glycolic Acid) Nanoparticles: Design and Delivery Prospectives. *Drug Discov. Today* **2015**, *20* (1), 95–104.

(44) Jokerst, J. V.; Lobovkina, T.; Zare, R. N.; Gambhir, S. S. Nanoparticle PEGylation for Imaging and

Therapy. *Nanomedicine (Lond).* **2011**, *6* (4), 715.

(45) Shi, J.; Xiao, Z.; Kamaly, N.; Farokhzad, O. C. Self-Assembled Targeted Nanoparticles: Evolution of Technologies and Bench to Bedside Translation. *Acc. Chem. Res.* **2011**, *44* (10), 1123–1134.

(46) Kim, E.; Yang, J.; Choi, J.; Suh, J. S.; Huh, Y. M.; Haam, S. Synthesis of Gold Nanorod-Embedded Polymeric Nanoparticles by a Nanoprecipitation Method for Use as Photothermal Agents. *Nanotechnology* **2009**, *20* (36).

(47) Łukasiewicz, S.; Mikołajczyk, A.; Błasiak, E.; Fic, E.; Dziedzicka-Wasylewska, M. Polycaprolactone Nanoparticles as Promising Candidates for Nanocarriers in Novel Nanomedicines. *Pharmaceutics* **2021**, *13* (2), 191.

(48) Tang, X.; Loc, W. S.; Dong, C.; Matters, G. L.; Butler, P. J.; Kester, M.; Meyers, C.; Jiang, Y.; Adair, J. H. The Use of Nanoparticulates to Treat Breast Cancer. *Nanomedicine* **2017**, *12* (19), 2367–2388.

(49) Nakagawa, T.; Gonda, K.; Kamei, T.; Cong, L.; Hamada, Y.; Kitamura, N.; Tada, H.; Ishida, T.; Aimiya, T.; Furusawa, N.; Nakano, Y.; Ohuchi, N. X-Ray Computed Tomography Imaging of a Tumor with High Sensitivity Using Gold Nanoparticles Conjugated to a Cancer-Specific Antibody via Polyethylene Glycol Chains on Their Surface. *Sci. Technol. Adv. Mater.* **2016**, *17* (1), 387–397.

(50) Wang, J.; Sun, X.; Mao, W.; Sun, W.; Tang, J.; Sui, M.; Shen, Y.; Gu, Z. Tumor Redox Heterogeneity-Responsive Prodrug Nanocapsules for Cancer Chemotherapy. *Adv. Mater.* **2013**, *25* (27), 3670–3676.

(51) Yang, C.; Uertz, J.; Chithrani, D. B. Colloidal Gold-Mediated Delivery of Bleomycin for Improved Outcome in Chemotherapy. *Nanomater. 2016, Vol. 6, Page 48* **2016**, *6* (3), 48.

(52) Albanese, A.; Tang, P. S.; Chan, W. C. W. The Effect of Nanoparticle Size, Shape, and Surface Chemistry on Biological Systems. *Annu. Rev. Biomed. Eng.* **2012**, *14*, 1–16.

(53) Wu, D.; Si, M.; Xue, H. Y.; Wong, H. L. Nanomedicine Applications in the Treatment of Breast Cancer: Current State of the Art. *Int. J. Nanomedicine* **2017**, *12*, 5879–5892.

(54) Goldenbogen, B.; Brodersen, N.; Gramatica, A.; Loew, M.; Liebscher, J.; Herrmann, A.; Egger, H.; Budde, B.; Arbuzova, A. Reduction-Sensitive Liposomes from a Multifunctional Lipid Conjugate and Natural Phospholipids: Reduction and Release Kinetics and Cellular Uptake. *Langmuir* **2011**, *27* (17), 10820–10829.

(55) Wang, T.; Wu, X.; Guo, C.; Zhang, K.; Xu, J.; Li, Z.; Jiang, S. Development of Inhibitors of the Programmed Cell Death-1/Programmed Cell Death-Ligand 1 Signaling Pathway. *J. Med. Chem.* **2019**, *62* (4), 1715–1730.

(56) Li, W.; Shao, B.; Liu, C.; Wang, H.; Zheng, W.; Kong, W.; Liu, X.; Xu, G.; Wang, C.; Li, H.; Zhu, L.; Yang, Y. Noninvasive Diagnosis and Molecular Phenotyping of Breast Cancer through Microbead-Assisted Flow Cytometry Detection of Tumor-Derived Extracellular Vesicles. *Small Methods* **2018**, *2* (11), 1800122.

(57) Jorns, J. M. Breast Cancer Biomarkers Challenges in Routine Estrogen Receptor, Progesterone Receptor, and HER2/Neu Evaluation. *Arch Pathol Lab Med* **2019**, *143* (12), 1444–1449.

(58) Colomer, R.; Aranda-López, I.; Albanell, J.; García-Caballero, T.; Ciruelos, E.; López-García, M. Á.; Cortés, J.; Rojo, F.; Martín, M.; Palacios-Calvo, J. Biomarkers in Breast Cancer: A Consensus

Statement by the Spanish Society of Medical Oncology and the Spanish Society of Pathology. *Clin. Transl. Oncol.* **2018**, *20* (7), 815–826.

(59) Torgovnick, A.; Schumacher, B. DNA Repair Mechanisms in Cancer Development and Therapy. *Front. Genet.* **2015**, *6* (157), 1–15.

(60) Jemal, A.; Bray, F.; Center, M. M.; Ferlay, J.; Ward, E.; Forman, D. Global Cancer Statistics. *CA. Cancer J. Clin.* **2011**, *61* (2), 69–90.

(61) Borrego-Soto, G.; Ortiz-López, R.; Rojas-Martínez, A. Ionizing Radiation-Induced DNA Injury and Damage Detection in Patients with Breast Cancer. *Genet. Mol. Biol.* **2015**, *38* (4), 420–432.

(62) Wu, N.; Zhang, J.; Zhao, J.; Mu, K.; Zhang, J.; Jin, Z.; Yu, J.; Liu, J. Precision Medicine Based on Tumorigenic Signaling Pathways for Triple-Negative Breast Cancer. *Oncol. Lett.* **2018**, *16* (4), 4984–4996.

(63) Liu, J. K. H. The History of Monoclonal Antibody Development - Progress, Remaining Challenges and Future Innovations. *Ann. Med. Surg.* **2014**, *3* (4), 113–116.

(64) Li, Y.; Li, F.; Jiang, F.; Lv, X.; Zhang, R.; Lu, A.; Zhang, G. A Mini-Review for Cancer Immunotherapy: Molecular Understanding of PD-1/ PD-L1 Pathway & Translational Blockade of Immune Checkpoints. *Int. J. Mol. Sci.* **2016**, *17* (7), 1151–1172.

(65) Waks, A. G.; Winer, E. P. Breast Cancer Treatment: A Review. *JAMA - J. Am. Med. Assoc.* **2019**, *321* (3), 288–300.

(66) Zhan, M. M.; Hu, X. Q.; Liu, X. X.; Ruan, B. F.; Xu, J.; Liao, C. From Monoclonal Antibodies to Small Molecules: The Development of Inhibitors Targeting the PD-1/PD-L1 Pathway. *Drug Discov. Today* **2016**, *21* (6), 1027–1036.

(67) Sasikumar, P. G.; Ramachandra, M. Small-Molecule Immune Checkpoint Inhibitors Targeting PD-1/PD-L1 and Other Emerging Checkpoint Pathways. *BioDrugs* **2018**, *32* (5), 481–497.

(68) Pauken, K. E.; Torchia, J. A.; Chaudhri, A.; Sharpe, A. H.; Freeman, G. J. Emerging Concepts in PD-1 Checkpoint Biology. *Semin. Immunol.* **2021**, *52*, 101480.

(69) Khalil, D. N.; Budhu, S.; Gasmi, B.; Zappasodi, R.; Hirschhorn-Cymerman, D.; Plitt, T.; De Henau, O.; Zamarin, D.; Holmgaard, R. B.; Murphy, J. T.; Wolchok, J. D.; Merghoub, T. The New Era of Cancer Immunotherapy: Manipulating T-Cell Activity to Overcome Malignancy. *Adv. Cancer Res.* **2015**, *128*, 1–68.

(70) Kumar, P. P.; Newland, J. R. Radiation Oncogenesis. *J. Natl. Med. Assoc.* **1980**, *72* (7), 687–690.

(71) Zhang, A. wei; Guo, W. hua; Qi, Y. fei; Wang, J. zhen; Ma, X. xing; Yu, D. xin. Synergistic Effects of Gold Nanocages in Hyperthermia and Radiotherapy Treatment. *Nanoscale Res. Lett.* **2016**, *11* (1), 279–293.

(72) Sibuyi, N. R. S.; Moabelo, K. L.; Fadaka, A. O.; Meyer, S.; Onani, M. O.; Madiehe, A. M.; Meyer, M. Multifunctional Gold Nanoparticles for Improved Diagnostic and Therapeutic Applications: A Review. *Nanoscale Res. Lett. 2021 161* **2021**, *16* (1), 1–27.

(73) Zhang, R.; Kiessling, F.; Lammers, T.; Pallares, R. M. Clinical Translation of Gold Nanoparticles. *Drug Deliv. Transl. Res.* **2023**, *13* (2), 378–385.

(74) Vlamidis, Y.; Voliani, V. Bringing Again Noble Metal Nanoparticles to the Forefront of Cancer Therapy. *Front. Bioeng. Biotechnol.* **2018**, *6* (OCT).

(75) Nukaly, H. Y.; Ansari, S. A. An Insight Into the Physicochemical Properties of Gold Nanoparticles in Relation to Their Clinical and Diagnostic Applications. *Cureus* **2023**, *15* (4).

(76) Anik, M. I.; Mahmud, N.; Al Masud, A.; Hasan, M. Gold Nanoparticles (GNPs) in Biomedical and Clinical Applications: A Review. *Nano Sel.* **2022**, *3* (4), 792–828.

(77) Albanese, A.; Chan, W. C. W. Effect of Gold Nanoparticle Aggregation on Cell Uptake and Toxicity. *ACS Nano* **2011**, *5* (7), 5478–5489.

(78) Guo, Q.; Huang, F.; Goncalves, C.; del Rincón, S. V.; Miller, W. H. *Translation of Cancer Immunotherapy from the Bench to the Bedsid*^{e,} 1st ed.; Elsevier Inc., 2019; Vol. 143.

(79) Arruebo, M.; Vilaboa, N.; Sáez-Gutierrez, B.; Lambea, J.; Tres, A.; Valladares, M.; González-Fernández, Á. Assessment of the Evolution of Cancer Treatment Therapies. *Cancers (Basel).* **2011**, *3* (3), 3279–3330.

(80) Chhabra, N.; Kennedy, J. A Review of Cancer Immunotherapy Toxicity: Immune Checkpoint Inhibitors. *J. Med. Toxicol.* **2021**, *17* (4), 411–424.

(81) Wu, Y.; Chen, W.; Xu, Z. P.; Gu, W. PD-L1 Distribution and Perspective for Cancer Immunotherapy— Blockade, Knockdown, or Inhibition. *Front. Immunol.* **2019**, *10* (AUG), 2022–2036.

(82) Hu, Z.; Shen, R.; Campbel, A.; McMichael, E.; Yu, L.; Ramaswamy, B.; London, C. A.; Xu, T.; Carson, W. E. Targeting Tissue Factor for Immunotherapy of Triple-Negative Breast Cancer Using a Second-Generation ICON. *Cancer Immunol. Res.* **2018**, *6* (6), 671–684.

(83) Sweis, R. F.; Luke, J. J. Mechanistic and Pharmacologic Insights on Immune Checkpoint Inhibitors. *Pharmacological Research*. Academic Press June 1, 2017, pp 1–9.

(84) Sievers, E. L.; Senter, P. D. Antibody-Drug Conjugates in Cancer Therapy. *Annu. Rev. Med.* **2013**, *64*, 15–29.

(85) Diamantis, N.; Banerji, U. Antibody-Drug Conjugates - An Emerging Class of Cancer Treatment. *Br. J. Cancer* **2016**, *114* (4), 362–367.

(86) Williams, G. H.; Stoeber, K. The Cell Cycle and Cancer. *J. Pathol.* **2012**, *226* (2), 352–364.

(87) Marschall, A. L. J.; Frenzel, A.; Schirrmann, T.; Schüngel, M.; Dübel, S. Targeting Antibodies to the Cytoplasm. *mAbs*. Taylor & Francis January 2011, pp 3–16.

(88) Slastnikova, T. A.; Ulasov, A. V.; Rosenkranz, A. A.; Sobolev, A. S. Targeted Intracellular Delivery of Antibodies: The State of the Art. *Front. Pharmacol.* **2018**, *9* (OCT).

(89) Nichols, J. W.; Bae, Y. H. EPR: Evidence and Fallacy. *J. Control. Release* **2014**, *190*, 451–464.

(90) Sindhwani, S.; Syed, A. M.; Ngai, J.; Kingston, B. R.; Maiorino, L.; Rothschild, J.; MacMillan, P.; Zhang, Y.; Rajesh, N. U.; Hoang, T.; Wu, J. L. Y.; Wilhelm, S.; Zilman, A.; Gadde, S.; Sulaiman, A.; Ouyang, B.; Lin, Z.; Wang, L.; Egeblad, M.; Chan, W. C. W. The Entry of Nanoparticles into Solid Tumours. *Nat. Mater.* **2020**, *19* (5), 566–575.

(91) Zhao, X.; Liu, P. Reduction-Responsive Core-Shell-Corona Micelles Based on Triblock Copolymers:

Novel Synthetic Strategy, Characterization, and Application as a Tumor Microenvironment-Responsive Drug Delivery System. *ACS Appl. Mater. Interfaces* **2015**, *7* (1), 166–174.

(92) Lai, Y.; Wei, X.; Lin, S.; Qin, L.; Cheng, L.; Li, P. Current Status and Perspectives of Patient-Derived Xenograft Models in Cancer Research. *J. Hematol. Oncol.* **2017**, *10* (1), 106–120.

(93) Hida, K.; Maishi, N.; Torii, C.; Hida, Y. Tumor Angiogenesis—Characteristics of Tumor Endothelial Cells. *Int. J. Clin. Oncol.* **2016**, *21* (2), 206–212.

(94) Brülisauer, L.; Gauthier, M. A.; Leroux, J. C. Disulfide-Containing Parenteral Delivery Systems and Their Redox-Biological Fate. *J. Control. Release* **2014**, *195*, 147–154.

(95) Wang, X.; Xuan, Z.; Zhu, X.; Sun, H.; Li, J.; Xie, Z. Near-Infrared Photoresponsive Drug Delivery Nanosystems for Cancer Photo-Chemotherapy. *J. Nanobiotechnology* **2020**, *18* (1), 1–19.

(96) Mura, S.; Nicolas, J.; Couvreur, P. Stimuli-Responsive Nanocarriers for Drug Delivery. *Nat. Mater.* **2013**, *12* (11), 991–1003.

(97) Karimi, M.; Ghasemi, A.; Sahandi Zangabad, P.; Rahighi, R.; Moosavi Basri, S. M.; Mirshekari, H.; Amiri, M.; Shafaei Pishabad, Z.; Aslani, A.; Bozorgomid, M.; Ghosh, D.; Beyzavi, A.; Vaseghi, A.; Aref, A. R.; Haghani, L.; Bahrami, S.; Hamblin, M. R. Smart Micro/Nanoparticles in Stimulus-Responsive Drug/Gene Delivery Systems. *Chem. Soc. Rev.* **2016**, *45* (5), 1457–1501.

(98) Cruje, C.; Yang, C.; Uertz, J.; Van Prooijen, M.; Chithrani, B. D. Optimization of PEG Coated Nanoscale Gold Particles for Enhanced Radiation Therapy. *RSC Adv.* **2015**, *5* (123), 101525–101532.

(99) Shi, L.; Zhang, J.; Zhao, M.; Tang, S.; Cheng, X.; Zhang, W.; Li, W.; Liu, X.; Peng, H.; Wang, Q. Effects of Polyethylene Glycol on the Surface of Nanoparticles for Targeted Drug Delivery. *Nanoscale* **2021**, *13* (24), 10748–10764.

(100) Tunger, A.; Sommer, U.; Wehner, R.; Kubasch, A. S.; Grimm, M.-O.; Bachmann, M. P.; Platzbecker, U.; Bornhäuser, M.; Baretton, G.; Schmitz, M. The Evolving Landscape of Biomarkers for Anti-PD-1 or Anti-PD-L1 Therapy. *J. Clin. Med.* **2019**, *8* (10), 1534.

(101) Liu, L. Y.; Ma, X. Z.; Ouyang, B.; Ings, D. P.; Marwah, S.; Liu, J.; Chen, A. Y.; Gupta, R.; Manuel, J.; Chen, X. C.; Gage, B. K.; Cirlan, I.; Khuu, N.; Chung, S.; Camat, D.; Cheng, M.; Sekhon, M.; Zagorovsky, K.; Abdou Mohamed, M. A.; Thoeni, C.; Atif, J.; Echeverri, J.; Kollmann, D.; Fischer, S.; Bader, G. D.; Chan, W. C. W.; Michalak, T. I.; McGilvray, I. D.; MacParland, S. A. Nanoparticle Uptake in a Spontaneous and Immunocompetent Woodchuck Liver Cancer Model. *ACS Nano* **2020**, *14* (4), 4698–4715.

(102) Kumar, M.; Kulkarni, P.; Liu, S.; Chemuturi, N.; Shah, D. K. Nanoparticle Biodistribution Coefficients: A Quantitative Approach for Understanding the Tissue Distribution of Nanoparticles. *Adv. Drug Deliv. Rev.* **2023**, *194*.

(103) Ding, C.; Li, Z. A Review of Drug Release Mechanisms from Nanocarrier Systems. *Mater. Sci. Eng. C* **2017**, *76*, 1440–1453.

(104) Piccolo, O.; Lincoln, J. D.; Melong, N.; Orr, B. C.; Fernandez, N. R.; Borsavage, J.; Berman, J. N.; Robar, J.; Ha, M. N. Radiation Dose Enhancement Using Gold Nanoparticles with a Diamond Linear Accelerator Target: A Multiple Cell Type Analysis. *Sci. Reports 2022 121* **2022**, *12* (1), 1–14.

(105) Chames, P.; Van Regenmortel, M.; Weiss, E.; Baty, D. Therapeutic Antibodies: Successes, Limitations and Hopes for the Future. *Br. J. Pharmacol.* **2009**, *157* (2), 220–233.

(106) Wang, Y.; Wang, H.; Yao, H.; Li, C.; Fang, J. Y.; Xu, J. Regulation of PD-L1: Emerging Routes for Targeting Tumor Immune Evasion. *Front. Pharmacol.* **2018**, *9* (MAY), 1–13.

(107) Zhou, L.; Jiao, X.; Liu, S.; Hao, M.; Cheng, S.; Zhang, P.; Wen, Y. Functional DNA-Based Hydrogel Intelligent Materials for Biomedical Applications. *J. Mater. Chem. B* **2020**, *8* (10), 1991–2009.

(108) Agrawal, P.; Tatode, A.; Umekar, M. Solid Lipid Nanoparticle for the Delivery of Docetaxel: A Review. *J. Drug Deliv. Ther.* **2020**, *10* (5-s), 224–228.

(109) Mohanty, R.; Chowdhury, C. R.; Arega, S.; Sen, P.; Ganguly, P.; Ganguly, N. CAR T Cell Therapy: A New Era for Cancer Treatment (Review). *Oncol. Rep.* **2019**, *42* (6), 2183–2195.

(110) Emami, F.; Banstola, A.; Vatanara, A.; Lee, S.; Kim, J. O.; Jeong, J. H.; Yook, S. Doxorubicin and Anti-PD-L1 Antibody Conjugated Gold Nanoparticles for Colorectal Cancer Photochemotherapy. *Mol. Pharm.* **2019**, *16* (3), 1184–1199.

(111) Ott, P. A.; Hodi, F. S.; Robert, C. CTLA-4 and PD-1/PD-L1 Blockade: New Immunotherapeutic Modalities with Durable Clinical Benefit in Melanoma Patients. *Clin. Cancer Res.* **2013**, *19* (19), 5300–5309.

(112) Šmahel, M. PD-1/PD-L1 Blockade Therapy for Tumors with Downregulated MHC Class I Expression. *Int. J. Mol. Sci.* **2017**, *18* (6).

(113) Capasso, A.; Lang, J.; Pitts, T. M.; Jordan, K. R.; Lieu, C. H.; Davis, S. L.; Diamond, J. R.; Kopetz, S.; Barbee, J.; Peterson, J.; Freed, B. M.; Yacob, B. W.; Bagby, S. M.; Messersmith, W. A.; Slansky, J. E.; Pelanda, R.; Eckhardt, S. G. Characterization of Immune Responses to Anti-PD-1 Mono and Combination Immunotherapy in Hematopoietic Humanized Mice Implanted with Tumor Xenografts. *J. Immunother. Cancer* **2019**, *7* (1), 37–53.

(114) Myers, G. Immune-Related Adverse Events of Immune Checkpoint Inhibitors: A Brief Review. *Curr. Oncol.* **2018**, *25* (5), 342–347.

(115) Grasselly, C.; Denis, M.; Bourguignon, A.; Talhi, N.; Mathe, D.; Tourette, A.; Serre, L.; Jordheim, L. P.; Matera, E. L.; Dumontet, C. The Antitumor Activity of Combinations of Cytotoxic Chemotherapy and Immune Checkpoint Inhibitors Is Model-Dependent. *Front. Immunol.* **2018**, *9* (OCT), 2100.

(116) Yang, Y. S.; Carney, R. P.; Stellacci, F.; Irvine, D. J. Enhancing Radiotherapy by Lipid Nanocapsule-Mediated Delivery of Amphiphilic Gold Nanoparticles to Intracellular Membranes. *ACS Nano* **2014**, *8* (9), 8992–9002.

(117) Matesich, M. A.; Shapiro, C. L. Second Cancers after Breast Cancer Treatment. *Semin. Oncol.* **2003**, *30* (6), 740–748.

(118) Belousov, A. V.; Morozov, V. N.; Krusanov, G. A.; Kolyvanova, M. A.; Shtil, A. A. The Effect of Gold Nanoparticle Surface Modification with Polyethylene Glycol on the Absorbed Dose Distribution upon Irradiation with 137 Cs and 60 Co Photons. *Biophys. (Russian Fed.)* **2019**, *64* (1), 23–30.

(119) Rahman, W. N.; Corde, S.; Yagi, N.; Abdul Aziz, S. A.; Annabell, N.; Geso, M. Optimal Energy for Cell Radiosensitivity Enhancement by Gold Nanoparticles Using Synchrotron-Based

Monoenergetic Photon Beams. *Int. J. Nanomedicine* **2014**, *9* (1), 2459–2467.

(120) Sabbaghizadeh, R.; Shamsudin, R.; Deyhimihaghighi, N.; Sedghi, A. Enhancement of Dose Response and Nuclear Magnetic Resonance Image of PAGAT Polymer Gel Dosimeter by Adding Silver Nanoparticles. *PLoS One* **2017**, *12*, 1–18.

(121) Almeida, J. P. M.; Figueroa, E. R.; Drezek, R. A. Gold Nanoparticle Mediated Cancer Immunotherapy. *Nanomedicine Nanotechnology, Biol. Med.* **2014**, *10* (3), 503–514.

(122) Marei, H. E.; Cenciarelli, C.; Hasan, A. Potential of Antibody–Drug Conjugates (ADCs) for Cancer Therapy. *Cancer Cell Int. 2022 221* **2022**, *22* (1), 1–12.

(123) Polewski, M. D.; Reveron-Thornton, R. F.; Cherryholmes, G. A.; Marinov, G. K.; Cassady, K.; Aboody, K. S. Increased Expression of System Xc- in Glioblastoma Confers an Altered Metabolic State and Temozolomide Resistance. *Mol. Cancer Res.* **2016**, *14* (12), 1229–1242.

(124) Vitale, D. L.; Icardi, A.; Rosales, P.; Spinelli, F. M.; Sevic, I.; Alaniz, L. D. Targeting the Tumor Extracellular Matrix by the Natural Molecule 4-Methylumbelliferone: A Complementary and Alternative Cancer Therapeutic Strategy. *Front. Oncol.* **2021**, *11*, 3938.

(125) Hainfeld, J. F.; Slatkin, D. N.; Smilowitz, H. M. The Use of Gold Nanoparticles to Enhance Radiotherapy in Mice. *Phys. Med. Biol.* **2004**, *49* (18).

(126) Li, P.; Shi, Y. wen; Li, B. xin; Xu, W. cai; Shi, Z. liang; Zhou, C.; Fu, S. Photo-Thermal Effect Enhances the Efficiency of Radiotherapy Using Arg-Gly-Asp Peptides-Conjugated Gold Nanorods That Target Aαvβ3 in Melanoma Cancer Cells. *J. Nanobiotechnology* **2015**, *13* (1), 52–60.

(127) Brower, V. Tracking Chemotherapy's Effects on Secondary Cancers. *J. Natl. Cancer Inst.* **2013**, *105* (19), 1421–1422.

(128) Yu, D.; Zhang, Y.; Lu, H.; Zhao, D. Silver Nanoparticles Coupled to Anti-EGFR Antibodies Sensitize Nasopharyngeal Carcinoma Cells to Irradiation. *Mol. Med. Rep.* **2017**, *16* (6), 9005–9010.

(129) Chen, J. M. M.; Chen, K. C.; Chiu, S. C.; Chen, R. Y.; Hsia, J. Y.; Huang, Y. R. J.; Yu, C. T. R. Differential Contribution of Protein Phosphatase 1α to Cell Transformation of Different Cell Types. *Oncol. Rep.* **2019**, *42* (4), 1598–1608.

(130) Caldarella, A.; Crocetti, E.; Bianchi, S.; Vezzosi, V.; Urso, C.; Biancalani, M.; Zappa, M. Female Breast Cancer Status According to ER, PR and HER2 Expression: A Population Based Analysis. *Pathol. Oncol. Res.* **2011**, *17* (3), 753–758.

(131) Carey, L. A.; Perou, C. M.; Livasy, C. A.; Dressler, L. G.; Cowan, D.; Conway, K.; Karaca, G.; Troester, M. A.; Chiu, K. T.; Edmiston, S.; Deming, S. L.; Geradts, J.; Cheang, M. C. U.; Nielsen, T. O.; Moorman, P. G.; Earp, H. S.; Millikan, R. C. Race, Breast Cancer Subtypes, and Survival in the Carolina Breast Cancer Study. *J. Am. Med. Assoc.* **2006**, *295* (21), 2492–2502.

(132) Tobias, J. S. Recent Advances in Endocrine Therapy for Postmenopausal Women with Early Breast Cancer: Implications for Treatment and Prevention. *Ann. Oncol.* **2004**, *15* (12), 1738–1747.

(133) Zhang, Y.; Wang, M.; Liu, W.; Peng, X. Optical Imaging of Triple-Negative Breast Cancer Cells in Xenograft Athymic Mice Using an ICAM-1-Targeting Small-Molecule Probe. *Mol. Imaging Biol.* **2019**, *21* (5), 835–841.

(134) Buisseret, L.; Pommey, S.; Allard, B.; Garaud, S.; Bergeron, M.; Cousineau, I.; Ameye, L.; Bareche,

Y.; Paesmans, M.; Crown, J. P. A.; Di Leo, A.; Loi, S.; Piccart-Gebhart, M.; Willard-Gallo, K.; Sotiriou, C.; Stagg, J. Clinical Significance of CD73 in Triple-Negative Breast Cancer: Multiplex Analysis of a Phase III Clinical Trial. *Ann. Oncol.* **2018**, *29* (4), 1056–1062.

(135) Lafont, V.; Michaud, H.-A.; Bonnefoy, N. CD73: A New Biomarker in Triple-Negative Breast Cancer. *Transl. Cancer Res.* **2018**, *7* (5), S594–S596.

(136) Qin, T.; Zeng, Y.; Qin, G.; Xu, F.; Lu, J.; Fang, W.; Xue, C.; Zhan, J.; Zhang, X.; Zheng, Q.; Peng, R.; Yuan, Z.; Zhang, L.; Wang, S. High PD-L1 Expression Was Associated with Poor Prognosis in 870 Chinese Patients with Breast Cancer. *Oncotarget* **2015**, *6* (32), 33792–33981.

(137) Li, C. W.; Lim, S. O.; Chung, E. M.; Kim, Y. S.; Park, A. H.; Yao, J.; Cha, J. H.; Xia, W.; Chan, L. C.; Kim, T.; Chang, S. S.; Lee, H. H.; Chou, C. K.; Liu, Y. L.; Yeh, H. C.; Perillo, E. P.; Dunn, A. K.; Kuo, C. W.; Khoo, K. H.; Hsu, J. L.; Wu, Y.; Hsu, J. M.; Yamaguchi, H.; Huang, T. H.; Sahin, A. A.; Hortobagyi, G. N.; Yoo, S. S.; Hung, M. C. Eradication of Triple-Negative Breast Cancer Cells by Targeting Glycosylated PD-L1. *Cancer Cell* **2018**, *33* (2), 187-201.e10.

(138) Soliman, H.; Khalil, F.; Antonia, S. PD-L1 Expression Is Increased in a Subset of Basal Type Breast Cancer Cells. *PLoS One* **2014**, *9* (2), e88557.

(139) Li, X.; Dai, H.; Wang, H.; Han, W. Exploring Innate Immunity in Cancer Immunotherapy: Opportunities and Challenges. *Cell. Mol. Immunol.* **2021**, *18* (6), 1607.

(140) Schirrmacher, V. From Chemotherapy to Biological Therapy: A Review of Novel Concepts to Reduce the Side Effects of Systemic Cancer Treatment (Review). *Int. J. Oncol.* **2019**, *54* (2), 407–419.

(141) Barlesi, F.; Vansteenkiste, J.; Spigel, D.; Ishii, H.; Garassino, M.; de Marinis, F.; Özgüroğlu, M.; Szczesna, A.; Polychronis, A.; Uslu, R.; Krzakowski, M.; Lee, J. S.; Calabrò, L.; Arén Frontera, O.; Ellers-Lenz, B.; Bajars, M.; Ruisi, M.; Park, K. Avelumab versus Docetaxel in Patients with Platinum-Treated Advanced Non-Small-Cell Lung Cancer (JAVELIN Lung 200): An Open-Label, Randomised, Phase 3 Study. *Lancet Oncol.* **2018**, *19* (11), 1468–1479.

(142) Yang, J.; Hu, L. Immunomodulators Targeting the PD-1/PD-L1 Protein-Protein Interaction: From Antibodies to Small Molecules. *Med. Res. Rev.* **2019**, *39* (1), 265–301.

(143) Zarganes-Tzitzikas, T.; Konstantinidou, M.; Gao, Y.; Krzemien, D.; Zak, K.; Dubin, G.; Holak, T. A.; Dömling, A. Inhibitors of Programmed Cell Death 1 (PD-1): A Patent Review (2010-2015). *Expert Opin. Ther. Pat.* **2016**, *26* (9), 973–977.

(144) Sharpe, A. H.; Pauken, K. E. The Diverse Functions of the PD1 Inhibitory Pathway. *Nat. Rev. Immunol.* **2018**, *18* (3), 153–167.

(145) Butte, M. J.; Peña-Cruz, V.; Kim, M.-J.; Freeman, G. J.; Sharpe, A. H. Interaction of Human PD-L1 and B7-1. *Mol. Immunol.* **2008**, *45* (13), 3567–3572.

(146) Kythreotou, A.; Siddique, A.; Mauri, F. A.; Bower, M.; Pinato, D. J. PD-L1. *J. Clin. Pathol.* **2018**, *71* (3), 189–194.

(147) Wang, L. L.; Li, Z. H.; Hu, X. H.; Muyayalo, K. P.; Zhang, Y. H.; Liao, A. H. The Roles of the PD-1/PD-L1 Pathway at Immunologically Privileged Sites. *Am. J. Reprod. Immunol.* **2017**, *78* (2), e12710.

(148) Rittmeyer, A.; Barlesi, F.; Waterkamp, D.; Park, K.; Ciardiello, F.; von Pawel, J.; Gadgeel, S. M.;

Hida, T.; Kowalski, D. M.; Dols, M. C.; Cortinovis, D. L.; Leach, J.; Polikoff, J.; Barrios, C.; Kabbinavar, F.; Frontera, O. A.; De Marinis, F.; Turna, H.; Lee, J. S.; Ballinger, M.; Kowanetz, M.; He, P.; Chen, D. S.; Sandler, A.; Gandara, D. R. Atezolizumab versus Docetaxel in Patients with Previously Treated Non-Small-Cell Lung Cancer (OAK): A Phase 3, Open-Label, Multicentre Randomised Controlled Trial. *Lancet* **2017**, *389* (10066), 255–265.

(149) Sharpe, A.; Butte, M.; Oyama, S. Modulators of Immunoinhibitory Receptor PD-1, and Methods of Use Thereof. WO2011082400A2, 2011.

(150) Alsaab, H. O.; Sau, S.; Alzhrani, R.; Tatiparti, K.; Bhise, K.; Kashaw, S. K.; Iyer, A. K. PD-1 and PD-L1 Checkpoint Signaling Inhibition for Cancer Immunotherapy: Mechanism, Combinations, and Clinical Outcome. *Front. Pharmacol.* **2017**, *8* (561), 1–20.

(151) Letendre, P.; Monga, V.; Milhem, M.; Zakharia, Y. Ipilimumab: From Preclinical Development to Future Clinical Perspectives in Melanoma. *Futur. Oncol.* **2017**, *13* (7), 625–636.

(152) Kazandjian, D.; Suzman, D. L.; Blumenthal, G.; Mushti, S.; He, K.; Libeg, M.; Keegan, P.; Pazdur, R. FDA Approval Summary: Nivolumab for the Treatment of Metastatic Non-Small Cell Lung Cancer With Progression On or After Platinum-Based Chemotherapy. *Oncologist* **2016**, *21* (5), 634–642.

(153) Sul, J.; Blumenthal, G. M.; Jiang, X.; He, K.; Keegan, P.; Pazdur, R. FDA Approval Summary: Pembrolizumab for the Treatment of Patients With Metastatic Non-Small Cell Lung Cancer Whose Tumors Express Programmed Death-Ligand 1. *Oncologist* **2016**, *21* (5), 643–650.

(154) Weinstock, C.; Khozin, S.; Suzman, D.; Zhang, L.; Tang, S.; Wahby, S.; Goldberg, K. B.; Kim, G.; Pazdur, R. U.S. Food and Drug Administration Approval Summary: Atezolizumab for Metastatic Non–Small Cell Lung Cancer. *Clin. Cancer Res.* **2017**, *23* (16), 4534–4539.

(155) Apolo, A. B.; Infante, J. R.; Balmanoukian, A.; Patel, M. R.; Wang, D.; Kelly, K.; Mega, A. E.; Britten, C. D.; Ravaud, A.; Mita, A. C.; Safran, H.; Stinchcombe, T. E.; Srdanov, M.; Gelb, A. B.; Schlichting, M.; Chin, K.; Gulley, J. L. Avelumab, an Anti–Programmed Death-Ligand 1 Antibody, In Patients With Refractory Metastatic Urothelial Carcinoma: Results From a Multicenter, Phase Ib Study. *J. Clin. Oncol.* **2017**, *35* (19), 2117–2124.

(156) Antonia, S. J.; Villegas, A.; Daniel, D.; Vicente, D.; Murakami, S.; Hui, R.; Yokoi, T.; Chiappori, A.; Lee, K. H.; de Wit, M.; Cho, B. C.; Bourhaba, M.; Quantin, X.; Tokito, T.; Mekhail, T.; Planchard, D.; Kim, Y.-C.; Karapetis, C. S.; Hiret, S.; Ostoros, G.; Kubota, K.; Gray, J. E.; Paz-Ares, L.; de Castro Carpeño, J.; Wadsworth, C.; Melillo, G.; Jiang, H.; Huang, Y.; Dennis, P. A.; Özgüroğlu, M. Durvalumab after Chemoradiotherapy in Stage III Non–Small-Cell Lung Cancer. *N. Engl. J. Med.* **2017**, *377* (20), 1919–1929.

(157) Markham, A.; Duggan, S. Cemiplimab: First Global Approval. *Drugs* **2018**, *78* (17), 1841–1846.

(158) Ning, W.-J.; Liu, X.; Zeng, H.-Y.; An, Z.-Q.; Luo, W.-X.; Xia, N.-S. Recent Progress in Antibody-Based Therapeutics for Triple-Negative Breast Cancer Recent Progress in Antibody-Based Therapeutics for Triple-Negative Breast Cancer. *Expert Opin. Drug Deliv.* **2022**, *19* (7), 815–832.

(159) Yi, M.; Zheng, X.; Niu, M.; Zhu, S.; Ge, H.; Wu, K. Combination Strategies with PD-1/PD-L1 Blockade: Current Advances and Future Directions. *Mol. Cancer* **2022**, *21* (1), 1–27.

(160) Saini, K. S.; Punie, K.; Twelves, C.; Bortini, S.; de Azambuja, E.; Anderson, S.; Criscitiello, C.; Awada, A.; Loi, S. Antibody-Drug Conjugates, Immune-Checkpoint Inhibitors, and Their Combination in Breast Cancer Therapeutics. *Expert Opin. Biol. Ther.* **2021**, *21* (7), 945–962.

(161) He, L.; Wang, L.; Wang, Z.; Li, T.; Chen, H.; Zhang, Y.; Hu, Z.; Dimitrov, D. S.; Du, J.; Liao, X. Immune Modulating Antibody-Drug Conjugate (IM-ADC) for Cancer Immunotherapy. *J. Med. Chem.* **2021**, *64* (21), 15716–15726.

(162) Sau, S.; Petrovici, A.; Alsaab, H. O.; Bhise, K.; Iyer, A. K. PDL-1 Antibody Drug Conjugate for Selective Chemo-Guided Immune Modulation of Cancer. *Cancers (Basel).* **2019**, *11* (232), 1–12.

(163) Ventola, C. L. Progress in Nanomedicine: Approved and Investigational Nanodrugs. *P T* **2017**, *42* (12), 742–755.

(164) Butterworth, K. T.; McMahon, S. J.; Taggart, L. E.; Prise, K. M. Radiosensitization by Gold Nanoparticles: Effective at Megavoltage Energies and Potential Role of Oxidative Stress. *Transl. Cancer Res.* **2013**, *2* (4).

(165) Xu, Z.; Liu, S.; Kang, Y.; Wang, M. Glutathione-Responsive Polymeric Micelles Formed by a Biodegradable Amphiphilic Triblock Copolymer for Anticancer Drug Delivery and Controlled Release. *ACS Biomater. Sci. Eng.* **2015**, *1* (7), 585–592.

(166) Park, M. V. D. Z.; Lankveld, D. P. K.; van Loveren, H.; de Jong, W. H. The Status of in Vitro Toxicity Studies in the Risk Assessment of Nanomaterials. *Nanomedicine* **2009**, *4* (6), 669–685.

(167) Yang, C.; Bromma, K.; Chithrani, D. Peptide Mediated in Vivo Tumor Targeting of Nanoparticles through Optimization in Single and Multilayer in Vitro Cell Models. *Cancers (Basel).* **2018**, *10* (3), 84–100.

(168) Patra, C. R.; Bhattacharya, R.; Wang, E.; Katarya, A.; Lau, J. S.; Dutta, S.; Muders, M.; Wang, S.; Buhrow, S. A.; Safgren, S. L.; Yaszemski, M. J.; Reid, J. M.; Ames, M. M.; Mukherjee, P.; Mukhopadhyay, D. Targeted Delivery of Gemcitabine to Pancreatic Adenocarcinoma Using Cetuximab as a Targeting Agent. *Cancer Res.* **2008**, *68* (6), 1970–1978.

(169) Sohail, M. F.; Rehman, M.; Sarwar, H. S.; Naveed, S.; Salman, O.; Bukhari, N. I.; Hussain, I.; Webster, T. J.; Shahnaz, G. Advancements in the Oral Delivery of Docetaxel: Challenges, Current State-of-the-Art and Future Trends. *Int. J. Nanomedicine* **2018**, *13*, 3145–3161.

(170) Paciotti, G. F.; Myer, L.; Weinreich, D.; Goia, D.; Pavel, N.; McLaughlin, R. E.; Tamarkin, L. Colloidal Gold: A Novel Nanoparticle Vector for Tumor Directed Drug Delivery. *Drug Deliv. J. Deliv. Target. Ther. Agents* **2004**, *11* (3), 169–183.

(171) Katt, M. E.; Placone, A. L.; Wong, A. D.; Xu, Z. S.; Searson, P. C. In Vitro Tumor Models: Advantages, Disadvantages, Variables, and Selecting the Right Platform. *Front. Bioeng. Biotechnol.* **2016**, *4* (12), 1–17.

(172) Blevins, D. J.; Hanley, R.; Bolduc, T.; Powell, D. A.; Gignac, M.; Walker, K.; Carr, M. D.; Hof, F.; Wulff, J. E. In Vitro Assessment of Putative PD-1/PD-L1 Inhibitors: Suggestions of an Alternative Mode of Action. *ACS Med. Chem. Lett.* **2019**, *10* (8), 1187–1192.

(173) Walker, K. L. Structural Features of the Extracellular Region of Programmed Cell Death Ligand-1 and the Implications for Therapeutic Targeting, 2019.

(174) Tan, Y. H.; Liu, M.; Nolting, B.; Go, J. G.; Gervay-Hague, J.; Liu, G. Y. A Nanoengineering Approach for Investigation and Regulation of Protein Immobilization. *ACS Nano* **2008**, *2* (11), 2374–2384.

(175) Skalniak, L.; Zak, K. M.; Guzik, K.; Magiera, K.; Musielak, B.; Pachota, M.; Szelazek, B.; Kocik, J.;

Grudnik, P.; Tomala, M.; Krzanik, S.; Pyrc, K.; Dömling, A.; Dubin, G.; Holak, T. A. Small-Molecule Inhibitors of PD-1/PD-L1 Immune Checkpoint Alleviate the PD-L1-Induced Exhaustion of T-Cells. *Oncotarget* **2017**, *8* (42), 72167–72181.

(176) Weinmann, H. Cancer Immunotherapy: Selected Targets and Small-Molecule Modulators. *ChemMedChem* **2016**, *11* (5), 450–466.

(177) Konstantinidou, M.; Zarganes-Tzitzikas, T.; Magiera-Mularz, K.; Holak, T. A.; Dömling, A. Immune Checkpoint PD-1/PD-L1: Is There Life Beyond Antibodies? *Angew. Chemie - Int. Ed.* **2018**, *57* (18), 4840–4848.

(178) Huck, B. R.; Kötzner, L.; Urbahns, K. Small Molecules Drive Big Improvements in Immuno-Oncology Therapies. *Angew. Chemie* **2018**, *57*, 412–4428.

(179) Hughes, J. P.; Rees, S.; Kalindjian, S. B.; Philpott, K. L.; Philpott, K.; Building, H. Principles of Early Drug Discovery Correspondence. **2011**.

(180) Li, Q.; Cai, T.; Huang, Y.; Xia, X.; Cole, S.; Cai, Y.; Li, Q.; Cai, T.; Huang, Y.; Xia, X.; Cole, S. P. C.; Cai, Y. A Review of the Structure, Preparation, and Application of NLCs, PNPs, and PLNs. *Nanomaterials* **2017**, *7* (6), 122.

(181) Liu, Y.; Pan, J.; Feng, S. S. Nanoparticles of Lipid Monolayer Shell and Biodegradable Polymer Core for Controlled Release of Paclitaxel: Effects of Surfactants on Particles Size, Characteristics and in Vitro Performance. *Int. J. Pharm.* **2010**, *395*, 243–250.

(182) Whang, C.-H.; Yoo, E.; Hur, S. K.; Kim, K. S.; Kim, D.; Jo, S. A Highly GSH-Sensitive SN-38 Prodrug with an “OFF-to-ON” Fluorescence Switch as a Bifunctional Anticancer Agent. *Chem. Commun.* **2018**, *54* (65), 9031–9034.

(183) Walther, R.; Rautio, J.; Zelikin, A. N. Prodrugs in Medicinal Chemistry and Enzyme Prodrug Therapies. *Adv. Drug Deliv. Rev.* **2017**, *118*, 65–77.

(184) Elsherbeny, R. H.; Hassan, M. M.; El-Hossary, W. H.; Shata, M. S.; Darwish, W. M. Folate-Targeted Polymeric Nanoparticles for Efficient Dual (Chemo-Photothermal) Therapy of Oral Squamous Carcinoma. *Int. J. Polym. Mater. Polym. Biomater.* **2020**, *1*, 1–8.

(185) Sun, G.; He, Z.; Hao, M.; Xu, Z.; Hu, X. Y.; Zhu, J. J.; Wang, L. Bifunctional Supramolecular Prodrug Vesicles Constructed from a Camptothecin Derivative with a Water-Soluble Pillar[5]Arene for Cancer Diagnosis and Therapy. *Chem. Commun.* **2019**, *55* (73), 10892–10895.

(186) Wang, S.; Zhang, S.; Liu, J.; Liu, Z.; Su, L.; Wang, H.; Chang, J. PH-And Reduction-Responsive Polymeric Lipid Vesicles for Enhanced Tumor Cellular Internalization and Triggered Drug Release. *ACS Appl. Mater. Interfaces* **2014**, *6* (13), 10706–10713.

(187) Liu, Y.; Zhu, S.; Gu, K.; Guo, Z.; Huang, X.; Wang, M.; Amin, H. M.; Zhu, W.; Shi, P. GSH-Activated NIR Fluorescent Prodrug for Podophyllotoxin Delivery. *ACS Appl. Mater. Interfaces* **2017**, *9* (35), 29496–29504.

(188) Bargh, J. D.; Isidro-Llobet, A.; Parker, J. S.; Spring, D. R. Cleavable Linkers in Antibody-Drug Conjugates. *Chem. Soc. Rev.* **2019**, *48* (16), 4361–4374.

(189) Li, K.; Tian, H. Development of Small-Molecule Immune Checkpoint Inhibitors of PD-1/PD-L1 as a New Therapeutic Strategy for Tumour Immunotherapy. *J. Drug Target.* **2018**, *1*, 1–13.

(190) Yi, M.; Zheng, X.; Niu, M.; Zhu, S.; Ge, H.; Wu, K. Combination Strategies with PD-1/PD-L1 Blockade: Current Advances and Future Directions. *Mol. Cancer* **2021**, *21*, 28.

(191) Bastaki, S.; Irandoust, M.; Ahmadi, A.; Hojjat-Farsangi, M.; Ambrose, P.; Hallaj, S.; Edalati, M.; Ghalamfarsa, G.; Azizi, G.; Yousefi, M.; Chalajour, H.; Jadidi-Niaragh, F. PD-L1/PD-1 Axis as a Potent Therapeutic Target in Breast Cancer. *Life Sci.* **2020**, *247* (October 2019), 117437.

(192) Chrétien, S.; Zerdes, I.; Bergh, J.; Matikas, A.; Foukakis, T. Beyond PD-1/PD-L1 Inhibition: What the Future Holds for Breast Cancer Immunotherapy. *Cancers (Basel).* **2019**, *11* (5), 628.

(193) Wojas-Krawczyk, K.; Kalinka, E.; Grenda, A.; Krawczyk, P.; Milanowski, J. Beyond PD-L1 Markers for Lung Cancer Immunotherapy. *Int. J. Mol. Sci.* **2019**, *20* (8), 1915–1932.

(194) Sasikumar, P. G. N.; Ramachandra, M.; Naremaddepalli, S. S. S. Peptidomimetic Compounds as Immunomodulators. US20130237580, 2013.

(195) Sasikumar, P. G. N.; Ramachandra, M.; Naremaddepalli, S. S. S. 1,2,4-Oxadiazole Derivatives As Immunomodulators. WO2015033299A1, 2015.

(196) Sasikumar, P. G. N.; Ramachandra, M.; Prasad, A.; Naremaddepalli, S. S. S. 3-Substituted-1,2,4-Oxadiazole and Thiadiazole Compounds As Immunomodulators. WO2016142886A2, 2016.

(197) Teicher, B. A.; Chari, R. V. J. Antibody Conjugate Therapeutics: Challenges and Potential. *Clin. Cancer Res.* **2011**, *17* (20), 6389–6397.

(198) Fu, Z.; Li, S.; Han, S.; Shi, C.; Zhang, Y. Antibody Drug Conjugate: The "Biological Missile" for Targeted Cancer Therapy. *Signal Transduct. Target. Ther.* **2022**, *7* (1), 1–25.

(199) Curis Inc. A Study of CA-170 (Oral PD-L1, PD-L2 and VISTA Checkpoint Antagonist) in Patients With Advanced Tumors and Lymphomas - Full Text View - ClinicalTrials.gov https://clinicaltrials.gov/ct2/show/NCT02812875?term=NCT02812875&rank=1 (accessed Dec 6, 2018).

(200) Hanley, R. Inhibitors of the PD1/PD-L1 Interaction: Missteps, Mechanisms, and Mysteries, Unversity of Victoria, 2017.

(201) Magiera-Mularz, K.; Skalniak, L.; Zak, K. M.; Musielak, B.; Rudzinska-Szostak, E.; Berlicki, Ł.; Kocik, J.; Grudnik, P.; Sala, D.; Zarganes-Tzitzikas, T.; Shaabani, S.; Dömling, A.; Dubin, G.; Holak, T. A. Bioactive Macrocyclic Inhibitors of the PD-1/PD-L1 Immune Checkpoint. *Angew. Chemie - Int. Ed.* **2017**, *56* (44), 13732–13735.

(202) Santarpia, M.; González-Cao, M.; Viteri, S.; Karachaliou, N.; Altavilla, G.; Rosell, R. Programmed Cell Death Protein-1/Programmed Cell Death Ligand-1 Pathway Inhibition and Predictive Biomarkers: Understanding Transforming Growth Factor-Beta Role. *Transl. Lung Cancer Res.* **2015**, *4* (6), 728–742.

(203) Collins, M.; Ling, V.; Carreno, B. M. The B7 Family of Immune-Regulatory Ligands. *Genome Biol.* **2005**, *6* (6), 223.

(204) Li, C. W.; Lim, S. O.; Xia, W.; Lee, H. H.; Chan, L. C.; Kuo, C. W.; Khoo, K. H.; Chang, S. S.; Cha, J. H.; Kim, T.; Hsu, J. L.; Wu, Y.; Hsu, J. M.; Yamaguchi, H.; Ding, Q.; Wang, Y.; Yao, J.; Lee, C. C.; Wu, H. J.; Sahin, A. A.; Allison, J. P.; Yu, D.; Hortobagyi, G. N.; Hung, M. C. Glycosylation and Stabilization of Programmed Death Ligand-1 Suppresses T-Cell Activity. *Nat. Commun.* **2016**, *7*, 12632.

(205) Bally, A. P. R.; Austin, J. W.; Boss, J. M. Genetic and Epigenetic Regulation of PD-1 Expression. *J. Immunol.* **2016**, *196* (6), 2431–2437.

(206) Liang, S. C.; Latchman, Y. E.; Buhlmann, J. E.; Tomczak, M. F.; Horwitz, B. H.; Freeman, G. J.; Sharpe, A. H. Regulation of PD-1, PD-L1, and PD-L2 Expression during Normal and Autoimmune Responses. *Eur. J. Immunol.* **2003**, *33* (10), 2706–2716.

(207) Shi, L.; Chen, S.; Yang, L.; Li, Y. The Role of PD-1 and PD-L1 in T-Cell Immune Suppression in Patients with Hematological Malignancies. *J. Hematol. Oncol.* **2013**, *6* (1), 74–79.

(208) Geng, L.; Huang, D.; Liu, J.; Qian, Y.; Deng, J.; Li, D.; Hu, Z.; Zhang, J.; Jiang, G.; Zheng, S. B7-H1 up-Regulated Expression in Human Pancreatic Carcinoma Tissue Associates with Tumor Progression. *J. Cancer Res. Clin. Oncol.* **2008**, *134* (9), 1021–1027.

(209) Mu, C. Y.; Huang, J. A.; Chen, Y.; Chen, C.; Zhang, X. G. High Expression of PD-L1 in Lung Cancer May Contribute to Poor Prognosis and Tumor Cells Immune Escape through Suppressing Tumor Infiltrating Dendritic Cells Maturation. *Med. Oncol.* **2011**, *28* (3), 682–688.

(210) Azuma, K.; Ota, K.; Kawahara, A.; Hattori, S.; Iwama, E.; Harada, T.; Matsumoto, K.; Takayama, K.; Takamori, S.; Kage, M.; Hoshino, T.; Nakanishi, Y.; Okamoto, I. Association of PD-L1 Overexpression with Activating EGFR Mutations in Surgically Resected Nonsmall-Cell Lung Cancer. *Ann. Oncol.* **2014**, *25* (10), 1935–1940.

(211) Shin, S.-J.; Jeon, Y. K.; Cho, Y. M.; Lee, J.-L.; Chung, D. H.; Park, J. Y.; Go, H. The Association Between PD-L1 Expression and the Clinical Outcomes to Vascular Endothelial Growth Factor-Targeted Therapy in Patients With Metastatic Clear Cell Renal Cell Carcinoma. *Oncologist* **2015**, *20* (11), 1253–1260.

(212) Zhu, X.; Lang, J. Soluble PD-1 and PD-L1: Predictive and Prognostic Significance in Cancer. *Oncotarget* **2017**, *8* (57), 97671–97682.

(213) Saito, R.; Abe, H.; Kunita, A.; Yamashita, H.; Seto, Y.; Fukayama, M. Overexpression and Gene Amplification of PD-L1 in Cancer Cells and PD-L1 + Immune Cells in Epstein-Barr Virus-Associated Gastric Cancer: The Prognostic Implications. *Mod. Pathol.* **2017**, *30* (3), 427–439.

(214) Sidaway, P. Dostarlimab Effective in DMMR LARC. *Nat. Rev. Clin. Oncol. 2022* **2022**, 1–1.

(215) Gong, J.; Chehrazi-Raffle, A.; Reddi, S.; Salgia, R. Development of PD-1 and PD-L1 Inhibitors as a Form of Cancer Immunotherapy: A Comprehensive Review of Registration Trials and Future Considerations. *J. Immunother. Cancer* **2018**, *6* (1), 8–25.

(216) Borghaei, H.; Paz-Ares, L.; Horn, L.; Spigel, D. R.; Steins, M.; Ready, N. E.; Chow, L. Q.; Vokes, E. E.; Felip, E.; Holgado, E.; Barlesi, F.; Kohlhäufl, M.; Arrieta, O.; Burgio, M. A.; Fayette, J.; Lena, H.; Poddubskaya, E.; Gerber, D. E.; Gettinger, S. N.; Rudin, C. M.; Rizvi, N.; Crinò, L.; Blumenschein, G. R.; Antonia, S. J.; Dorange, C.; Harbison, C. T.; Graf Finckenstein, F.; Brahmer, J. R. Nivolumab versus Docetaxel in Advanced Nonsquamous Non-Small-Cell Lung Cancer. *N. Engl. J. Med.* **2015**, *373* (17), 1627–1639.

(217) Brahmer, J.; Reckamp, K. L.; Baas, P.; Crinò, L.; Eberhardt, W. E. E.; Poddubskaya, E.; Antonia, S.; Pluzanski, A.; Vokes, E. E.; Holgado, E.; Waterhouse, D.; Ready, N.; Gainor, J.; Arén Frontera, O.; Havel, L.; Steins, M.; Garassino, M. C.; Aerts, J. G.; Domine, M.; Paz-Ares, L.; Reck, M.; Baudelet, C.; Harbison, C. T.; Lestini, B.; Spigel, D. R. Nivolumab versus Docetaxel in Advanced Squamous-Cell Non-Small-Cell Lung Cancer. *N. Engl. J. Med.* **2015**, *373* (2), 123–135.

(218) Herbst, R. S.; Baas, P.; Kim, D. W.; Felip, E.; Pérez-Gracia, J. L.; Han, J. Y.; Molina, J.; Kim, J. H.; Arvis, C. D.; Ahn, M. J.; Majem, M.; Fidler, M. J.; De Castro, G.; Garrido, M.; Lubiniecki, G. M.; Shentu, Y.; Im, E.; Dolled-Filhart, M.; Garon, E. B. Pembrolizumab versus Docetaxel for Previously Treated, PD-L1-Positive, Advanced Non-Small-Cell Lung Cancer (KEYNOTE-010): A Randomised Controlled Trial. *Lancet* **2016**, *387* (10027), 1540–1550.

(219) Reck, M.; Rodríguez-Abreu, D.; Robinson, A. G.; Hui, R.; Csőszi, T.; Fülöp, A.; Gottfried, M.; Peled, N.; Tafreshi, A.; Cuffe, S.; O'Brien, M.; Rao, S.; Hotta, K.; Leiby, M. A.; Lubiniecki, G. M.; Shentu, Y.; Rangwala, R.; Brahmer, J. R. Pembrolizumab versus Chemotherapy for PD-L1–Positive Non–Small-Cell Lung Cancer. *N. Engl. J. Med.* **2016**, *375* (19), 1823–1833.

(220) Chupak, L.; Zheng, X. Compounds as Useful Immunomodulators. WO2015034820A1, 2014.

(221) Sasikumar, P. G. N.; Ramachandra, M.; Vadlamani, S. K.; Vemula, K. R.; Satyam, L. K.; Subbarao, K.; Shrimali, K. R.; Kandepu, S. Immunosuppression Modulating Compounds. US2011031873A1, 2011.

(222) Sasikumar, P. G. N.; Ramachandra, M. Immunomodulating Cyclic Compounds from the Bc Loop of Human Pd1. WO2013144704A1, 2013.

(223) Müller, K. M.; Arndt, K. M.; Plückthun, A. Model and Simulation of Multivalent Binding to Fixed Ligands. *Anal. Biochem.* **1998**, *261* (2), 149–158.

(224) Quinn, J. G.; O'Neill, S.; Doyle, A.; McAtamney, C.; Diamond, D.; MacCraith, B. D.; O'Kennedy, R. Development and Application of Surface Plasmon Resonance-Based Biosensors for the Detection of Cell-Ligand Interactions. *Anal. Biochem.* **2000**, *281* (2), 135–143.

(225) Gopinath, S. C. B. Biosensing Applications of Surface Plasmon Resonance-Based Biacore Technology. *Sensors Actuators B Chem.* **2010**, *150* (2), 722–733.

(226) Oliveira, L. C.; Lima, A. M. N.; Thirstrup, C.; Neff, H. F. *Surface Plasmon Resonance Sensors: A Materials Guide to Design, Characterization, Optimization, and Usag*^{e,} 2nd ed.; Ertl, G., Lüth, H., Car, R., Rocca, M. A., Fruend, H.-J., Eds.; Springer Nature Switzerland AG, 2019; Vol. 70.

(227) Olaru, A.; Bala, C.; Jaffrezic-Renault, N.; Aboul-Enein, H. Y. Surface Plasmon Resonance (SPR) Biosensors in Pharmaceutical Analysis. *Crit. Rev. Anal. Chem.* **2015**, *45* (2), 97–105.

(228) Zak, K. M.; Grudnik, P.; Guzik, K.; Zieba, B. J.; Musielak, B.; Dömling, A.; Dubin, G.; Holak, T. A. Structural Basis for Small Molecule Targeting of the Programmed Death Ligand 1 (PD-L1). *Oncotarget* **2016**, *7* (21), 30323–30335.

(229) Zak, K. M.; Grudnik, P.; Magiera, K.; Dömling, A.; Dubin, G.; Holak, T. A. Structural Biology of the Immune Checkpoint Receptor PD-1 and Its Ligands PD-L1/PD-L2. *Structure*. Cell Press August 1, 2017, pp 1163–1174.

(230) Hanley, R. P.; Horvath, S.; An, J.; Hof, F.; Wulff, J. E. Salicylates Are Interference Compounds in TR-FRET Assays. *Bioorganic Med. Chem. Lett.* **2016**, *26* (3), 973–977.

(231) Chen, T.; Li, Q.; Liu, Z.; Chen, Y.; Feng, F.; Sun, H. Peptide-Based and Small Synthetic Molecule Inhibitors on PD-1/PD-L1 Pathway: A New Choice for Immunotherapy? *Eur. J. Med. Chem.* **2019**, *161*, 378–398.

(232) Liu, J.; Yuan, Y.; Chen, W.; Putra, J.; Suriawinata, A. A.; Schenk, A. D.; Miller, H. E.; Guleria, I.;

Barth, R. J.; Huang, Y. H.; Wang, L. Immune-Checkpoint Proteins VISTA and PD-1 Nonredundantly Regulate Murine T-Cell Responses. *Proc. Natl. Acad. Sci. U. S. A.* **2015**, *112* (21), 6682–6687.

(233) Musielak, B.; Kocik, J.; Skalniak, L.; Magiera-Mularz, K.; Sala, D.; Czub, M.; Stec, M.; Siedlar, M.; Holak, T. A.; Plewka, J. CA-170 - A Potent Small-Molecule PD-L1 Inhibitor or Not? *Molecules* **2019**, *24* (15), 662668.

(234) Sasikumar, P. G.; Sudarshan, N. S.; Adurthi, S.; Ramachandra, R. K.; Samiulla, D. S.; Lakshminarasimhan, A.; Ramanathan, A.; Chandrasekhar, T.; Dhudashiya, A. A.; Talapati, S. R.; Gowda, N.; Palakolanu, S.; Mani, J.; Srinivasrao, B.; Joseph, D.; Kumar, N.; Nair, R.; Atreya, H. S.; Gowda, N.; Ramachandra, M. PD-1 Derived CA-170 Is an Oral Immune Checkpoint Inhibitor That Exhibits Preclinical Anti-Tumor Efficacy. *Commun. Biol.* **2021**, *4* (1), 1–12.

(235) Blevins, D. J.; Nazir, R.; Hossein Dabiri, S. M.; Akbari, M.; Wulff, J. E. The Effects of Cell Culture Conditions on Premature Hydrolysis of Traceless Ester-Linked Disulfide Linkers. *J. Drug Deliv. Sci. Technol.* **2022**, *78*, 103950.

(236) Wang, J.; Li, M.; Cui, X.; Lv, D.; Jin, L.; Khan, M.; Ma, T. Brevilin A Promotes Oxidative Stress and Induces Mitochondrial Apoptosis in U87 Glioblastoma Cells. *Onco. Targets. Ther.* **2018**, *11*, 7031–7040.

(237) Yang, H.; Miao, Y.; Chen, L.; Li, Z.; Yang, R.; Xu, X.; Liu, Z.; Zhang, L. M.; Jiang, X. Redox-Responsive Nanoparticles from Disulfide Bond-Linked Poly-(N-ε-Carbobenzyloxy-L-Lysine)-Grafted Hyaluronan Copolymers as Theranostic Nanoparticles for Tumor-Targeted MRI and Chemotherapy. *Int. J. Biol. Macromol.* **2020**, *148*, 483–492.

(238) Vrudhula, V. M.; MacMaster, J. F.; Li, Z.; Kerr, D. E.; Senter, P. D. Reductively Activated Disulfide Prodrugs of Paclitaxel. *Bioorganic Med. Chem. Lett.* **2002**, *12* (24), 3591–3594.

(239) Wang, Y.; Wang, X.; Deng, F.; Zheng, N.; Liang, Y.; Zhang, H.; He, B.; Dai, W.; Wang, X.; Zhang, Q. The Effect of Linkers on the Self-Assembling and Anti-Tumor Efficacy of Disulfide-Linked Doxorubicin Drug-Drug Conjugate Nanoparticles. *J. Control. Release* **2018**, *279*, 136–146.

(240) Wu, G.; Fang, Y.-Z.; Yang, S.; Lupton, J. R.; Turner, N. D. Glutathione Metabolism and Its Implications for Health. *J. Nutr.* **2004**, *134* (3), 489–492.

(241) Xu, Z.; Wang, D.; Xu, S.; Liu, X.; Zhang, X.; Zhang, H. Preparation of a Camptothecin Prodrug with Glutathione-Responsive Disulfide Linker for Anticancer Drug Delivery. *Chem. - An Asian J.* **2014**, *9* (1), 199–205.

(242) Saito, G.; Swanson, J. A.; Lee, K. D. Drug Delivery Strategy Utilizing Conjugation via Reversible Disulfide Linkages: Role and Site of Cellular Reducing Activities. *Adv. Drug Deliv. Rev.* **2003**, *55* (2), 199–215.

(243) Li, J.; Yang, X. L.; Liu, Y. H.; Wu, W. X.; Liu, B. Y.; Wang, N.; Yu, X. Q. Chemoenzymatic Synthesis of Dual-Responsive Graft Copolymers for Drug Delivery: Long-Term Stability, High Loading and Cell Selectivity. *J. Mater. Chem. B* **2018**, *6* (43), 6993–7003.

(244) Zheng, Y.; Shen, Y.; Meng, X.; Wu, Y.; Zhao, Y.; Wu, C. Stabilizing P-Dithiobenzyl Urethane Linkers without Rate-Limiting Self-Immolation for Traceless Drug Release. *ChemMedChem* **2019**, *14* (12), 1196–1203.

(245) Tharkar, P.; Varanasi, R.; Wong, W. S. F.; Jin, C. T.; Chrzanowski, W. Nano-Enhanced Drug Delivery

and Therapeutic Ultrasound for Cancer Treatment and Beyond. *Front. Bioeng. Biotechnol.* **2019**, *7*, 324.

(246) Karisma, V. W.; Wu, W.; Lei, M.; Liu, H.; Nisar, M. F.; Lloyd, M. D.; Pourzand, C.; Zhong, J. L. UVA-Triggered Drug Release and Photo-Protection of Skin. *Front. Cell Dev. Biol.* **2021**, *9*, 128.

(247) Cheetham, A. G.; Chakroun, R. W.; Ma, W.; Cui, H. Self-Assembling Prodrugs. *Chem. Soc. Rev.* **2017**, *46* (21), 6638–6663.

(248) Lin, C.; He, H.; Zhang, Y.; Xu, M.; Tian, F.; Li, L.; Wang, Y. Acetaldehyde-Modified-Cystine Functionalized Zr-MOFs for PH/GSH Dual-Responsive Drug Delivery and Selective Visualization of GSH in Living Cells. *RSC Adv.* **2020**, *10* (6), 3084–3091.

(249) Fang, J.; Seki, T.; Maeda, H. Therapeutic Strategies by Modulating Oxygen Stress in Cancer and Inflammation. *Adv. Drug Deliv. Rev.* **2009**, *61* (4), 290–302.

(250) Qiu, L.; Zhu, M.; Gong, K.; Chen, J. PH-Sensitive Degradable Polymeric Micelles for Bio-Triggered Targeted Anti-Tumor Drug Delivery. *J. Control. Release* **2017**, *259*, e86–e87.

(251) Dillon, K. M.; Powell, C. R.; Matson, J. B. Self-Immolative Prodrugs: Effective Tools for the Controlled Release of Sulfur Signaling Species. *Synlett* **2019**, *30* (5), 525–531.

(252) Powell, C. R.; Dillon, K. M.; Wang, Y.; Carrazzone, R. J.; Matson, J. B. A Persulfide Donor Responsive to Reactive Oxygen Species: Insights into Reactivity and Therapeutic Potential. *Angew. Chemie - Int. Ed.* **2018**, *57* (21), 6324–6328.

(253) Arslan, M.; Sanyal, R.; Sanyal, A. Thiol-Reactive Thiosulfonate Group Containing Copolymers: Facile Entry to Disulfide-Mediated Polymer Conjugation and Redox-Responsive Functionalizable Networks. *Polym. Chem.* **2020**, *11* (10), 1763–1773.

(254) Guo, F.; Li, G.; Ma, S.; Zhou, H.; Chen, X. Multi-Responsive Nanocarriers Based on β-CD-PNIPAM Star Polymer Coated MSN-SS-Fc Composite Particles. *Polymers (Basel).* **2019**, *11* (10), 1716.

(255) Seidi, F.; Jenjob, R.; Crespy, D. Designing Smart Polymer Conjugates for Controlled Release of Payloads. *Chem. Rev.* **2018**, *118* (7), 3965–4036.

(256) Shetty, C.; Noronha, A.; Pontarelli, A.; Wilds, C. J.; Oh, J. K. Dual-Location Dual-Acid/Glutathione-Degradable Cationic Micelleplexes through Hydrophobic Modification for Enhanced Gene Silencing. *Mol. Pharm.* **2020**, *17*, 3979–3989.

(257) Jazani, A. M.; Oh, J. K. Development and Disassembly of Single and Multiple Acid-Cleavable Block Copolymer Nanoassemblies for Drug Delivery. *Polym. Chem.* **2020**, *11* (17), 2934–2954.

(258) Miller, K. A.; Morado, E. G.; Samanta, S. R.; Walker, B. A.; Nelson, A. Z.; Sen, S.; Tran, D. T.; Whitaker, D. J.; Ewoldt, R. H.; Braun, P. V.; Zimmerman, S. C. Acid-Triggered, Acid-Generating, and Self-Amplifying Degradable Polymers. *J. Am. Chem. Soc.* **2019**, *141* (7), 2838–2842.

(259) Ikuta, Y.; Koseki, Y.; Onodera, T.; Oikawa, H.; Kasai, H. The Effect of Molecular Structure on the Anticancer Drug Release Rate from Prodrug Nanoparticles. *Chem. Commun.* **2015**, *51* (64), 12835–12838.

(260) Bohn, K.; Lange, A.; Chmielewski, J.; Hrycyna, C. A. Dual Modulation of Human P-Glycoprotein and ABCG2 with Prodrug Dimers of the Atypical Antipsychotic Agent Paliperidone in a Model of the Blood-Brain Barrier. *Mol. Pharm.* **2017**, *14* (4), 1107–1119.

(261) Bej, R.; Dey, P.; Ghosh, S. Disulfide Chemistry in Responsive Aggregation of Amphiphilic Systems. *Soft Matter* **2019**, *16* (1), 11–26.

(262) Zou, X. J.; Ma, Y. C.; Guo, L. E.; Liu, W. X.; Liu, M. J.; Zou, C. G.; Zhou, Y.; Zhang, J. F. A Lysosome-Targeted Fluorescent Chemodosimeter for Monitoring Endogenous and Exogenous Hydrogen Sulfide by in Vivo Imaging. *Chem. Commun.* **2014**, *50* (89), 13833–13836.

(263) Zhang, H.; Li, M.; Zhang, C.; Zhang, G.; Chao, J.; Shi, L.; Yao, Q.; Shuang, S.; Dong, C. The Design of Hydrogen Sulfide Fluorescence Probe Based on Dual Nucleophilic Reaction and Its Application for Bioimaging. *Spectrochim. Acta - Part A Mol. Biomol. Spectrosc.* **2019**, *207*, 150–155.

(264) Tian, Y.; Tian, R.; Chen, L.; Jin, R.; Feng, Y.; Bai, Y.; Chen, X.; Tian, Y.; Tian, R.; Chen, L.; Jin, R.; Feng, Y.; Bai, Y.; Chen, X. Redox-Responsive Nanogel with Intracellular Reconstruction and Programmable Drug Release for Targeted Tumor Therapy. *Macromol. Rapid Commun.* **2019**, *40* (8), 1800824.

(265) Pillow, T. H.; Sadowsky, J. D.; Zhang, D.; Yu, S. F.; Del Rosario, G.; Xu, K.; He, J.; Bhakta, S.; Ohri, R.; Kozak, K. R.; Ha, E.; Junutula, J. R.; Flygare, J. A. Decoupling Stability and Release in Disulfide Bonds with Antibody-Small Molecule Conjugates. *Chem. Sci.* **2016**, *8* (1), 366–370.

(266) Forman, H. J.; Zhang, H.; Rinna, A. Glutathione: Overview of Its Protective Roles, Measurement, and Biosynthesis. *Mol. Aspects Med.* **2009**, *30* (1–2), 1–12.

(267) Meister, A. Glutathione Metabolism and Its Selective Modification. *J. Biol. Chem.* **1988**, *263* (33), 17205–17208.

(268) Burns, J. A.; Butler, J. C.; Moran, J.; Whitesides, G. M. Selective Reduction of Disulfides by Tris(2-Carboxyethyl)Phosphine. *J. Org. Chem.* **1991**, *56* (8), 2648–2650.

(269) Dmitrenko, O.; Thorpe, C.; Bach, R. D. Mechanism of SN2 Disulfide Bond Cleavage by Phosphorus Nucleophiles. Implications for Biochemical Disulfide Reducing Agents. *J. Org. Chem.* **2007**, *72* (22), 8298–8307.

(270) Nagy, P. Kinetics and Mechanisms of Thiol–Disulfide Exchange Covering Direct Substitution and Thiol Oxidation-Mediated Pathways. *Antioxid. Redox Signal.* **2013**, *18* (13), 1623.

(271) Hacioglu, C.; Kar, F. Capsaicin Induces Redox Imbalance and Ferroptosis through ACSL4/GPx4 Signaling Pathways in U87-MG and U251 Glioblastoma Cells. *Metab. Brain Dis.* **2022**, *1*, 1–16.

(272) Zhong, W.; Yan, T.; Lim, R.; Oberley, L. W. Expression of Superoxide Dismutases, Catalase, and Glutathione Peroxidase in Glioma Cells. *Free Radic. Biol. Med.* **1999**, *27* (11–12), 1334–1345.

(273) Zhu, Z.; Du, S.; Du, Y.; Ren, J.; Ying, G.; Yan, Z. Glutathione Reductase Mediates Drug Resistance in Glioblastoma Cells by Regulating Redox Homeostasis. *J. Neurochem.* **2018**, *144* (1), 93–104.

(274) Sigma-Aldrich. Dulbecco's Modified Eagle's Medium (DME) Formulation https://www.sigmaaldrich.com/CA/en/technical-documents/technical-article/cell-culture-and-cell-culture-analysis/mammalian-cell-culture/dulbecco-modified-eagle-medium-formulation (accessed Apr 5, 2022).

(275) Sigma-Aldrich. RPMI-1640 Media Formulation https://www.sigmaaldrich.com/CA/en/technical-documents/technical-article/cell-culture-and-cell-culture-analysis/mammalian-cell-culture/media-formulations-rpmi-1640 (accessed Apr 5, 2022).

(276) Sigma-Aldrich. Minimum Essential Medium , Eagle , Modified Formulation https://www.sigmaaldrich.com/CA/en/technical-documents/technical-article/cell-culture-and-cell-culture-analysis/mammalian-cell-culture/mem-formulation (accessed Apr 5, 2022).

(277) Johnson, M. Fetal Bovine Serum. *Mater. Methods* **2012**, *2* (117).

(278) Heger, J. I.; Froehlich, K.; Pastuschek, J.; Schmidt, A.; Baer, C.; Mrowka, R.; Backsch, C.; Schleußner, E.; Markert, U. R.; Schmidt, A. Human Serum Alters Cell Culture Behavior and Improves Spheroid Formation in Comparison to Fetal Bovine Serum. *Exp. Cell Res.* **2018**, *365* (1), 57–65.

(279) Gstraunthaler, G.; Lindl, T.; Van Der Valk, J. A Plea to Reduce or Replace Fetal Bovine Serum in Cell Culture Media. *Cytotechnology* **2013**, *65* (5), 791–793.

(280) Bromma, K.; Rieck, K.; Kulkarni, J.; O'Sullivan, C.; Sung, W.; Cullis, P.; Schuemann, J.; Chithrani, D. B. Use of a Lipid Nanoparticle System as a Trojan Horse in Delivery of Gold Nanoparticles to Human Breast Cancer Cells for Improved Outcomes in Radiation Therapy. *Cancer Nanotechnol.* **2019**, *10* (1), 1–17.

(281) Tsoi, K. M.; Dai, Q.; Alman, B. A.; Chan, W. C. W. Are Quantum Dots Toxic? Exploring the Discrepancy between Cell Culture and Animal Studies. *Acc. Chem. Res.* **2013**, *46* (3), 662–671.

(282) Rahme, K.; Chen, L.; Hobbs, R. G.; Morris, M. A.; O'Driscoll, C.; Holmes, J. D. PEGylated Gold Nanoparticles: Polymer Quantification as a Function of PEG Lengths and Nanoparticle Dimensions. *RSC Adv.* **2013**, *3* (17), 6085–6094.

(283) Sebby, K. B.; Mansfield, E. Determination of the Surface Density of Polyethylene Glycol on Gold Nanoparticles by Use of Microscale Thermogravimetric Analysis. *Anal. Bioanal. Chem.* **2015**, *407* (10), 2913–2922.

(284) Xia, X.; Yang, M.; Wang, Y.; Zheng, Y.; Li, Q.; Chen, J.; Xia, Y. Quantifying the Coverage Density of Poly(Ethylene Glycol) Chains on the Surface of Gold Nanostructures. *ACS Nano* **2012**, *6* (1), 512–522.

(285) Hinterwirth, H.; Kappel, S.; Waitz, T.; Prohaska, T.; Lindner, W.; Lämmerhofer, M. Quantifying Thiol Ligand Density of Self-Assembled Monolayers on Gold Nanoparticles by Inductively Coupled Plasma–Mass Spectrometry. *ACS Nano* **2013**, *7* (2), 1129.

(286) Tsai, D. H.; DelRio, F. W.; MacCuspie, R. I.; Cho, T. J.; Zachariah, M. R.; Hackley, V. A. Competitive Adsorption of Thiolated Polyethylene Glycol and Mercaptopropionic Acid on Gold Nanoparticles Measured by Physical Characterization Methods. *Langmuir* **2010**, *26* (12), 10325–10333.

(287) Schlenoff, J. B.; Li, M.; Ly, H. Stability and Self-Exchange in Alkanethiol Monolayers. *J. Am. Chem. Soc.* **1995**, *117* (50), 12528–12536.

(288) Reimers, J. R.; Ford, M. J.; Halder, A.; Ulstrup, J.; Hush, N. S. Gold Surfaces and Nanoparticles Are Protected by Au(0)-Thiyl Species and Are Destroyed When Au(I)-Thiolates Form. *Proc. Natl. Acad. Sci. U. S. A.* **2016**, *113* (11), E1424–E1433.

(289) Koufaki, M.; Detsi, A. Design and Synthesis of Antioxidant α-Lipoic Acid Hybrids. *Methods Mol. Biol.* **2010**, *594*, 297–309.

(290) Shi, L.; Jing, C.; Ma, W.; Li, D. W.; Halls, J. E.; Marken, F.; Long, Y. T. Plasmon Resonance Scattering

Spectroscopy at the Single-Nanoparticle Level: Real-Time Monitoring of a Click Reaction. *Angew. Chemie - Int. Ed.* **2013**, *52* (23), 6011–6014.

(291) Gholijani, N.; Gharagozloo, M.; Kalantar, F.; Ramezani, A.; Amirghofran, Z. Modulation of Cytokine Production and Transcription Factors Activities in Human Jurkat t Cells by Thymol and Carvacrol. *Adv. Pharm. Bull.* **2015**, *5* (Suppl 1), 653–660.

(292) Yiemwattana, I.; Ngoenkam, J.; Paensuwan, P.; Kriangkrai, R.; Chuenjitkuntaworn, B.; Pongcharoen, S. Essential Role of the Adaptor Protein Nck1 in Jurkat T Cell Activation and Function. *Clin. Exp. Immunol.* **2012**, *167* (1), 99–107.

(293) Ahn, E.; Araki, K.; Hashimoto, M.; Li, W.; Riley, J. L.; Cheung, J.; Sharpe, A. H.; Freeman, G. J.; Irving, B. A.; Ahmed, R. Role of PD-1 during Effector CD8 T Cell Differentiation. *Proc. Natl. Acad. Sci. U. S. A.* **2018**, *115* (18), 4749–4754.

(294) Ross, S. H.; Cantrell, D. A. Signaling and Function of Interleukin-2 in T Lymphocytes. *Annu. Rev. Immunol.* **2018**, *36*, 411.

(295) Khalaf, H.; Jass, J.; Olsson, P. E. Differential Cytokine Regulation by NF-KB and AP-1 in Jurkat T-Cells. *BMC Immunol.* **2010**, *11*, 26.

(296) Sheppard, K. A.; Fitz, L. J.; Lee, J. M.; Benander, C.; George, J. A.; Wooters, J.; Qiu, Y.; Jussif, J. M.; Carter, L. L.; Wood, C. R.; Chaudhary, D. PD-1 Inhibits T-Cell Receptor Induced Phosphorylation of the ZAP70/CD3ζ Signalosome and Downstream Signaling to PKCθ. *FEBS Lett.* **2004**, *574* (1–3), 37–41.

(297) Kim, S. E.; Lee, B. R.; Lee, H.; Jo, S. D.; Kim, H.; Won, Y. Y.; Lee, J. Near-Infrared Plasmonic Assemblies of Gold Nanoparticles with Multimodal Function for Targeted Cancer Theragnosis. *Sci. Rep.* **2017**, *7* (1), 1–10.

(298) Ebert, E. C. IL-10 Enhances IL-2-Induced Proliferation and Cytotoxicity by Human Intestinal Lymphocytes. *Clin. Exp. Immunol.* **2000**, *119* (3), 426–432.

(299) Diehn, M.; Alizadeh, A. A.; Rando, O. J.; Liu, C. L.; Stankunas, K.; Botstein, D.; Crabtree, G. R.; Brown, P. O. Genomic Expression Programs and the Integration of the CD28 Costimulatory Signal in T Cell Activation. *Proc. Natl. Acad. Sci. U. S. A.* **2002**, *99* (18), 11796–11801.

(300) Okada, M.; Chikuma, S.; Kondo, T.; Hibino, S.; Machiyama, H.; Yokosuka, T.; Nakano, M.; Yoshimura, A. Blockage of Core Fucosylation Reduces Cell-Surface Expression of PD-1 and Promotes Anti-Tumor Immune Responses of T Cells. *Cell Rep.* **2017**, *20* (5), 1017–1028.

(301) Latchman, Y.; Wood, C. R.; Chernova, T.; Chaudhary, D.; Borde, M.; Chernova, I.; Iwai, Y.; Long, A. J.; Brown, J. A.; Nunes, R.; Greenfield, E. A.; Bourque, K.; Boussiotis, V. A.; Carter, L. L.; Carreno, B. M.; Malenkovich, N.; Nishimura, H.; Okazaki, T.; Honjo, T.; Sharpe, A. H.; Freeman, G. J. PD-L2 Is a Second Ligand for PD-1 and Inhibits T Cell Activation. *Nat. Immunol.* **2001**, *2* (3), 261–268.

(302) Chan, L. L. Y.; Rice, W. L.; Qiu, J. Observation and Quantification of the Morphological Effect of Trypan Blue Rupturing Dead or Dying Cells. *PLoS One* **2020**, *15* (1).

(303) Na, C. H.; Peng, J. Analysis of Ubiquitinated Proteome by Quantitative Mass Spectrometry. In *Methods in Molecular Biology*; Humana Press, Totowa, NJ, 2012; Vol. 893, pp 417–429.

(304) Ziemianowicz, D. S.; Bomgarden, R.; Etienne, C.; Schriemer, D. C. Amino Acid Insertion

Frequencies Arising from Photoproducts Generated Using Aliphatic Diazirines. *J. Am. Soc. Mass Spectrom.* **2017**, *28* (10), 2011–2021.

(305) Manzi, L.; Barrow, A. S.; Scott, D.; Layfield, R.; Wright, T. G.; Moses, J. E.; Oldham, N. J. Carbene Footprinting Accurately Maps Binding Sites in Protein–Ligand and Protein–Protein Interactions. *Nat. Commun. 2016 71* **2016**, *7* (1), 1–9.

(306) Alouane, A.; Labruère, R.; Le Saux, T.; Schmidt, F.; Jullien, L. Self-Immolative Spacers: Kinetic Aspects, Structure-Property Relationships, and Applications. *Angew. Chemie Int. Ed.* **2015**, *54* (26), 7492–7509.

(307) Hartmann, J. T.; Lipp, H. P. Camptothecin and Podophyllotoxin Derivatives: Inhibitors of Topoisomerase I and II - Mechanisms of Action, Pharmacokinetics and Toxicity Profile. *Drug Safety*. Springer International Publishing 2006, pp 209–230.

(308) Palakurthi, S. Challenges in SN38 Drug Delivery: Current Success and Future Directions. *Expert Opinion on Drug Delivery*. Taylor and Francis Ltd December 2, 2015, pp 1911–1921.

(309) Yao, Y. S.; Liu, J. L.; Xi, J.; Miu, B.; Liu, G. S.; Wang, S.; Meng, L.; Yao, Z. J. Total Synthesis of 7-Ethyl-10-Hydroxycamptothecin (SN38) and Its Application to the Development of C18-Functionalized Camptothecin Derivatives. *Chem. – A Eur. J.* **2011**, *17* (37), 10462–10469.

(310) Palakurthi, S. Challenges in SN38 Drug Delivery: Current Success and Future Directions. *Expert Opin. Drug Deliv.* **2015**, *12* (12), 1911–1921.

(311) Tsakos, M.; Schaffert, E. S.; Clement, L. L.; Villadsen, N. L.; Poulsen, T. B. Ester Coupling Reactions-an Enduring Challenge in the Chemical Synthesis of Bioactive Natural Products. *Nat. Prod. Rep.* **2015**, *32* (4), 605–632.

(312) Smith, J. R.; Collins, B. S. L.; Hesse, M. J.; Graham, M. A.; Myers, E. L.; Aggarwal, V. K. Enantioselective Rhodium(III)-Catalyzed Markovnikov Hydroboration of Unactivated Terminal Alkenes. *J. Am. Chem. Soc.* **2017**, *139* (27), 9148–9151.

(313) Vrettos, E. I.; Sayyad, N.; Mavrogiannaki, E. M.; Stylos, E.; Kostagianni, A. D.; Papas, S.; Mavromoustakos, T.; Theodorou, V.; Tzakos, A. G. Unveiling and Tackling Guanidinium Peptide Coupling Reagent Side Reactions towards the Development of Peptide-Drug Conjugates. *RSC Adv.* **2017**, *7* (80), 50519–50526.

(314) Fitzjarrald, V. P.; Pongdee, R. A Convenient Procedure for the Esterification of Benzoic Acids with Phenols: A New Application for the Mitsunobu Reaction. *Tetrahedron Lett.* **2007**, *48* (20), 3553–3557.

(315) Mitsunobu, O.; Yamada, M. Preparation of Esters of Carboxylic and Phosphoric Acid via Quaternary Phosphonium Salts. *Bull. Chem. Soc. Jpn.* **1967**, *40* (10), 2380–2382.

(316) Makarova, M.; Barrientos, R. C.; Torres, O. B.; Matyas, G. R.; Jacobson, A. E.; Sulima, A.; Rice, K. C. Synthesis of a Deuterated 6-AmHap Internal Standard for the Determination of Hapten Density in a Heroin Vaccine Drug Product. *J. Label. Compd. Radiopharm.* **2020**, *63* (13), 564–571.

(317) Zhao, F.; Zhao, Y.; Liu, Y.; Chang, X.; Chen, C.; Zhao, Y. Cellular Uptake, Intracellular Trafficking, and Cytotoxicity of Nanomaterials. *Small* **2011**, *7* (10), 1322–1337.

(318) Gill, M. R.; Vallis, K. A. Transition Metal Compounds as Cancer Radiosensitizers. *Chem. Soc. Rev.*

2019, *48* (2), 540–557.

(319) Noireaux, J.; Grall, R.; Hullo, M.; Chevillard, S.; Oster, C.; Brun, E.; Sicard-Roselli, C.; Loeschner, K.; Fisicaro, P. Gold Nanoparticle Uptake in Tumor Cells: Quantification and Size Distribution by Sp-ICPMS. *Separations* **2019**, *6* (1), 1–13.

(320) Dou, Y.; Li, C.; Li, L.; Guo, J.; Zhang, J. Bioresponsive Drug Delivery Systems for the Treatment of Inflammatory Diseases. *J. Control. Release* **2020**, *327*, 641–666.

(321) Igaz, N.; Szőke, K.; Kovács, D.; Buhala, A.; Varga, Z.; Bélteky, P.; Rázga, Z.; Tiszlavicz, L.; Vizler, C.; Hideghéty, K.; Kónya, Z.; Kiricsi, M. Synergistic Radiosensitization by Gold Nanoparticles and the Histone Deacetylase Inhibitor SAHA in 2D and 3D Cancer Cell Cultures. *Nanomaterials* **2020**, *10* (1), 158–178.

(322) Wojczykowski, K.; Meißner, D.; Jutzi, P.; Ennen, I.; Hütten, A.; Fricke, M.; Volkmer, D. Reliable Stabilization and Functionalization of Nanoparticles through Tridentate Thiolate Ligands. *Chem. Commun.* **2006**, No. 35, 3693–3695.

(323) Bennett, F.; Jiang, J.; Pasternak, A.; Dong, S.; Gu, X.; Scott, J. D.; Tang, H.; Zhao, Z.; Huang, Y.; Hunter, D.; Yang, D.; Zhang, Z.; Fu, J.; Bai, Y.; Zheng, Z.; Zhang, X.; Young, K.; Li, X. Metallo-Beta-Lactamase Inhibitors. WO/2016/206101, December 29, 2016.

(324) Brackmann, F.; Yufit, D. S.; Howard, J. A. K.; Es-Sayed, M.; De Meijere, A. Synthesis of Spirocyclopropanated Analogues of Imidacloprid and Thiacloprid. *European J. Org. Chem.* **2005**, *2005* (3), 600–609.

(325) Murphy, C. J.; Shi, X.; Jewell, A. D.; McGuire, A. F.; Bellisario, D. O.; Baber, A. E.; Tierney, H. L.; Lewis, E. A.; Sholl, D. S.; Sykes, E. C. H. Impact of Branching on the Supramolecular Assembly of Thioethers on Au(111). *J. Chem. Phys.* **2015**, *142* (10), 101915.

(326) Weidner, T.; Ballav, N.; Siemeling, U.; Troegel, D.; Walter, T.; Tacke, R.; Castner, D. G.; Zharnikov, M. Tripodal Binding Units for Self-Assembled Monolayers on Gold: A Comparison of Thiol and Thioether Headgroups. *J. Phys. Chem. C* **2009**, *113* (45), 19609–19617.

(327) Chithrani, D. B. Optimization of Bio-Nano Interface Using Gold Nanostructures as a Model Nanoparticle System. *Insciences J.* **2011**, 115–135.

(328) Celis-Gutierrez, J.; Blattmann, P.; Zhai, Y.; Jarmuzynski, N.; Ruminski, K.; Grégoire, C.; Ounoughene, Y.; Fiore, F.; Aebersold, R.; Roncagalli, R.; Gstaiger, M.; Malissen, B. Quantitative Interactomics in Primary T Cells Provides a Rationale for Concomitant PD-1 and BTLA Coinhibitor Blockade in Cancer Immunotherapy. *Cell Rep.* **2019**, *27* (11), 3315-3330.e7.

(329) Li, C. W.; Lim, S. O.; Xia, W.; Lee, H. H.; Chan, L. C.; Kuo, C. W.; Khoo, K. H.; Chang, S. S.; Cha, J. H.; Kim, T.; Hsu, J. L.; Wu, Y.; Hsu, J. M.; Yamaguchi, H.; Ding, Q.; Wang, Y.; Yao, J.; Lee, C. C.; Wu, H. J.; Sahin, A. A.; Allison, J. P.; Yu, D.; Hortobagyi, G. N.; Hung, M. C. Glycosylation and Stabilization of Programmed Death Ligand-1 Suppresses T-Cell Activity. *Nat. Commun.* **2016**, *7*.

(330) Uriel, J. Cell Injury, Retrodifferentiation and the Cancer Treatment Paradox. *Tumor Biol.* **2015**, *36* (10), 7365–7374.

(331) Kalyane, D.; Raval, N.; Maheshwari, R.; Tambe, V.; Kalia, K.; Tekade, R. K. Employment of Enhanced Permeability and Retention Effect (EPR): Nanoparticle-Based Precision Tools for Targeting of Therapeutic and Diagnostic Agent in Cancer. *Mater. Sci. Eng. C* **2019**, *98*, 1252–1276.

(332) Samadian, H.; Jafari, S.; Sepand, M. R.; Alaei, L.; Sadegh Malvajerd, S.; Jaymand, M.; Ghobadinezhad, F.; Jahanshahi, F.; Hamblin, M. R.; Derakhshankhah, H.; Izadi, Z. 3D Bioprinting Technology to Mimic the Tumor Microenvironment: Tumor-on-a-Chip Concept. *Mater. Today Adv.* **2021**, *12*, 100160.

(333) Kleijn, M.; Proud, C. G. The Regulation of Protein Synthesis and Translation Factors by CD3 AndCD28in Human Primary T Lymphocytes. *BMC Biochem.* **2002**, *3* (1), 1–12.

(334) Schietinger, A.; Greenberg, P. D. Tolerance and Exhaustion: Defining Mechanisms of T Cell Dysfunction. *Trends Immunol.* **2014**, *35* (2), 51–60.

(335) Khedri, M.; Abnous, K.; Rafatpanah, H.; Ramezani, M. An Optimized Protocol for the in Vitro Generation and Functional Analysis of Human PD1/PD-L1 Signal. *J. Recept. Signal Transduct.* **2018**, *38* (1), 31–36.

(336) Jiao, J.; Zhao, X.; Hou, R.; Wang, Y.; Chang, W.; Liang, N.; Liu, Y.; Xing, J.; Cao, Y.; Li, X.; Zhang, K. Comparison of Two Commonly Used Methods for Stimulating T Cells. *Biotechnol. Lett.* **2019**, *41* (12), 1361–1371.

(337) Bashoura, K. T.; Gondarenko, A.; Chen, H.; Shen, K.; Liu, X.; Huse, M.; Hone, J. C.; Kam, L. C. CD28 and CD3 Have Complementary Roles in T-Cell Traction Forces. *Proc. Natl. Acad. Sci. U. S. A.* **2014**, *111* (6), 2241–2246.

(338) Ai, W.; Li, H.; Song, N.; Li, L.; Chen, H. Optimal Method to Stimulate Cytokine Production and Its Use in Immunotoxicity Assessment. *Int. J. Environ. Res. Public Health* **2013**, *10* (9), 3834–3842.

(339) Chatila, T.; Silverman, L.; Miller, R.; Geha, R. Mechanisms of T Cell Activation by the Calcium Ionophore Ionomycin. *J. Immunol.* **1989**, *143* (4), 1283–1289.

(340) O'donovan, M. R.; Johns, S.; Wilcox, P. The Effect of PHA Stimulation on Lymphocyte Sub-Populations in Whole-Blood Cultures. *Mutagenesis* **1995**, *10* (4), 371–374.

(341) Potter, M. R.; Moore, M. PHA Stimulation of Separated Human Lymphocyte Populations. *Clin. Exp. Immunol.* **1975**, *21* (3), 456–467.

(342) Movafagh, A.; Heydary, H.; Mortazavi-Tabatabaei, S. A. R.; Azargashb, E. The Significance Application of Indigenous Phytohemagglutinin (PHA) Mitogen on Metaphase and Cell Culture Procedure. *Iran. J. Pharm. Res.* **2011**, *10* (4), 895–903.

(343) Antonioli, L.; Blandizzi, C.; Pacher, P.; Guilliams, M.; Haskó, G. Quorum Sensing in the Immune System. *Nat. Rev. Immunol.* **2018**, *18* (9), 537–538.

Supplementary Table of Contents:

Table of Supplementary Figures

Table of Supplementary Tables

Table of Supplementary Schemes

2. Supplementary Materials (Chapter 2)

Synthesis of Small Molecules 3–5

4a. Synthesis of Compound 3

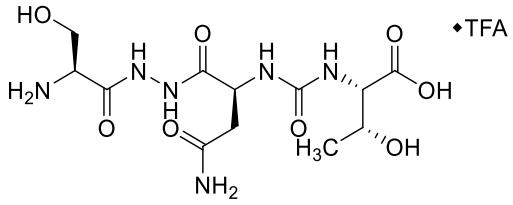

Compound **3**

This compound was described in US 2013/237580, Example 2 and similar chemistry was used herein to prepare this material at WuXi Apptec Co, Ltd. The characterization data for the compound is shown below. Nuclear Magnetic Resonance (NMR) analysis was conducted using a Varian 400 MHz spectrometer with an appropriate deuterated solvent. LCMS analysis was conducted using an Agilent 1200 & 1956A Waters Atlantis HILIC Silica 5 µM, 2.1 × 50 mm column, eluting with 90:10 to 40:60 H_2O:MeCN + 0.03% trifluoroacetic acid over 4 minutes at a flow rate of 0.6 mL/min. Detection methods are diode array (DAD) and evaporative light scattering (ELSD) detection as well as positive electrospray ionization. MS range was 100 – 1 000.

Preparation of Intermediate A: Benzyl *O*-(*tert*-butyl)-*N*-(1*H*-imidazole-1-carbonyl)-*L*-threoninate

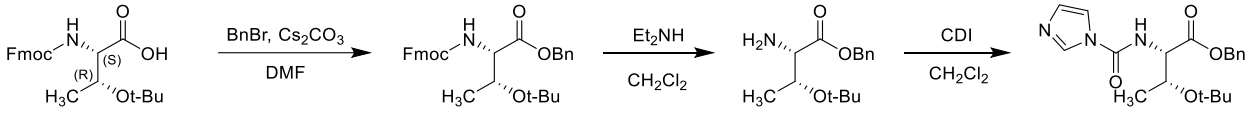

H-Thr(O^tBu)-O^tBu

Step 1: Synthesis of benzyl *N*-(((9*H*-fluoren-9-yl)methoxy)carbonyl)-*O*-(*tert*-butyl)-L-threoninate

To a solution of compound *N*-(((9*H*-fluoren-9-yl)methoxy)carbonyl)-*O*-(*tert*-butyl)-L-threonine (20.0 g, 50.3 mmol, 1.0 eq., Fisher, CAS# 71989-35-0) in *N,N*-dimethylformamide (200 mL, 0.25 M) was added cesium carbonate (19.6 g, 60.4 mmol, 1.2 eq.) at 15 °C, the mixture was cooled to 0 °C and benzyl bromide (10.3 g, 60.4 mmol, 1.2 eq.) was added drop-wise. After stirring for 10 min, the mixture was warmed up to 15 °C and stirred for 16 h. TLC (petroleum ether/ethyl acetate = 2:1, Rf (SM) = 0.07, Rf (Prod) = 0.7) showed the starting material was consumed completely. The mixture was cooled to 5 °C and diluted with water (500 mL) and ethyl acetate (300 mL). The aqueous layer was extracted with ethyl acetate (2 × 200 mL) and the combined organic layers were washed with brine (200 mL), dried over anhydrous sodium sulfate, and concentrated in vacuum. The residue was purified by silica gel chromatography (petroleum ether/ethyl acetate = 30:1-10:1) to give the title compound (22.8 g, 93% yield) as a white solid.

^{1}H NMR (400 MHz, $CDCl_3$) δ 7.70-7.68 (m, 2H), 7.65-7.50 (m, 2H), 7.32-7.23 (m, 9H), 5.55 (d, *J* = 9.0 Hz, 1H), 5.14 (d, *J* = 12.0 Hz, 1H), 5.01 (d, *J* = 12.0 Hz, 1H), 4.34-4.16 (m, 5H), 1.15 (d, *J* = 5.5 Hz, 3H), 1.03 (s, 9H).

Step 2: Synthesis of benzyl *O*-(*tert*-butyl)-*L*-threoninate

To a solution of benzyl *N*-(((9*H*-fluoren-9-yl)methoxy)carbonyl)-*O*-(*tert*-butyl)-L-threoninate (10.0 g, 20.5 mmol, 1.0 eq.) in anhydrous dichloromethane (100 mL, 0.2 M) was added *N,N*-diethylamine (7.5 g, 103 mmol, 5.0 eq.) at 15 °C, then the mixture was stirred at 15 °C for 12 h. TLC analysis (petroleum ether / ethyl acetate = 5:1, R_f (starting material = 0.4, product = 0)) showed the reaction was complete. The reaction mixture was concentrated under reduced pressure to give a residue. The residue was purified by column chromatography on silica gel (petroleum ether/ethyl acetate = 10:1) to give the title compound (4.5 g, 83% yield) as a yellow oil.

^{1}H NMR (400 MHz, $CDCl_3$) δ 7.37-7.26 (m, 5H), 5.20 (d, *J* = 12.0 Hz, 1H), 5.05 (d, *J* = 12.0 Hz, 1H), 4.04-3.99 (m, 1H), 3.32-3.31 (m, 1H), 1.23 (d, *J* = 6.0 Hz, 3H), 1.11 (s, 9H).

LCMS (ESI+): *m/z* 266 $(M+1)^+$

Step 3: Synthesis of benzyl *N*-(((9*H*-fluoren-9-yl)methoxy)carbonyl)-*O*-(*tert*-butyl)-L-threoninate

To a solution of benzyl *O*-(*tert*-butyl)-*L*-threoninate (4.5 g, 16.9 mmol, 1.0 eq.) in anhydrous dichloromethane (50 mL, 0.34 M) was added a solution of156midazoleazol-1-yl)methanone (4.12 g, 25.4 mmol, 1.5 eq.) in anhydrous dichloromethane (20 mL) at -20 °C, then the mixture was stirred at 0 °C for 2 h. LCMS showed the reaction was complete. The reaction was quenched with water (50 mL) and the mixture was separated using a separatory funnel and the aqueous phase was extracted with dichloromethane (2 × 50 mL). The combined organic phases were washed with brine (50 mL), dried over anhydrous sodium sulfate, and concentrated under reduced pressure to give afford the title compound (6.80 g, unpurified) as a colorless oil which was used directly in the next step.

LCMS (ESI+): *m/z* 360 $(M+1)^+$

Preparation of (((*S*)-1-(2-(*L*-seryl)hydrazinyl)-4-amino-1,4-dioxobutan-2-yl)carbamoyl)-*L*-threonine trifluoroacetate

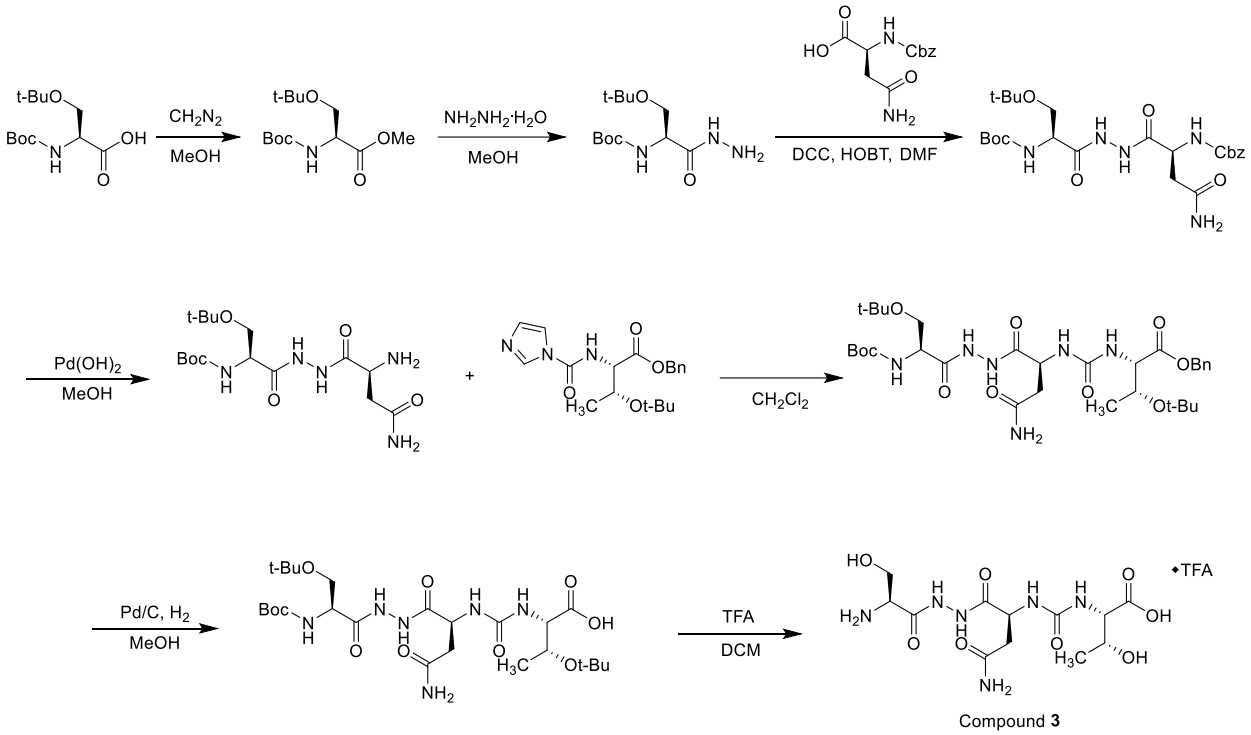

Step 1: Synthesis of methyl *N*-(*tert*-butoxycarbonyl)-*O*-(*tert*-butyl)-*L*-serinate

A solution of diazomethane (0.77 M, 397 mL, 4.0 eq.) in ether was decanted portion-wise to a solution of *N*-(*tert*-butoxycarbonyl)-*O*-(*tert*-butyl)-*L*-serine (20 g, 76.5 mmol, 1.0 eq., Alfa Aesar CAS# 13734-38-8) in methanol (200 mL, 0.1 M) at -5 °C. After addition, the mixture was warmed to 15 °C and stirred for 16 h at this temperature. TLC analysis (methanol/dichloromethane = 10:1, Rf (SM) = 0.3, petroleum ether/ethyl acetate = 2:1, Rf (Prod) = 0.7) showed the starting material was consumed completely. The mixture was concentrated in vacuum to give the title compound (22.8 g, unpurified) as a colorless oil, which was used directly for the next step.

^{1}H NMR (400 MHz, $CDCl_3$) δ 5.37 (d, J = 9.0 Hz, 1H), 4.35 (d, J = 9.0 Hz, 1H), 3.74 (dd, J_1 = 3.0 Hz, J_2 = 9.0 Hz 1H), 3.69 (s, 3H), 3.74 (dd, J_1 = 3.0 Hz, J_2 = 9.0 Hz 1H), 1.40 (s, 9H), 1.11 (s, 9H).

Step 2: Synthesis of *tert*-butyl (*S*)-(3-(*tert*-butoxy)-1-hydrazinyl-1-oxopropan-2-yl)carbamate

To a solution of methyl *N*-(*tert*-butoxycarbonyl)-*O*-(*tert*-butyl)-*L*-serinate (23 g, 83.5 mmol, 1.0 eq.) in methanol (230 mL, 0.36 M) was added hydrazine monohydrate (25.1 g, 501 mmol, 6.0 eq.) at 15 °C. The mixture was stirred at 15 °C for 16 h. TLC analysis (petroleum ether/ethyl acetate = 3:1, Rf (SM) = 0.7, methanol/dichloromethane = 15:1, Rf (Prod) = 0.4) showed the starting material was consumed completely. The mixture was concentrated under reduced pressure to remove the methanol. The residue was dissolved in ethyl acetate (150 mL) and washed with aqueous sodium bicarbonate (2 × 60 mL). The combined organic phases were dried over anhydrous sodium sulfate, filtered and the filtrate was concentrated under vacuum to give the title compound (15 g, 65% yield) as a colorless oil, which was used directly for the next step.

^{1}H NMR (400 MHz, $CDCl_3$) δ 7.76 (br.s, 1H), 5.39 (br.s, 1H), 4.18 (s, 1H), 3.89 (br.s, 2H), 3.75 (dd, J_1 = 2.8 Hz, J_2 = 9.0 Hz, 1H), 3.38 (t, *J* = 8.0 Hz, 1H), 1.43 (s, 9H), 1.16 (s, 9H).

Step 3: Synthesis of *tert*-butyl ((5*S*,10*S*)-5-(2-amino-2-oxoethyl)-13,13-dimethyl-3,6,9-trioxo-1-phenyl-2,12-dioxa-4,7,8-triazatetradecan-10-yl)carbamate

To a solution of *tert*-butyl (*S*)-(3-(*tert*-butoxy)-1-hydrazinyl-1-oxopropan-2-yl)carbamate (14.4 g, 53.9 mmol, 1.1 eq.) in *N,N*-dimethylformamide (140 mL, 0.39 M) was added dicyclohexylcarbodiimide (25.3 g, 123 mmol, 2.5 eq.) and HOBt (13.3 g, 98.1 mmol, 2.0 eq.) at 0°C. The resulting mixture was stirred 0 °C for 5 min and to the mixture was added dropwise a solution of ((benzyloxy)carbonyl)-*L*-asparagine (13.5 g, 49 mmol, 1.0 eq., Alfa Aesar CAS# 2304-96-3) in *N,N*-dimethylformamide (80 mL) at 0 °C. The mixture was stirred at this temperature for 1 h and then allowed to warm to 15 °C and stirred at 15 °C for 16 h. The resulting mixture was filtered to remove formed solid and the filtrate was poured into ice-water (300 mL) and a precipitate formed. The mixture was filtered, and the filtered cake was dried under *vacuum*. The filter cake was dissolved in *N,N*-dimethylformamide (250 mL) and poured into water (300 mL). The solid was separated out by filtration and the filtrate was dried in *vacuum* to give the title (9.6 g, unpurified) as an off-white solid. This solid contained *N,N*-dimethylformamide and urea byproduct.

^{1}H NMR (400 MHz, CD_3OD) δ 7.50-7.20 (m, 5 H), 5.12 (s, 2H), 4.63 (Br. s, 1H), 4.26 (Br. s, 1H), 3.62 (d, *J* = 4.5 Hz, 2H), 2.78 (dd, *J* = 15.5, 5.0 Hz, 1H), 2.64 (dd, *J* = 15.5, 8.0 Hz, 1H), 1.45 (s, 9H), 1.19 (s, 9H).

Step 4: Synthesis of *tert*-butyl ((*S*)-1-(2-(*L*-asparaginyl)hydrazinyl)-3-(*tert*-butoxy)-1-oxopropan-2-yl)carbamate

To a solution of *tert*-butyl ((5*S*,10*S*)-5-(2-amino-2-oxoethyl)-13,13-dimethyl-3,6,9-trioxo-1-phenyl-2,12-dioxa-4,7,8-triazatetradecan-10-yl)carbamate (7.0 g, 13.4 mmol, 1.00 eq.) in methanol (500 mL, 0.13 M) was added 10 wt% palladium hydroxide on carbon (3.0 g) and the mixture was stirred at 30 °C under a hydrogen atmosphere (50 psi) for 12 h. The reaction mixture was filtered through a celite pad, the filter cake was washed with methanol (3 × 150 mL), and the combined filtrate was concentrated under vacuum to give the title compound (6 g) as a purple solid which was used directly without purification in the next step.

^{1}H NMR (400 MHz, $CDCl_3$) δ 5.82-5.37 (m, 3H), 4.35-4.29 (m, 2 H), 3.79-3.71 (m, 2H), 3.48-3.44 (m, 2H), 2.74-2.70 (m, 1H), 2.01-1.89 (m, 2H), 1.46 (s, 9H), 1.22 (s, 9H).

LCMS (ESI+): *m/z* 390 $(M+1)^+$

Step 5: Synthesis of benzyl *N*-(((*S*)-4-amino-1-(2-(*N*-(*tert*-butoxycarbonyl)-*O*-(*tert*-butyl)-*L*-seryl)hydrazinyl)-1,4-dioxobutan-2-yl)carbamoyl)-*O*-(*tert*-butyl)-*L*-threoninate

To a solution of *tert*-butyl ((*S*)-1-(2-(*L*-asparaginyl)hydrazinyl)-3-(*tert*-butoxy)-1-oxopropan-2-yl)carbamate (7.7 g, 19.8 mmol, 1.0 eq.) in anhydrous dichloromethane (70 mL, 0.28 M) was added a solution of benzyl *O*-(*tert*-butyl)-*N*-(1*H*-imidazole-1-carbonyl)-*L*-threoninate (6.82 g, 19.0 mmol, 0.96 eq.) in anhydrous dichloromethane (30 mL) at 0 °C, then the mixture was stirred at 15 °C for 12 h. The reaction mixture was concentrated under vacuum and the residue was purified by preparative-HPLC (Column Daiso 250 × 50 mm, 10 μm, eluting with 35% to 65% MeCN in water (+0.1% TFA) over 20 minutes, followed by 100% MeCN in water (+0.1% TFA) for 15 minutes at a flow rate of 80 mL/min. The sample was

loaded onto the column over 16 injections. The desired compound (1.4 g, 10% yield) was obtained as a light-yellow solid.

^{1}H NMR (400 MHz, $CDCl_3$) δ 7.40-7.30 (m, 5H), 6.88-6.86 (m, 1H), 6.75 (br.s, 1H), 6.68 (br.s, 1H), 6.01 (br.s, 1H), 5.47 (d, *J* = 6.0 Hz, 1H), 5.17 (d, *J* = 12.0 Hz, 1H), 5.07-5.03 (m, 1H), 4.92-4.89 (m, 1H), 4.54 (d, *J* = 9.0 Hz, 1H), 4.27 (br.s, 1H), 4.18-4.15 (m, 1H), 3.75-3.73 (m, 1H), 3.36 (t, *J* = 8.5 Hz, 1H), 3.10 (t, *J* = 13.5 Hz, 1H), 2.59 (dd, J_1= 15.5 Hz, J_2= 4.0 Hz, 1H), 1.43 (s, 9H), 1.21 (s, 9H), 1.17 (d, *J* = 6.4 Hz, 3H), 1.06 (s, 9H).

LCMS (ESI+): *m/z* 681 $(M+1)^+$

Step 6: Synthesis of *N*-(((*S*)-4-amino-1-(2-(*N*-(*tert*-butoxycarbonyl)-*O*-(*tert*-butyl)-*L*-seryl)hydrazinyl)-1,4-dioxobutan-2-yl)carbamoyl)-*O*-(*tert*-butyl)-*L*-threonine

To a solution of benzyl *N*-(((*S*)-4-amino-1-(2-(*N*-(*tert*-butoxycarbonyl)-*O*-(*tert*-butyl)-*L*-seryl)hydrazinyl)-1,4-dioxobutan-2-yl)carbamoyl)-*O*-(*tert*-butyl)-*L*-threoninate (1.4 g, 2.37 mmol, 1.0 eq.) in methanol (50 mL, 0.05 M) was added 10 wt% palladium on carbon (700 mg) and the mixture was stirred at 30 °C under a hydrogen atmosphere (50 psi) for 3 h. The reaction mixture was filtered through a pad of celite, the filter cake was washed with methanol (3 × 50 mL) and the combined filtrate was concentrated under vacuum to afford the unpurified solid. The resulting solid was purified by preparative-HPLC (Instrument: Gilson 281 semi-preparative HPLC system) using a gradient of 65:35 to 35:65 H_2O:MeCN (+0.075% TFA) over 10 minutes, flushing with 100% MeCN for 2 minutes after the run. The column used was a Boston Green ODS 150 × 30 mm, 5 µm particle size, with a flow rate of 25 mL/min and monitoring at 220 and 254 nm wavelengths. The title compound (710 mg, 58% yield) was obtained as a white solid.

^{1}H NMR (400 MHz, d_6-DMSO) δ 9.92 (br.s, 1H), 9.80 (br.s, 1H), 6.86 (br.s, 1H), 6.75 (br.s, 1H), 6.57 (d, *J* = 8.5 Hz, 1H), 6.18 (d, *J* = 9.0 Hz, 1H), 4.45 (br.s, 1H), 4.07-4.04 (m, 4H), 3.48-3.44 (m, 1H), 3.39-3.35 (m, 1H), 2.42-2.41(m, 1H), 2.34-2.28 (m, 1H), 1.35 (s, 9H), 1.09 (s, 9H), 1.07 (s, 9H), 1.03 (d, *J* = 6.5 Hz, 3H).

LCMS (ESI+): *m/z* 591 $(M+1)^+$

Step 7: Synthesis of (((*S*)-1-(2-(*L*-seryl)hydrazinyl)-4-amino-1,4-dioxobutan-2-yl)carbamoyl)-*L*-threonine trifluoroacetate

To a solution of *N*-(((*S*)-4-amino-1-(2-(*N*-(*tert*-butoxycarbonyl)-*O*-(*tert*-butyl)-*L*-seryl)hydrazinyl)-1,4-dioxobutan-2-yl)carbamoyl)-*O*-(*tert*-butyl)-*L*-threonine (700 mg, 1.19 mmol, 1.0 eq.) in dichloromethane (30 mL) was added trifluoroacetic acid (30 mL) and the resulting mixture was stirred at 15 °C for 12 h. The reaction mixture was concentrated under vacuum to afford a residue. The resulting residue was purified by preparative-HPLC (Instrument: Gilson 281 semi-preparative HPLC system) using a gradient of 5:95 to 10:90 H_2O:MeCN (+0.075% TFA) over 12 minutes, flushing with 100% MeCN for 7 minutes after the run. The column used was an Atlantis Hilic Silica 150 × 19 mm, 5 µm particle size, with a flow rate of 25 mL/min and monitoring at 220 and 254 nm wavelengths. The title compound (trifluoroacetate salt, 102 mg, 23 % yield) was obtained as a white solid.

^{1}H NMR (400 MHz, D_2O) δ 4.70-4.65 (m, 1H), 4.34-4.30 (m, 1H), 4.25-4.22 (m, 2H), 4.02-3.99 (m, 2H), 2.92-2.75 (m, 2H), 1.20 (d, *J* = 2.8 Hz, 3H).

LCMS (ESI+): *m/z* 379 $(M+1)^+$

4b. Synthesis of Compound **4**

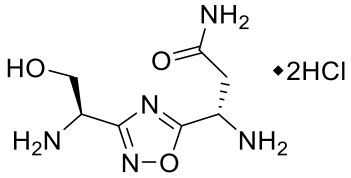

Compound **4**

This compound was described in WO 2015/033299, Example 1 and identical chemistry was used herein to prepare this material at Santai Labs. The characterization data for the final compound is shown below. Nuclear Magnetic Resonance (NMR) analysis was conducted using a Bruker 400 MHz spectrometer with an appropriate deuterated solvent. LCMS analysis was conducted using a Shimadzu lC-ATvp with an API 150EX detector using an Agilent Zorbax Eclipse lDB-C18 3.5 µM, 2.1 × 50 mm column, eluting with 95:5 to 20:80 H_2O:MeCN + 0.02% formic acid over 4 minutes.

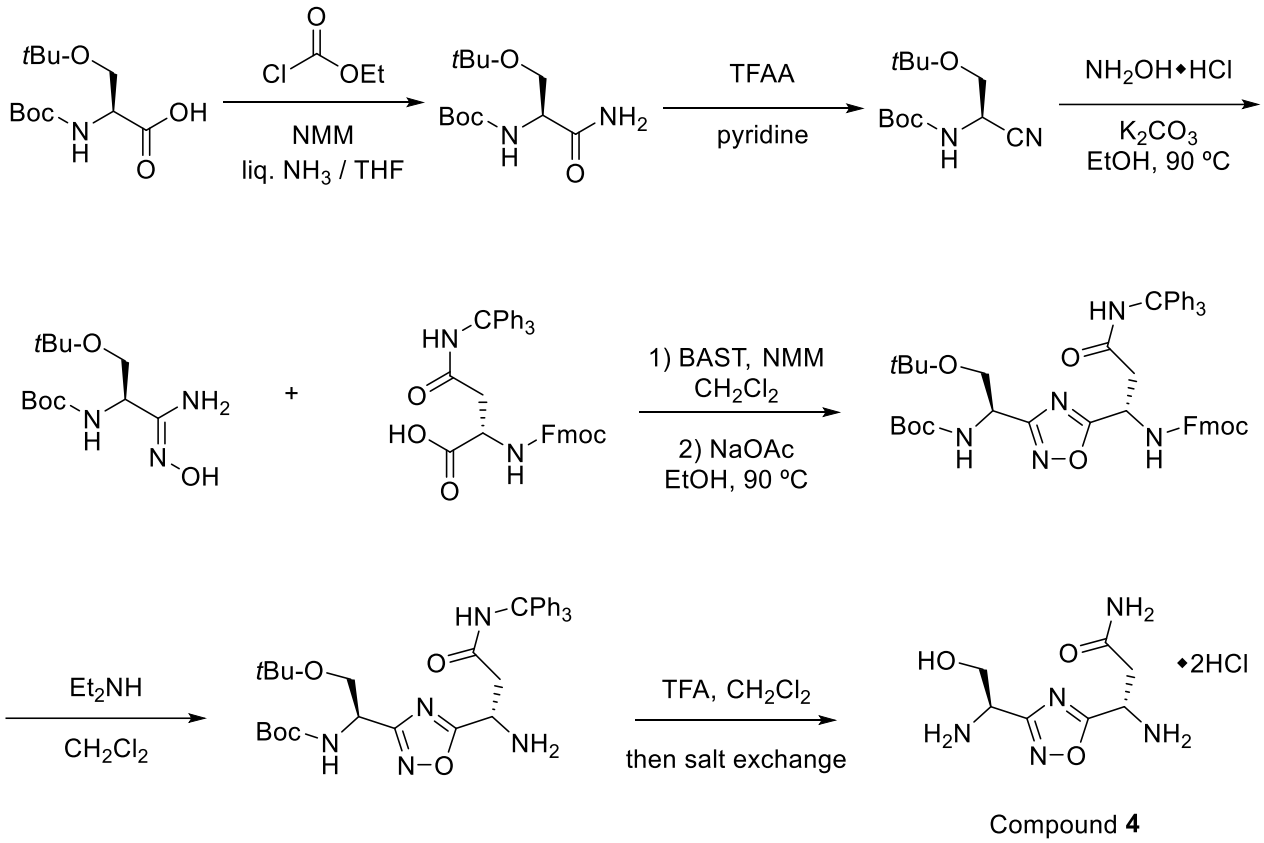

Compound **4**

^{1}H NMR (400 MHz, CD_3OD) δ 5.21-5.19 (bs, 1H), 4.07 (bs, 1H), 4.03-4.00 (m, 2H), 3.23-3.22 (m, 2H).

^{13}C NMR (100 MHz, D_2O) δ 176.36, 172.26, 166.06, 59.89, 49.20, 44.86, 34.66.

LCMS (ESI+): *m/z* 238 $(M+23)^+$

4c. Synthesis of Compound **5**

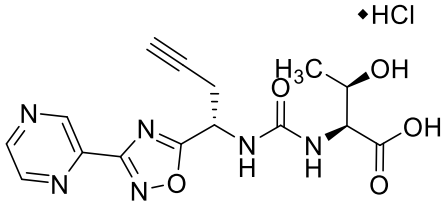

Compound **5**

This compound was described in WO 2016/142886, Example 32 and identical chemistry was used herein to prepare this material at Santai Labs. The characterization data for the final compound is shown below. Nuclear Magnetic Resonance (NMR) analysis was conducted using a Bruker 400 MHz spectrometer with an appropriate deuterated solvent. LCMS analysis was conducted using a Shimadzu lC-ATvp with an API 150EX detector using an Agilent Zorbax Eclipse IDB-C18 3.5 µM, 2.1 × 50 mm column, eluting with 95:5 to 20:80 H_2O:MeCN + 0.02% formic acid over 4 minutes.

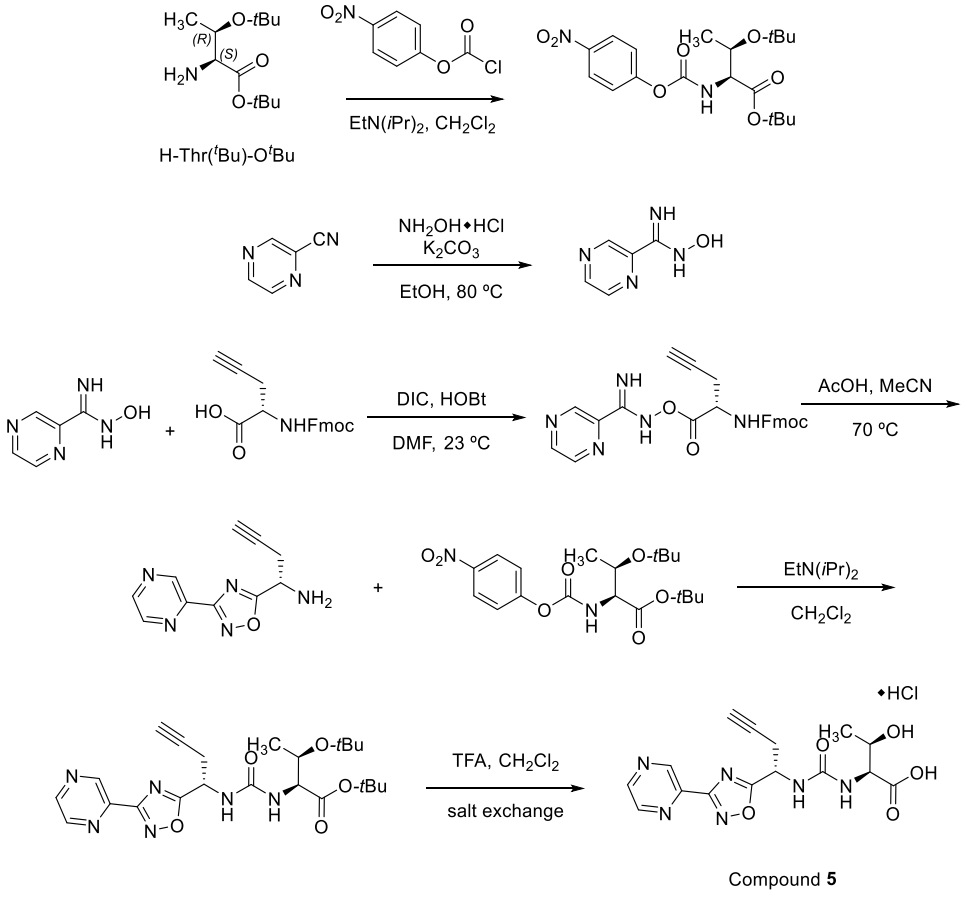

^{1}H NMR (400 MHz, CD_3OD) δ 9.33 (s, 1H), 8.79 (d, *J* = 7.0 Hz, 2H), 5.39 (t, *J* = 6.0 Hz, 1H), 4.31 (d, *J* = 7.0 Hz), 4.25 (s, 1H), 2.98 (m, 2H), 2.45 (s, 1H), 1.21 (d, *J* = 6.0 Hz).

LCMS (ESI+): *m/z* 361 $(M+1)^+$

4d. Synthesis of Compound 6

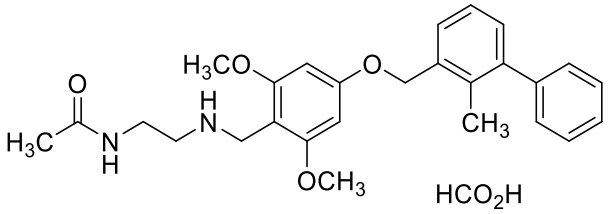

Compound **6**

This compound was described in WO 2015/034820 and similar chemistry was used herein to prepare this material at Inception Sciences Vancouver. Nuclear Magnetic Resonance (NMR) analysis was conducted using a Varian Mercury 300 MHz spectrometer with an appropriate deuterated solvent. LCMS analysis was conducted using a Waters Acquity UPLC with a QDA MS detector using a Waters C18 BEH 1.7 µM, 2.1 × 50 mm column, eluting with 95:5 to 0:100 H_2O:MeCN + 0.1% formic acid at a flow rate of 0.6 mL/min over 3.5 minutes. The QDA MS detector was set up to scan under both positive and negative mode ions ranging from 100-1200 Daltons.

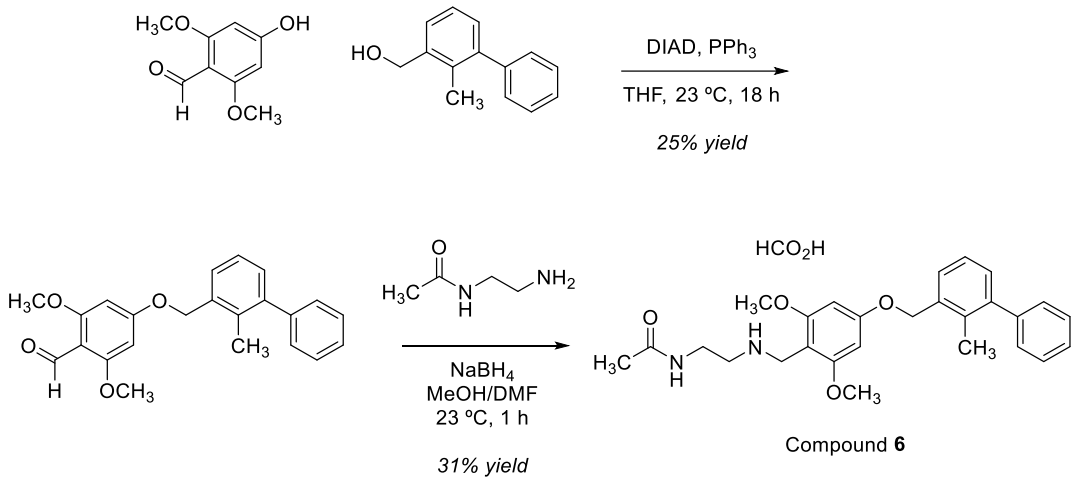

Step 1: Synthesis of 2,6-dimethoxy-4-((2-methyl-’1,1'-biphenyl]-3-yl)methoxy)benzaldehyde

Into a 20 mL sample vial equipped with a magnetic stir bar and under N_2 was added 3-hydroxymethyl 2-methylbiphenyl (1.08 g, 5.49 mmol, 1.0 eq., TCI CAS# 76350-90-8), 2,6-dimethoxy-4-hydroxybenzaldehyde (1.00 g, 5.49 mmol, 1.0 eq., Aldrich CAS# 22080-96-2), triphenylphosphine (2.16 g, 8.23 mmol, 1.5 eq.) and THF (2.0 mL, 2.8 M). The solution was treated with drop-wise addition of di-*iso*-propyl azodicarboxylate (1.62 mL, 8.23 mmol, 1.5 eq.) over 10 minutes and the red-orange solution was stirred at 23 ˚C for 18 h overnight. The reaction mixture was loaded directly onto a 20 g silica gel pre-cartridge and dried. Purification by column chromatography through silica gel (80 g) on an automated Teledyne ISCO Rf200, eluting with 80:20 to 20:80 hexanes:EtOAc as a gradient over 25 minutes, collecting all peaks. The desired product was isolated, concentrated, and dried under vacuum to afford an off-white solid (535 mg, 27% yield).

^{1}H NMR (300 MHz, $CDCl_3$) δ 10.37 (s, 1H), 7.41-7.26 (m, 8H), 6.20 (s, 2H), 5.16 (s, 2H), 3.89 (s, 6H), 2.27 (s, 3H).

LCMS (ESI+): *m/z* 363 $(M+1)^+$

Step 2: Synthesis of *N*-(2-((2,6-dimethoxy-4-((2-methyl-'1,1'-biphenyl]-3-yl)methoxy)benzyl)amino)ethyl) acetamide

Into a 20 mL sample vial equipped with a magnetic stir bar and under N_2 was added 2,6-dimethoxy-4-((2-methyl-'1,1'-biphenyl]-3-yl)methoxy)benzaldehyde (250 mg, 0.69 mmol, 1.0 eq.), DMF (2 mL, 0.35 M), acetic acid (40 µL, 0.69 mmol, 1.0 eq.) and *N*-(2-amino)ethyl acetamide (211 mg, 2.07 mmol, 3.0 eq.). The yellow-orange mixture was heated to 40 ˚C for 1 h and then cooled to room temperature. The solution was treated with $NaBH_4$ (76 mg, 2.07 mmol, 3.0 eq.) added portion-wise over 10 minutes and the mixture was stirred at 23 ˚C for 1 h. LCMS analysis after this time reveals product formation. The mixture was cooled to 0 ˚C and quenched with drop-wise addition of water (3 mL) and concentrated under reduced pressure. The unpurified reaction mixture was suspended in MeOH and loaded onto a 5 g C18 pre-cartridge and dried. Purification by reverse-phase column chromatography through C18 media (26 g) on an automated Teledyne ISCO Rf200, eluting with 100:0 to 40:60 H_2O:MeCN + 0.1% HCO_2H as a gradient over 20 minutes afforded the formate salt of the desired compound as a clear film (106 mg, 31% yield).

^{1}H NMR (300 MHz, $CDCl_3$) δ 8.47 (br.s, 1H), 7.42-7.26 (m, 8H), 6.23 (s, 2H), 5.08 (s, 2H), 4.13 (br.s, 2H), 3.83 (s, 6H), 3.49 (br.s, 2H), 2.98 (br.s, 2H), 2.26 (3H, s), 1.96 (3H, s).

LCMS (ESI+): *m/z* 449 $(M+1)^+$

Supplementary Sensorgram and Binding Figures

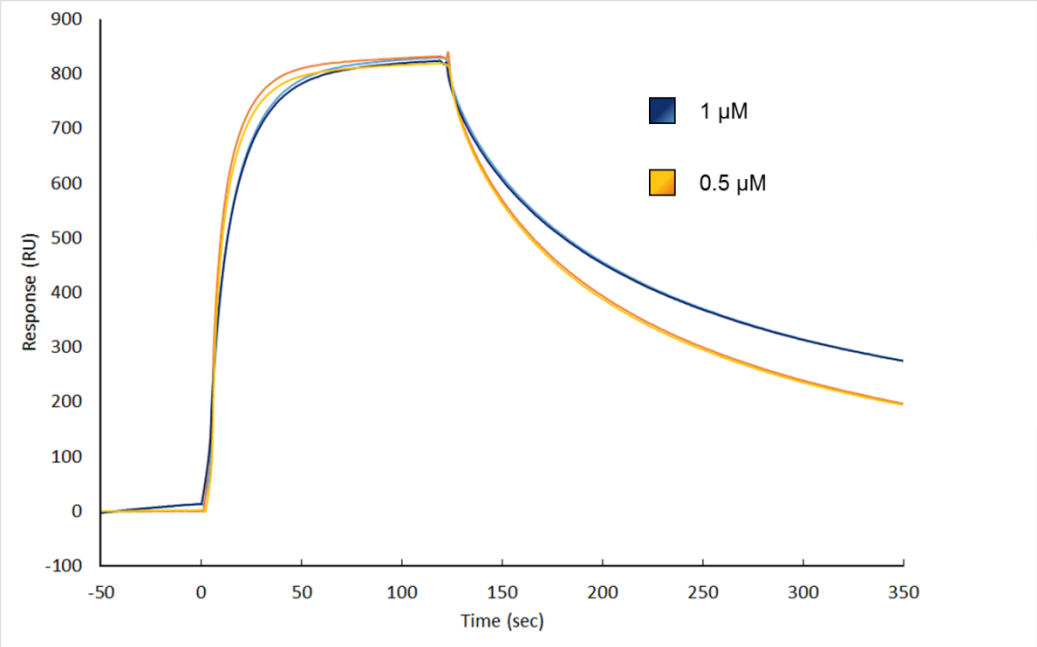

Figure S2.1. Representative sensorgrams for PD-1 binding to surface-bound PD-L1. The legend indicates the concentration of PD-1 used in each duplicate experiment.

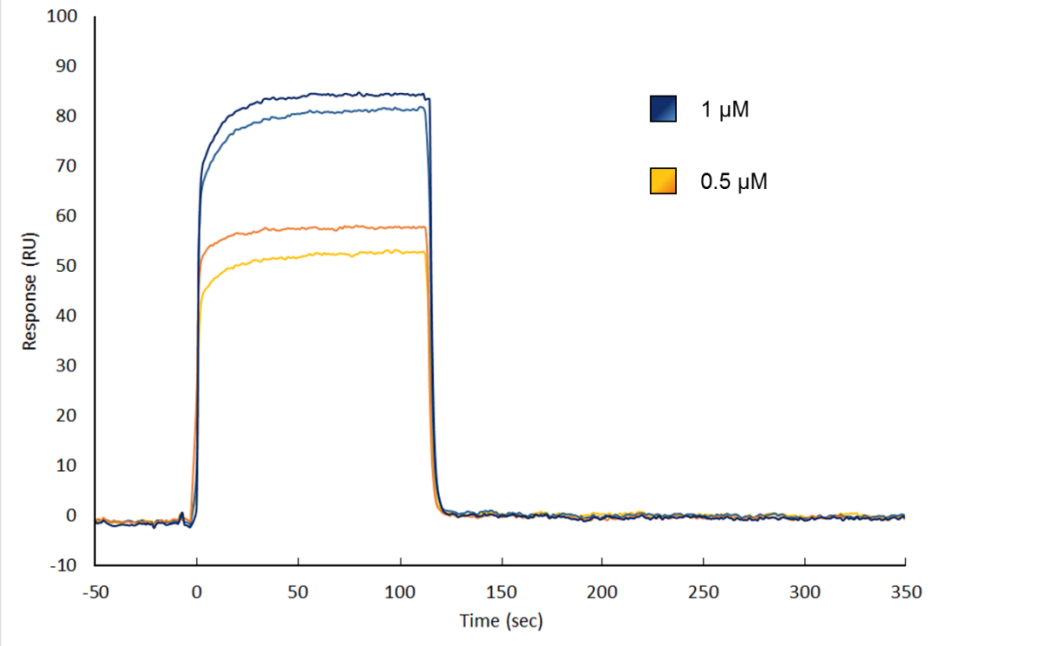

Figure S2.2. Representative sensorgrams for PD-L1 binding to surface-bound PD-1. The legend indicates the concentration of PD-L1 used in each duplicate experiment.

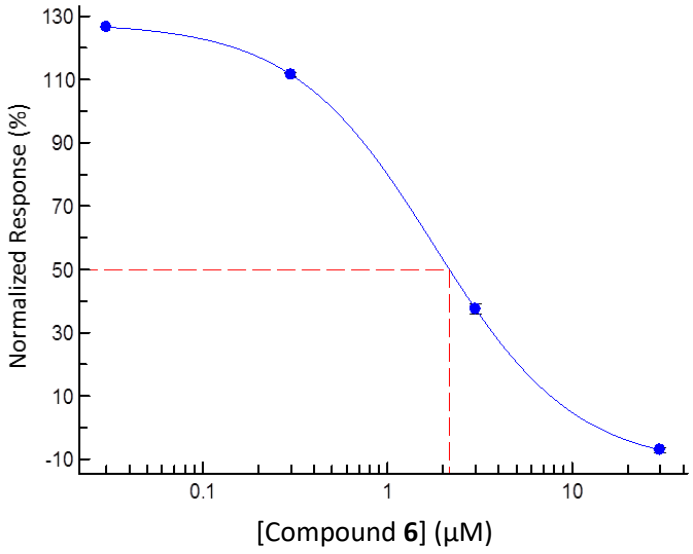

*Figure S2.3. Titration of compound **6** as an inhibitor of soluble PD-1 (at 15 µM) binding to a PD-L1 SA chip. The measured IC_{50} was 2.2 µM.*

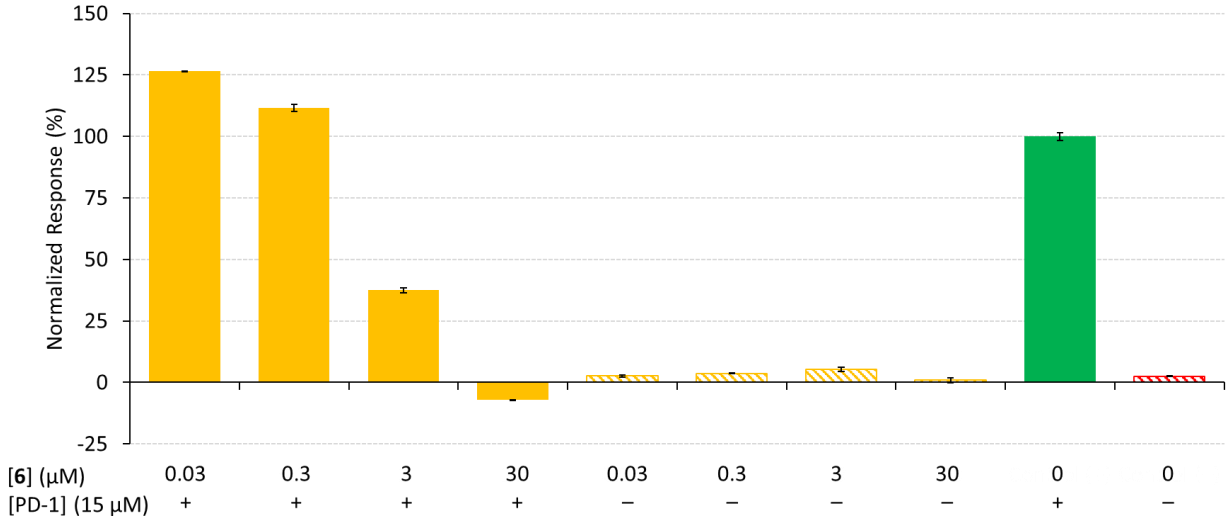

*Figure S2.4. Complete SPR data (including measurements with and without soluble PD-1) demonstrating inhibition of the PD-1/PD-L1 interaction with compound **6**. Soluble PD-1 (at 15 µM) was flowed across surface-bound PD-L1 with and without compound **6** at varying concentrations. The response is normalized to the protein interaction (PD-1 only, green). Error bars represent variance between duplicate analyses.*

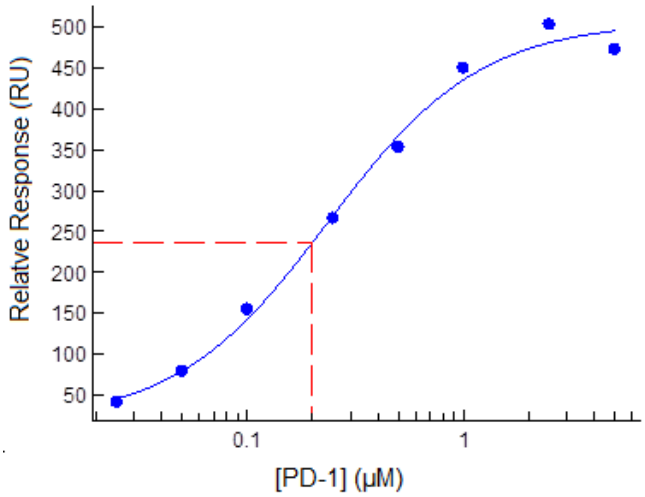

Figure S2.5. Measurement of the affinity for soluble PD-1 to surface-bound PD-L2. The effective K_D for the interaction was determined to be 199 nM by SPR.

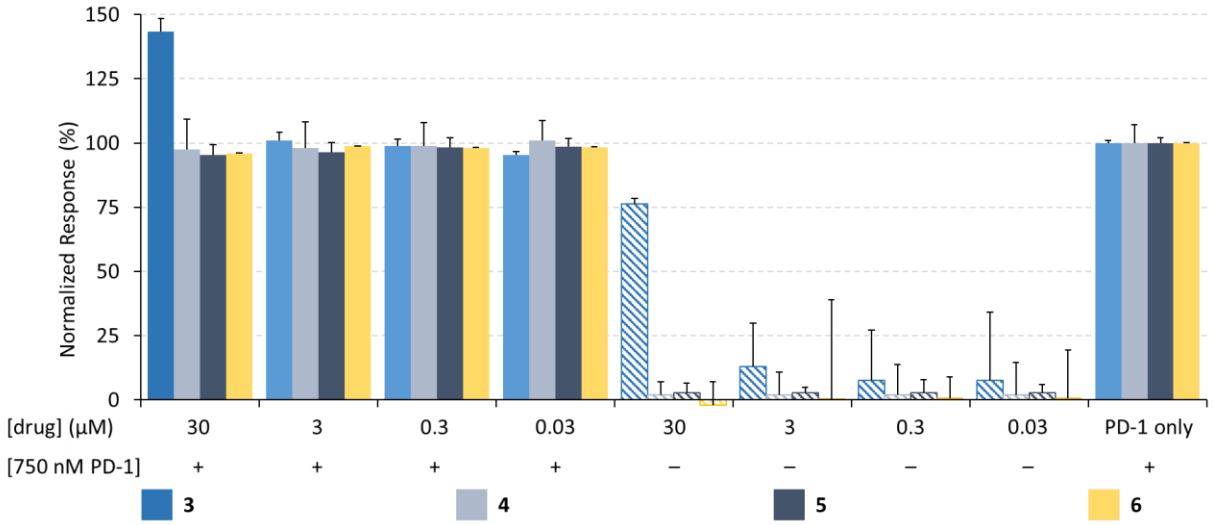

*Figure S2.6. Neither the Aurigene compounds (**3**–**5**) nor the BMS compound (**6**) were effective inhibitors of the PD-1/PD-L2 interaction, nor do any of the tested compound bind directly to surface-bound PD-L2. Soluble PD-1 was flowed across surface-bound PD-L2 with and without test compounds at various concentrations. The response is normalized to the control protein concentration (PD-1 only). Responses were measured in triplicate and error bars represent standard deviation. Hashed data indicate direct binding between the small molecules and the ligand, PD-L2, in the absence of PD-1.*

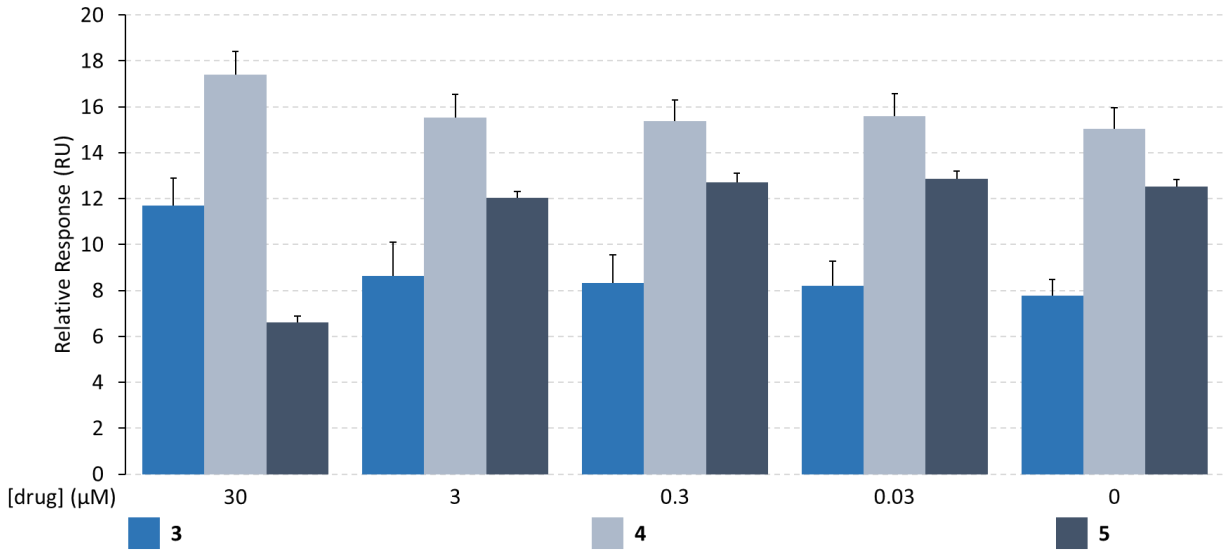

*Figure S2.7. The Aurigene compounds (**3**–**5**) do not bind to surface-bound VISTA protein. Test compounds at four different concentrations were flowed across surface-bound VISTA, but no significant binding (relative to the blank sample) was detected. Responses were measured in triplicate and error bars represent standard deviation. The expected maximal responses were 44, 25, and 42 RU for binding of any of the compounds **3**–**5**, respectively.*

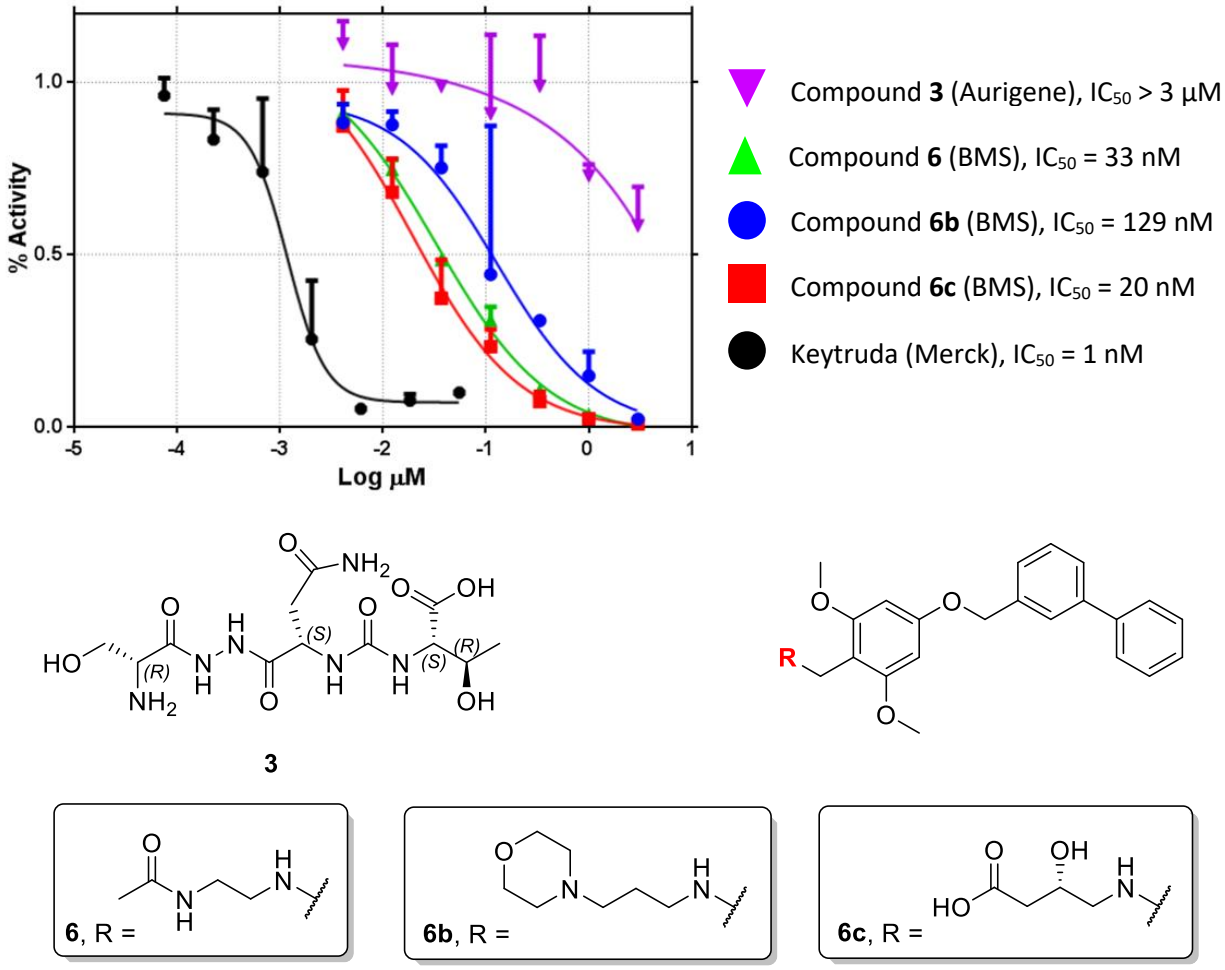

*Figure S 2.8. In a confirmatory ELISA assay, three compounds claimed by BMS (**6, 6b, 6c**) showed potent inhibition of the PD-1/PD-L1 interaction, but the Aurigene compound **3** showed no significant inhibition.* Experiment performed by Dr. Ronan Hanley, and figure modified from their thesis publication. The use of this figure was necessary to demonstrate the "efficacy" of the molecules in a non-SPR method. Keytruda is PD-L1-targeting monoclonal antibody currently in clinical use used another positive control.

Spectral Characterization of Compound 3–6

These works were previously described in the works presented by Dr. Ronan Hanley's doctoral thesis,[200] and described as published in the Synthesis of Small Molecules subsection above.

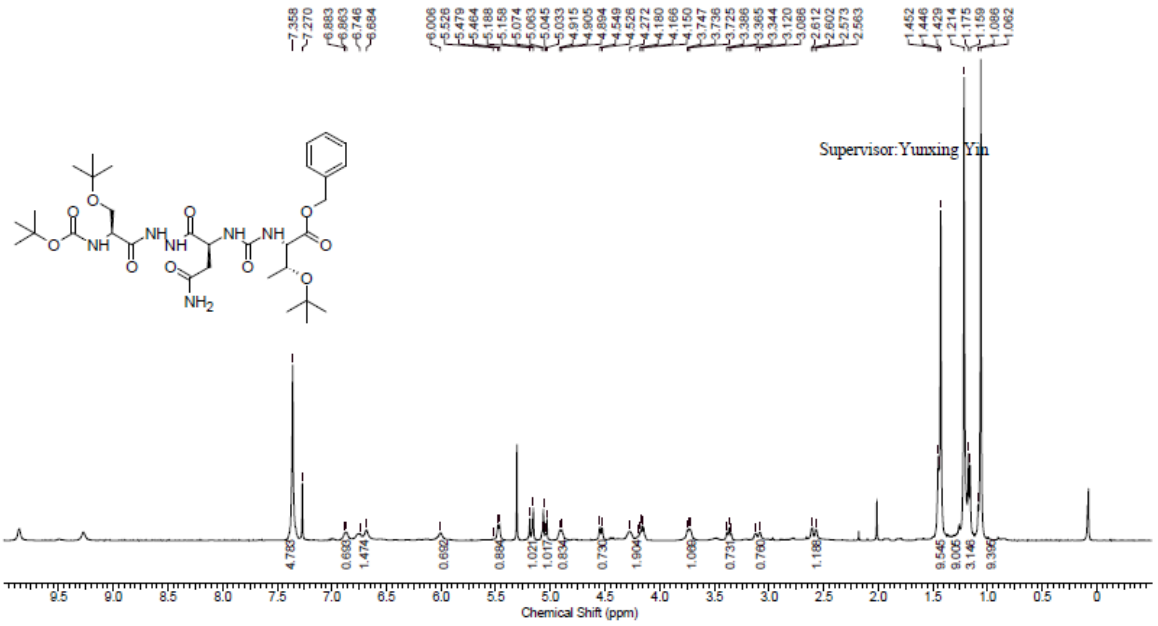

*Figure S2.9. ^{1}H NMR spectrum for fully protected precursor leading to compound **3**.*

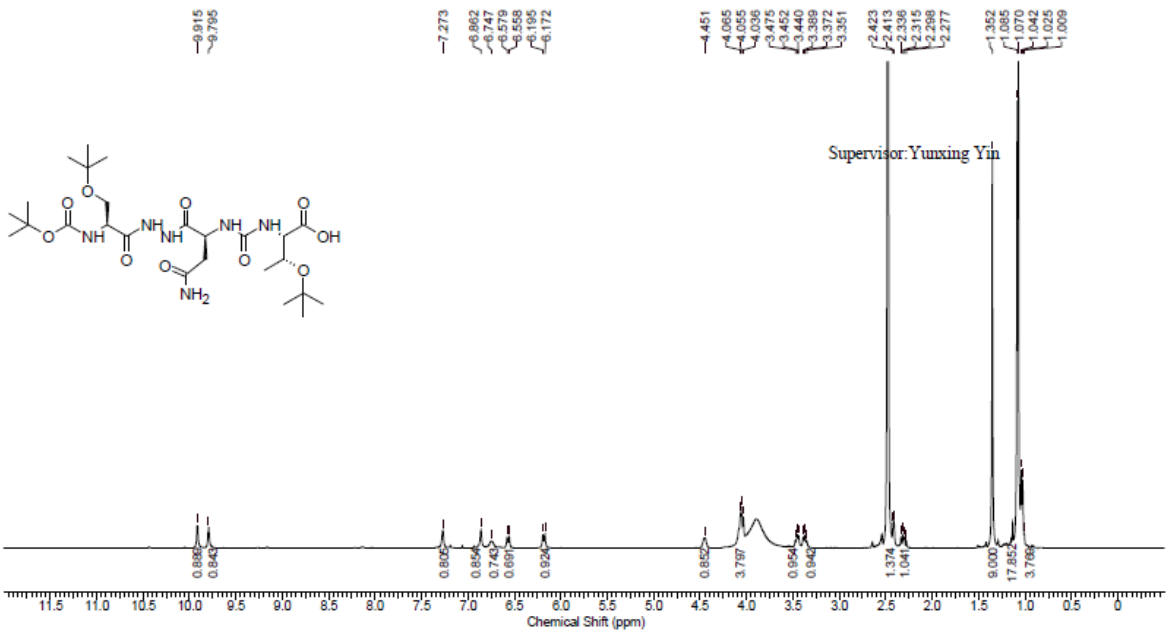

*Figure S2.10. ^{1}H NMR spectrum for penultimate intermediate leading to compound **3**.*

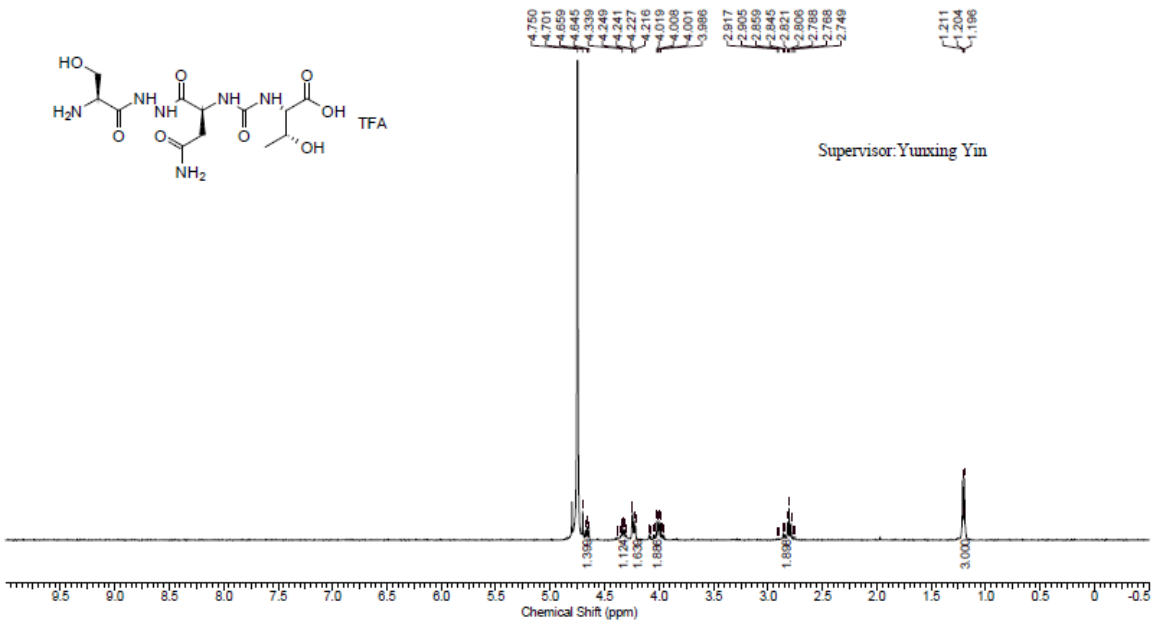

*Figure S2.11. [1]H NMR spectrum for compound **3**.*

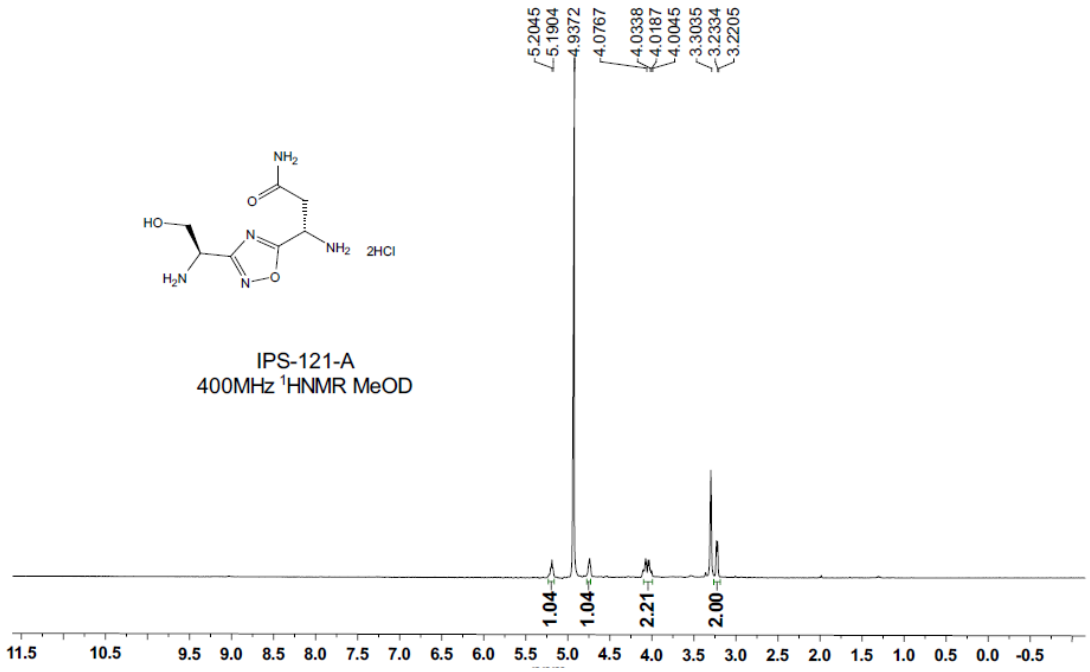

*Figure S2.12. [1]H NMR spectrum for compound **4**.*

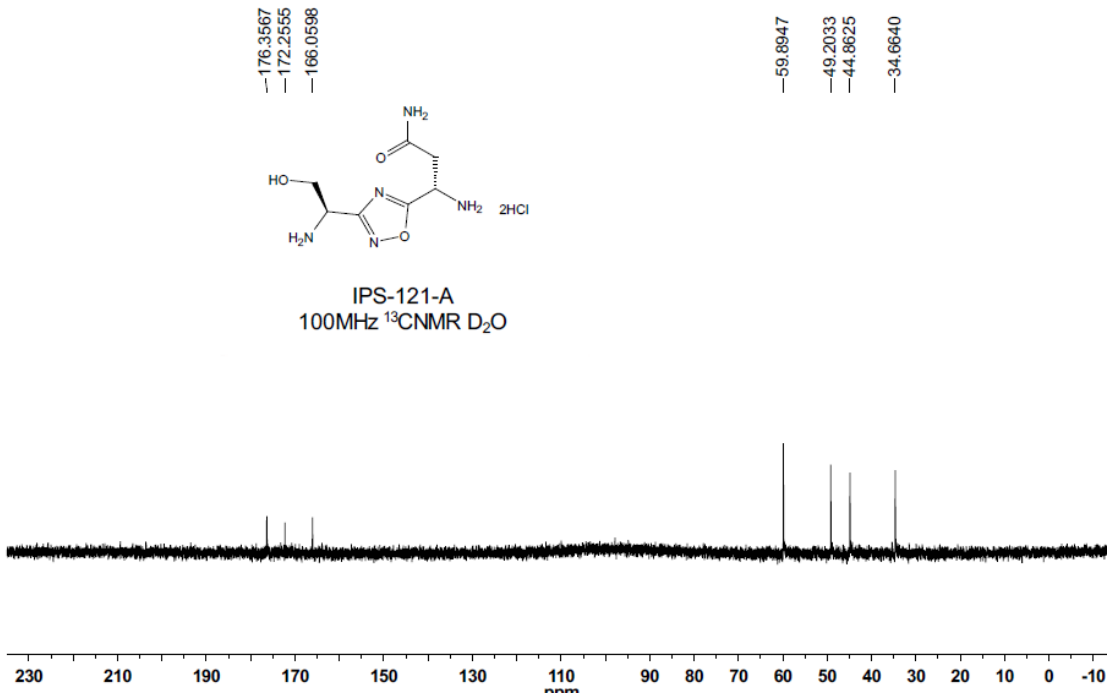

*Figure S2.13. ^{13}C NMR spectrum for compound **4**.*

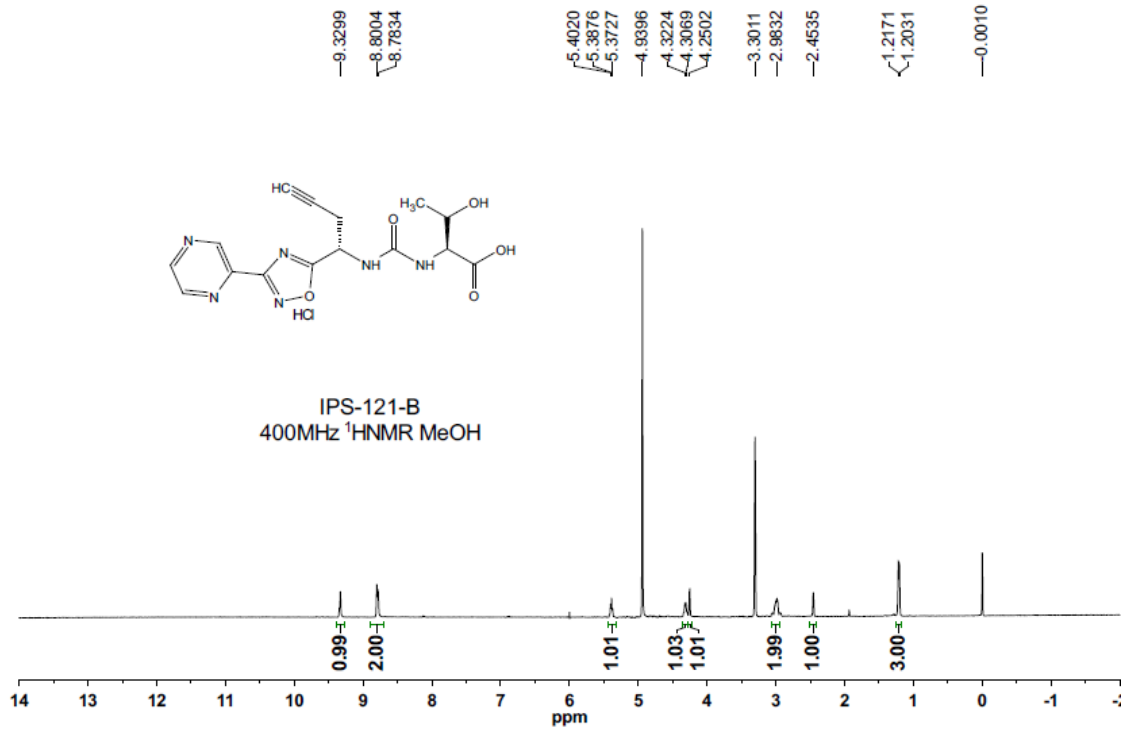

*Figure S2.14. ^{1}H NMR spectrum for compound **5**.*

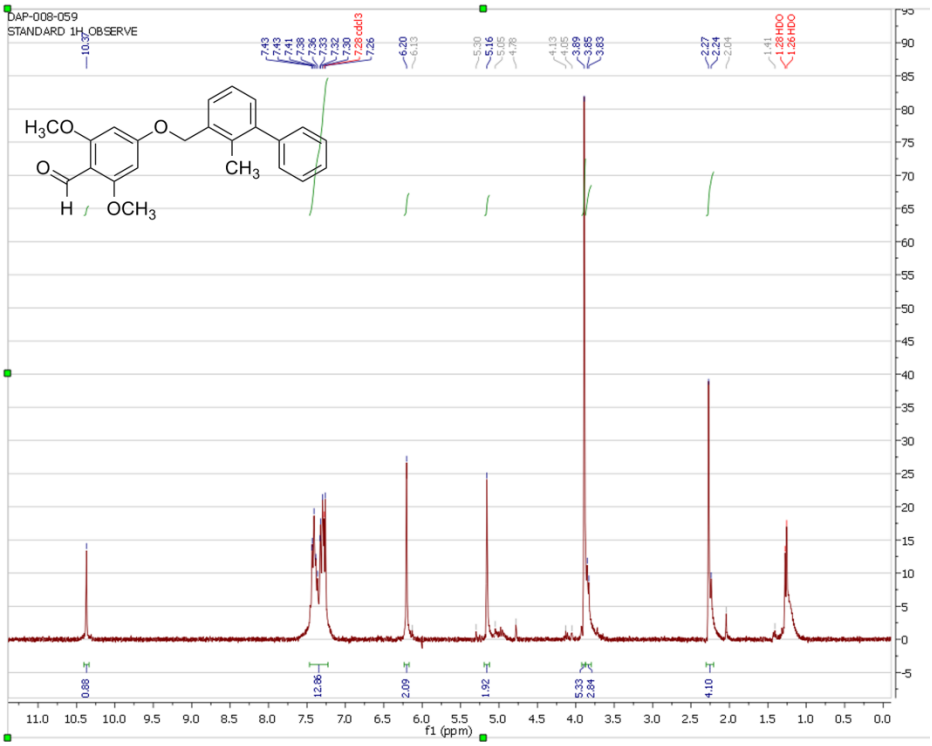

*Figure S2.15. ^{1}H NMR spectrum for 2,6-dimethoxy-4-((2-methyl-'1,1'-biphenyl]-3-yl)methoxy) benzaldehyde (aldehyde intermediate en route to compound **6**).*

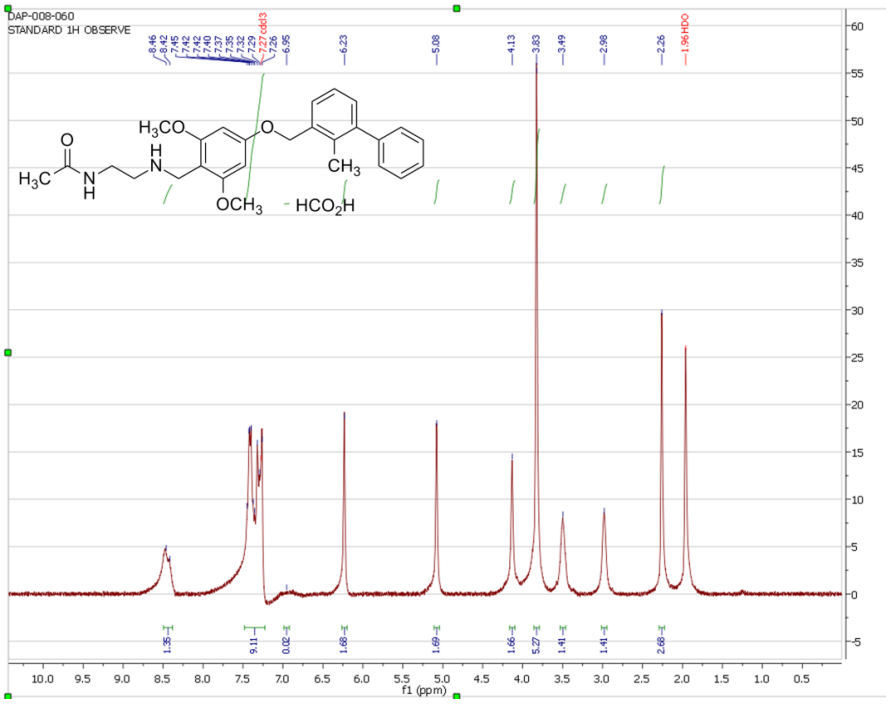

*Figure S2.16. ^{1}H NMR spectrum for compound **6**.*

3. Supplementary Materials (Chapter 3)

Syntheses of Compounds 7–9

Synthesis of Compound 7

Compound **7** was synthesized using conventional peptide coupling based on that of the work of Zou *et al*. In a round bottom flask, 235 mg of 3,3'-dithiodipropionic acid (1.1 mmol) was mixed with 2.2 mol eq. 4-methyl umbelliferone (4-MU, 430 mg), 2.2 mol eq. EDC (462 mg), and 0.3 mol eq. DMAP (43 mg) in anhydrous DCM (30 mL) stirred for 18 hours at 25 °C under inert atmosphere. The crude mixture was concentrated *in vacuo* and the product was purified using a gradient column starting at 100% DCM and slowly increasing amounts of MeOH. Prodrug **7** was isolated as a fine colourless powder at 56% yield.

^{1}H NMR δ (DCM–d_2): 2.45 (3H, s), 3.12 (4H, m), 6.26 (1H, s), 7.13 (1H, app dd, 8.3 Hz, 2.3 Hz), 7.14 (1H, app s), 7.66 (1H, d, 8.3 Hz).

^{13}C NMR δ (DCM–d_2): 18.53, 29.71, 32.86, 34.20, 110.20, 114.48, 117.89, 125.62, 152.10, 152.90, 154.17, 160.12, 169.77.

The relevant spectra are found on page 191.

Synthesis of Compound 8

Compound **8** was made using similar peptide coupling conditions. In a round bottom flask, 240 mg of 3,3'-dithiodbutyric acid (1 mmol) was weighed with 2.1 mol eq. 4-MU (370 mg), 2.1 mol eq. EDC (410 mg), and 0.3 mol eq. DMAP (40 mg) in anhydrous DCM (30 mL) stirred for 18 hours at 25 °C under inert atmosphere. The crude mixture was concentrated *in vacuo*, and the product was purified using a gradient column starting at 100% DCM and slowly increasing amounts of MeOH. The isolated product had a 70% yield.

^{1}H NMR δ (DCM–d_2): 2.17 (2H, qt), 2.41 (3H, s), 2.76 (2H, t), 2.84 (2H, t), 6.22 (1H, s), 7.07 (1H, app dd), 7.10 (1H, app d), 7.62 (1H, d).

^{13}C NMR δ (DCM–d_2): 18.63, 24.11, 32.70, 37.70, 110.34, 114.50, 118.01, 118.06, 125.67, 152.26, 153.16, 154.28, 160.31, 171.05.

The relevant spectra are found on page 192.

Synthesis of Compound 9

Compound **9** was from commercially available γ-butyrolactone (GBL, Sigma) in five steps as presented in Scheme S3.1. The relevant NMR spectra are found on pages 193–200.

All commercial materials were used as received without any further purification. 3,3-dimethyldihydrofuran-2(3H)-one (**13**)[1], 3,3-dimethyldihydrothiophen-2(3H)-one (**14**)[2] and'4,4'-disulfanediylbis(2,2-dimethylbutanoic acid) (**15**)[3] were synthesized by the reported methods in the supplementary references.

IR spectra were recorded using a Perkin-Elmer ATR spectrometer, and wavenumbers (ν) were reported in cm^{-1}. In addition, high-resolution electrospray ionization mass spectrometry (HRMS) data were acquired using a Thermo Scientific Orbitrap Exactive Plus spectrometer.

3,3-dimethyldihydrofuran-2(3H)-one (**13**)

In a flame-dried flask under argon, sodium hydride (60% in mineral oil, 5.58 g, 139 mmol) was added to tetrahydrofuran (40 mL) at 0 °C in portions. Remove the ice bath, stir the suspension solution at room temperature for 5 minutes, and heat at 70 °C. At 70 °C was added, a solution of methyl iodide (9.0 mL, 145 mmol) and γ-butyrolactone (GBL) (4.4 mL, 58.1 mmol) in tetrahydrofuran (10 mL) over 30 minutes. After 3 h, the mixture was cooled at 0 °C, quenched with saturated aqueous ammonium chloride (100 mL) and extracted with ethyl acetate (3 × 100 mL). The combined organic layers were dried over magnesium sulfate, concentrated under reduced pressure, filtered through a silica plug (2cm), and washed with diethyl ether (150 mL). The solution was concentrated to afford 3,3-dimethyldihydrofuran-2(3H)-one (**13**) as a colorless oil. (5.44 g, 82%). The ATR-IR diagnostic peak was 1762 cm^{-1}.

^{1}H NMR (500 MHz, $CDCl_3$) δ 4.25 (t, *J* = 7.0 Hz, 2H), 2.10 (t, *J* = 7.0 Hz, 2H), 1.25 (s, 6H)^{13}C NMR (126 MHz, $CDCl_3$) δ 182.37, 64.77, 38.62, 37.08, 24.21.
IR (diamond-ATR): 2971, 2933, 2875, 2255, **1762**, 1615, 145, 1389, 1367, 1263, 1230, 1203, 1167, 1103, 1027, 998, 965, 907, 755, 729 cm^{-1}

3,3-dimethyldihydrothiophen-2(3H)-one (**14**)

In a round bottom flask connected with condenser added 3,3-dimethyldihydrofuran-2(3H)-one (**13**) (4.56 g, 40 mmol), potassium thioacetate (7.31 g, 1.6 eq, 64 mmol) in N,N-dimethylacetamide (50 mL) and heated at 160 °C for 4 h. The reaction mixture was cooled at room temperature, and water (150 mL) was added and extracted with hexane (3 × 150 mL). The combined organic layer was washed with saturated sodium chloride, dried over magnesium sulfate and the solvent evaporated to afford 3,3-dimethyldihydrothiophen-2(3H)-one (**14**) as a pale-yellow oil (3.71 g, 71 %). ATR-IR had shown the diagnostic thioester peak at 1697 cm^{-1}.
^{1}H NMR (500 MHz, $CDCl_3$) δ 3.24 (t, *J* = 6.6 Hz, 2H), 2.10 (t, *J* = 6.6 Hz, 2H), 1.16 (s, 6H)
^{13}C NMR (126 MHz, $CDCl_3$) δ 213.24, 48.97, 40.28, 28.19, 23.54

ATR-IR C=O(S), 1697 cm^{-1}'4,4'-disulfanediylbis(2,2-dimethylbutanoic acid) (**15**)

3,3-dimethyldihydrothiophen-2(3H)-one (**14**) (2.60 g, 20 mmol) was suspended in an aqueous NaOH solution [3.20 g, 80 mmol, 4 eq, in 8 ml water) and the resulting mixture was then heated to 110 °C for 20 minutes in preheated oil bath. The mixture was then cooled at 0 ºC and dropwise added HCl (35%, 16 mL). Subsequent extraction with diethyl ether (3 × 50 mL), drying over $MgSO_4$ and concentrated under reduced pressure.
The crude residue from the above reaction mixture was dissolved in MeOH (100 mL), NaOH (800 mg, 20 mmol) and KI (2g, 12 mmol, 0.6 eq), iodine (2.53 g, 10 mmol, 0.5 eq) was added portion-wise and the solution was stirred for 2 h. The brown reaction mixture was decolored with a saturated sodium sulfite solution, the solvents concentrated under reduced pressure, the residue dissolved in EtOAc (100 mL), and the resulting solution washed with HCl solution (1 M, 100 mL) and water (100 mL). The organic phase was dried over $MgSO_4$, filtered, and concentrated under reduced pressure. Purification of the crude material by crystallization. The crude material was treated with Et_2O to give'4,4'-disulfanediylbis(2,2-dimethylbutanoic acid) (**15**) as a white solid (1.76 g, 59%). The diagnostic ATR-IR peaks were the broad OH stretch from 3600 – 2400 cm^{-1} and a strong 1689 cm^{-1} for the carbonyl stretch.

^{1}H NMR (500 MHz, $CDCl_3$) δ 2.70 – 2.61 (m, 4H), 1.99 – 1.90 (m, 4H), 1.24 (s, 12H). ^{13}C NMR (126 MHz, $CDCl_3$) δ 184.25, 42.16, 39.88, 33.90, 25.05. HRMS (ESI-) m/z [M-H] calculated for $C_{12}H_{21}O_4S_2$: 293.08813, found: 293.08867.

bis(4-methyl-2-oxo-2H-chromen-7-yl)
’4,4'-disulfanediylbis(2,2-dimethylbutanoate) (**9**)’4,4'-disulfanediylbis(2,2-dimethylbutanoic acid) (**15**) (294.1 mg, 1.0 mmol), 4-dimethylaminopyridine (DMAP, 122.2 mg, 0.6 mmol), 1-(3-dimethylaminopropyl)-3-ethylcarbodiimidehydrochloride (EDC, 575.1 mg, 3 mmol) and 7-hydroxy-4-methylcoumarin (4-MU) (387.3 mg, 2.2 mmol) was mixed in 20 ml anhydrous dichloromethane. The mixture was stirred at room temperature 24 h and then at 40 °C for another 24h. Cool at room temperature and the solvent was removed under reduced pressure. The resulting residue was purified by silica gel column chromatography using pentane: dichloromethane (1:2) to pure dichloromethane to yield the target compound **9** as off-white solids. (416.2 mg, 68 %).
^{1}H NMR (500 MHz, $CDCl_3$) δ 7.56 (d, *J* = 8.6 Hz, 2H), 7.06 (d, *J* = 2.3 Hz, 2H), 7.01 (dd, *J* = 8.6, 2.3 Hz, 2H), 6.24 (d, *J* = 1.4 Hz, 2H), 2.76 – 2.71 (m, 4H), 2.41 (s, 6H), 2.12 – 2.07 (m, 4H), 1.36 (s, 12H).
^{13}C NMR (126 MHz, $CDCl_3$) δ 175.07, 160.42, 154.12, 153.32, 151.97, 125.44, 117.98, 117.77, 114.48, 114.47, 110.30, 42.67, 40.12, 34.33, 25.05, 18.71.
IR (diamond-ATR): 3067, 2972, 2925, 1750, 1722, 1706, 1626, 1614, 1570, 1499, 1474, 1459, 1388, 1369, 1330, 1255, 1193, 1129, 1095, 1066, 1037, 1017, 983, 915, 883, 861, 7990, 750, 738 cm^{-1}.
HRMS (ESI+) m/z [M+Na] calculated for $C_{32}H_{34}O_8S_2Na$: 633.1592, found: 633.15873.

Synthesis of *bis*-SN-38 Conjugate 10

*Preliminary Synthesis of Compound **10***

In general, the esterification of SN-38 followed the similar reaction conditions as its 4-MU analogs, where 2.2 mol eq. phenol were reacted with 1 mol eq. dithiodiacid (or diacyl chloride, **16**), with > 2 mol eq. base under anhydrous conditions, with DCM used as the solvent. For reactions which resulted in an insoluble urea byproduct, these were filtered off and rinsed with DCM and hexane prior to column chromatography. Crude spectra were analyzed in d_6-DMSO to ascertain presence of *bis*-product (Figure 6.5).

SN-38 was characterized using reference spectra and HSQC to characterize the diagnostic protons on phenol ring and differentiate from rest of the molecule, prior to confirming successful conversion of **10** with the crude reaction mixture. There was no change in the chemical shift attributed to the tertiary alcohol, confirming its inactivity with acyl chloride **16**. Notably the absence of the phenol proton at 10.3 ppm was another indicator of successful conjugation to the disulfide tether.

^{1}H NMR: 0.87 (3H, t), 1.25 (3H, t), 1.85 (2H, dq), 3.04–3.21 (4H, dq – disulfide tether), 5.2 (2H, s), 5.4 (2H, s), 6.49 (1H, s, 3° OH), 7.26 (1H, s), 7.62 (1H, dd), 7.88 (1H, d), 8.14 (1H, d)

*Synthesis of Compound **16***

486.3 mg DTDPA was charged in a flask with 2.2 mol eq. oxalyl chloride and catalytic DMF, and anhydrous DCM. The vessel was left to react overnight. The solvent was pulled by vacuum. The resulting pale-yellow liquid was characterized by ^{1}H NMR, ^{13}C NMR and ATR-IR to confirm no presence of acid.

^{1}H NMR (300 MHz, d6-DMSO): 2.87 (t, 2 H), 2.62 (t, 2H). Absence of broad -OH.
^{13}C NMR (126 MHz, d6-DMSO): 172.89, 33.69, 33.15.

ATR-IR: 1785 cm^{-1} (C=O stretch), absence of broad -OH stretching.

Other Supplementary Data and Associated Tables

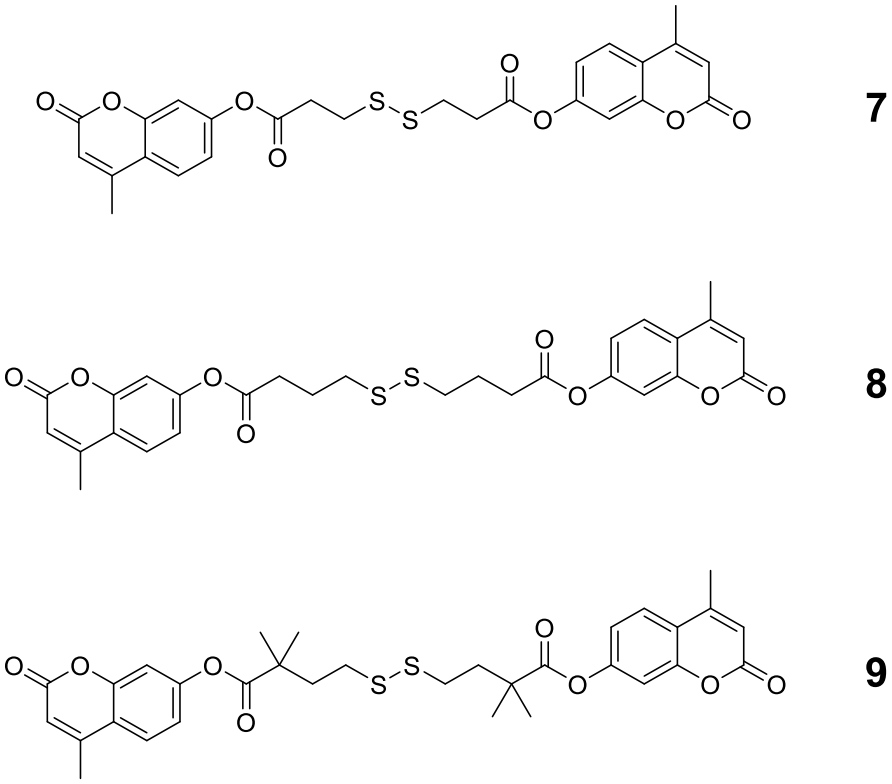

*Figure S3.1. Full structures of compounds **7–9**.*

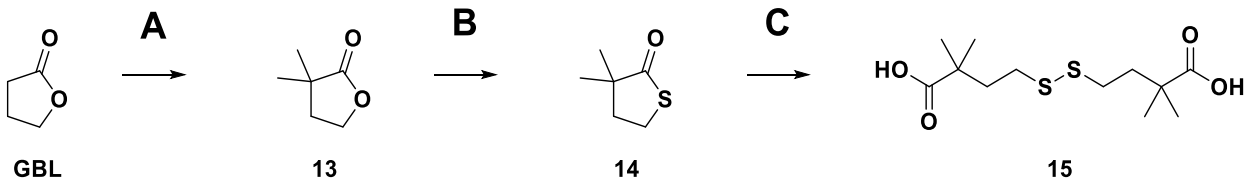

*Scheme S3.1. Synthesis of dithiodiacid precursor (**15**) for synthesis of compound **9**. **A**. Methylation of 5.65 g (65 mmol) gamma butyrolactone (GBL) with 2.1 mol eq. methyl iodide and 2.1 mol eq. sodium hydride (60%) refluxed in anhydrous THF 24 h. **B**. The intermediate lactone is thiolated by dissolving with 1.1 mol eq. potassium thioacetate (KAcS) in DMA and refluxing for 5 h. **C**. The thiolactone intermediate is opened by refluxing in 50% NaOH solution, the solution is acidified and extracted in diethyl ether (Et_2O) with 1.1 mol I_2 to oxidize 24 h.*

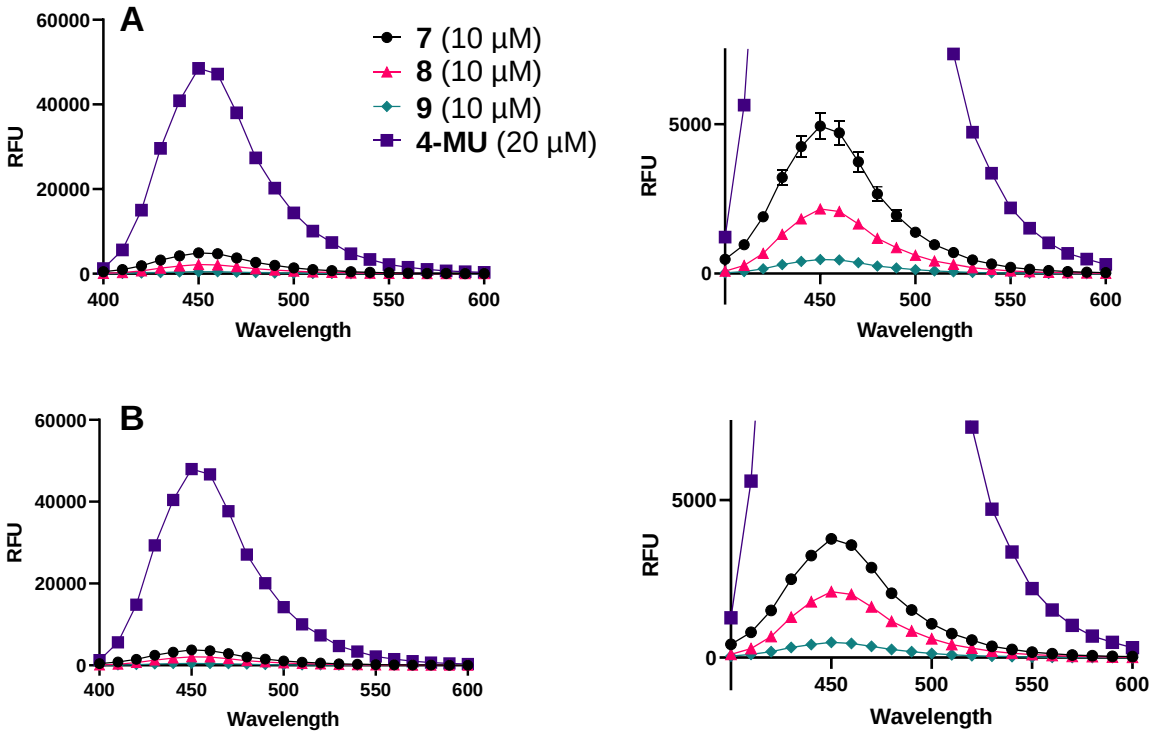

*Figure S3.2. Scanning emission of fluorescence of compounds **7**–**9** and 4-MU between 400 nm and 600 nm with a fixed excitation at 315 nm. **A**. Performed at 1.5% MeCN. **B**. Performed at 5% MeCN. Increased acetonitrile concentration had no effect on quenching fluorescence intensity. Bars represent standard error of mean (SEM) of four replicates.*

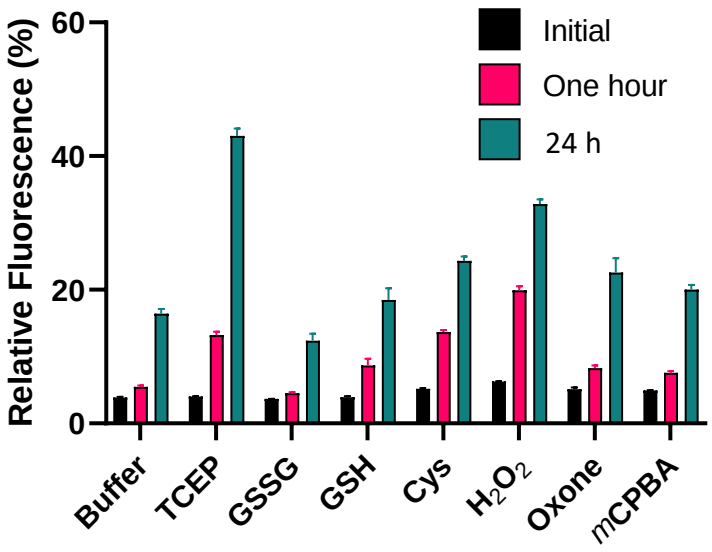

*Figure S3.3. Compound **7** was incubated in 30 mol eq. of various compounds in Tris buffer (1.5% MeCN) and measured for fluorescence (ex 315 nm, em 445 nm). Relative intensities were normalized to 2 mol eq. 4-MU. The relevant statistical analyses of one-hour time-dependent release from reagents, reagent-dependent to buffer control, and 24 h time-dependent release from reagents are found in Table S3.1, Table S3.2, and Table S3.3, respectively.*

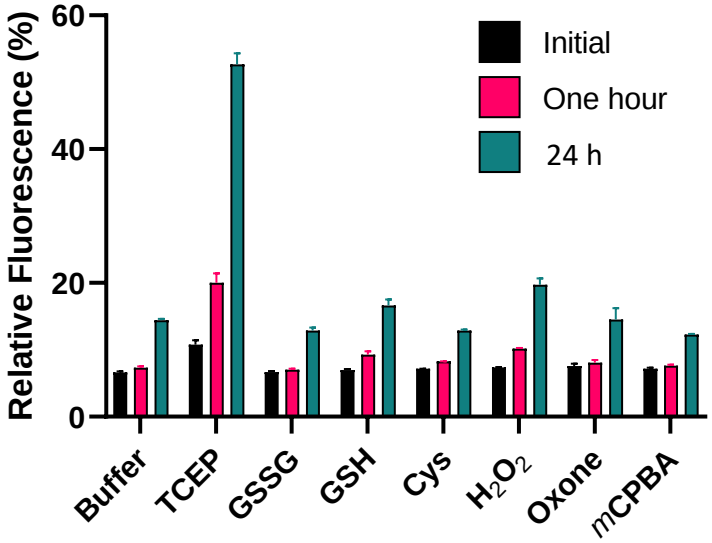

*Figure S3.4. Compound **8** incubated in 30 mol eq. of various compounds in Tris buffer (1.5% MeCN) and measured for fluorescence (ex 315 nm, em 445 nm). Relative intensities were normalized to 2 mol eq. 4-MU. The relevant statistical analyses of one-hour time-dependent release from reagents, reagent-dependent to buffer control, and 24 h time-dependent release from reagents are found in Table S3.1, Table S3.2, and Table S3.3, respectively.*

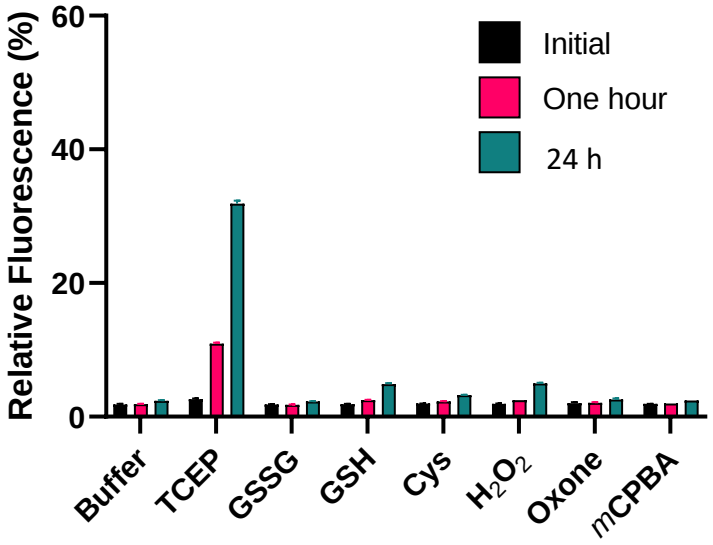

*Figure S3.5. Compound **9** incubated in 30 mol eq. of various compounds in Tris buffer (1.5% MeCN) and measured for fluorescence (ex 315 nm, em 445 nm). Relative intensities were normalized to 2 mol eq. 4-MU. The relevant statistical analyses of one-hour time-dependent release from reagents, reagent-dependent to buffer control, and 24 h time-dependent release from reagents are found in Table S3.1, Table S3.2, and Table S3.3, respectively.*

*Table S3.1. Time-dependent statistical analysis of 4-MU liberated from compounds **7**–**9** in Tris buffer. The emission intensity was normalized to fluorescence intensity of 2 mol eq. 4-MU. The normalized intensities were compared time zero and time 60 min, to determine the impact of release from various compounds. These data are associated with Figure 3.1, Figure S3.3, Figure S3.4, Figure S3.5.*

1 h	Compound **7** (Figure 3.1A)		Compound **8** (Figure 3.1B)		Compound **9** (Figure S3.5)	
Buffer	*	0.0166	ns	>0.5	ns	>0.5
TCEP	****	<0.0001	****	<0.0001	****	<0.0001
GSSG	ns	0.4941	ns	>0.5	ns	>0.5
GSH	****	<0.0001	**	0.0034	****	0.0001
Cys	****	<0.0001	ns	0.4834	*	0.0328
H_2O_2	****	<0.0001	***	0.0003	****	<0.0001
Oxone	****	<0.0001	ns	>0.5	ns	>0.5
*m*CPBA	****	<0.0001	ns	>0.5	ns	>0.5

*Table S3.2. Statistical analyses comparing normalized 4-MU intensity from compounds **7–9** after one hour incubation relative to potential autofluorescence in buffer. These data are associated with Figure 3.1, Figure S3.3, Figure S3.4, Figure S3.5.*

1 h	Compound **7** (Figure 3.1A)		Compound **8** (Figure 3.1B)		Compound **9** (Figure S3.5)	
Buffer vs.		P-value		P-value		P-value
TCEP	****	<0.0001	****	<0.0001	****	<0.0001
GSSG	ns	0.9212	ns	0.9995	ns	0.9902
GSH	*	0.0241	ns	0.192	**	0.0091
Cys	****	<0.0001	ns	0.8774	ns	0.1092
H_2O_2	****	<0.0001	*	0.0219	**	0.0067
Oxone	ns	0.0659	ns	0.9542	ns	0.8543
*m*CPBA	ns	0.2552	ns	0.9996	ns	0.9924

*Table S3.3. Statistical analyses comparing normalized 4-MU intensity from compounds **7–9** after 24 h incubation relative to background fluorescence observed in Tris buffer (1.5% v/v MeCN). These data are associated with Figure 3.1, Figure S3.3, Figure S3.4, Figure S3.5.*

O/N	Compound **7** (Figure S3.3)		Compound **8** (Figure S3.4)		Compound **9** (Figure S3.5)	
Buffer vs.		P-value		P-value		P-value
TCEP	****	<0.0001	****	<0.0001	****	<0.0001
GSSG	**	0.0023	ns	0.4202	ns	0.9825
GSH	ns	0.2701	ns	0.1032	****	<0.0001
Cys	****	<0.0001	ns	0.4011	****	<0.0001
H_2O_2	****	<0.0001	****	<0.0001	****	<0.0001
Oxone	****	<0.0001	ns	0.9999	ns	0.7921
*m*CPBA	**	0.0082	ns	0.1165	ns	0.9997

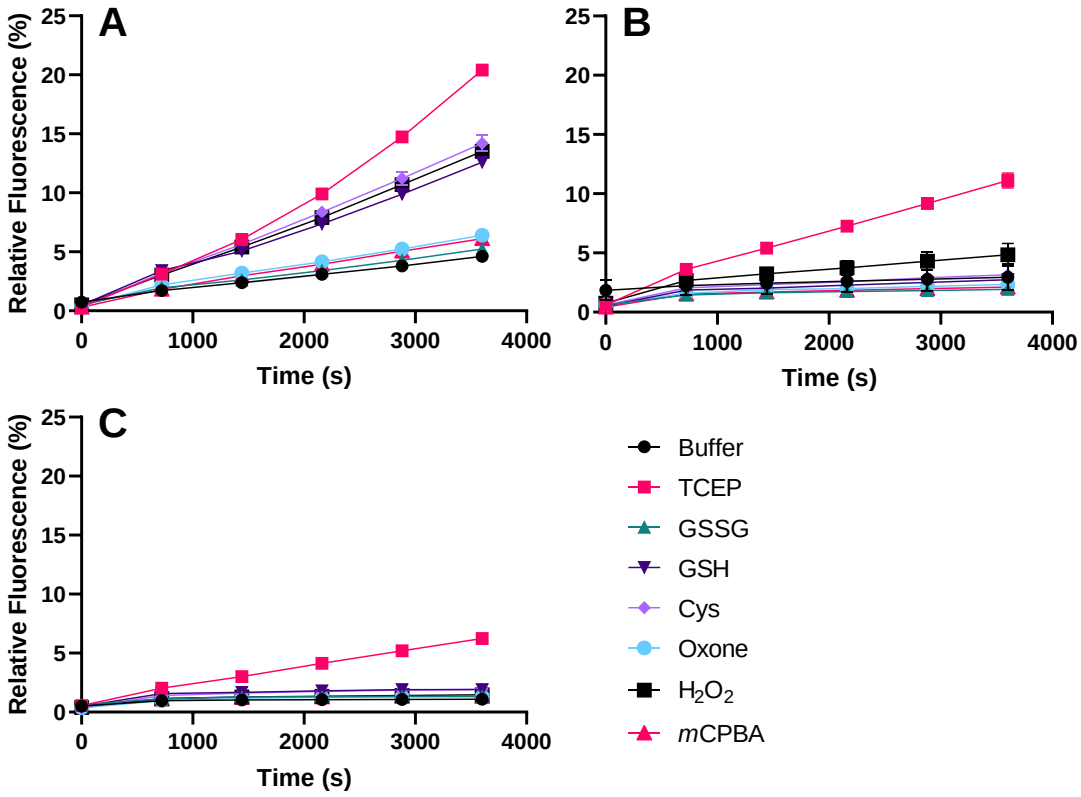

*Figure S3.6. Monitored release of 4-MU from compounds **7** (**A**), **8** (**B**), and **9** (**C**), respectively. This assay had higher MeCN content to account for potential solubility problem (5% v/v). Relative intensity is normalized to 2 mol eq. 4-MU. Bars represent SEM and n = 4. Relevant statistical analyses found in Table S3.4 (time-dependent, reagent-independent comparison) and Table S3.5 (time-independent, reagent-dependent comparison).*

*Table S3.4. Statistical analysis of Figure S3.6. Time-dependent emission intensity of 4-MU released from compounds **7–9** after one hour incubation with 30 mol eq. reagent in 5% v/v MeCN.*

Reagent	Compound **7** (t_0 v t_60)		Compound **8** (t_0 v t_60)		Compound **9** (t_0 v t_60)	
Buffer	****	<0.0001	ns	0.5655	ns	0.0733
TCEP	****	<0.0001	****	<0.0001	****	<0.0001
GSSG	****	<0.0001	ns	0.3443	*	0.0100
GSH	****	<0.0001	*	0.0404	****	<0.0001
Cys	****	<0.0001	**	0.0025	****	<0.0001
H_2O_2	****	<0.0001	****	<0.0001	****	<0.0001
Oxone	****	<0.0001	ns	0.0929	***	0.0005
*m*CPBA	****	<0.0001	ns	0.1076	***	0.0009

*Table S3.5. Statistical analyses of Figure S3.6 comparing normalized 4-MU intensity from compounds **7–9** after one hour incubation relative to respective background hydrolysis in Tris buffer with 5% v/v MeCN.*

Buffer vs.	Compound **7**		Compound **8**		Compound **9**	
TCEP	****	<0.0001	****	<0.0001	****	<0.0001
GSSG	ns	0.7866	ns	0.9999	ns	0.8279
GSH	****	<0.0001	ns	0.6977	*	0.0282
Cys	****	<0.0001	ns	0.2740	*	0.0110
H_2O_2	****	<0.0001	**	0.0012	ns	0.4980
Oxone	*	0.0215	ns	0.9599	ns	0.8841
*m*CPBA	ns	0.0703	ns	0.9994	ns	0.8650

*Table S3.6. Statistical analysis of Figure 3.2. A Two-way ANOVA analysis was performed to compare 4-MU intensities between cell lines from traceless linkers **7** or **8** after an 24 h incubation period.*

	Compound **7**		Compound **8**	
10 µM		P-value		P-value
U87 vs. HNDF	*	0.0168	ns	0.6402
U87 vs. U251	*	0.01	ns	0.3355
HNDF vs. U251	ns	0.3037	ns	0.221
20 µM				
U87 vs. HNDF	**	0.0059	ns	0.425
U87 vs. U251	*	0.0121	ns	0.5809
HNDF vs. U251	*	0.0496	ns	0.1405

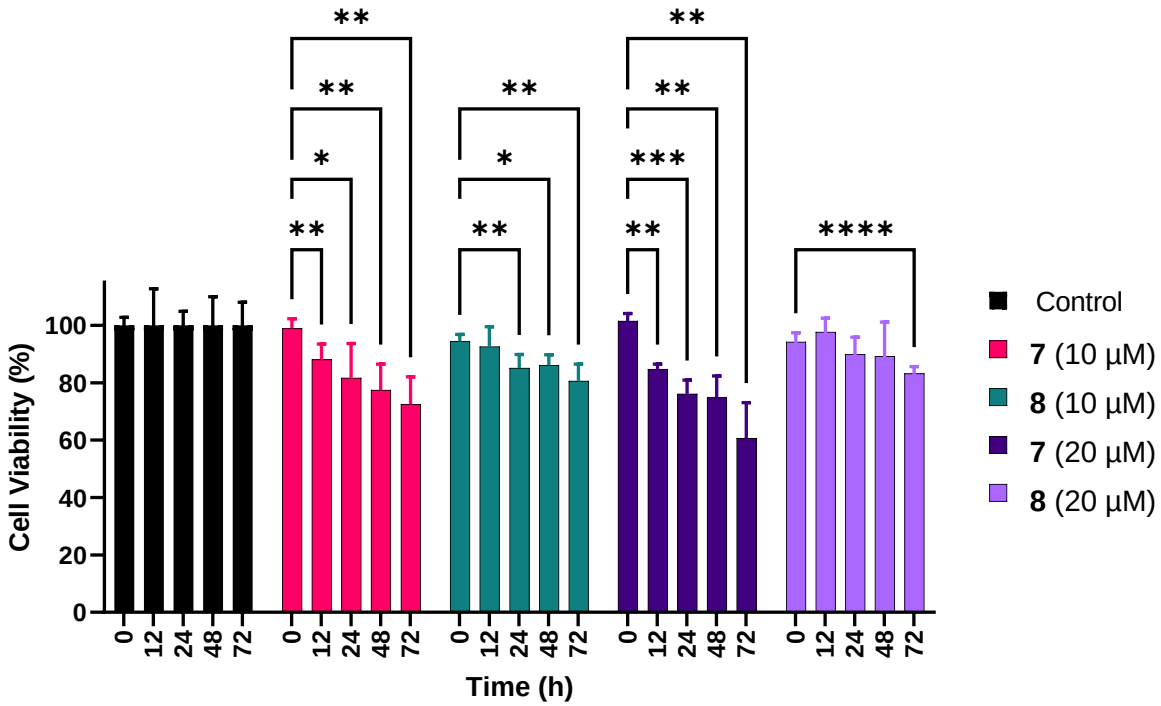

*Figure S3.7. U-87 cell viability when incubated with 10 µM or 20 µM of compound **7** or **8**. No concerning dose-dependent toxicity within a 24 h period from either compound. Statistical analysis found in Table S3.7.*

Table S3.7. Statistical analysis of cell viability in Figure S3.7.

Time (h)	Control		10 µM Compound **7**		20 µM Compound **7**		10 µM Compound **8**		20 µM Compound **8**	
0 vs. 12	ns	>0.999	*	0.0424	*	0.0155	ns	0.963	ns	0.7438
0 vs. 24	ns	>0.999	ns	0.0863	**	0.0044	*	0.0326	ns	0.696
0 vs. 48	ns	>0.999	*	0.011	*	0.0349	*	0.0491	ns	0.8866
0 vs. 72	ns	>0.999	**	0.008	**	0.0057	*	0.0159	***	0.0002
12 vs. 24	ns	>0.999	ns	0.3086	ns	0.1424	ns	0.0958	*	0.0445
12 vs. 48	ns	>0.999	*	0.0142	ns	0.3522	ns	0.1555	ns	0.2297
12 vs. 72	ns	>0.999	**	0.0021	*	0.0481	ns	0.167	**	0.0049
24 vs. 48	ns	>0.999	ns	0.3358	ns	0.9967	ns	0.9935	ns	>0.999
24 vs. 72	ns	>0.999	ns	0.0527	ns	0.0605	ns	0.4624	ns	0.2571
48 vs. 72	ns	>0.999	ns	0.2239	ns	0.2555	ns	0.6213	ns	0.7106

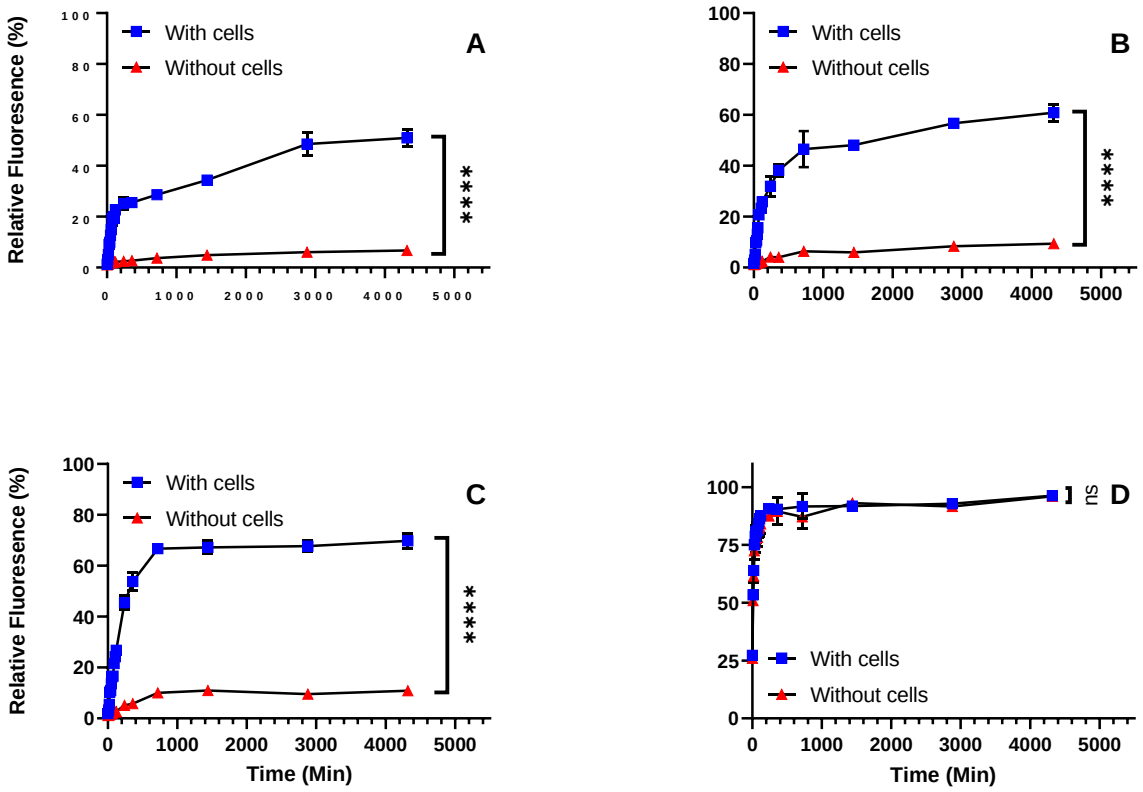

*Figure S3.8. Long-term (3 d) monitoring of 4-MU release from traceless linker **7** attributed to U-87 glioma cells in DPBS. **A**. The traceless disulfide linker **7** was incubated in DPBS of increasing complexity up to 72 h, either with or without U-87 glioma cells in DPBS. **B**. The DPBS is supplemented with 4.5 g/L glucose. **C**. The DPBS is supplemented with 4.5 g/L glucose and 0.5 g/L glutamine. **D**. The DPBS supplemented with glucose and glutamine and 10% FBS (v/v). Error bars represent SEM of at least four replicates, and statistics were measured at the 72 h timepoint. Compound intensity was normalized to 2 mol eq. 4-MU, expressed as a percentage. The full statistical analysis is found in Table S3.8.*

Table S3.8. Statistical analyses of Figure 3.3 and Figure S3.8.

	Within 120 min (Figure 3.3)		Within 3 days (Figure S3.8)	
		P-Value		P-Value
DPBS	****	<0.0001	****	<0.0001
+ 4.5 g/L glucose	****	<0.0001	****	<0.0001
+ 0.5 g/L glutamine	****	<0.0001	****	<0.0001
+ 10% FBS	ns	0.7571	ns	0.2102

Table S3.9. Statistical analysis of Figure 3.4. Columns 1 and 2 were a One-way ANOVA analysis investigating average intensities of the conditions (rows) in a time-dependent manner. Columns 3 – 5 were a Two-way ANOVA comparing the intensities to the molecules at one-hour, independently and to each other, respectively.

	Compound **7** ($T_{0\ min}$) vs. Compound **7** ($T_{60\ min}$)		Compound **8** ($T_{0\ min}$) vs. Compound **8** ($T_{60\ min}$)		Compound **7** ($T_{60\ min}$) vs. Media ($T_{60\ min}$)		Compound **8** ($T_{60\ min}$) vs. Media ($T_{60\ min}$)		Compound **7** ($T_{60\ min}$) vs. Compound **8** ($T_{60\ min}$)	
–TCEP, –FBS	****	<0.0001	*	0.0120	***	0.0006	**	0.0041	***	0.0003
–TCEP, +FBS	****	<0.0001	****	<0.0001	****	<0.0001	****	<0.0001	ns	0.1924
+TCEP, –FBS	****	<0.0001	****	<0.0001	***	0.0003	***	0.0002	**	0.0021
+TCEP, +FBS	****	<0.0001	****	<0.0001	*	0.0104	***	0.0003	ns	0.2899

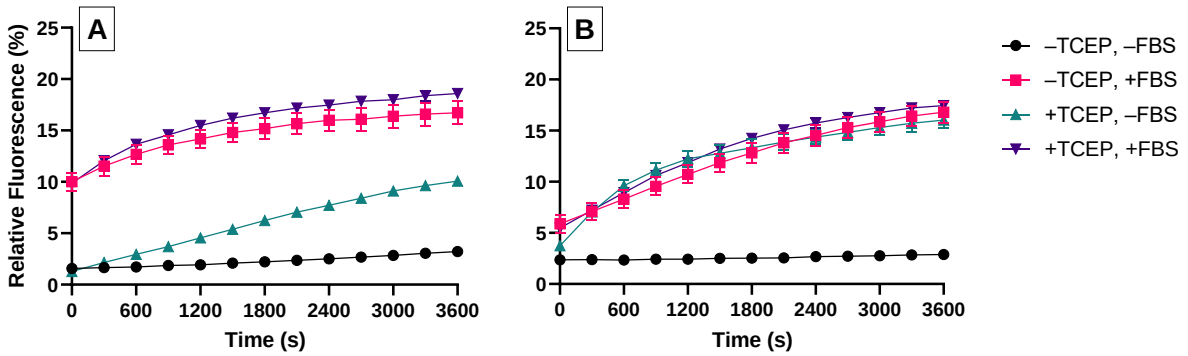

*Figure S3.9. Kinetic release of 4-MU from compounds **7** or **8** in complete media, RPMI 1640, treated with 10% FBS and/or 30 mol eq. TCEP. The relevant statistical analysis is found in Table S3.10.*

Table S3.10. The complete statistical analysis of Figure S3.9. Columns 1 and 2 were a One-way ANOVA analysis investigating average intensities of the conditions (rows) in a time-dependent manner. Columns 3–5 were a Two-Way ANOVA comparing the intensities to the molecules at one-hour, independently and to each other, respectively.

	Compound **7** ($T_{0\ min}$) vs. Compound **7** ($T_{60\ min}$)		Compound **8** ($T_{0\ min}$) vs. Compound **8** ($T_{60\ min}$)		Compound **7** ($T_{60\ min}$) vs. Media ($T_{60\ min}$)		Compound **8** ($T_{60\ min}$) vs. Media ($T_{60\ min}$)		Compound **7** ($T_{60\ min}$) vs. Compound **8** ($T_{60\ min}$)	
–TCEP, –FBS	ns	0.2423	ns	0.9274	***	0.0003	****	<0.0001	*	0.0110
–TCEP, +FBS	****	<0.0001	****	<0.0001	**	0.0014	***	0.0004	ns	0.9149
+TCEP, –FBS	****	<0.0001	****	<0.0001	**	0.0016	**	0.0025	**	0.0073
+TCEP, +FBS	****	<0.0001	****	<0.0001	***	0.0006	***	0.0007	ns	0.1529

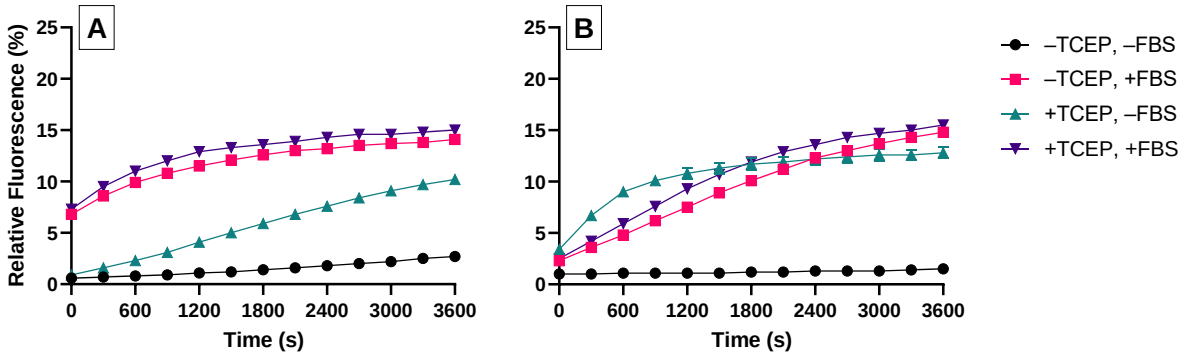

*Figure S3.10. Kinetic release of 4-MU from compounds **7** and **8** in minimal media, MEM, treated with 10% FBS and/or 30 mol eq. TCEP. The statistical analysis found in Table S3.11.*

Table S3.11. Statistical analysis of Figure S3.10. Columns 1 and 2 were a One-way ANOVA analysis investigating average intensities of the conditions (rows) in a time-dependent manner. Columns 3–5 were a Two-Way ANOVA comparing the intensities to the molecules at one-hour, independently and to each other, respectively.

	Compound **7** ($T_{0\ min}$) vs. Compound **7** ($T_{60\ min}$)		Compound **8** ($T_{0\ min}$) vs. Compound **8** ($T_{60\ min}$)		Compound **7** ($T_{60\ min}$) vs. Media ($T_{60\ min}$)		Compound **8** ($T_{60\ min}$) vs. Media ($T_{60\ min}$)		Compound **7** ($T_{60\ min}$) vs. Compound **8** ($T_{60\ min}$)	
–TCEP, –FBS	****	<0.0001	ns	0.3041	****	<0.0001	**	0.0013	**	0.0011
–TCEP, +FBS	****	<0.0001	****	<0.0001	***	0.0010	****	<0.0001	**	0.0015
+TCEP, –FBS	****	<0.0001	****	<0.0001	****	<0.0001	**	0.0017	*	0.0392
+TCEP, +FBS	****	<0.0001	****	<0.0001	****	<0.0001	****	<0.0001	ns	0.1623

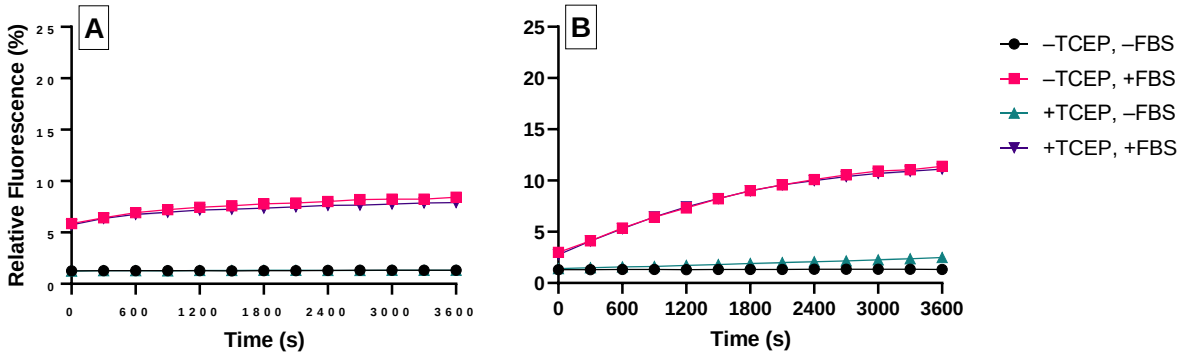

*Figure S3.11. Kinetic release of 4-MU from compounds **7** or **8** in MilliQ water treated with 10% FBS and/or 30 mol eq. TCEP. Statistical analysis found in Table S3.12.*

Table S3.12. Statistical analysis of Figure S3.11. Columns 1 and 2 were a One-way ANOVA analysis investigating average intensities of the conditions (rows) in a time-dependent manner. Columns 3–5 were a Two-Way ANOVA comparing the intensities to the molecules at one-hour, independently and to each other, respectively.

	Compound **7** ($T_{0\ min}$) vs. Compound **7** ($T_{60\ min}$)		Compound **8** ($T_{0\ min}$) vs. Compound **8** ($T_{60\ min}$)		Compound **7** ($T_{60\ min}$) vs. Media ($T_{60\ min}$)		Compound **8** ($T_{60\ min}$) vs. Media ($T_{60\ min}$)		Compound **7** ($T_{60\ min}$) vs. Compound **8** ($T_{60\ min}$)	
–TCEP, –FBS	ns	0.9910	ns	>0.9999	****	<0.0001	***	0.0001	ns	0.9114
–TCEP, +FBS	****	<0.0001	****	<0.0001	***	0.0007	***	0.0010	**	0.0044
+TCEP, –FBS	ns	0.9745	***	0.0002	***	0.0002	****	<0.0001	****	<0.0001
+TCEP, +FBS	****	<0.0001	****	<0.0001	****	<0.0001	***	0.0009	**	0.0093

Table S3.13. Statistical analysis of Figure 3.5 and Figure 3.6.

	Compound **7** (Figure 3.5)		Compound **8** (Figure 3.5)		Compound **9** (Figure 3.6)	
MilliQ vs. FBS (37 °C)	****	<0.0001	****	<0.0001	***	0.0009
MilliQ vs. FBS (37 °C) + 1% PIC	****	<0.0001	****	<0.0001	*	0.02
MilliQ vs. FBS (100 °C)	****	<0.0001	***	0.0005	Ns	0.383
MilliQ vs. FBS (100 °C) + 1% PIC	****	<0.0001	ns	0.2287	Ns	>0.5
FBS (37 °C) vs. FBS (100 °C)	**	0.0013	****	<0.0001	*	0.0309
FBS (37 °C) vs. FBS (37 °C) + 1% PIC	*	0.0246	*	0.0164	****	<0.0001
FBS (100 °C) vs. FBS (100 °C) + 1% PIC	**	0.0037	*	0.0314	*	0.0338
FBS (37 °C) + 1% PIC vs. FBS (100 °C) + 1% PIC	****	<0.0001	****	<0.0001	**	0.0012

NMR Spectra for Compound **7**

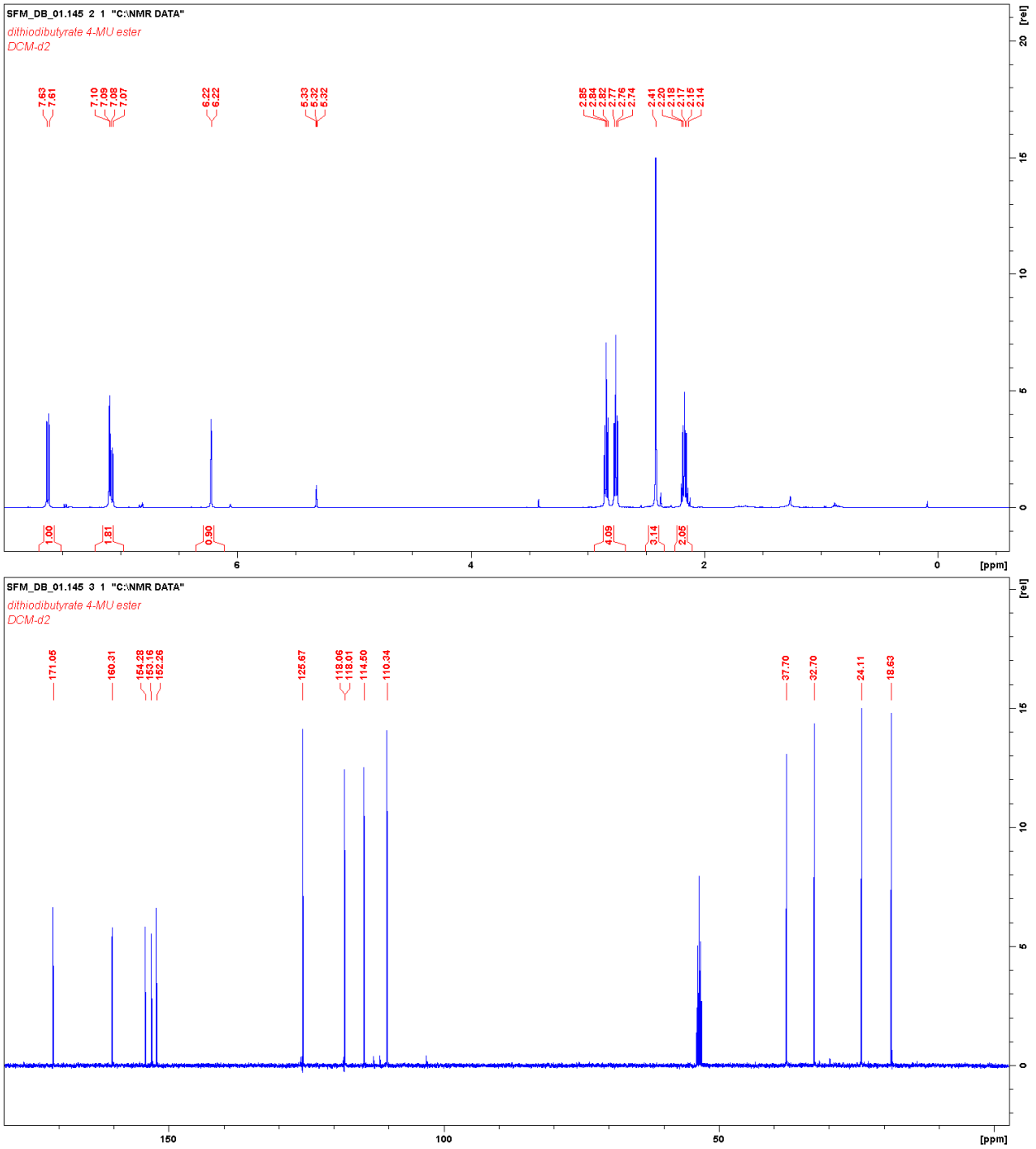

*Figure S3.12. ^{1}H and ^{13}C NMR spectra of compound **7** in d_2-DCM.*

NMR Spectra for Compound **8**

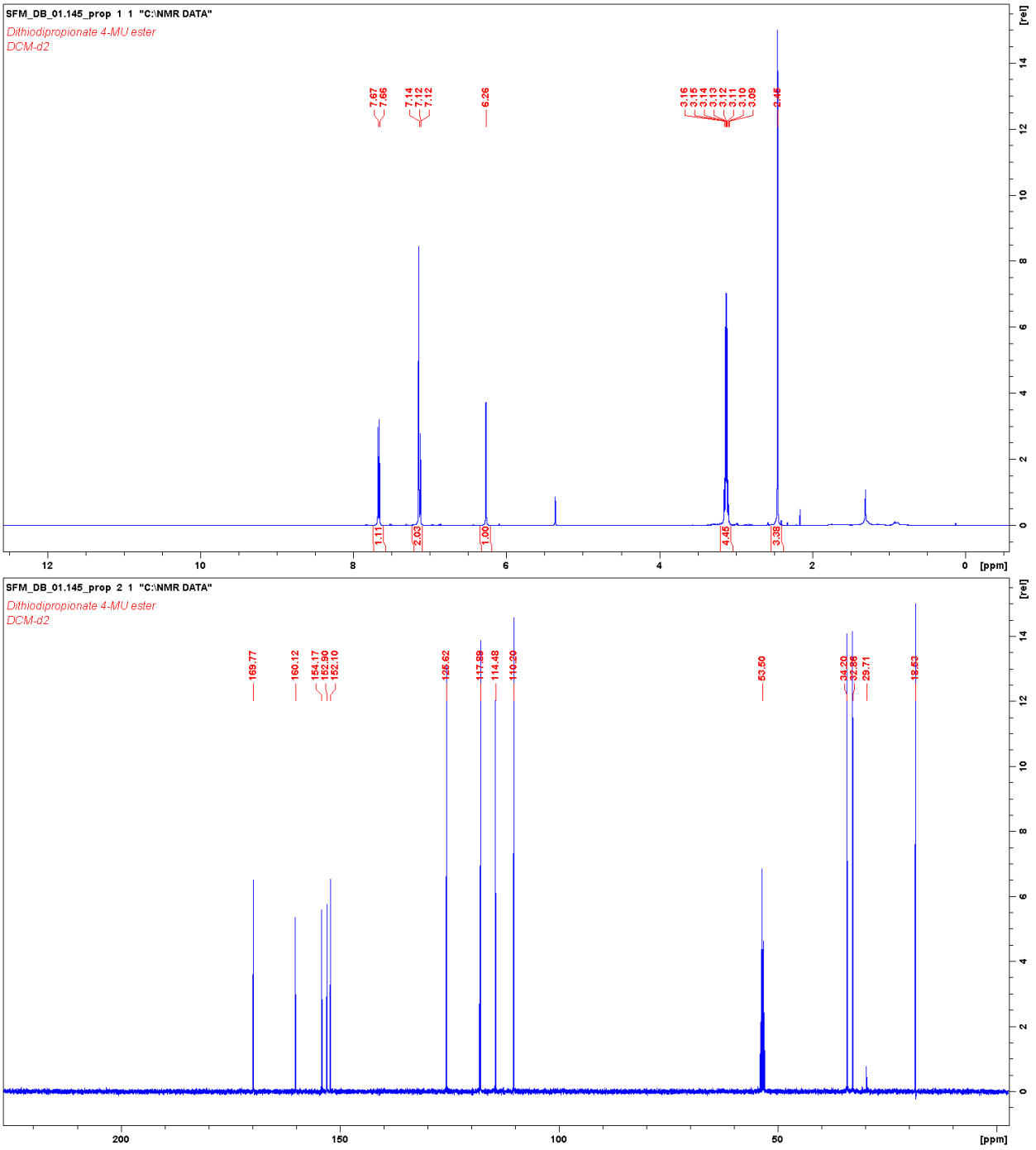

*Figure S3.13. ^{1}H and ^{13}C NMR spectra of compound **8** in d_2-DCM.*

dihydrofuran-2(3H)-one / γ-butyrolactone (GBL)

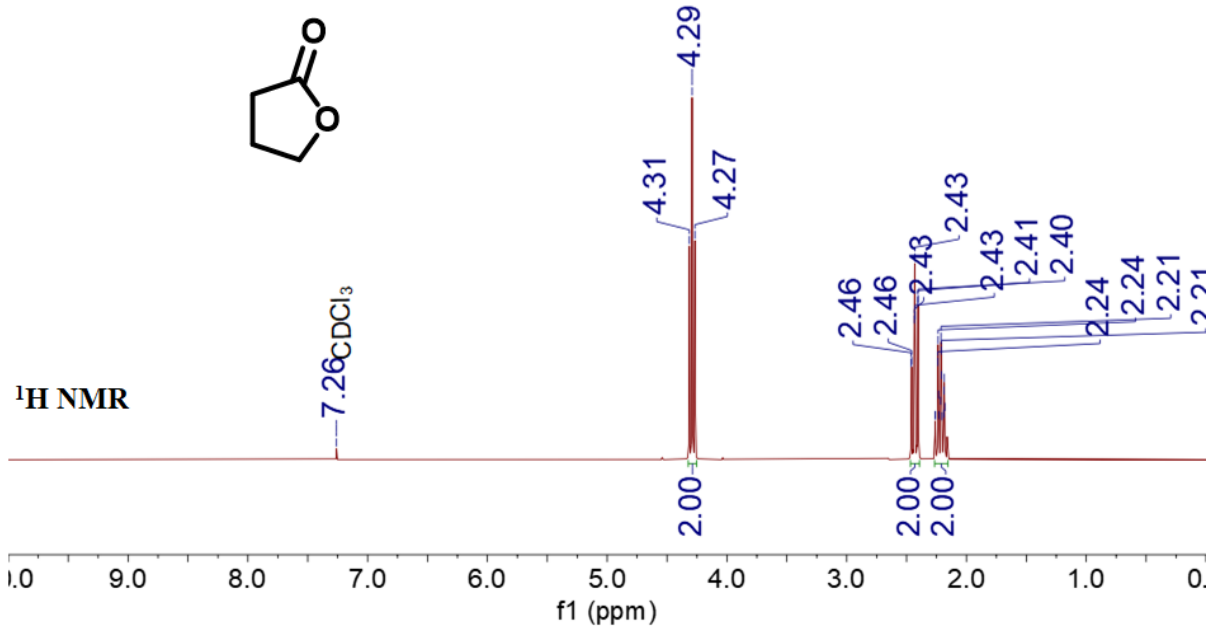

Figure S3.14. ^{1}H NMR spectra of dihydrofuran-2(3H)-one in $CDCl_3$.

3,3-dimethyldihydrofuran-2(3H)-one (13)

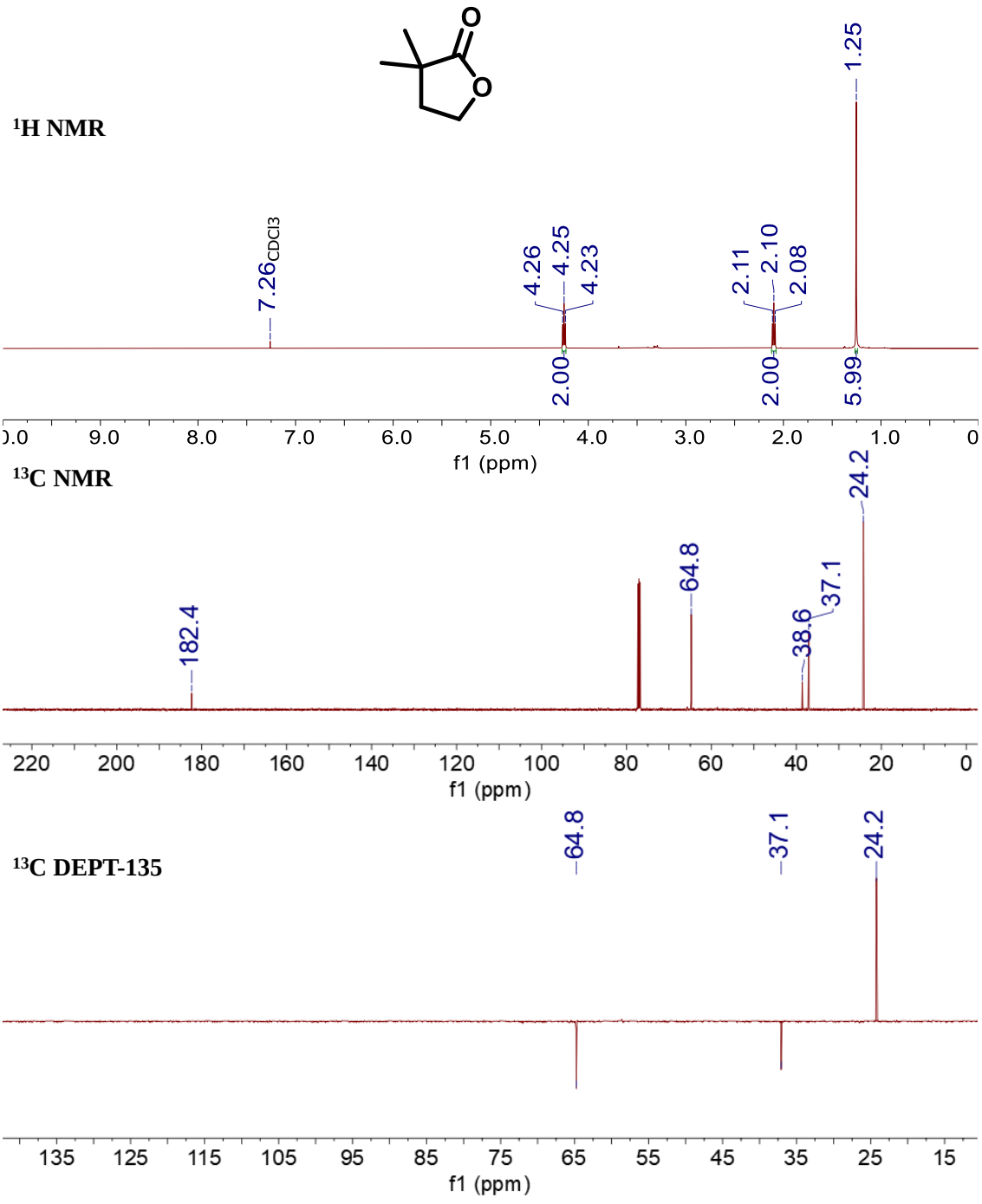

*Figure S3.15. ^{1}H, ^{13}C and ^{13}C DEPT-135 NMR spectrum of 3,3-dimethyldihydrofuran-2(3H)-one (**13**) in $CDCl_3$.*

3,3-dimethyldihydrothiophen-2(3H)-one (14)

^{1}H NMR

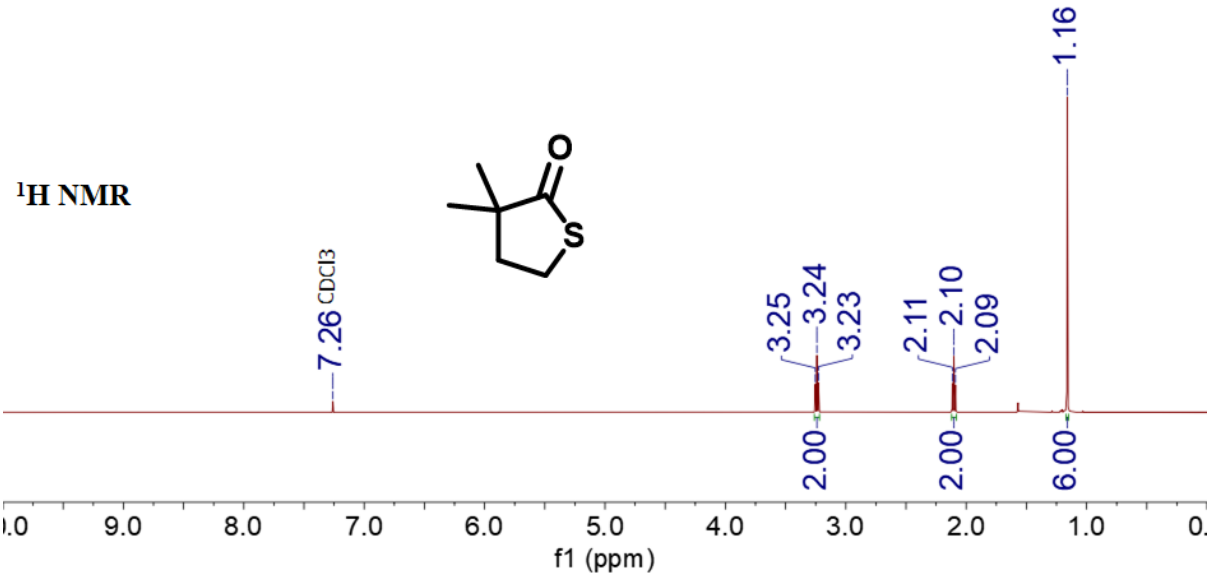

^{13}C NMR

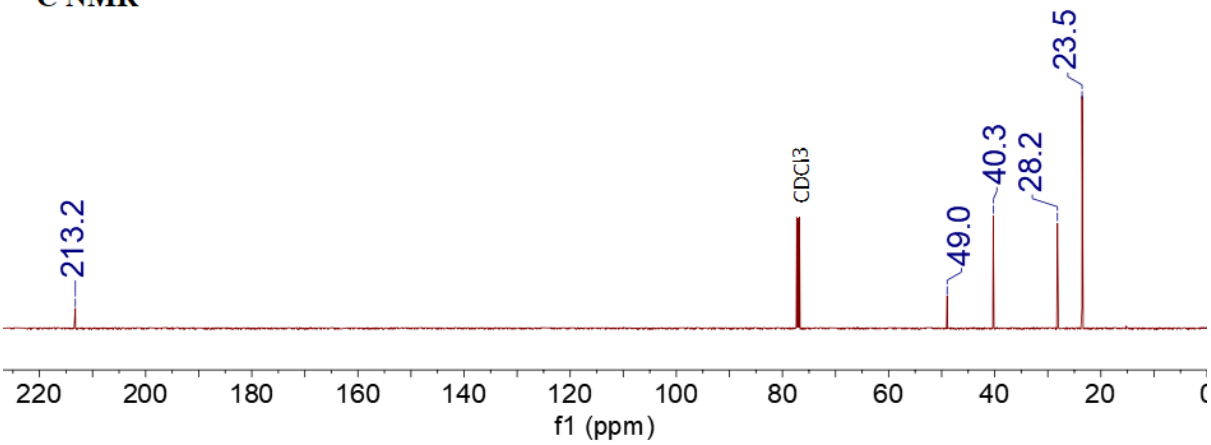

^{13}C DEPT-135

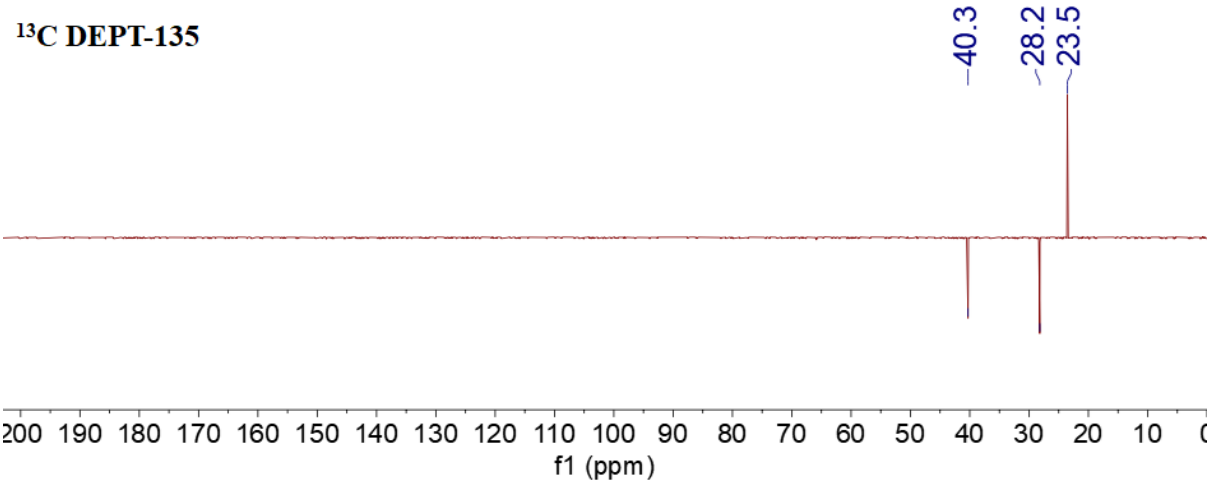

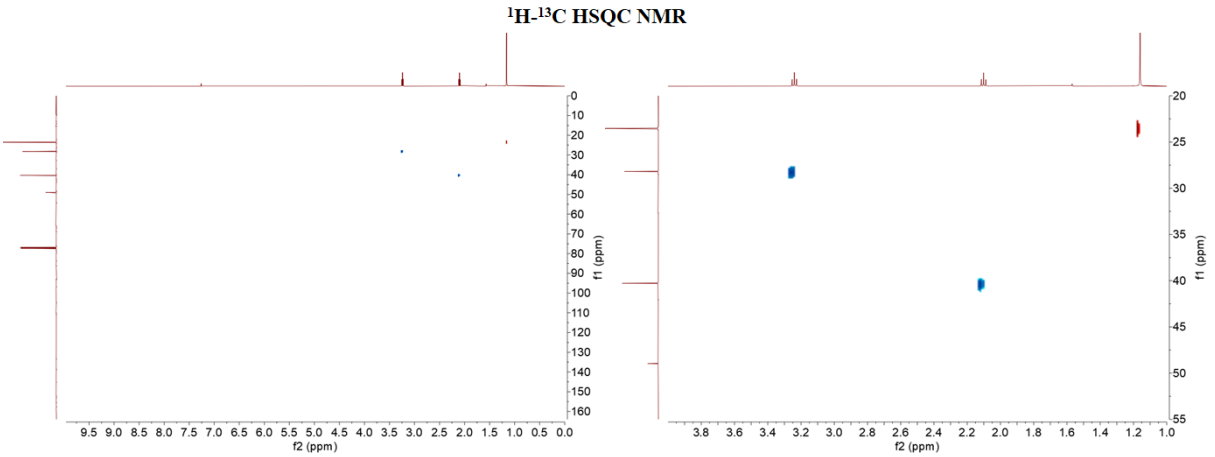

*Figure S3.16. ^{1}H, ^{13}C ,^{13}C DEPT-135 and ^{1}H-^{13}C HSQCNMR spectrum of 3,3-dimethyldihydrothiophen-2(3H)-one (**14**) in $CDCl_3$.*

4,4'-disulfanediylbis(2,2-dimethylbutanoic acid) (15)

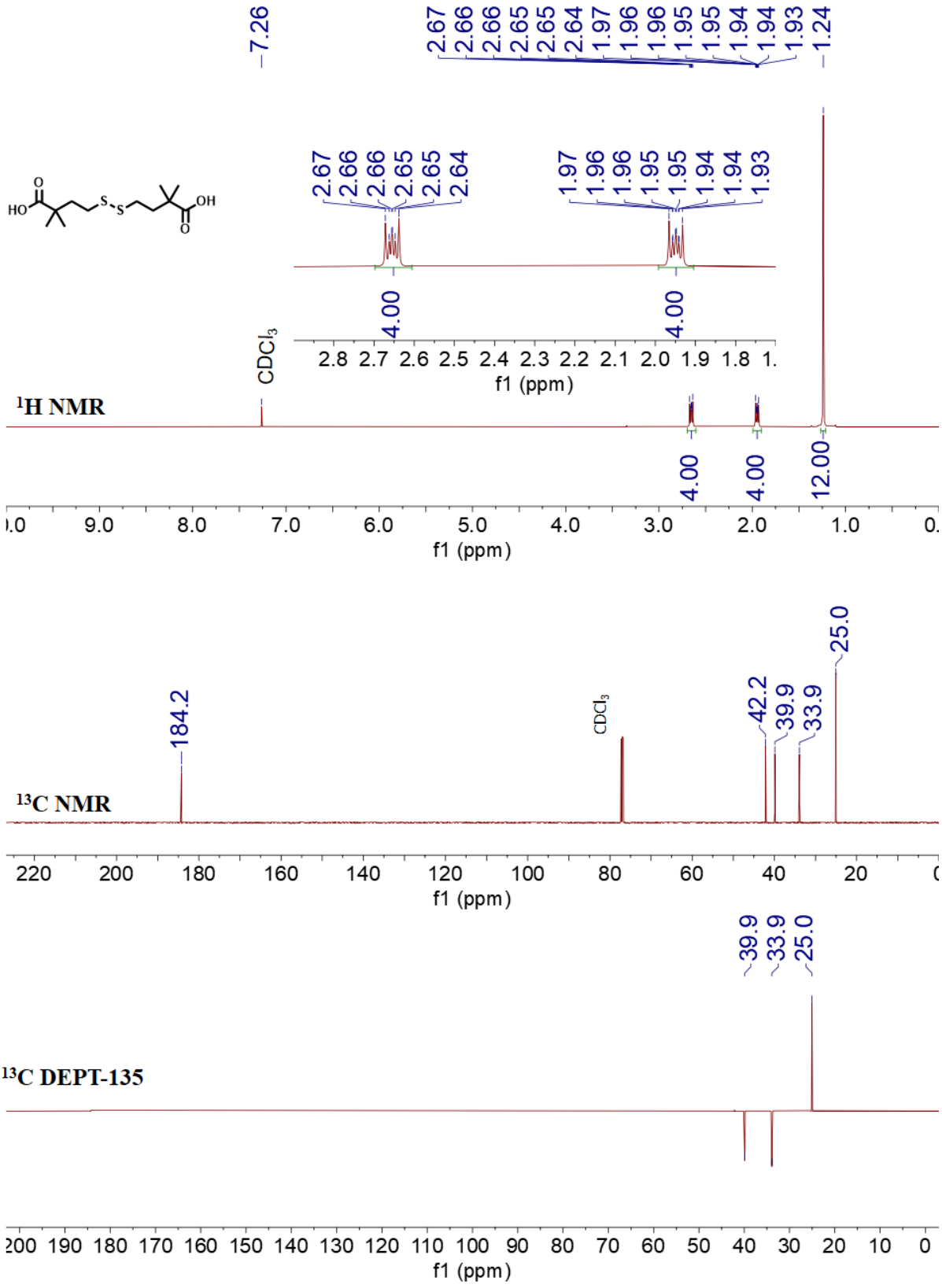

^{1}H-^{13}C HSQC NMR

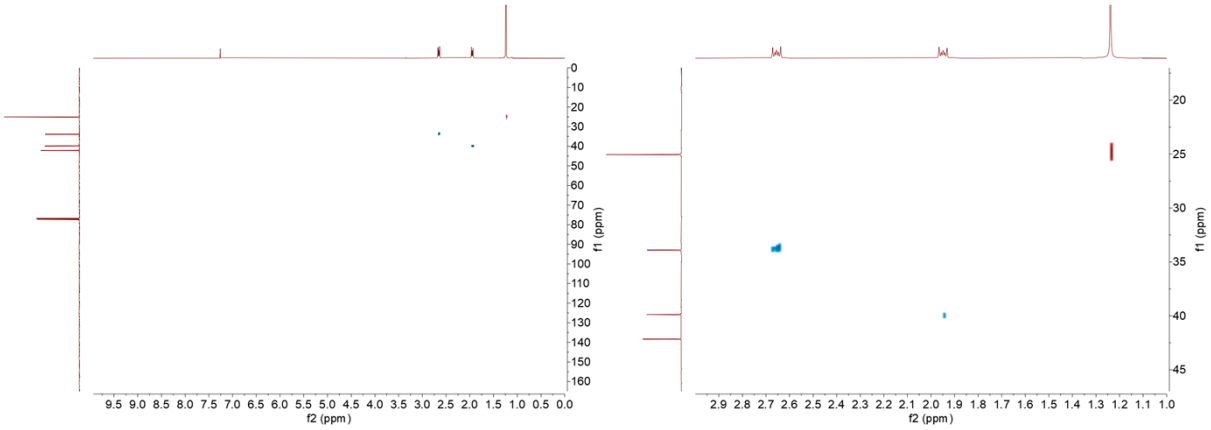

*Figure S3.17. ^{1}H, ^{13}C ,^{13}C DEPT-135 and ^{1}H-^{13}C HSQCNMR spectrum of 4,4'-disulfanediylbis(2,2-dimethylbutanoic acid) (**15**) in $CDCl_3$.*

bis(4-methyl-2-oxo-2H-chromen-7-yl) 4,4'-disulfanediylbis(2,2-dimethylbutanoate) (9)

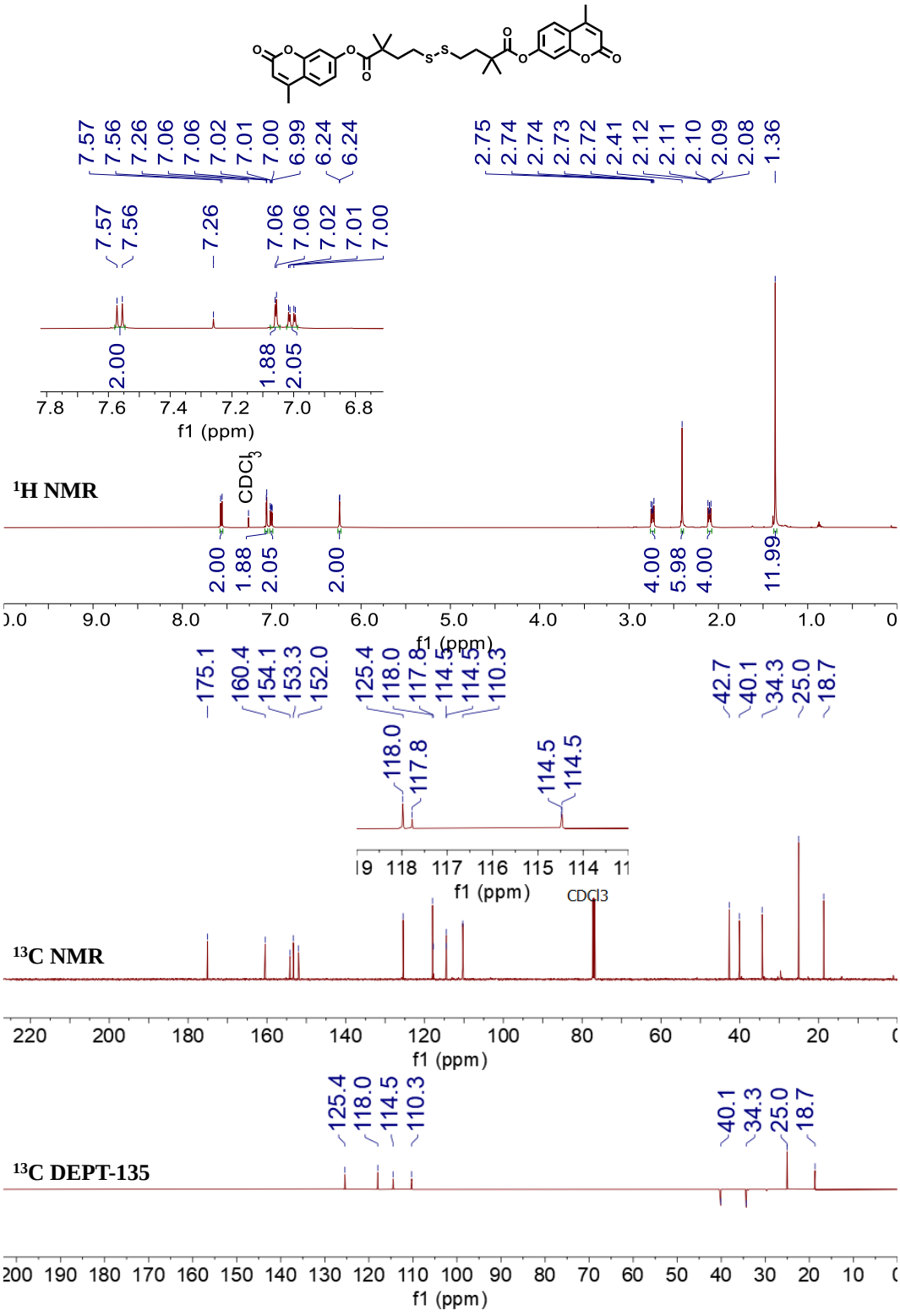

*Figure S3.18. ^{1}H, ^{13}C, and ^{13}C DEPT-135 spectra of bis(4-methyl-2-oxo-2H-chromen-7-yl) 4,4'-disulfanediylbis(2,2-dimethylbutanoate) (**9**) in $CDCl_3$.*

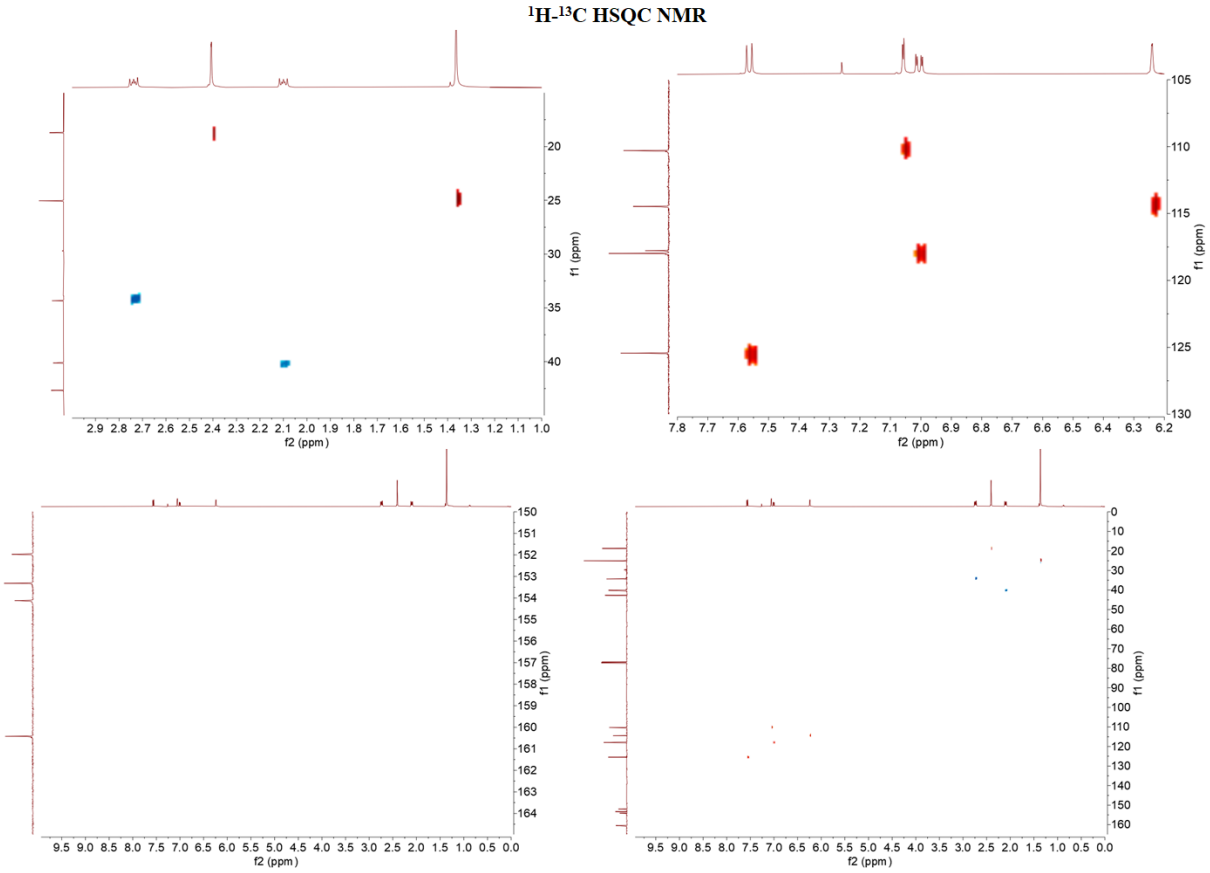

*Figure S3.19. ^{1}H-^{13}C HSQCNMR spectrum of bis(4-methyl-2-oxo-2H-chromen-7-yl) 4,4'-disulfanediylbis (2,2-dimethylbutanoate) (**9**) in $CDCl_3$.*

ATR-IR Spectra for Compound **16**

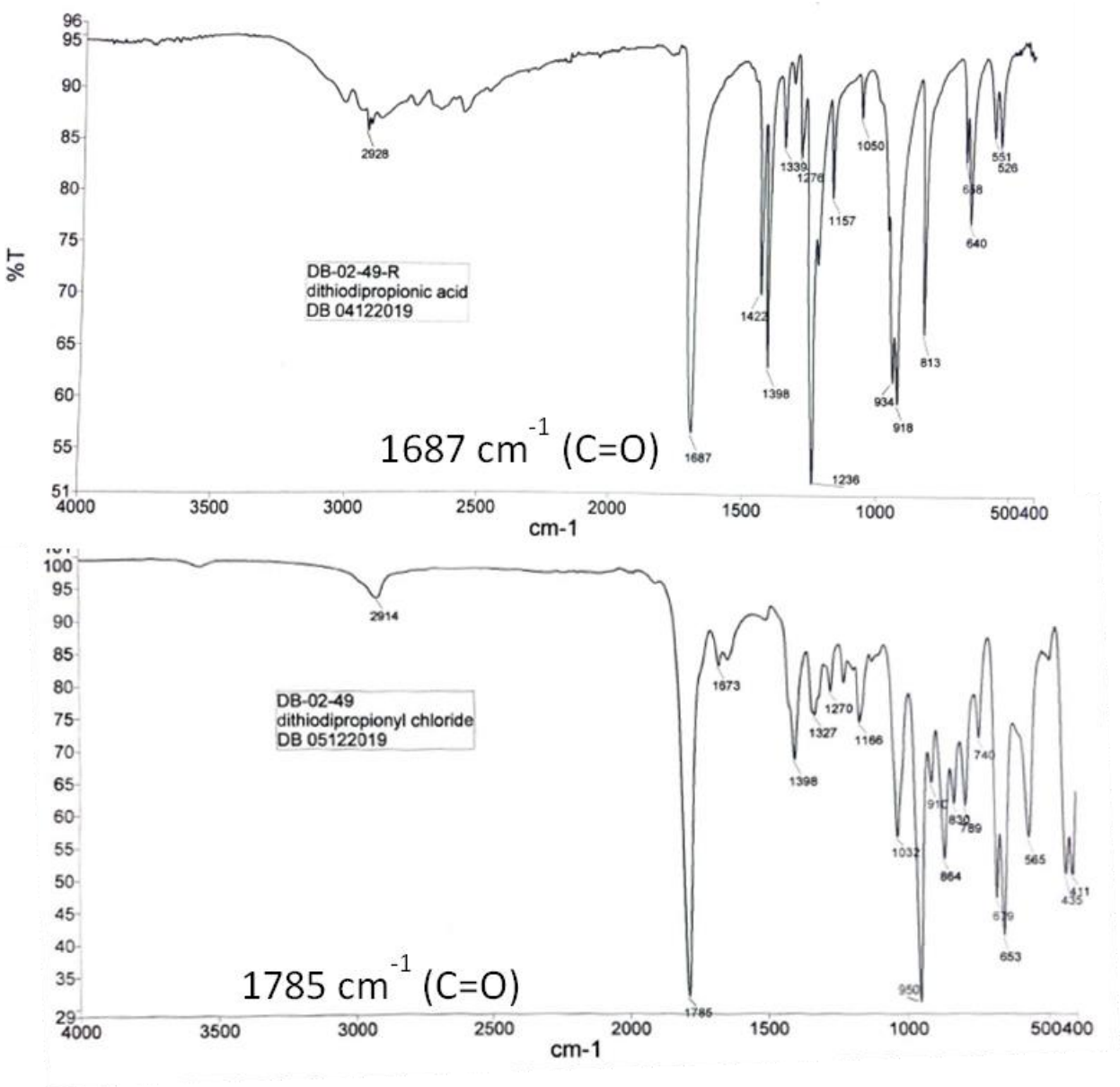

*Figure S3.20. Comparative ATR-IR spectra of starting material (DTDPA, top) and expected product **16** (bottom). The absence of the broad O-H stretches (> 3 000 cm^{-1}) in the top spectrum, and the change in C=O stretch from 1687 cm^{-1} to 1785 cm^{-1} is indicative of successful atom replacement in the synthesis of the diacyl chloride.*

4. Supplementary Materials (Chapter 4)

These are more comprehensive data for the batch characterization, where TEM was the major resource in determining the size of the AuNP cores. DLS was used as an orthogonal technique as measuring core volume and visualize any agglomeration and instability of the particles. UV-vis spectroscopy was also used as determining the concentration of the particles by the relationship of the SPR absorbance peak and core absorbance at 450 nm.

Table S4.1. Composite data of citrate-coated AuNPs cores characterized from TEM, DLS, and UV-vis. The range is calculated from the standard error of the mean (SEM). The conditions for "suitable" were whether the measure core size was near expected (15 nm) and if the dispersity shown by DLS was < 0.15 within three samples.

Date	Expected Particle Size (nm)	Actual Size (TEM)	Actual Size (DLS) PDI?	Actual Size (UV-vis)[19]	Suitable?
4 Feb 2019	15	16.7 ± 2.6	N/A	N/A	
22 May 2019		14.5 ± 0.1	N/A	N/A	
19 Aug 2019		14.5 ± 0.9	75.4 ± 6.6 0.17 ± 0.05	9	Yes
19 Jan 2020		16.4 ± 0.4	N/A	13	Yes
27 Jan 2021		15.4 ± 4.4	45.8 ± 6.1 0.23 ± 0.05	16	High dispersity
19 Mar 2021		11.9 ± 0.2; 13.2 ± 0.1	71.7 ± 10.5 0.15 ± 0.04	12	Yes
30 Jun 2021		16.5 ± 0.1	52.6 ± 2.9 0.13 ± 0.02	N/A	Yes
6 Mar 2022; 15 Mar 2022		9.5 ± 1.8; 12.9 ± 1.5; 14.4 ± 0.8	N/A	15	Yes

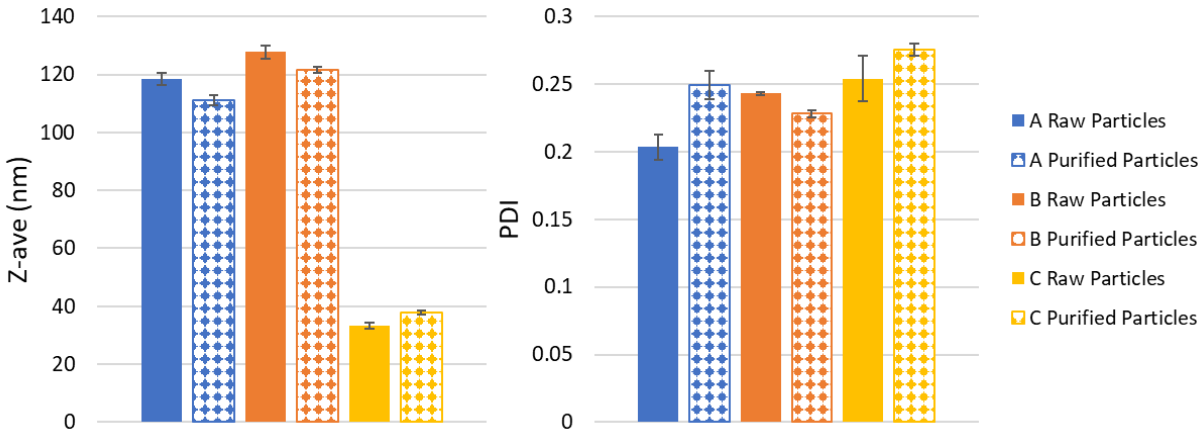

Figure S4.1. Sizing AuNPs post-functionalization. The formulation was 35% αLA-αPD-L1 and 75% PEG_{2000}. Raw particles are measured one hour after mixing, purified particles are centrifuged to remove any unbound molecules. The bars represent the average of two replicates.

Table S4.2. Calculated molecular weights of 15 nm AuNPs functionalized with PEG_{2000} and αPD-L1 antibodies. The increase in MW between functionalized and bare particles is negligible.

AuNP MW *d* = 15 nm (g/mol)	Total molecules PEG_{2000} per AuNP (700)		Total molecules mAb per AuNP (26)			%Increase MW
$2.06 \cdot 10^7$	%Coating PEG_{2000}	Partition MW PEG_{2000}	%Coating mAb	Partition MW mAb	Total MW	*f*-AuNP / AuNP
Vehicle Controls (PEG only)	100	1.40E+06	0	0.00E+00	2.20E+07	1.07
	95	1.33E+06	5	1.95E+05	2.21E+07	1.07
	90	1.26E+06	10	3.90E+05	2.22E+07	1.08
	85	1.19E+06	15	5.85E+05	2.24E+07	1.09
	80	1.12E+06	20	7.80E+05	2.25E+07	1.09
Optimized Formulation	75	1.05E+06	25	9.75E+05	2.26E+07	1.10
	…		…			
Least Stable	50	7.00E+05	50	1.95E+06	2.32E+07	1.13

HBS-EP$^+$ Running Buffer for SPR and Sample Preparation

HBS-EP$^+$ was produced in house using materials from Sigma-Aldrich using the final concentrations as described by the manufacturer (Cytiva). The 10X concentrate buffer is 1.5 M NaCl, 0.1 M HEPES, 30 mM EDTA, and 0.5% v/v P20 (a.k.a. Tween 20), that upon dilution will have a final pH ~ 7.4. Both the concentrate and active buffer are filtered and degassed through a 0.22 µm PES filter.

General Conjugation of αPD-L1

25 mg αPD-L1 (BioXCell) are reconstitutionalized in HBS-EP$^+$ buffer as a 3.33 µM stock solution (0.5 mg/mL)

In situ Conjugation of GSH-mAb

A solution of GSSG, NHS, and EDC is prepared and mixed at room temperature for 2 h to form *in situ* $(NHS)_x$-GSSG conjugates, where conjugation of NHS may range from 1 to 4 (Figure 4.9). Afterwards, αPD-L1 is added to ligate and let stir overnight at room temperature. The reaction mixture was purified using centrifugation spin-columns with a MWCO of 3 000 g/mol.

Prior to purification, the columns were cleaned ahead of time by marking the reservoir for the expected maximum and minimum volumes of 400 µL and 100 µL, respectively, and spinning down 70% ethanol, twice. The columns were then rinsed with HBS-EP$^+$ running buffer to remove any remaining alcohol. The columns were spun at 10 000 x g for 10 min in a benchtop MiniSpin^{TM} centrifuge using 1.5 mL Eppendorf tubes, these conditions were found most consistent in the expected 4x concentration. The retentate is resuspended in fresh buffer to the 400 µL and concentrated, this is repeated at least 5 times to keep the antibody concentration the same, while the small molecules are pulled down (Figure 4.8).

The mAb-conjugate solution is then treated with 5 mol eq. TCEP to reduce the GSSG to GSH, incubated overnight and the buffer is exchanged two more times using the process above to further remove the small molecules. During the optimization of *in situ* EDC/NHS coupling, we repeated this process with dithiodibutyric acid (**17**) and observed overall worse functionalization (data not shown). We sought to optimize conjugation conditions where the *in situ* NHS-ester formation was done under slightly acidic conditions in an acetate buffer, pH 5.5, and saw no change in functionalization. This method is not suitable long-term but was great for determining initial conjugation conditions.

Example mixture for *in situ* formation of mAb-thiol conjugation with oxidized glutathione (GSSG).

Table S4.3. Example volumes used for 500 µL spin-column *in situ* formation of NHS-ester and GSSG-conjugated mAbs. One-pot method used excess of coupling agents with respect to the antibody (αPD-L1).

Molecule (FW, g/mol)	Concentration (mol/L)	Volume (µL)	Concentration (final) (mol/L)	Quench with Ethanolamine (mol/L)	Mol eq. αPD-L1	Mol eq. αPD-L1 (quench)
EDC	0.4	10	0.01	0.0097	24 000	23 414
NHS	0.1	10	0.025	0.0024	6 000	5 854
GSSG	3.1	10	$7.75 \cdot 10^{-5}$	$7.56 \cdot 10^{-5}$	186	181
αPD-L1	$3.33 \cdot 10^{-6}$	50	$4.17 \cdot 10^{-7}$	$4.07 \cdot 10^{-7}$	1	1
Volume 1 (remainder is HBS-EP$^+$)		320 µL				
MEA[a]	1	10	–	0.024	–	58 968

[a]MEA: (mono)ethanolamine

In Situ Conjugation of αLA-mAb

Similar to NHS-esterification of glutathione, αLA was pre-mixed with excess NHS and EDC in the HBS-EP$^+$ running buffer to generate the NHS ester *in situ*. Prior to mixing, αLA was first dissolved in DMSO or DMF to make a 1 mg/mL stock solution. This 100% organic stock was then further dilute into the HBS-EP$^+$ where the final concentration was < 20% v/v as the working stock that was used in generating the NHS-ester. After overnight mixing, the αPD-L1 mAb was added as the limiting reagent to a fixed concentration of 0.5 mg/mL and continued to incubate overnight. The following day, the solution was dialyzed with a 3 000 MWCO filter at a 1:200 ratio, twice, to remove any small molecules and reduce the organic solvent concentration by 40 000×. The BCA (bicinchoninic acid) assay from Pierce™ was used to assess the protein concentration post-dialysis, anticipating ~0.5 mg/mL concentration for the thiolated antibodies. The samples were measured using the known molar absorptivity coefficient for monoclonal antibodies of 210 000 $M^{-1}cm^{-1}$.

Isolation of non-thiolated mAb occurs upon AuNP functionalization and purification, where during centrifugation unbound mAb will remain in the supernatant. By removing as much of the solvent without disrupting the AuNP pellet, we may resuspend in fresh buffer and continue to remove unbound mAb. The supernatants were collected and measured for any protein by BCA assay, after two spin-downs, the antibody in the supernatants was no longer detectable. These values were corroborated by flowing the particles and the supernatants for binding with PD-L1.

mAb Protein Determination by Bicinchoninic Acid (BCA) Assay

Samples were prepared as directed in the Pierce™ BCA Protein Assay Kit (Cat. 23225). In brief, the protein concentration is standardized to 1 mg/mL serial dilution of BSA provided. A SpectraMax M5 plate reader was used to monitor chelation of the Cu^+ reagent to the mAbs by measuring the absorbance at 562 nm. Samples measured in a 96-well flat-bottom plate (Corning Costar) and read for absorbance from the top.

Synthesis of αLA-NHS ester (22)

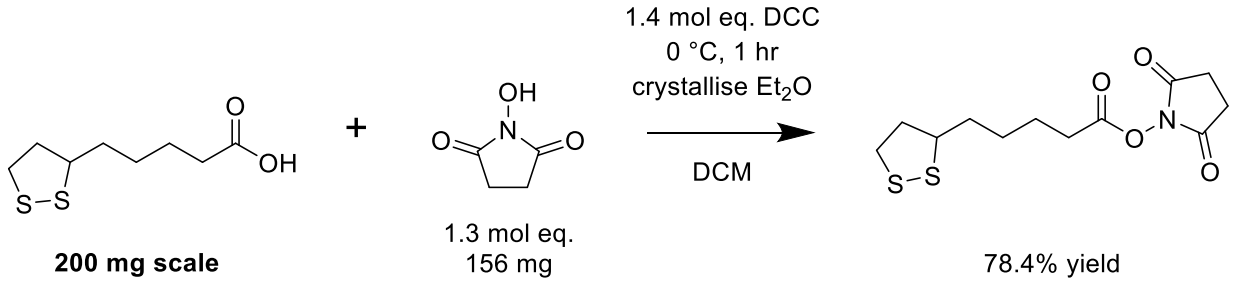

Figure S4.2. Synthesis of αLA-NHS (**22**).

Procedure was followed as described by Shi *et al*.[289,290] In brief, 200 mg αLA (1 mmol) was dissolved in anhydrous DCM charged with 1.3 mol eq. NHS, and dropwise an addition of 1.4 mol eq. DCC was slowly added to the vessel. The reaction stirred on ice for 1 h, and crystallized with diethyl ether (Et_2O) to remove any urea byproduct. The crude product was dried on a vacuum flask with rinsed with methanol. The colourless powder was then characterized by ^1H, ^{13}C, and ATR-IR. Stocks were then made by dissolving the powder in anhydrous DMF, working solutions were subsequently dilute into appropriate buffer with a maximum of 20% v/v DMF.

^{1}H NMR (300 MHz, $CDCl_3$): 3.57 (1H), 3.16 (2H), 2.83 (4H), 2.62 (2H), 2.46 (1H), 1.91 (2H), 1.78–1.69 (3H), 1.57 (2H).
^{13}C NMR (126 MHz, $CDCl_3$): 192.5, 169.4, 56.2, 40.3, 38.7, 34.6, 30.9, 24.5, 25.7, 24.5 ppm. ATR-IR: 1728 cm^{-1} (C=O)

Our findings of stock concentrations determined that in order to prepare stoichiometrically appropriate aliquots of the NHS-ester for mAb conjugation required minimal toxic organic solvents, and found that serially diluting the NSH ester was necessary. Initial findings observed that 20% v/v DMF (with concentrations > 10 mg/mL NHS ester) would result in aggregation. A 20 mg/mL solution (100% DMF) was stable, but when 20x dilute in water would crash out. However, when the same 100% DMF stock was 5x dilute (4 mg/mL, 20% DMF), it could be safely dilute further to 5% DMF without observing any particulate. This was the chosen method for making stoichiometric stock solutions was two-steps serial dilution from a 20 mg/mL (100% DMF) down to 5 mg/mL (100% DMF).

Conjugation and Purification of αLA-αPD-L1

20 mg/mL **22** in a DMF stock solution was dilute in HBS-EP^{+} running buffer to 4 mg/mL (20% DMF). This allowed for a quantitative addition of the NHS ester to the mAb for peptide conjugation while minimizing the DMF concentration (5% in 1 mL). The solution was left to incubate overnight by gentle stirring, and the sample was then dialyzed through a 3000 MWCO membrane into fresh HBS-EP^{+} v/v 1:200, twice to remove any unwanted byproducts and organic solvent.

Removal of non-thiolated mAb occurs upon AuNP functionalization and purification, where during centrifugation unbound mAb will remain in the supernatant. The supernatants were collected and measured for any protein by BCA assay, after two spin-downs, the antibody in the supernatants was no longer detectable. These values were corroborated by flowing the particles and the supernatants for binding with PD-L1.

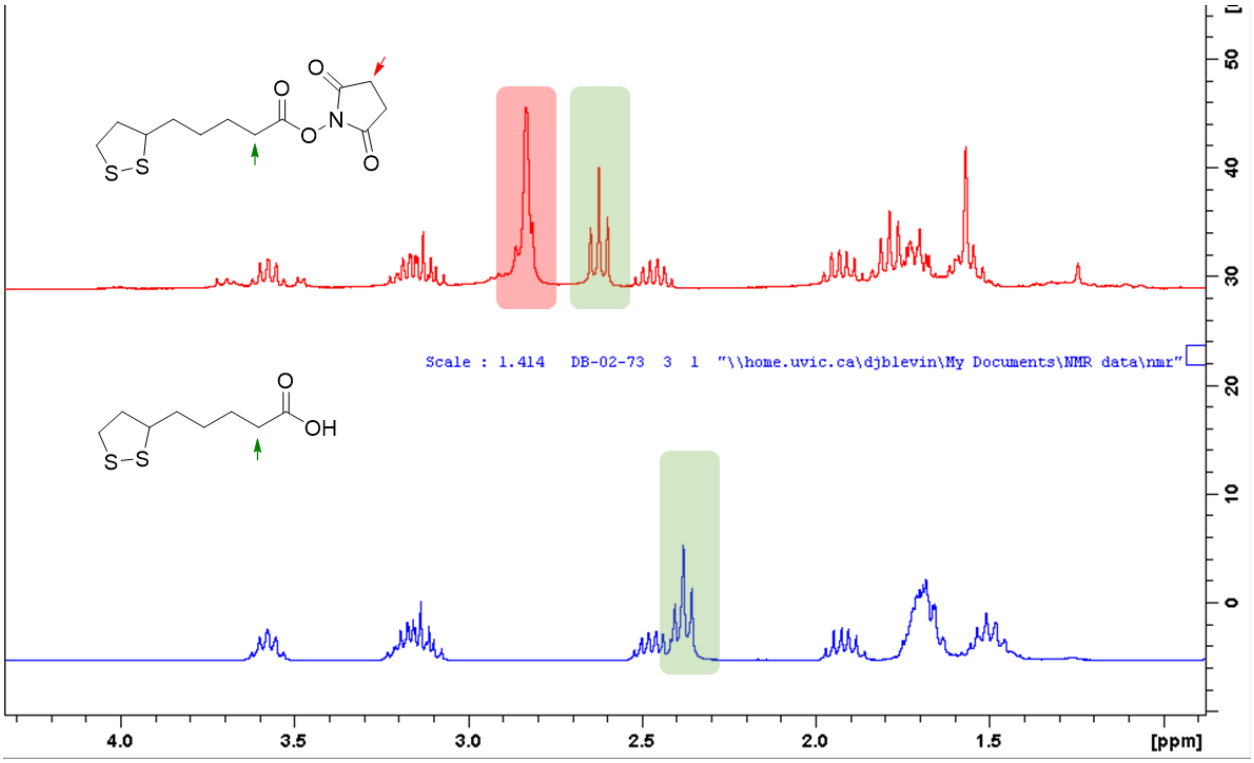

Figure S4.3. ^{1}H NMR of αLA-NHS ester (top) and αLA reference (bottom). Arrows highlight largest chemical shifts upon conjugation.

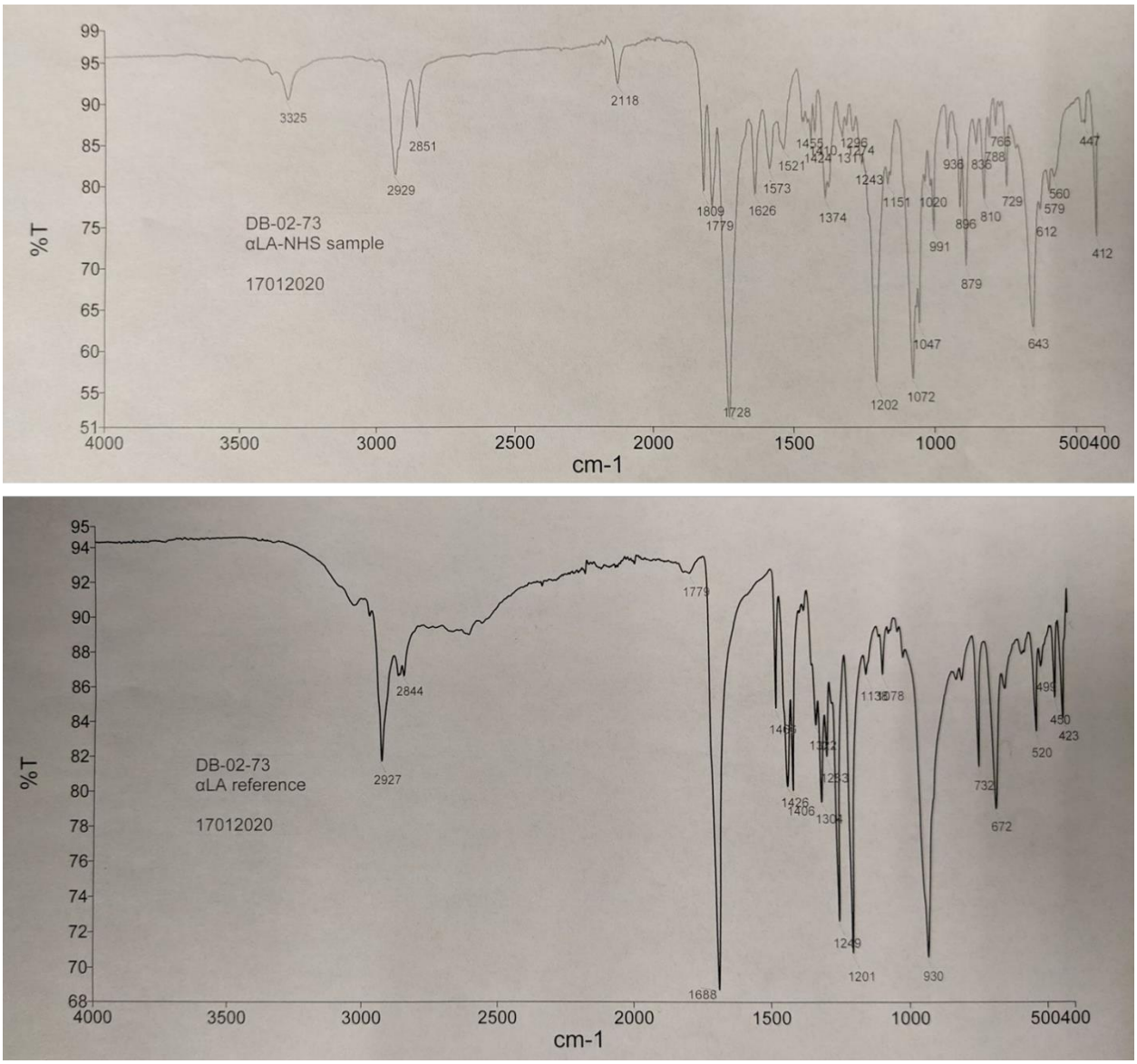

Figure S4.4. Comparative ATR-IR spectra of αLA-NHS ester (top) and αLA reference (bottom).

5. Supplementary Materials (Chapter 5)

This section is primarily for supplementary troubleshooting of T cell culturing and stimulation prior to acquiring the data needed for Figures 5.1–5.3, and hopefully will be useful to another graduate student who may be struggling with how to optimize in an isolated environment. It is important to be transparent with all the evidence, especially as the output for the immunotherapeutic characterization of the particles used a hemocytometer rather than a biochemical technique like an ELISA or cell staining. Showing the improvement in the handling could be helpful to others who are new to culturing techniques, and may be a first step to better communication in science and collaborative efforts for those unfamiliar in the field.

Optimizing T Cell Activation

To validate our claim of immunotherapeutic effects, we require activated immune cells that produce PD-1. We aim to evaluate the blockading effect that was observed in SPR and continue to observe that function in a higher complexity environment, as this will more appropriately mimic tissues. We expect that the phenotypic outcome of high cell density will be indicative of a pro-inflammatory response as induced by stimulants, and that this effect will not be deterred when the targeting particles are present. We anticipate that by incubating stimulated T cells with PD-L1, we will observe no or low growth in cell density, therefore confirming that the PD-L1 is suppressing the antigenic signals from the stimulants. Then by adding our functionalized particles we hope to observe a significantly higher cell density, regardless of PD-L1 presence. Other *in vitro* immune cell experiments in the literature inspired the planning for T cell recovery. However, there is a lack of appropriate description around how to approach optimizing the stimulation conditions.[291,292]

Based on previous work reported by Kleijn and Proud we expect that incubation of the Jurkat cells with stimulants will lead to an increase in proliferation, and therefore we expect a higher cell density overnight as our primary readout of recovery (Scheme S5.1).[333] We want to attribute the higher cell density as an indicator of T cell activation, but would require an orthogonal readout to verify this claim. An ELISA was chosen to measure the pro-inflammatory cytokines (e.g., IL-2) to verify the effects induced by the immunostimulants. The presence of these cytokines would also be indicative of an activated T cell response, and therefore we should anticipate higher cytokine concentrations when T cells are unimpeded by immunosuppressive proteins such as PD-L1 (Scheme S5.2).

Throughout the initial series of optimization, the stimulants contributed to consistently higher cell density than without them. Jurkat cells without stimulation are anergic and will fail to be cytotoxic, therefore will display no activity nor have a higher cell density.[334] If naïve (unstimulated) Jurkat cells were co-incubated with PD-L1-presenting cells, we expect that the *f*-AuNPs would show no efficacy of recovery, and likely the Jurkat cell population would be overtaken by the cancer cells, making it difficult to assess if recovery was occurring. If our *f*-AuNPs are efficacious, we would expect that the Jurkat cells would be able to actively reduce TNBC proliferation, but this would only be apparent if the Jurkat cells are mature and capable of recognizing PD-L1. Monitoring two independent cell populations by hemocytometer alone would be quite difficult and therefore other techniques would be required to monitor the efficacy of the particles between cell populations. One possibility to do so is by flow cytometer or an ELISA where evidence of an immunotherapeutic effect from the AuNPs would be measured by the presence of cytokines or target-specific fluorophores.

More consistent reads of cell density and sample handling led to better hemocytometer cell count data. However, this could not be corroborated with an ELISA as the cytokine levels were often below the detection limit (Figure S5.9). Initially, we thought that the Jurkat cells were contaminated and therefore unable to be stimulated, so the same stimulation conditions were used on a different series of Jurkat cells donated from the Lum lab. We wanted to demonstrate the consistency in the stimulation patterns observed to remove any possibility of insensitivity or contamination. Unfortunately, no cytokines were detected over at least four separate IL-2 and IL-6 kits with two separate Jurkat cell lines. Eventually sample preparation and the stimulation conditions were optimized through empirical evidence of consistent cell density, and reporting by hemocytometer became more quantitative. This was used as our readout for our cellular recovery assay.

Using αCD3 and αCD28 Antibodies

Antigen-presenting cells (APCs) are the initiators of T cell activation in white blood cells. They bind to naïve lymphoblasts through the T cell receptor, and cause a signal transduction that cascades into the nucleus, which changes the genetic expression of the cell to mature and differentiate the white blood cell.[145,335–337] These antibodies behave as the APCs and target the T cell receptor of naïve cells, which activate the immune system in a similar way resulting in a proliferative state producing cytokines and interleukins indicative of an immune response.

Using PMA and Ionomycin

Phorbol 12-myristate 13-acetate (PMA) is another stimulating agent for the immune system that induces pro-inflammatory proliferation.[292,295,338] PMA targets protein kinase C (PKC), which causes the signal cascade from cell surface to nucleus. Using PMA bypasses activation via the TCR, but still results in more pro-inflammatory effector genes (i.e., cytokines) and lymphoblast maturation. Complementary to PMA is ionomycin, a Ca^{2+}-chelating agent, which activates a separate pathway of transcription factors induced by the higher effective concentration of calcium cations.[339] Both molecules override the need for T cell receptor activation, and directly induce proliferative effects via the downstream PKC:mitogen cascade.[292,295,339]

Sigma-Aldrich have a 500x concentrate of PMA commercially available that may be directly added to cells, but it is not explicit what the concentration in is relation to (i.e., well volume, cell seeding number, cell density). During initial stimulation with Jurkat cells and PMA/ionomycin, we diluted into a working concentration of 50 ng/mL and 1 µg/mL, respectively, such that we may use the mass of stimulant in relation with the number of cells present. We had observed variable levels of cell density that could be correlated with stimulation, where the presence of stimulant resulted in a higher cell density. Cell growth and stimulation was measuring by cell counts using hemocytometer, taking aliquots from overnight and two-day growth experiments (Figure S5.1) and normalizing the densities to non-stimulated controls. In these preliminary cases for stimulation, we required consistent and robust growth patterns prior to any potential suppression and recovery experiments with PD-L1 and our AuNPs.

Wenchao *et al*. performed a comparative study of cytokine production in lymphocytes by various stimulation methods, and they found that PMA/ionomycin induce production of pro-inflammatory cytokines, IL-2 and IL-6.[338] Although they were using white blood cells isolated from whole blood samples, we expect that Jurkat cells being lymphoblasts would achieve stimulation cytokine production by similar stimulation. This was also proven in the literature by the work of Yiemwattana *et al*. where they had directly measured IL-2 production in activated Jurkat cells.[292] We found that despite ionomycin having

synergistic use with PMA, it has no significant effect on stimulation or proliferative growth within a two-day incubation period (Figure S5.1). Despite the comprehensive comparison of stimulants in the article by Wenchao *et al.*, the concentrations of the stimulants are provided, but not in any relation to the cells (or in their case, blood), regardless they were capable of detecting the presence of IL-6 and IL-2 at low µM concentrations with PMA as high as 25 ng/mL.

Using PHA

Phytohemagglutinin (PHA) is a protein isolated from red kidney beans that similarly targets T cell receptors to induce genetic activation of T cell cytotoxicity.[340–342] When PHA binds to the TCR, it triggers the same calcium-dependent pathways as PMA/ionomycin.

Jiao *et al*. performed a similar optimization protocol for general lymphoblasts and found that 50 µg/mL (per $1{\cdot}10^6$ cells) was optimal at stimulating mitogen and immune activity.[336] Our findings were similar (Figure S5.11).

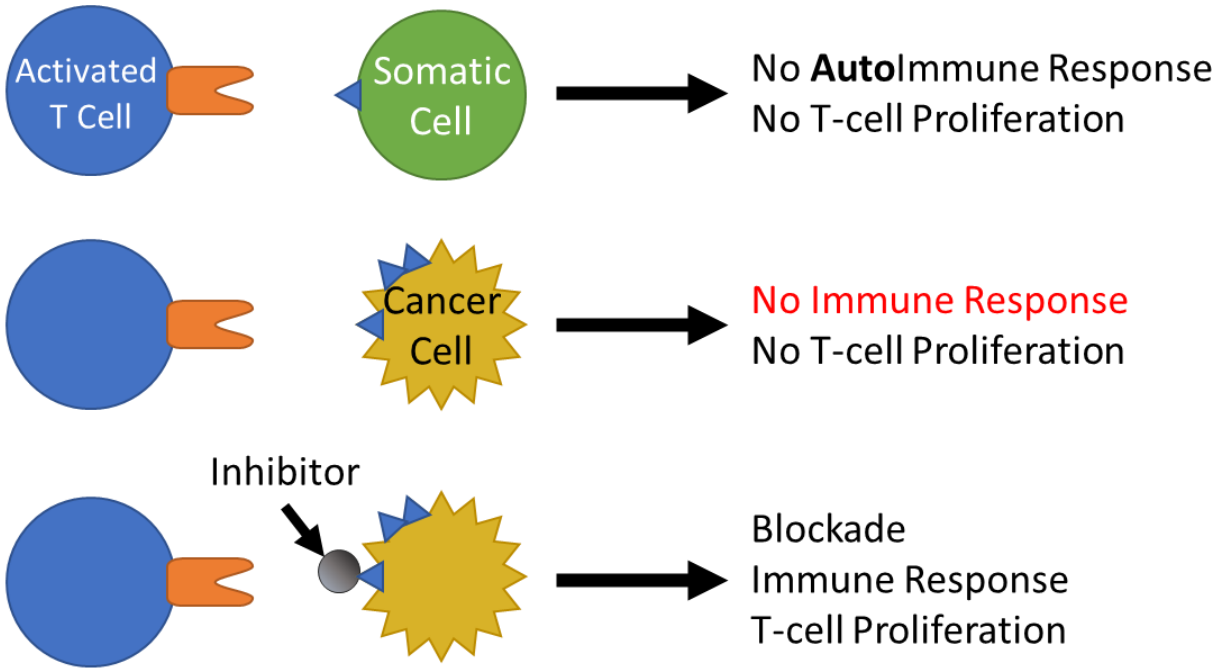

Scheme S5.1 The anticipated outcomes of T cell activation, immune exhaustion, and recovery. The presence of PD-L1 binding to PD-1 on stimulated T cells in somatic tissues suppresses T cell activity, which prevents autoimmune attacks. However, PD-L1-presenting cancers use this to evade the immune response. By incorporating an inhibitor that targets and blocks PD-L1, we reinstate that initial immune activity and observe higher T cell density with mature T cells.

When scouting the stimulation effects we found the following cases, which eventually led to robust stimulation of the Jurkat cells.

1. Early stimulation experiments used ratios of final concentrations in the well to attempt to stimulate the white blood cells. There was no explicit value for where these ratios are applied making it difficult to assign a relationship between stimulants, the cells, and their seeding density.
    a. The problem was whether the stimulants may be toxic at higher concentrations, and whether the addition diluted the cell density, and therefore increased potency?

b. For example, “10X” was thought to be the equivalent concentration of stimulant per number of cells per well (i.e., 10X conc., 1X at $10 \cdot 10^6$ cell/mL). Therefore, we would need a 1/10 volume to correct for concentration. Or if it was the volume of stimulant added to the well, it could affect the cell density and this dilution factor would need to be accounted for.

2. High concentrations of stimulants would show some degree of toxicity on the cells, showing no apparent growth or stimulation relative to the basal growth control (Figure S5.5).
3. PHA/ionomycin demonstrated consistently higher cell counts relative to non-activated cells and was chosen as the appropriate stimulant for our Jurkat white blood cells.
4. More aged cell lines were insensitive to stimulating conditions (i.e., cells passaged at least a dozen times were less likely to react to the stimulants).

Finalizing Stimulation Protocol

Monitoring Stimulation between Two Separate Jurkat Cell Lines, Independently

The Jurkat cell proliferation was monitored by cell count via hemocytometer, and the growth levels were normalized to an unstimulated control (Figure S5.1). As the cells matured beyond passage 15, they became insensitive to stimulation. Despite the observed apparent stimulation by PMA in the later passage numbers (> P16), these Jurkat cells are genetically different from their earlier passages. Therefore, any observed efficacy at these higher cell counts should be interpreted with caution.

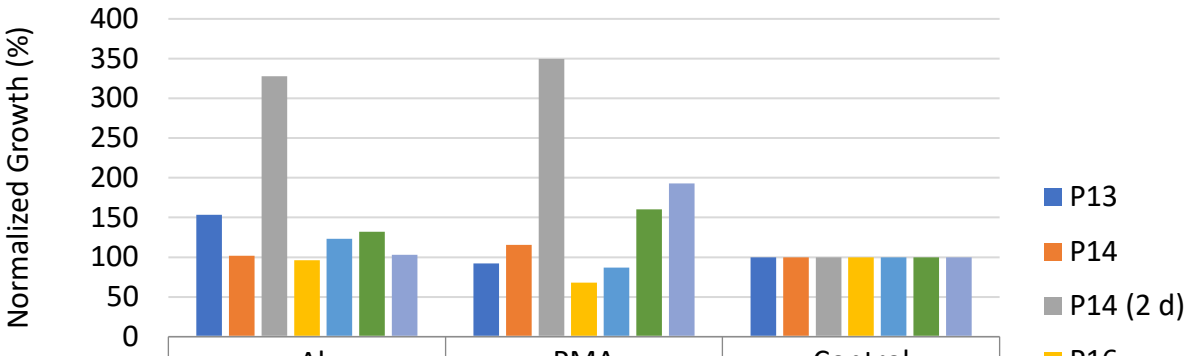

	mAb	PMA	Control
P13	154	92	100
P14	102	116	100
P14 (2 d)	328	350	100
P16	96	68	100
P19	123	87	100
P21	132	160	100
P22	103	193	100

Figure S5.1 Overnight cell density of Jurkat cells as stimulated by PMA or αC3/αCD28 mAbs, monitoring stimulability of the cells as they are passaged. Jurkat cells from our lab (Wulff, **W**) were monitored for proliferation induced by PMA/ionomycin or antibodies (αCD3 and αCD28) to optimize stimulation conditions attributed to T cell activation, while also monitoring any insensitivity as the cell matured due to higher passage numbers. The cell density was measured by hemocytometer counting one well of seeded cells over at least 4 squares, at least twice. The cell densities observed were normalized with respect to the cell density of basal growth Jurkat cells. "P14 (2 d)" was the measured cell density from at least two days of incubation post-stimulation normalized to two days of basal growth. During these preliminary scouting conditions, the cell densities were averages of one biological replicate (one well) from 2 or 3 sample reads as counted by hemocytometer.

These preliminary scouting conditions do not have error bars, as they were not run in duplicate. Initially we prioritized observing consistent of cell growth conditions and optimizing stimulation conditions (Figures S5.1–S5.7). Once the stimulation conditions were established, the culturing conditions were then done in duplicate to validate the reproducibility of induced stimulation and PD-L1-induced inhibition *in vitro* (Figure S5.12–S5.17). In all cases with αCD3/αCD28 mAb stimulation, we observe a lack induced proliferation in the Jurkat cells, once the passage number exceeds 15. This is indicated by the cell densities showing no exceptional increase relative to the basal growth controls.

The high cell density observed in the two-day growth of passage 14 (P14, 2d) was from another cell experiment where an aliquot of P14 was expanded and allowed to propagate further for another day. Although these appear promising, the level of stimulation was not reproducible and thus multiple-day incubations were not pursued.

The amount of stimulant added to the wells was proportional the seeding density, per $1{\cdot}10^6$ cells per mL. Interestingly, when the Jurkat cells were allowed to continuously grow for two days, the cell density grew more than 12-fold for both stimulating conditions. This included our basal control, where typically overnight growth is between 2- and 8-fold higher density than the initial seeding density. This much higher cell density gave us concern of a possible contamination of the Jurkat cells. Alongside the relatively late

passage number (P14), this warranted investigating a younger Jurkat cell line to corroborate our findings (Figure S5.2). It should be noted that these subsequent stimulation data were also obtained as single data points.

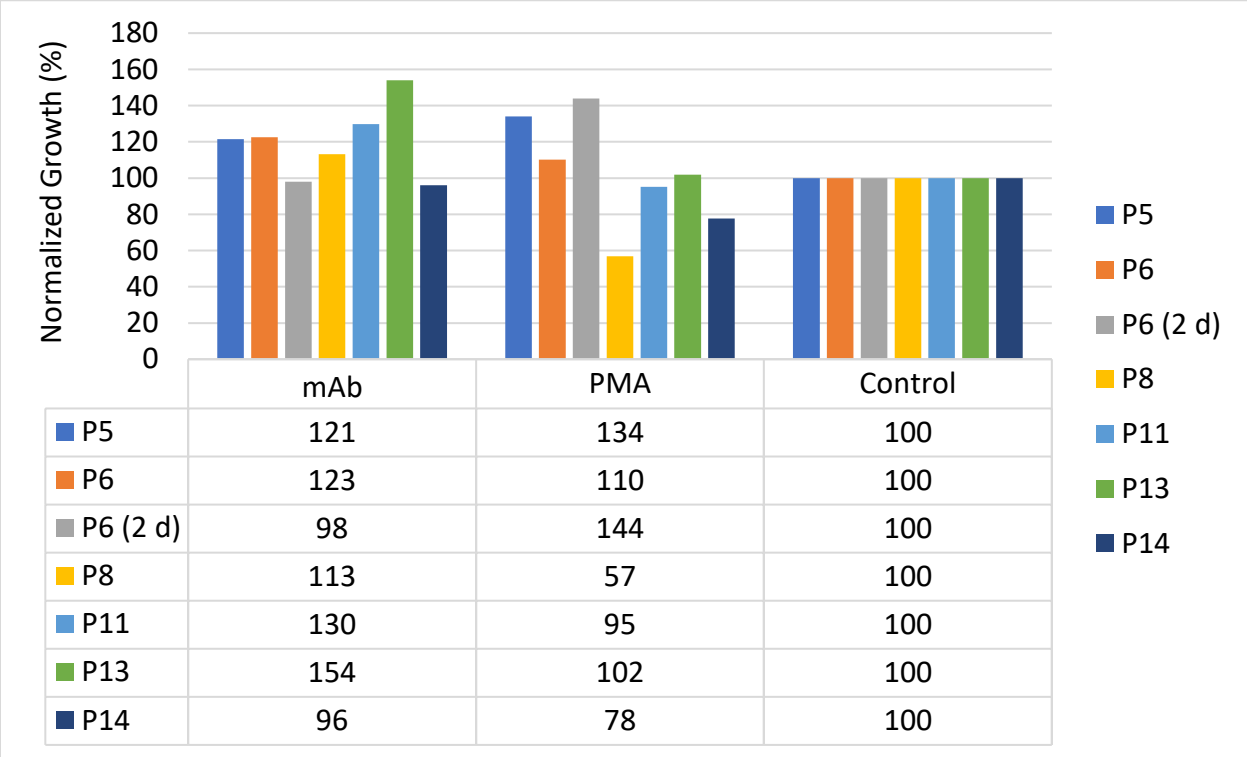

	mAb	PMA	Control
P5	121	134	100
P6	123	110	100
P6 (2 d)	98	144	100
P8	113	57	100
P11	130	95	100
P13	154	102	100
P14	96	78	100

Figure S5.2 Younger passage numbers are more responsive overall to stimulation. Jurkat cells borrowed from the Lum (**L**) lab were used to validate our growth and stimulation observations with PMA and mAbs, as well determine if the lack of stimulant-induced growth in the Wulff Jurkat cells was due to contamination or simply over-maturation.

Figure S5.2 follows a separate linage of Jurkat cells donated from the Lum lab and shows how they respond similarly under the same stimulation conditions. These Jurkat cells are a lower passage number and therefore younger. We wanted to validate the claim that naïve cells (i.e., lower passage numbers) are more appropriate as an *in vitro* model, as well as confirm that our Wulff Jurkat cells were not exhausted nor contaminated. The purpose of repeating the experiment with a separate cell line helps demonstrate the consistency of handling between experiments when each plate and cell line is its own data point without a replicate. The general trend observed with the Jurkat cells with lower passage numbers (i.e., < P10) had a better overall response to both stimulating agents, mAb and PMA/ionomycin. Interestingly, the less passaged Jurkat cells did not reflect the expansion trend (Figure S5.2) expected in the two-day growth seen previously (Figure S5.1). Although the PMA/ionomycin had 1.4x more cells than the control series, these values did not compare to the Wulff Jurkat cells 2 d in Figure S5.1, indicating that exceeding a 24 h incubation period is not suitable.

When comparing passages, P13 and P14 from both Jurkat cell lines, they showed similar levels of cell density after normalization to basal growth. This is promising in terms of experimental consistency as the two unique cell lines of similar maturation were able to produce similar cell density levels, independent of the stimulants.

In conclusion, we found that both Jurkat cell lines were capable of stimulation from APC-like antibodies, αCD3 and αCD28, as well as PMA. We also found that the stimulation conditions could be replicated, not only between passages, but also between separate lineages of the same cell line. Furthermore, when passage numbers exceeded 15 the cells were often insensitive to stimulation. These cells are unlikely to have the same genetic expression as their earliest passage. These stimulating conditions and guidelines were then maintained in subsequent cell assays, this standardization allowed for better collection of our cell data and helped reduce experimental bias.

Well Volume and Seed Density Does Not Appear to Influence Stimulation

While continuing our scouting of stimulation optimization, we wanted to determine the appropriate growth conditions for stimulation by directly measuring high and low seeding densities to determine if quorum-sensing of cells may be affecting stimulation.

Figure S5.3 shows the normalized cell density of the two Jurkat cell lines, where 100 000 cells were seeded in 350 µL well and incubated overnight in the presence of mAb or PMA/ionomycin. Unstimulated Jurkat cells had an increase in cell density by 2.8-fold, whereas both stimulants affected both Jurkat cell lines, resulting in a 3.5-fold increase in density with respect to the seeding density. While the stimulating effects of PMA had shown a similar magnitude on both cell lines, the older series of Jurkat cells (W) had broader variation in the cell count overall indicating some form insensitivity once the cells are passaged beyond 10 times.

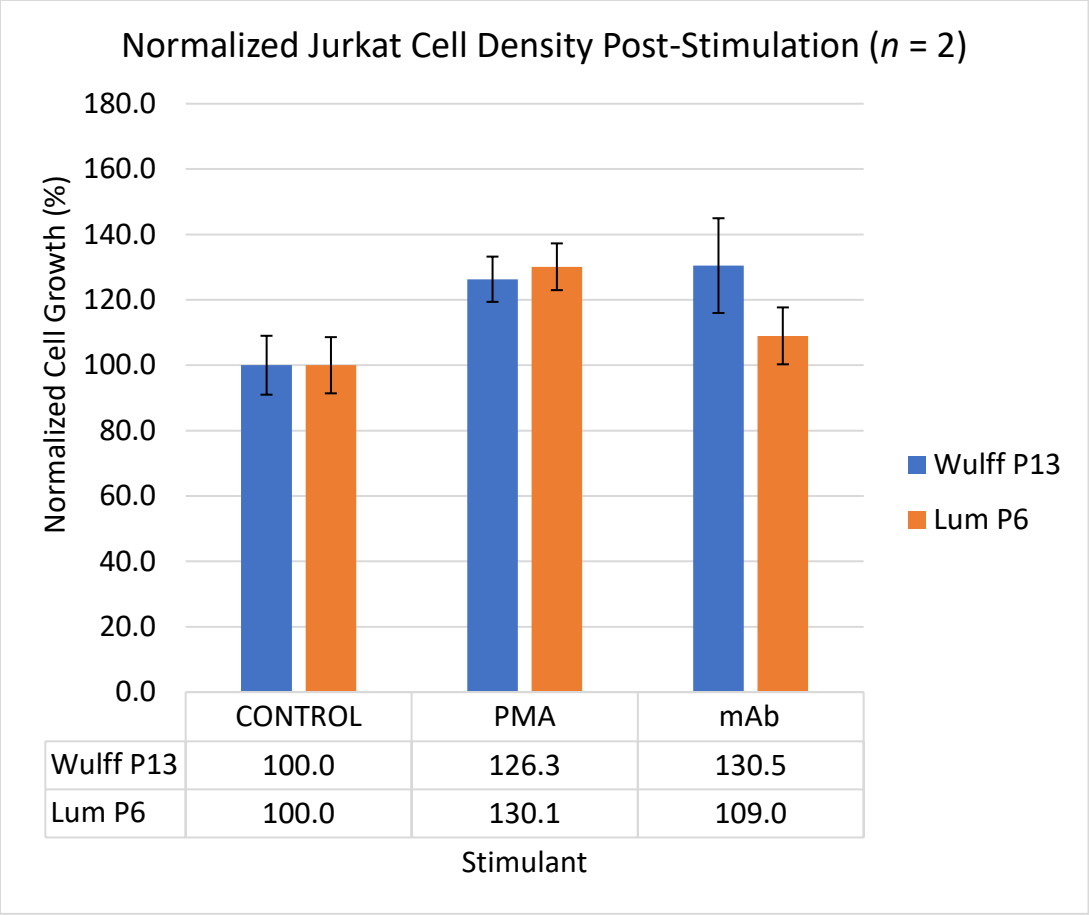

	CONTROL	PMA	mAb
Wulff P13	100.0	126.3	130.5
Lum P6	100.0	130.1	109.0

Figure S5.3 Jurkat cells were seeded at 285 000 cells/mL and given PMA/ionomycin (PMA) or a monoclonal antibody (mAb) cocktail and grown overnight. The stimulated Jurkat cells were then measured the following day by hemocytometer and the density was compared to the respective non-stimulated control. The values presented in the table are observed densities normalized to unstimulated growth. This is a technical singlet, where samples from the same well were measured twice.

When the stimulation was performed in a larger volume 12-well plate rather than a 96-well plate, we observed similar intensities of growth after normalization to unstimulated cells (Figure S5.4). Approximately 200 000 cells were seeded in a 3-mL well with a final volume of 2.6 mL (~77 000 cells / mL). These cells were stimulated with the same mAb cocktail or PMA/ionomycin mixture with respect to the number of cells present. Unfortunately, there was large variation in cell density observed in the basal growth control. This is attributed to poor sample preparation, where poor agitation of the wells aliquots resulted in varied observed cell densities. This was later rectified when we were no longer scouting conditions for stimulation. Regardless, we observed an overall trend of higher density when stimulants are present in both small (350 µL) and large (2600 µL) volumes. In both cases of high and low-density seeding we do observe similar magnitudes of cell density the following day, where the presence of the stimulants has a 30% increase in cell density relative to the basal growth population, indicating there may not be an apparent dependency on seeding density under these stimulating conditions.

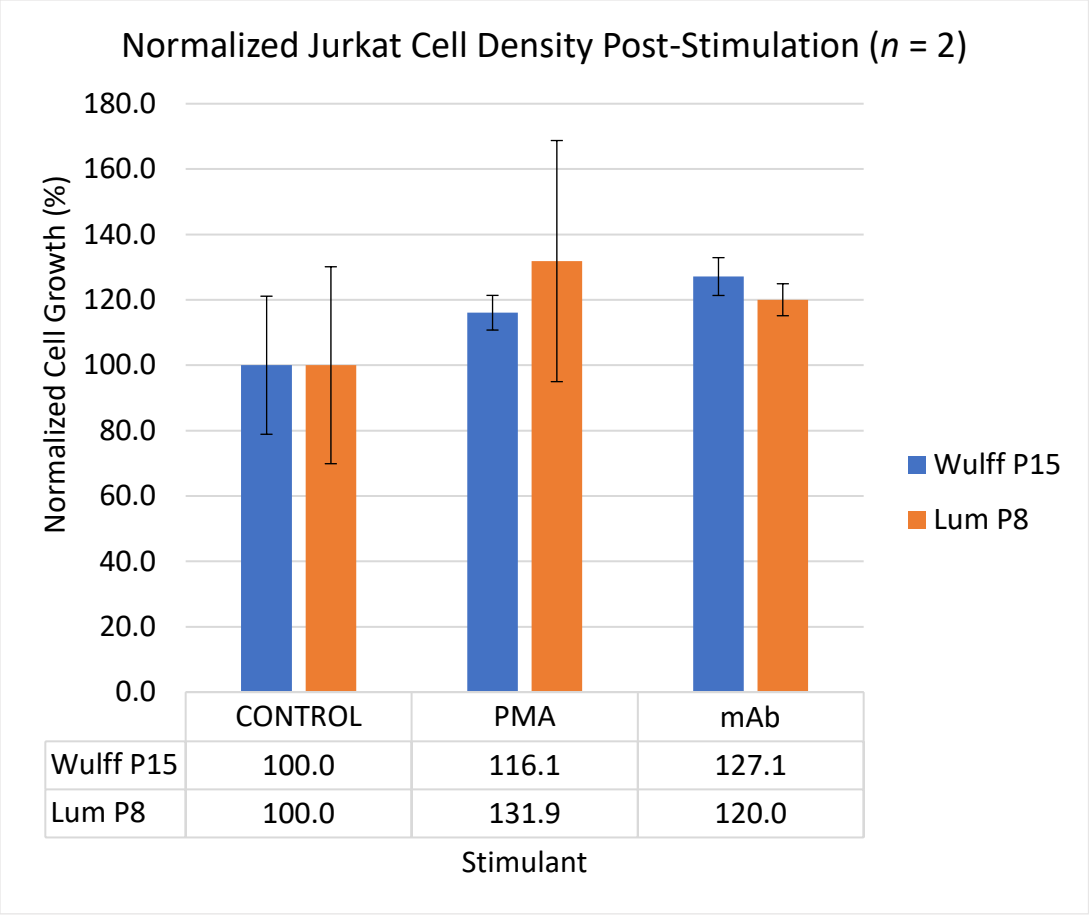

	CONTROL	PMA	mAb
Wulff P15	100.0	116.1	127.1
Lum P8	100.0	131.9	120.0

Figure S5.4. Two separate Jurkat cell lines were seeded at a lower density of 77 000 cells/mL and given PMA/ionomycin or a monoclonal antibody cocktail and grown overnight. The stimulated Jurkat cells were then measured the following day by hemocytometer and density was evaluated with a non-stimulated control. The values presented in the table are observed densities normalized to unstimulated growth. This is a technical singlet, where samples from the same well were measured twice.

Quorum sensing in cells is what allows crosstalk between stimulated and unstimulated cells.[343] We aimed to measure if the overall cell density had a detrimental effect on the proliferation of the white blood cells. We found no difference in the magnitude of normalized cell growth between a low density (Figure S5.4) and high density (Figure S5.3). If the lower density seeds had shown a high rate of growth (i.e., higher density within growth period), this may indicate that overseeding may have hindered stimulation. However, all cases where stimulant was present resulted in higher cell density. This indicates that the density may not be an inhibiting factor to achieve T cell activation. If there were density-dependent conditions attributed to quorum sensing and stimulation, then another series would be required to determine those extremes. Similarly, there could be other variables that affect the stimulability of the Jurkat cells and trying to investigate the possibility of discreet parameters was outside of the scope of this project.

Overstimulation and Toxicity

Our assumption in stimulating cells with commercial reagents is based on a volumetric ratio between the stimulant and the initial cell density. However, it is uncertain if this ratio is based on the seeding density in the well or the final concentration (the addition of the stimulant will dilute the concentrations of cells and the stimulant). In some cases, the literature describes the optimal concentrations of the stimulant

but not explicitly with any relation to how many cells. We aimed to verify our assumption of 1 stimulant per 1 000 000 cells per mL, and if the ratio can be proportionally related to the seeding density.

This is significant because these compounds may also be toxic at proportionally high concentrations. By more closely following the stimulating conditions, we may obtain a better understanding of how to approach optimizing the stimulation of the white blood cells.

If 1 µg αCD3 and 5 µg αCD28 are required to stimulate 1 000 000 cells in a well, then if we wanted to seed 250 000 cells, we would require final masses of 0.25 µg αCD3 and 1.25 µg αCD28, respectively. If we stimulated based on density rather than the cell number, a lower volume/higher concentration would require effectively more stimulant, increasing the risk of toxicity. This assumption was carried forward during our investigation to stimulate the two Jurkat cell lines.

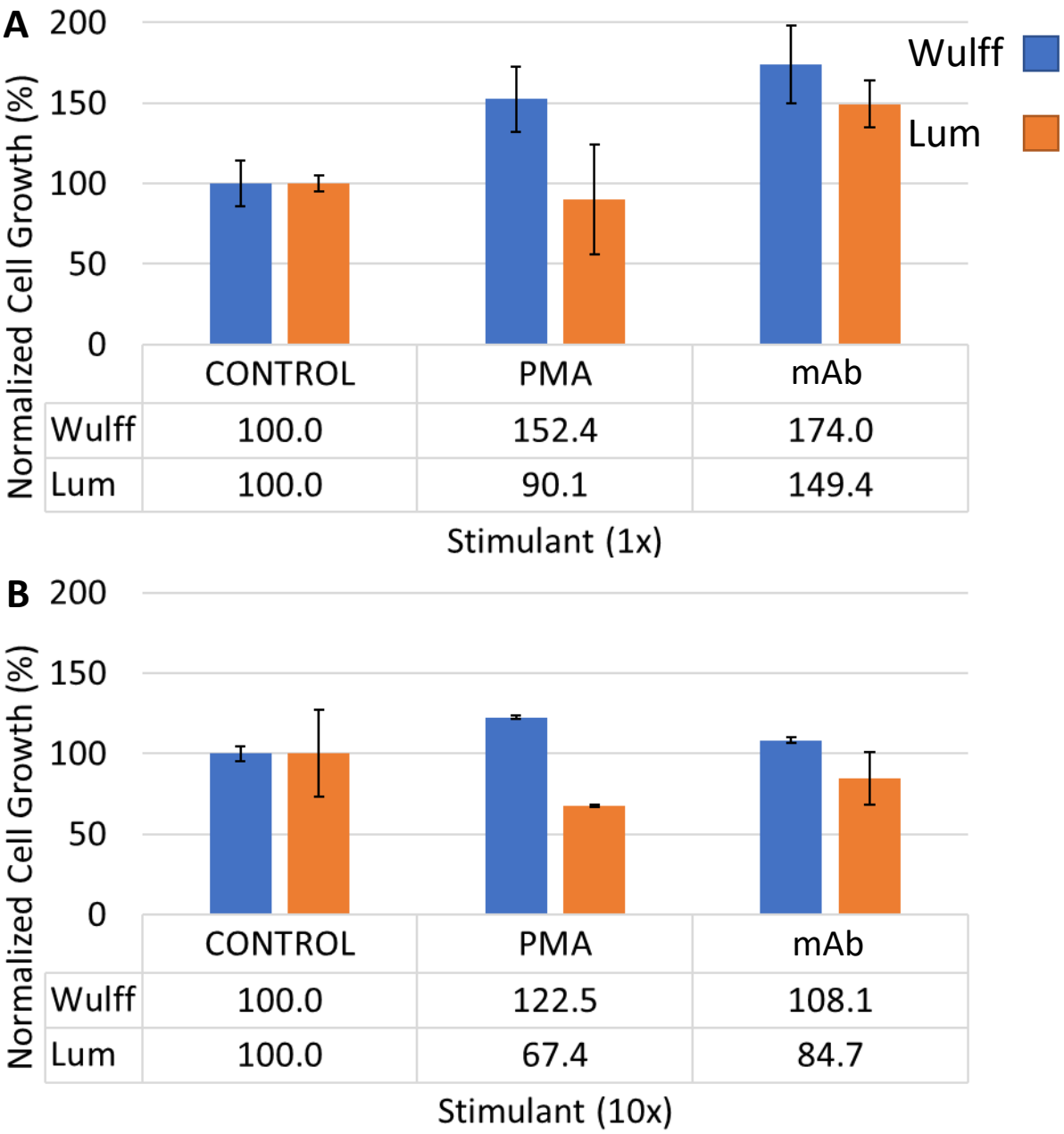

Figure S5.5. High concentrations of stimulants have negative impacts on the proliferation of Jurkat cells. The two Jurkat cell lines were exposed to either **A**. 1x (1 vol. eq. per 10^6 cells) or **B**. 10x (10 vol. eq per 10^6 cells) of either mAb cocktail or PMA/ionomycin to induce a proinflammatory response. The growth was normalized with a non-stimulated control series of the same cell line. These values are averages of two cell counts measured by hemocytometer, but from one well measured twice. The blue data set were Jurkat cells that were on passage 15 and orange data had cells on passage 8. The 1x stimulant data was also used in the composite data presented in Figures S5.7C and S5.7D.

Figure S5.5 shows that if the stimulant concentration is too high, we obtain less growth overall, indicating that the concentration may be toxic above a certain threshold. Both Jurkat cell lines that were stimulated with a 10:1 ratio of stimulant per 1 000 000 cells (Figure S5.5B) had consistency lower cell densities when compared to their 1:1 equivalent (Figure S5.5A). The apparent depression in the Jurkat cell viability from

either stimulant (90% population relative to unstimulated) can be more attributed to the variance when the sample was measured, due to the wide 40% margin, than as an indicator of no or low stimulation of the white blood cells. This further indicated better handling of samples was required for the hemocytometer for it to be an appropriate readout for these experiments.

The takeaway is the 1:1 stimulant to cells ratio had a higher overall cell density, and the 10:1 had consistently lower cell density. We see that the higher (10x) concentration of stimulants had a worse effect on the lower passage of Jurkat cells (from the Lum Lab), indicating the potential toxicity of the stimulants. It is possible that the Wulff cells, being a later passage number, may be less sensitive to stimulation. Conversely, we see that the "more appropriate" 1x amount of stimulant had more proliferative effects indicative of T cell activation in both cell lines. When the 1:1 ratio was repeated in the following passage (Figure S5.6), the observed cell population with stimulant populations are greater than their respective basal growth conditions; this is indicative of stimulation. These stimulation conditions were repeated to show the general trend of stimulation and reproducibility of these experiments (Figure S5.7).

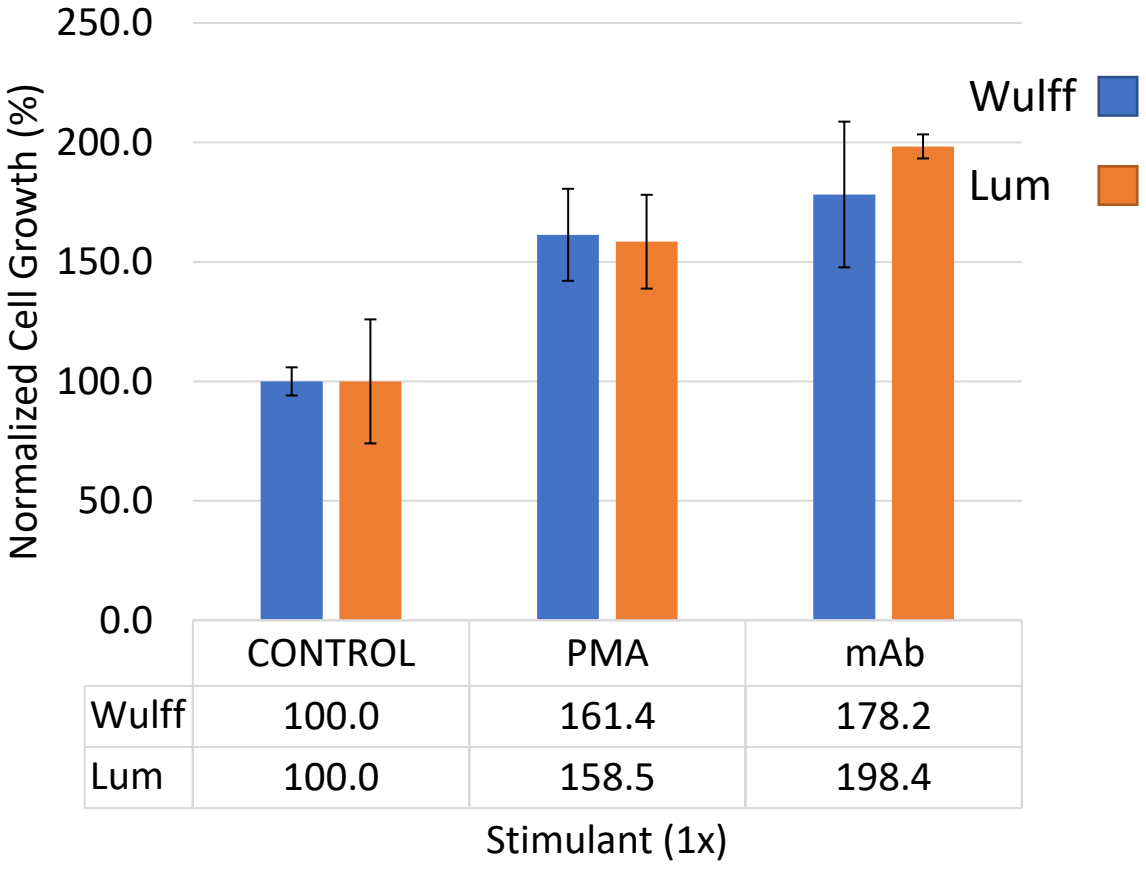

	CONTROL	PMA	mAb
Wulff	100.0	161.4	178.2
Lum	100.0	158.5	198.4

Figure S5.6. The two Jurkat cell lines were passaged and given another 1x of PMA or mAb cocktail. The cells were counted by hemocytometer the following day and density was normalized to their respective non-stimulated control. The values presented in the table are observed densities normalized to unstimulated growth. This is a technical singlet, where samples are from the same well were measured twice. The blue data set were Jurkat cells that were on passage 16 and orange data had cells on passage 9, respectively. The 1x stimulant data was also used in the composite data presented in Figures S5.7C and D.

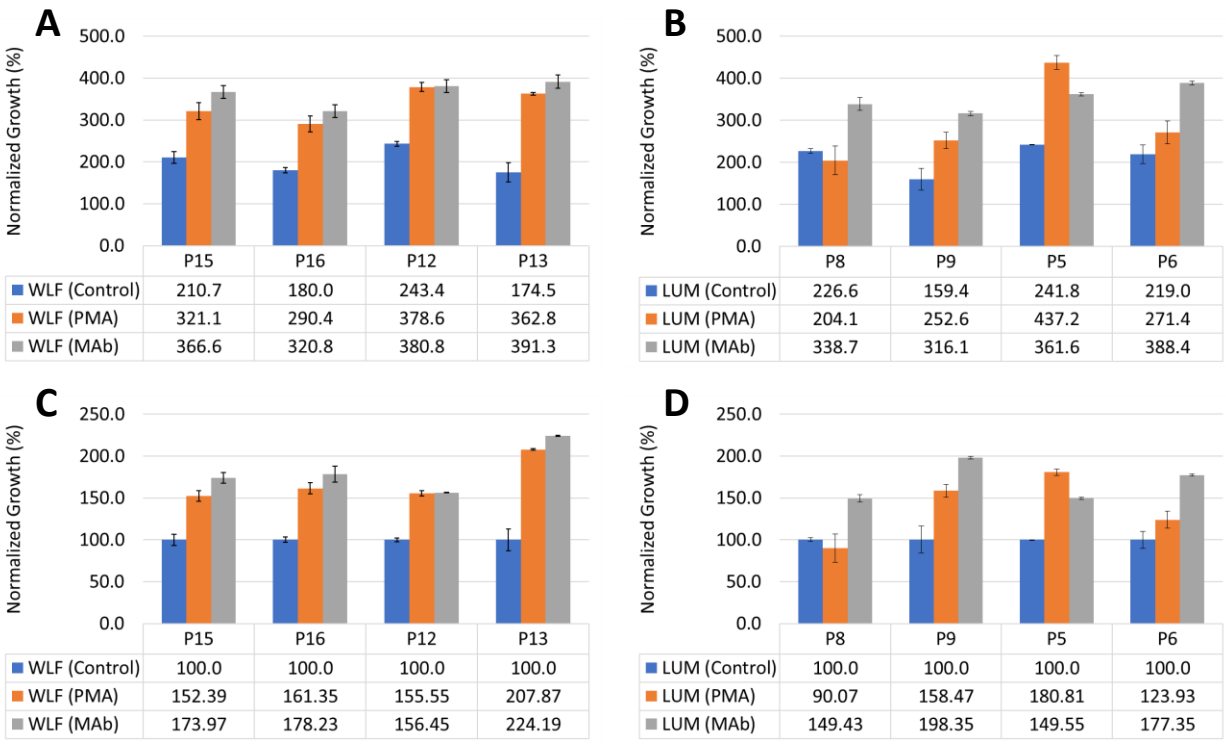

Figure S5.7. Comparison of cell growth between two Jurkat cell lines (Wulff – W, Lum – L) stimulated with either 1x PMA or mAb cocktail. The top row displays the normalized growth of Jurkat cells with respect to the initial seeding densities (**A**, **B**), and the bottom row shows the induced growth with respect to basal unstimulated growth (**C**, **D**) for the respective cell lines Wulff (W) and Lum (L) Jurkat cell lines. The cell density was calculated as a sample average of three hemocytometer reads of the same well, and the bars are relative error. The seeding densities were 213 (**A**), 267 (**B**), 250 (**C**), and 250 (**D**) (x1 000) cell/mL for both cell lines at the corresponding passage numbers.

Using a second series of Jurkat cells helped affirm that the stimulants are causing the higher cell density observed overnight by inducing a T cell response. The consistent growth patterns suggest that both Jurkat cell lines were being activated by the stimulants (Figure S5.7). If the cells are being stimulated, then we should also expect that they are matured and have a higher expression of PD-1 and cytokines. The independent monitoring of two separate cell lines resulting in consistent stimulation data over time removes variables initially affiliated to contamination and mishandling, and empirically shows that the technique is replicable, while also indicating that the stimulants are inducing proliferation.

The following day the cells were counted via hemocytometer and the %-growth was determined in respect to that initial seeding density (Figure S5.7A, B). However, to ascertain growth attributed to stimulants, we looked at the density when normalized to basal cell growth population (Figure S5.7C and D). The overall trend observed was that both stimulants were able to consistently induce a higher cell density of the Jurkat cells. Despite the promise of higher cell densities attributed to stimulants, we wanted to corroborate our findings by quantifying cytokine content post-stimulation using an ELISA. However, we could not obtain any corroborating data to support this claim (i.e., ELISA detecting cytokines).

ELISAs Require a Lot of Optimization…

Upon T cell activation, we expected higher genetic expression PD-1 and pro-inflammatory interleukins.[207,291,337] To measure the cytokines, we wanted to employ an enzyme-linked immunosorbent assay (ELISA) for IL-2, a pro-inflammatory cytokine. We expected that by observing a significant increase in the presence of IL-2 caused by a stimulant, we could ascertain that our T cells were truly "activated" and matured lymphoblasts.

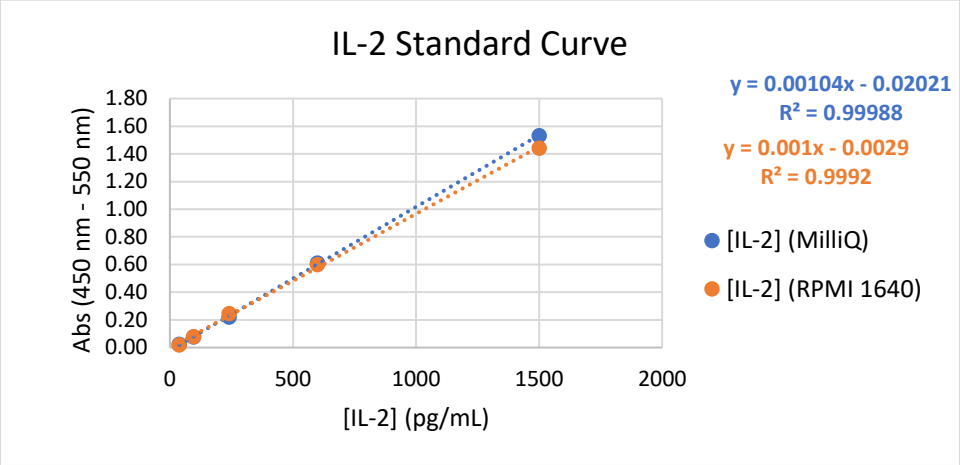

Figure S5.8. Complete growth media has no apparent effect on detecting the IL-2 standard. Presented are two standard curves where IL-2 was reconstituted in either RPMI 1640 complete growth media (1% Pen/Strep, 10% FBS) or MilliQ water.

By knowing that the media does not interfere with IL-2 binding to the wells as concluded from Figure S5.8, this should allow us to measure the cellular supernatant directly when assessing the various stimulation samples from Figure S5.7 (Figure S5.9).

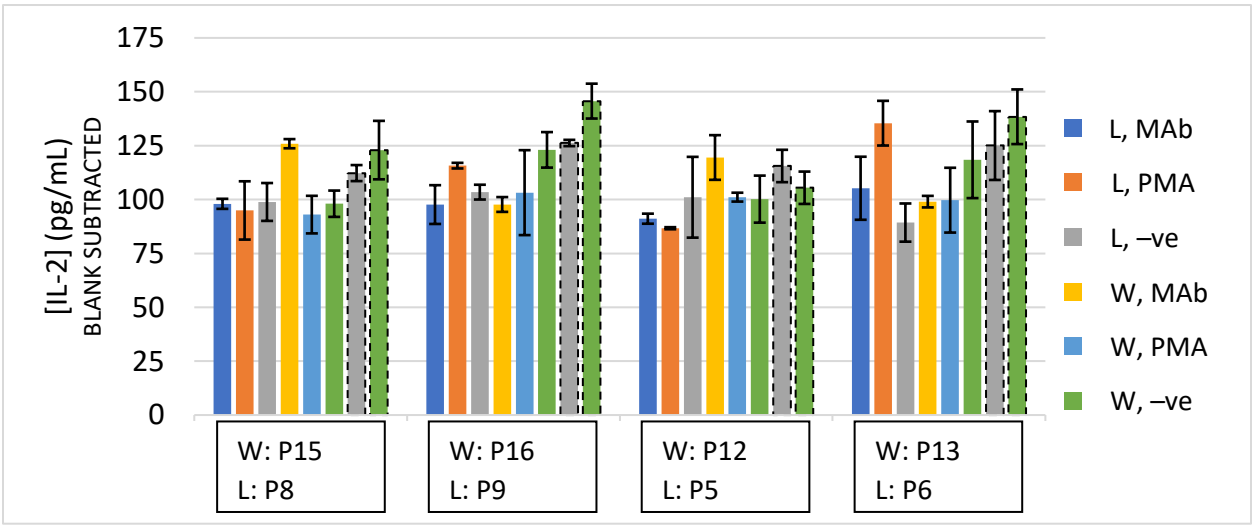

Figure S5.9. Correlated values of IL-2 detected in two independently stimulated Jurkat cell lines passaged over time (W – Wulff, L – Lum). These values were determined from the absorbance of samples and correlated with the media-based standard curve (Figure S5.8). The bars represent the variance of two measurements. All samples were diluted 10-fold, except for samples outlined, which were not diluted.

Unfortunately, there is no difference in the measured absorbance intensity between stimulated Jurkat cells and their respective controls. Therefore, we cannot validate that the cells were activated as the absorbance intensity was near the lower limits of detection for the cytokines. We anticipated that higher cell density attributed to stimulants would be equally as apparent with a proper reporter species (i.e., more cells from stimulant, indicates higher amount of cytokine). However, as we did not detect any IL-2 we continued to investigate the stimulation conditions.

PHA as a Stimulant

As both PMA/ionomycin and the costimulatory antibodies were not inducing detectable amount of IL-2, we investigated another immunostimulant, phytohemagglutinin (PHA).

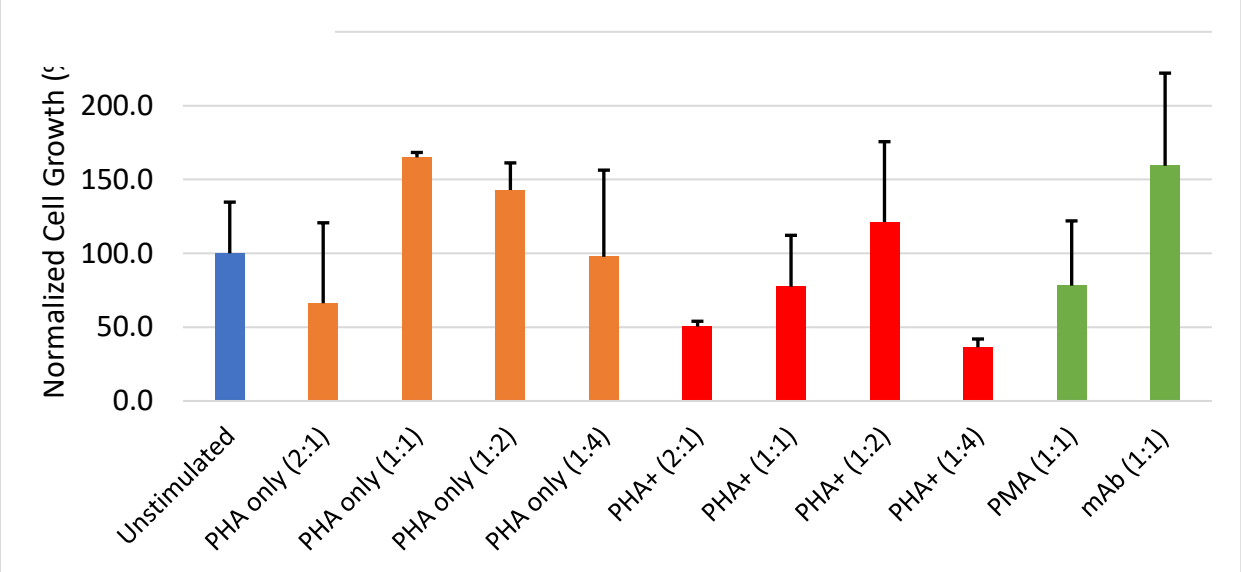

Figure S5.10. Scouting conditions to determine PHA as a stimulant for T cell activation. In a 12-well plate, 100 000 Jurkat cells were stimulated with PHA alone, or PHA and ionomycin (1 µM) (PHA+). After an overnight incubation, wells were agitated using a micropipette to disperse cells and were counted using at least two independent reads from a hemocytometer to determine an average of the population. We titrated varied concentrations of the PHA to scope where it has the most prominent effect on T cell growth and therefore attributed to T cell activation. The bars are the standard deviation of the collective sample. The previous stimulants were also measured to maintain experimental consistency; PMA contains 1 µM ionomycin and mAb is the previously described cocktail mixture of αCD3 and αCD28.

Figure S5.10 shows the titration of PHA ratios to stimulate 100 000 Jurkat cells (Lum P7) with a similar ratio as described previously. It is more evident that when there is twice as much stimulant (2:1), regardless of the presence of ionomycin we see a decrease in cell population, indicating potential toxicity. The presence of ionomycin did not have any effect on the stimulation conditions (red data). There is an apparent increase in Jurkat cell density at lower ratios of PHA. The apparent stimulation is completely removed when PHA is reduced further (1:4). Interestingly, the 1:4 ratio without ionomycin (orange) had no apparent effect of stimulation. These samples were measured by hemocytometer as previously described, where the presented value is the average calculated cell density of a single well measured twice. Therefore, these error bars should be taken with caution. The takeaway was that PHA alone could be a suitable stimulant for the Jurkat cells as it displayed similar growth as the PMA and mAb cocktail.

When the experiment was repeated with both Jurkat cell lines, the sensitivity to stimulation as predicated by cell maturation becomes more apparent as the Wulff Jurkat cells consistently show lower density

overall regardless of the stimulation source (Figure S5.11). This experiment was repeated once more with lower passage numbers from both cell lines and observed the similar overall trend (Figure S5.12) reinforcing that PHA would be a suitable stimulant for consistent Jurkat activation. Unfortunately, when these samples were evaluated in an ELISA, the detection of the cytokines was persistently below the limit of detection (data not shown). The cell count stimulation experiment was repeated once more to improve the signal-to-noise ratio. This reduced the error and emphasized the effects of the stimulants on Jurkat cell growth (Figure S5.13). The subsequent passages were then used to make a composite figure to show the consistent higher density attributed to the stimulants (Figure S5.14), which further indicated that cells grown beyond passage number 13 become more insensitive to stimulation.

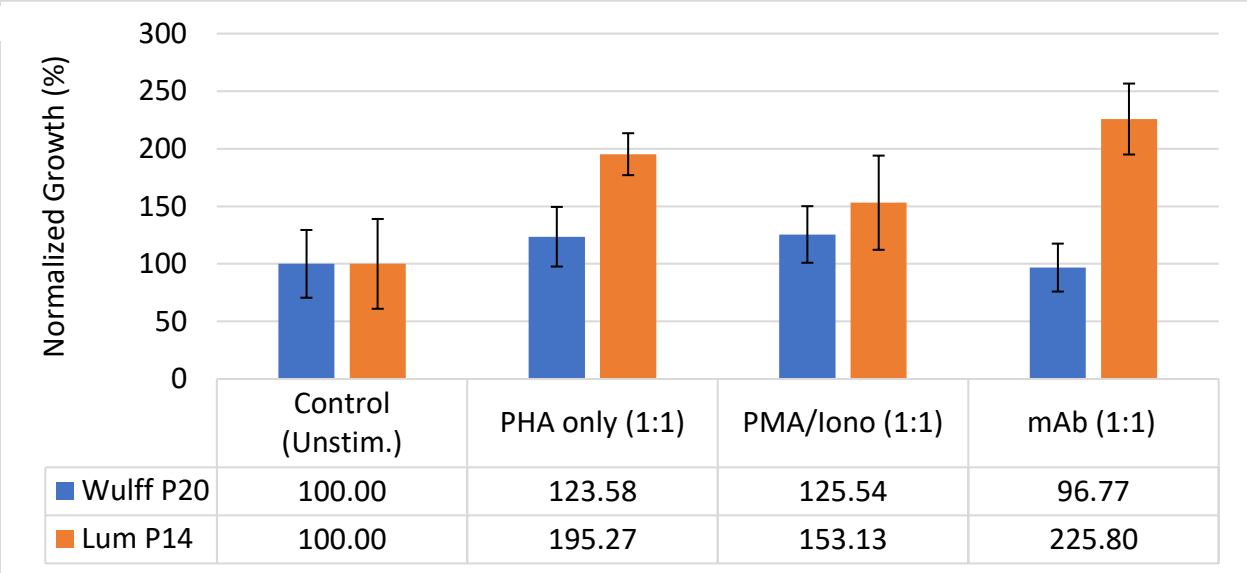

	Control (Unstim.)	PHA only (1:1)	PMA/Iono (1:1)	mAb (1:1)
Wulff P20	100.00	123.58	125.54	96.77
Lum P14	100.00	195.27	153.13	225.80

Figure S5.11. Older Jurkat cells are less susceptible to stimulation. Comparison of stimulation when given 1x stimulant to two separate Jurkat cell lines. The blue data set were Jurkat cells that were on passage 20 and orange data had cells on passage 14. These are calculated sample averages of at least three hemocytometer measurements and the bars are standard deviations, which are normalized to an unstimulated control.

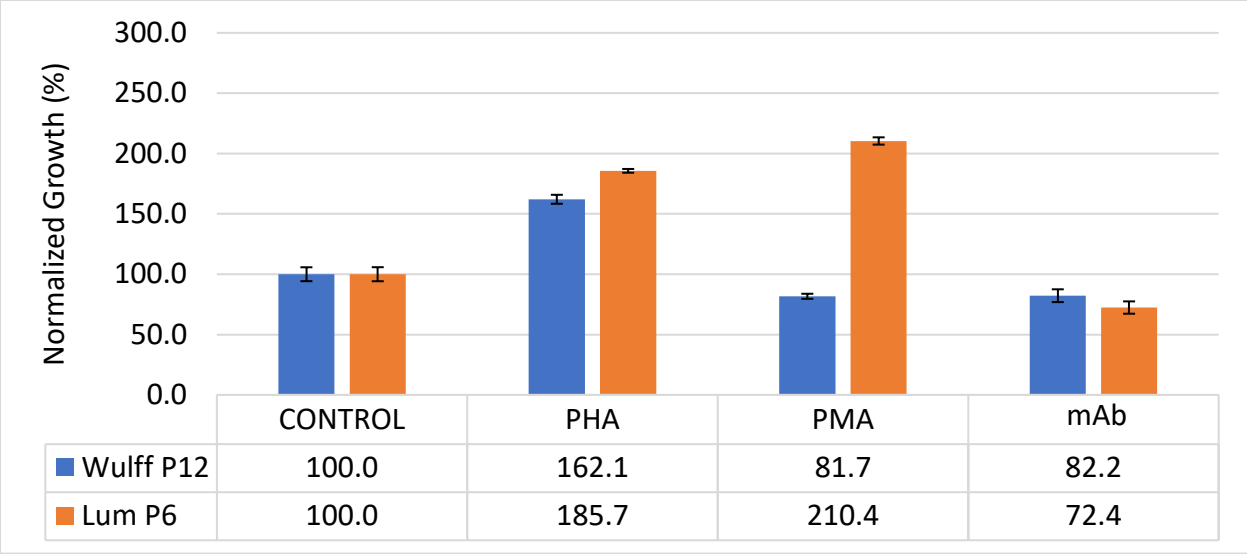

	CONTROL	PHA	PMA	mAb
Wulff P12	100.0	162.1	81.7	82.2
Lum P6	100.0	185.7	210.4	72.4

Figure S5.12. Jurkat cells from fresh split were stimulated again to corroborate previous PHA-stimulation-optimization findings. The blue data set were Jurkat cells that were on passage 12 and orange data had cells on passage 6. Jurkat cells were monitored for stimulation with various proinflammatory stimulants. These are calculated sample averages of at least three hemocytometer measurements and the bars are standard deviations.

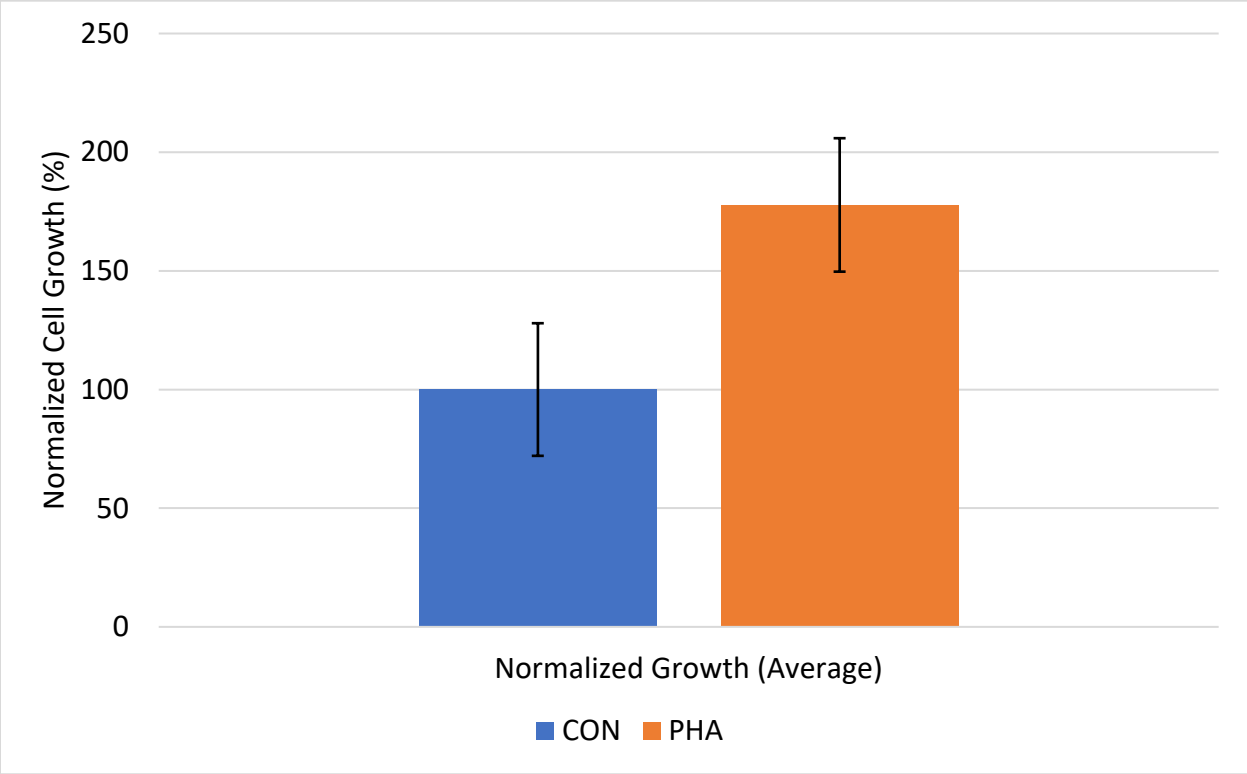

Figure S5.13. PHA yield consistently higher cell density relative to basal growth, indicating sufficient stimulation of the Jurkat cells. Four wells were independently seeded with 100 000 Jurkat cells (Passage 9) and grown overnight either with 1x PHA or equivalent volume of media. The bars represent error of the duplicates of at least three hemocytometer reads, where $n = 2$.

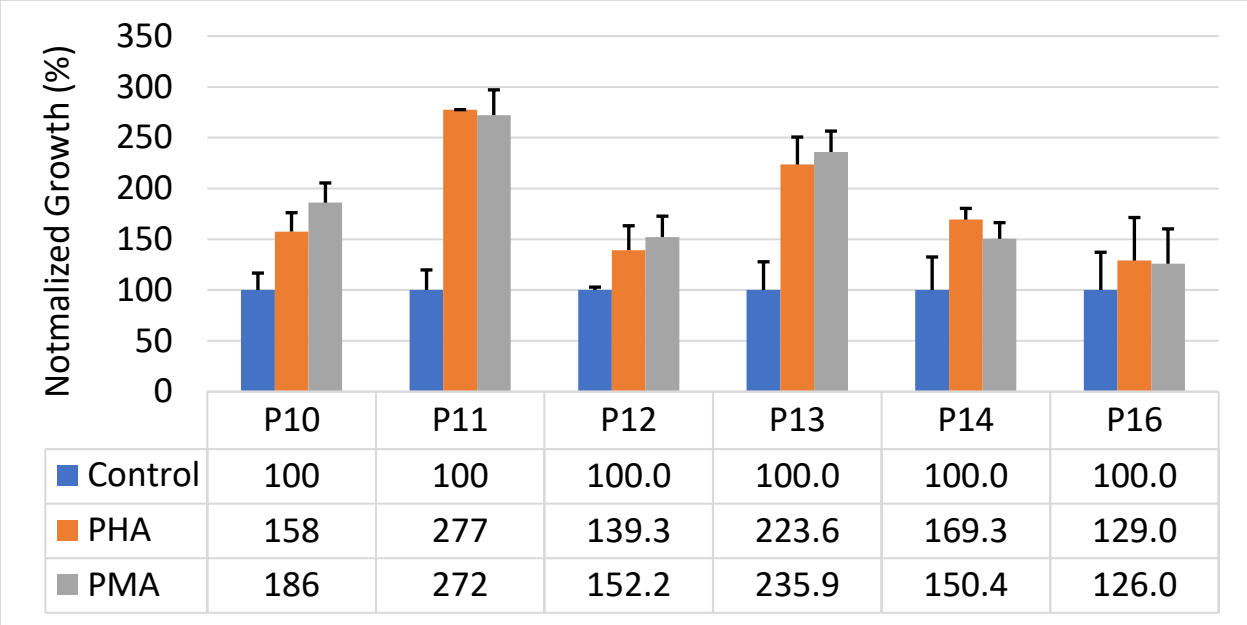

	P10	P11	P12	P13	P14	P16
Control	100	100	100.0	100.0	100.0	100.0
PHA	158	277	139.3	223.6	169.3	129.0
PMA	186	272	152.2	235.9	150.4	126.0

Figure S5.14. Jurkat cells were monitored for stimulation with either PHA or PMA to visualize when the cell become insensitive in later passage numbers. The bars represent standard error of two biological replicates of two independent wells of seeded with 250 000 cell/mL, and were spiked with stimulant (PMA or PHA) or complete growth media (control) and grown overnight. The cells were measured the following day by hemocytometer. The cell density values were normalized with respect to the unstimulated Jurkat cell growth. Control and PHA-stimulated samples from P10 and P11 were evaluated for production of IL-6 and IL-2 by ELISA (unfortunately, detection was below the absorbance limit). The Jurkat passage P13 is also shown in Figure S5.16 (blue data). Relative growth with respect the seeding density is shown in Figure S5.15 and relevant statistical data is found in Table S5.1.

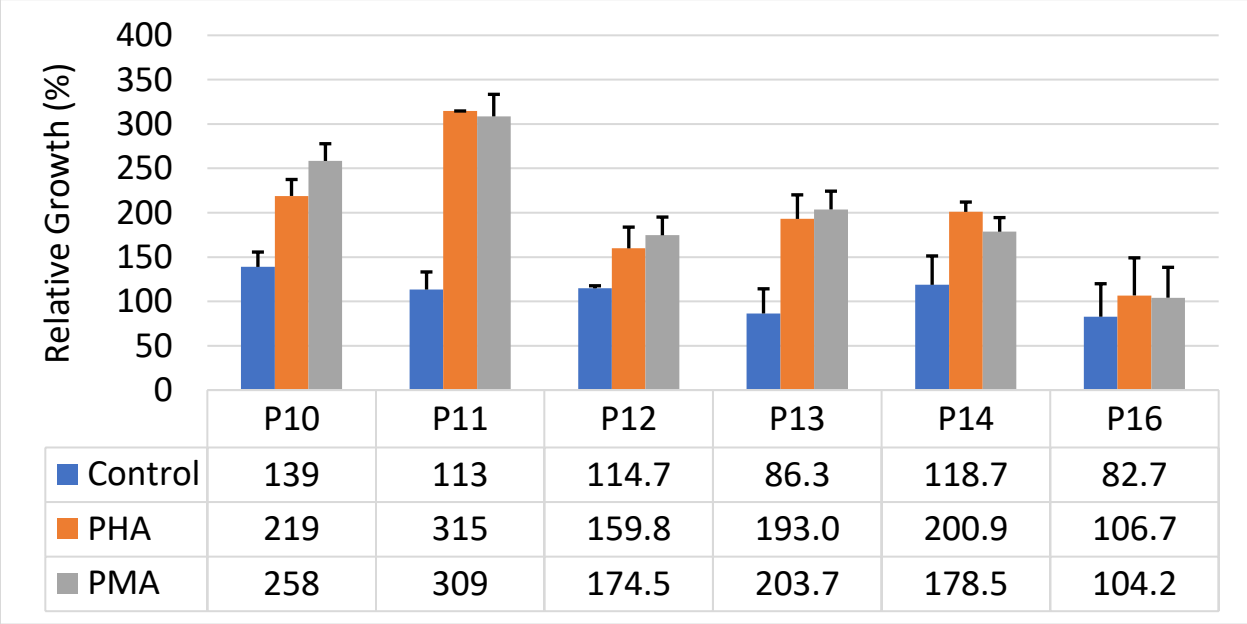

	P10	P11	P12	P13	P14	P16
Control	139	113	114.7	86.3	118.7	82.7
PHA	219	315	159.8	193.0	200.9	106.7
PMA	258	309	174.5	203.7	178.5	104.2

Figure S5.15. Relative growth of Jurkat cells expressed as percent with respect to the initial seeding density of 250 000 cell/mL. This was done to determine if basal growth conditions were showing signs of contamination, measuring if the growth rates were unusually fast. The bars are relative with respect to standard deviation of the observed populations of at least 3 measured samples by hemocytometer, where smaller bars indicate more robust sample collection.

Apparent Immunosuppression of T Cell Activation in the Presence of Solubilized PD-L1

Given the apparent success of T cell activation with PHA, we attempted to shut down the activity by co-incubating PD-L1 with the stimulated T cells. Due to the immunosuppressive activity between PD-1 and PD-L1, we expect to observe no change in cell density between basal growth and PD-L1+stimulant conditions. This would indicate that PD-L1 is binding to PD-1 and is shutting down the proliferative signal.

To investigate the immunosuppressing effects of PD-L1 on immunostimulated lymphoblasts, we incubated PHA-stimulated Jurkat cells with an aliquot of 400 nM solubilized PD-L1, where each well had a final concentration of 11 nM PD-L1. The cells were allowed to grow overnight and counted using hemocytometer (Figure S5.15). In both cases where a stimulant was added, the Jurkat cells population was much greater than the respective basal growth control (blue data). However, when PD-L1 was also present (orange data), there was no significant difference in the cell density relative to the basal growth control. This is indicative of the turn-down effects on stimulation that PD-L1 has on T cells, and we used this model to further investigate potential recovery by disrupting the PD-1/PD-L1 interaction.

The Presence of PD-L1 Inhibits Immune Stimulation *In Vitro*

The stimulation conditions were finalized as 1 µg PHA per 10^6 Jurkat cells, this was the ratio required to observe consistently higher next day cell density when compared to an unstimulated control. We continued our studies by intentionally trying to deter the growth by co-incubating with PD-L1 and following the passages through time (Figure S5.16). We expected that the addition of PD-L1 will bind to PD-1 on the Jurkat cells and prevent the pro-inflammatory response induced by the stimulants, showing no significant growth with respect to the non-stimulated cells.

The Jurkat cells were stimulated with either PHA or PMA, and with or without 11 nM solubilized PD-L1. The cells were grown overnight, and cell density counted as previously described using the hemocytometer. In all cases, the presence of PD-L1 resulted in no apparent “growth” when compared to the non-stimulated control.

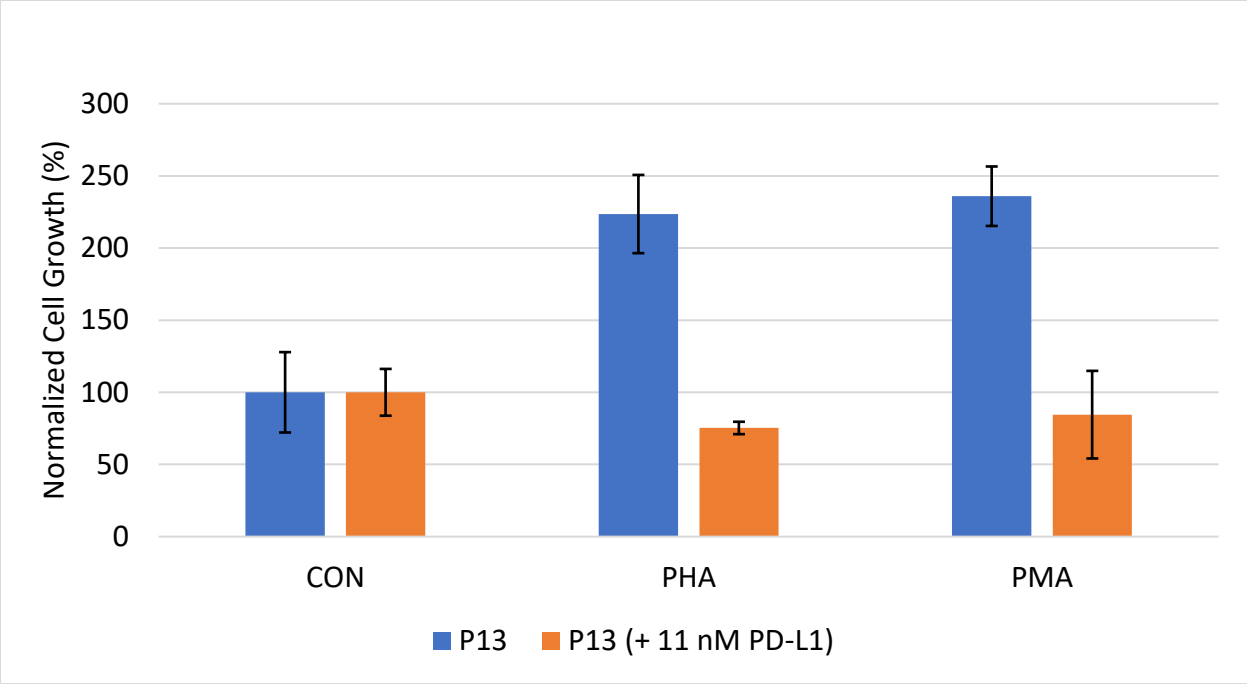

Figure S5.16. The presence of solubilized PD-L1 prevents the stimulated growth phenotype of Jurkat cells attributed to stimulants, PHA and PMA. The bars are standard deviation of two biological replicates of at least three hemocytometer measurements. Statistical data can be found in Table S5.1. This data is also presented as P13 in Figure S5.14, and relevant statistical data is found in Table S5.2.

Figure S5.16 shows that PD-L1 deters the stimulating effects of PHA and PMA, as the PD-L1^{+} samples (orange) show no significant growth with respect to the unstimulated controls. Using a One-way ANOVA analysis, the increase in cell density from either stimulant showed no significant growth with respect its basal equivalent (Table S5.1). However, PHA-stimulated Jurkat cells had a P-value close to significance ($P = 0.061$), indicating that PHA does have a proliferative effect on the density of the cells. Although a significant decrease in cell density was observed ($P = 0.036$), when PHA-stimulated/PD-L1 inhibited Jurkat cells (PHA, orange) was compared with their PD-L1 incubated control (CON, orange). This decrease was not relevant as the protein is not considered toxic and is more likely due to data collection error, as all wells with PD-L1 present shared a similar magnitude of cell density to the unstimulated Jurkat cells.

Our experiments continued to follow the passages of the Jurkat cells with these stimulants to visualize their insensitivity in later passage numbers (Figure S5.16). P13 shows the largest contrast of how PD-L1 can reduce proliferation, where 11 nM PD-L1 (hashed data) results in no apparent stimulated cell growth with respect to basal control. Given that the presence of PHA always yielded a higher cell density with respect to the basal growth control, and that this phenotype is no longer present when PD-L1 is added, we can expect that the PHA is causing T cell activation and therefore inducing proliferative effects for a proinflammatory response.

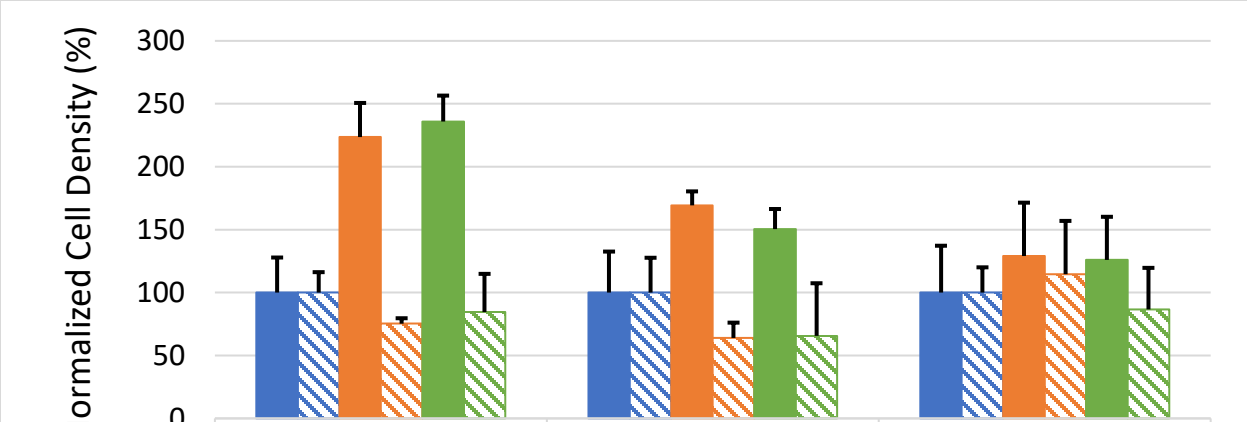

	P13	P14	P16
CON	100	100	100
CON (PD-L1)	100	100	100
PHA	224	169	129
PHA (PD-L1)	75	64	115
PMA	236	150	126
PMA (PD-L1)	85	66	87

Figure S5.17. PD-L1 prevents the proliferative effects induced by PHA (orange) and PMA (green), displaying cell densities equal to the basal growth control. The hashed data are stimulated Jurkat cells treated with PD-L1; P13 contains 11 nM, and P14 and P15 contain 18.5 nM PD-L1. The bars represent standard error of two biological replicates, where each well was measured a sample at least thrice when counted by hemocytometer. P13 data is also displayed in Figure S5.16. The statistical data is show in Table S5.2 and Table S5.3.

When PD-L1 was added to the stimulated Jurkat cells, we observed only unstimulated levels of cell density. This indicated that the PD-L1 was suppressing the T cell activation signal induced by the stimulants (Figure S5.16). With confirmation that PD-L1 was shutting down the stimulation, we sought to recover that "stimulant only" phenotype but in the presence of PD-L1 by employing our antibodies with or without particles. As observed previously, when the passage number exceeded 14, the sensitivity for stimulation became less apparent and there was no significant change in any population (Table S5.2), which gave a cutoff window for when cell studies should be terminated, and a new split should be considered.

Statistical Tables of Figures S5.14–5.17

The following data were collected by a One-way ANOVA paired student t-test, comparing the mean cell densities of Jurkat cells affected by either PHA or PMA and in the presence or absence of the PD-L1 immunosuppressive protein.

Table S5.1. Testing for stimulant impact on cell density over time in Figure S5.14. Although each well was only measured once, the test was looking at specifically whether the stimulants significantly affecting proliferation, and if at what passage number they become insensitive.

P10	*P-value*	Significance?
CON vs. PHA	0.15	ns
CON vs. PMA	0.29	ns
PMA vs. PHA	0.72	ns
P11		
CON vs. PHA	0.06	ns
CON vs. PMA	0.1	ns
PMA vs. PHA	0.93	ns
P12		
CON vs. PHA	0.38	ns
CON vs. PMA	0.39	ns
PMA vs. PHA	0.46	ns
P13		
CON vs. PHA	0.12	ns
CON vs. PMA	0.24	ns
PMA vs. PHA	0.90	ns
+ 11 nM PD-L1		
CON vs. PHA	0.23	ns
CON vs. PMA	0.27	ns
PMA vs. PHA	0.44	ns
P14		
CON vs. PHA	0.089	ns
CON vs. PMA	0.076	ns
PMA vs. PHA	0.12	ns
+ 18.5 nM PD-L1		
CON vs. PHA	0.20	ns
CON vs. PMA	0.81	ns
PMA vs. PHA	0.81	ns
P16		
CON vs. PHA	0.14	ns
CON vs. PMA	0.58	ns
PMA vs. PHA	0.96	ns
+ 18.5 nM PD-L1		

CON vs. PHA	0.91	ns
CON vs. PMA	0.67	ns
PMA vs. PHA	0.34	ns

Table S5.2. Statistical data table of Figure S5.16, comparing the relevant populations before normalizing to the respective basal controls.

P13	*P-value*	Significance?
CON vs. PHA	0.061	ns
CON vs. PMA	0.12	ns
CON vs. CON (PD-L1)	0.24	ns
CON vs. PHA (PD-L1)	0.38	ns
CON vs. PMA (PD-L1)	0.26	ns
PHA vs. PMA	0.45	ns
PHA vs. CON (PD-L1)	0.15	ns
PHA vs. PHA (PD-L1)	0.11	ns
PHA vs. PMA (PD-L1)	0.090	ns
PMA vs. CON (PD-L1)	0.079	ns
PMA vs. PHA (PD-L1)	0.068	ns
PMA vs. PMA (PD-L1)	0.076	ns
CON (PD-L1) vs. PHA (PD-L1)	0.036	*
CON (PD-L1) vs. PMA (PD-L1)	0.067	ns
PHA (PD-L1) vs. PMA (PD-L1)	0.21	ns

Table S5.3. Statistical data table of Figure S5.17, comparing the relevant populations before normalizing to their respective controls as they were passaged over time. The data for P13 is found in Table S5.1.

P14	*P-value*	Significance?
CON vs. PHA	0.045	*
CON vs. PMA	0.038	*
CON vs. CON (PD-L1)	0.31	ns
CON vs. PHA (PD-L1)	0.21	ns
CON vs. PMA (PD-L1)	0.0055	**
PHA vs. PMA	0.062	ns
PHA vs. CON (PD-L1)	0.024	*
PHA vs. PHA (PD-L1)	0.055	ns
PHA vs. PMA (PD-L1)	0.033	*
PMA vs. CON (PD-L1)	0.011	*
PMA vs. PHA (PD-L1)	0.079	ns
PMA vs. PMA (PD-L1)	0.026	*

CON (PD-L1) vs. PHA (PD-L1)	0.19	ns
CON (PD-L1) vs. PMA (PD-L1)	0.057	ns
PHA (PD-L1) vs. PMA (PD-L1)	0.41	ns
P16		
CON vs. PHA	0.072	ns
CON vs. PMA	0.29	ns
CON vs. CON (PD-L1)	0.49	ns
CON vs. PHA (PD-L1)	0.10	ns
CON vs. PMA (PD-L1)	0.15	ns
PHA vs. PMA	0.48	ns
PHA vs. CON (PD-L1)	0.28	ns
PHA vs. PHA (PD-L1)	0.21	ns
PHA vs. PMA (PD-L1)	0.056	ns
PMA vs. CON (PD-L1)	0.099	ns
PMA vs. PHA (PD-L1)	0.16	ns
PMA vs. PMA (PD-L1)	0.21	ns
CON (PD-L1) vs. PHA (PD-L1)	0.46	ns
CON (PD-L1) vs. PMA (PD-L1)	0.33	ns
PHA (PD-L1) vs. PMA (PD-L1)	0.17	ns

Statistical Analysis for Cell Count Immune Exhaustion Recovery Assay in Figures 5.1–5.3

Table S5.4 Statistical analysis for Figure 5.1 monitoring Jurkat cell density upon stimulation of PHA, inhibition with PD-L1, and apparent recovery with αPD-L1 functionalized AuNPs.

P6	P-value	Significance?
Basal vs. PHA Stimulated	0.0007	***
Basal vs. + 32 nM PD-L1	0.9918	ns
Basal vs. + 1.3 nM f-AuNPs	<0.0001	****
Basal vs. + 0.38 nM PEG NPs	0.0651	ns
Basal vs. + 5.7 nM mAb	0.0002	***
Basal vs. + 0.38 nM PEG NPs (– PD-L1)	0.0025	**
PHA Stimulated vs. + 32 nM PD-L1	0.0002	***
PHA Stimulated vs. + 1.3 nM f-AuNPs	0.854	ns
PHA Stimulated vs. + 0.38 nM PEG NPs	<0.0001	****
PHA Stimulated vs. + 5.7 nM mAb	0.9918	ns
PHA Stimulated vs. + 0.38 nM PEG NPs (– PD-L1)	0.9847	ns
+ 32 nM PD-L1 vs. + 1.3 nM f-AuNPs	<0.0001	****
+ 32 nM PD-L1 vs. + 0.38 nM PEG NPs	0.2022	ns
+ 32 nM PD-L1 vs. + 5.7 nM mAb	<0.0001	****
+ 32 nM PD-L1 vs. + 0.38 nM PEG NPs (– PD-L1)	0.0008	***
+ 1.3 nM f-AuNPs vs. + 0.38 nM PEG NPs	<0.0001	****
+ 1.3 nM f-AuNPs vs. + 5.7 nM mAb	0.9961	ns
+ 1.3 nM f-AuNPs vs. + 0.38 nM PEG NPs (– PD-L1)	0.4349	ns
+ 0.38 nM PEG NPs vs. + 5.7 nM mAb	<0.0001	****
+ 0.38 nM PEG NPs vs. + 0.38 nM PEG NPs (– PD-L1)	<0.0001	****
+ 5.7 nM mAb vs. + 0.38 nM PEG NPs (– PD-L1)	0.7696	ns

Table S5.5. Statistical analysis of Figure 5.2.

P9	P-value	Significance?
Basal vs. PHA Stimulated	<0.0001	****
Basal vs. + 32 nM PD-L1	0.99	ns
Basal vs. + 0.46 nM f-AuNPs	<0.0001	****
Basal vs. + 0.61 nM PEG NPs	0.9984	ns
Basal vs. + 5.7 nM mAb	<0.0001	****
Basal vs. + 1.8 nM PEG NPs (– PD-L1)	0.0007	***
PHA Stimulated vs. + 32 nM PD-L1	<0.0001	****
PHA Stimulated vs. + 0.46 nM f-AuNPs	0.6344	ns
PHA Stimulated vs. + 0.61 nM PEG NPs	<0.0001	****
PHA Stimulated vs. + 5.7 nM mAb	0.5755	ns
PHA Stimulated vs. + 1.8 nM PEG NPs (– PD-L1)	0.1998	ns
+ 32 nM PD-L1 vs. + 0.46 nM f-AuNPs	<0.0001	****
+ 32 nM PD-L1 vs. + 0.61 nM PEG NPs	>0.99	ns
+ 32 nM PD-L1 vs. + 5.7 nM mAb	<0.0001	****
+ 32 nM PD-L1 vs. + 1.8 nM PEG NPs (– PD-L1)	0.0002	***
+ 0.46 nM f-AuNPs vs. + 0.61 nM PEG NPs	<0.0001	****
+ 0.46 nM f-AuNPs vs. + 5.7 nM mAb	>0.99	ns
+ 0.46 nM f-AuNPs vs. + 1.8 nM PEG NPs (– PD-L1)	0.0104	*
+ 0.38 nM PEG NPs vs. + 5.7 nM mAb	<0.0001	****
+ 0.38 nM PEG NPs vs. + 1.8 nM PEG NPs (– PD-L1)	0.0003	***
+ 5.7 nM mAb vs. + 1.8 nM PEG NPs (– PD-L1)	0.0087	**

Table S5.6. Statistical analysis of Figure 5.3.

P11	P-value	Significance?
Basal vs. PHA Stimulated	<0.0001	****
Basal vs. + 32 nM PD-L1	0.9045	ns
Basal vs. + 0.53 nM f-AuNPs	<0.0001	****
Basal vs. + 0.49 nM PEG NPs	>0.99	ns
Basal vs. + 5.7 nM mAb	<0.0001	****
Basal vs. + 0.49 nM PEG NPs (– PD-L1)	<0.0001	****
PHA Stimulated vs. + 32 nM PD-L1	<0.0001	****
PHA Stimulated vs. + 0.53 nM f-AuNPs	0.9357	ns
PHA Stimulated vs. + 0.49 nM PEG NPs	<0.0001	****
PHA Stimulated vs. + 5.7 nM mAb	0.9286	ns
PHA Stimulated vs. + 0.49 nM PEG NPs (– PD-L1)	0.1188	ns
+ 32 nM PD-L1 vs. + 0.53 nM f-AuNPs	<0.0001	****
+ 32 nM PD-L1 vs. + 0.49 nM PEG NPs	0.8329	ns
+ 32 nM PD-L1 vs. + 5.7 nM mAb	<0.0001	****
+ 32 nM PD-L1 vs. + 0.49 nM PEG NPs (– PD-L1)	<0.0001	****
+ 0.53 nM f-AuNPs vs. + 0.49 nM PEG NPs	<0.0001	****
+ 0.53 nM f-AuNPs vs. + 5.7 nM mAb	>0.99	ns
+ 0.53 nM f-AuNPs vs. + 0.49 nM PEG NPs (– PD-L1)	0.5245	ns
+ 0.49 nM PEG NPs vs. + 5.7 nM mAb	<0.0001	****
+ 0.38 nM PEG NPs vs. + 0.49 nM PEG NPs (– PD-L1)	<0.0001	****
+ 5.7 nM mAb vs. + 0.49 nM PEG NPs (– PD-L1)	0.539	ns